COMPARISON OF CRYSTALLOGRAPHIC AND CONTINUUM YIELD SURFACES FOR TEXTURED POLYCRYSTALS

by

Ph Lequeu

A Thesis Submitted to the Faculty of Graduate Studies and Research in Partial Fulfilment of the Requirements for the Degree of Doctor of Philosophy

Department of Mining and Metallurgical Engineering
McGill University
Montreal, Canada

August 1986

ABSTRACT

Two opposite approaches have been used in the past for the prediction of plastic anisotropy in deformed materials : (i) the crystallographic Taylor-Bishop and Hill approach; and (ii) that of continuum mechanics. The latter method has proved its ability to represent the plastic anisotropy of metals in a simple way. However, major deficiencies in the predictions obtained by this means are observed, which are reviewed in the present report.

An alternative method, called CMTP (continuum mechanics of textured polycrystals), is described, which combines aspects of both the crystallographic and continuum approaches. Two parameter yield functions are used, the principal axes of which are selected to coincide with the $<100>$ axes of the texture component of interest. These two parameters are adjusted so that the continuum loci give best fits to the Bishop and Hill polyhedron pertaining to a disoriented single crystal displaying a given scatter width. The macroscopic yield locus for a metal containing several texture components is calculated by combining the appropriate CMTP surfaces, each of which corresponds to an observed ideal orientation. Stress and strain rate characteristics are deduced from the size and shape of this locus, respectively. Three types of averaging procedure are used in this work : the Taylor (uniform strain), Sachs (uniform stress direction) and Kochendorfer (law of mixtures) grain interaction models.

Typical experimental pole figures for FCC and BCC metals are decomposed into a limited number of texture components, each of which is characterized in terms of its Miller indices, volume fraction and scatter width. A comparison between the CMTP predictions and Bishop and Hill calculations for yield surfaces as well as strain rate $R(\theta)$ and yield stress $\sigma(\theta)/\sigma(0)$ ratios is carried out using the three deformation models mentioned above. The CMTP predictions give satisfactory results when compared with experimental observations reported in the literature. The present method is also employed to account for the axial strains produced during free end torsion testing as well as for the 'anomalous behaviour' of rolled sheet in terms of the texture displayed by the material under consideration.

RESUME

Deux approches ont été généralement utilisées pour la prévision de l'anisotropie plastique de matériaux déformés. La première, de nature purement cristallographique, se refère aux travaux de Bishop et Hill ainsi que de Taylor. La seconde, à l'inverse, consiste essentiellement en une description macroscopique du comportement du polycristal étudié. Sa formulation extrêmement simple lui confère un certain nombre de faiblesses qui sont discutées dans ce rapport.

Une méthode intermédiaire, appelée CMTP (continuum mechanics of textured polycrystals) est décrite. Elle combine les principaux attraits des deux modèles cités plus haut, à savoir simplicité et prise en compte directe de la texture du matériau. Pour cela, une surface d'écoulement continue est utilisée, dont les axes principaux coincident avec les axes <100> de la composante de texture considérée. Les deux paramètres qu'elle contient sont calculés de telle sorte que la surface continue s'ajuste le mieux possible à la surface d'écoulement cristallographique d'un monocristal désorienté. La courbe limite d'écoulement plastique d'un polycristal contenant plusieurs orientations idéales est alors calculée en moyennant de façon appropriée les surfaces correspondant à chacune d'elles. Les propriétés de contrainte et de vitesse de déformation sont alors déduites respectivement à partir de la taille et de la forme de cette courbe résultante. Trois modèles de déformation plastique ont été utilisés pour la dérivation de ces propriétés plastiques; le premier, dû à Taylor, suppose que tous les grains sont soumis au même état de déformation; le second (hypothèse de Sachs) soumet tous les cristaux à la même direction de contrainte; finalement le modèle de Kochendörfer permet de calculer la vitesse de déformation du polycrystal soumis à une traction uniaxiale par une simple loi des mélanges.

Des figures de poles typiques des métaux CFC et CC sont décomposées en un nombre fini d'orientations idéales. Chacune d'elles est caractèrisée par ses indices de Miller, sa fraction volumique et sa dispersion. Les prévisions obtenues par la méthode CMTP ainsi que par un calcul classique de Bishop et

Hill sont comparées à des résultats expérimentaux publiés dans la littérature, comprenant surfaces d'écoulement, coefficients d'anisotropie R(θ) et rapports de contraintes d'écoulement $\sigma(\theta)/\sigma(0)$. Il en résulte qu'un bon accord d'ensemble est obtenu entre les propriétés plastiques expérimentales et celles calculées par la méthode CMTP. De façon analogue, les déformations axiales produites lors d'un essai de torsion à longueur libre ainsi que le comportement 'anormal' de certaines tôles laminées sont expliqués grace à cette technique par la présence dans le matériau de certaines composantes de texture.

ACKNOWLEDGEMENTS

The author would like to express his sincere gratitude to Professor J. J. Jonas, director of this research, for his support and constant encouragement. He is also indebted to Professor F. Montheillet, who introduced him with great patience to the exciting fields of mechanical metallurgy and texture.

Que Brigitte Bacroix trouve ici l'expression de mes plus sincères remerciements pour sa constante disponibilité, son aide efficace et sa bonne humeur permanente.

The author also thanks Drs. J. L. Bassani, J. Driver, P. Gilormini and R. Fortunier for their many fruitful suggestions and for a number of stimulating discussions. The author is also grateful to Dr. M. Arminjon of IRSID (France) as well as to Drs. D.J. Lloyd and M. Búll of the ALCAN Laboratories (Kingston) for permission to refer to some of their unpublished work. He also expresses his particular appreciation to his friends in the laboratory who shared the same interests, as well as to Lorraine Mello and Carole Rousseau for their help and constant good humor.

"On a beau avoir une santé de fer,
on finit toujours par rouiller"
J. Prévert

à celles et ceux que j'aime

TABLE OF CONTENTS

LIST OF FIGURES

Figure | Page

LIST OF TABLES

LIST OF APPENDICES

CHAPTER 1

INTRODUCTION

Because of the fabrication processes employed in its manufacture, e.g. solidification, hot and cold rolling, annealing, etc., a sheet of metal is frequently anisotropic. Its constituent grains adopt elongated shapes and specific preferred orientations. As a consequence of this crystallographic anisotropy, the physical properties and particularly the mechanical properties of the polycrystal as a whole are anisotropic.

In processes such as press forming, deep drawing and stamping, the limit strains attainable along either of the two extreme strain paths (drawing or stretching), depend on the anisotropy characteristics of the sheet. Because of the effect of anisotropy on metal formability, e.g. of steel sheets in the motorcar industry and aluminum alloys in the production of beverage cans, numerous attempts have been made to both predict and control the anisotropy.

For this purpose, it is necessary to know (i) the influence of the metallurgical parameters affecting texture evolution during the fabrication process and (ii) the relation between the texture and the plastic properties. It is the latter topic which is the main concern of this study.

Texture information can be obtained relatively easily by means of pole figures or CODF (crystallite orientation distribution function) data, both of which are derived from X-ray diffraction measurements. Only qualitative and semi quantitative estimates of the ideal orientations are given by the former, whereas the latter is an accurate, albeit more sophisticated representation of the grain distribution.

Having quantified the texture information, we then face the problem of calculating the macroscopic plastic properties. The following sequence has frequently been used :

1. Define the single crystal yield surface.
2. Define the plastic deformation model.
3. Calculate the polycrystal yield surface using the texture data.
4. Derive the plastic flow properties.

One can ask why the calculation begins with the single crystal yield surface The main reason is that the plastic behaviour of a single crystal is quite well known and understood. The yield locus can be readily derived from knowledge of the slip systems activated in the crystal. Assuming for example that plastic deformation occurs on the {111} crystallographic planes in the <110> crystallographic directions, Bishop and Hill [1] showed that the single crystal yield surface for FCC metals is a polyhedron in stress space, whose characteristics have been well identified.

The second critical step is then concerned with the transition single crystal → polycrystal. Since the texture has a crystallographic (and hence microscopic) nature and since the plastic behaviour is a polycrystalline (and hence macroscopic) characteristic, it is necessary to make some assumptions regarding the interactions between the individual grains of the workpiece.For example, assuming homogeneity of the deformations in the polycrystal [2] generally leads to different results than when the polycrystal is considered as a superposition of single crystals, without any interaction [3].

Texture data, single crystal yield surface, plastic deformation model . we now have everything in hand to calculate the polycrystal yield locus. The texture information is used to reorient the yield surfaces of the individual crystals into the testpiece axes, and the plastic deformation model provides the averaging technique to be used over the complete set of grains. This sequence leads to the polycrystal locus.

The plastic properties, as expressed by yield strength or strain rate characteristics, are then readily deduced from the size and shape, respectively, of this overall yield surface.

This crystallographic approach is considered to give a reasonably accurate estimate of some important plastic properties. However, the two first steps in the computation sequence described above are based on questionable assumptions. What is the 'exact' single crystal yield surface and what are the 'exact' interactions between the individual grains? Obviously each grain has its own characteristics of shape, orientation, hardness and degree of disorientation, for example. All these parameters influence the size and shape of the yield locus applicable to each grain and/or the interaction each crystallite has with its neighbours. Furthermore, because of the hundreds or even thousands of grains involved in this type of approach, extensive computations have to be carried out to obtain reasonable predictions, leading to incompatibility with on-line measurements or the rapid analysis of data.

A potential alternative to the above approach exists in the analyses of continuum plasticity. According to this method, the calculation sequence described above is greatly simplified and reduces to :

1. Determination of the polycrystal yield surface from a finite number of experiments
2. Derivation of the plastic properties in analytic form

As can be seen, no reference is made to the orientations of the individual grains, so that this approach remains essentially macroscopic. The yield locus of the polycrystal under consideration is described by an assumed analytical function, the parameters of which are determined experimentally. As an example, the quadratic yield function derived by Hill [4] in 1948 for orthotropic materials contains six parameters. However, only two experiments are needed in the particular case of plane stress loading and only one if planar isotropy is further assumed. The extreme simplicity of such continuum approaches makes them especially suitable for engineering applications related to metal forming. The different anisotropic yield criteria proposed in the literature are not, however, of general applicability and only lead to rough estimates of the plastic properties. Two of the main limitations of such continuum approaches can be summed up as follows :

1. They do not take account of the crystallographic texture, which is the primary source of plastic anisotropy.
2. Generally more than one experiment is necessary to derive the parameters of the yield function.

The prediction of the yield surfaces and plastic properties of anisotropic media has thus been approached by two alternative extreme methods. On the one hand, the crystallographic (Bishop and Hill) analysis is unsuitable for the rapid assessment of macroscopic properties; on the other, the continuum approach is seriously limited in many instances since it does not take account of the texture of the material and is generally restricted to fairly simple cases.

Recently, Montheillet et al. [5] have proposed an alternative method which combines aspects of both the previous approaches; it is known as the continuum mechanics of textured polycrystals (CMTP). This has been the first attempt to correlate analytically the plastic anisotropy of a polycrystal with its texture. It is somewhat surprising that such a general theory is missing in the literature. The method is based on a modification of Hill's anisotropic continuum theory which permits the observed ideal orientations to be linked directly with the consequent plastic anisotropy of the material. The macroscopic stress and strain rate characteristics can thus be readily obtained from knowledge of the texture components displayed by the polycrystal.

In this report, the continuum yield surfaces found in the literature are first reviewed critically, with special attention being paid to their applications in metal forming. The principles of the CMTP method are then described in detail and it is shown how plastic properties and texture data can be correlated in a fairly simple way. Specific polycrystal yield surfaces are then described by the CMTP method and the corresponding plastic properties are calculated. Finally, these are compared with crystallographic (Bishop and Hill) predictions and with experimental observations taken from the literature.

CHAPTER II

CONTINUUM YIELD SURFACES AND PLASTIC PROPERTIES - A REVIEW -

Crystallographic texture is recognized to be the primary source of plastic anisotropy. The non-isotropic distribution of grain orientations leads to non-isotropic macroscopic properties. As described above, two extreme approaches have been used to describe this anisotropy, namely the crystallographic and continuum or macroscopic approaches.

In the former, plastic deformation is usually assumed to be accommodated by the activation of five independent slip systems. Each grain is generally considered to undergo the same uniform strain as the aggregate. For FCC metals, the five activated $\{111\}$ $<1\bar{1}0>$ systems are those for which the absolute sum of the glide shears is a minimum [2]. The Taylor model was confirmed some 13 years later by Bishop and Hill [1,6] through the use of the principle of maximum work. These two basic analyses have been proved to be strictly equivalent [7]. They were used by Backofen and coworkers [8,9] in successful attempts to predict yield surfaces and R-values for textured sheets (see also Ref. [10]). Recently, both full and relaxed constraint models have been used by Canova et al.[11]. Yield surfaces with fairly sharp corners were obtained in this way for two deformation paths, rolling and torsion, and reasonable agreement was observed between predicted and experimental R-values. Furthermore, the crystallographic methods for the calculation of macroscopic anisotropic properties have received considerable attention during the past two decades [12-15] in correlation with development of the CODF (crystallite orientation distribution function) analysis (see for example Ref. [16]). However, the mathematical complexity of these approaches makes them difficult to manipulate and is not conducive to a ready physical understanding of the phenomenon (i.e. of the link between a given ideal orientation and its effect on formability). Furthermore, they require extensive computer calculations and are thus unsuitable in their current form for rapid on-line measurements.

The anisotropic continuum plasticity theory of Hill [4,17], on the other hand, has the great advantage of simplicity. However, because of some important deficiencies in its predictions, more complicated yield criteria have been proposed, which are nevertheless simple enough to be used for engineering applications. It is the purpose of the discussion that follows to develop some of these points.

II.1. SOME GENERAL PROPERTIES OF CONTINUUM YIELD SURFACES

To begin with, it is very important to point out two major characteristics of the continuum yield loci described in the literature :

- They are all expressed in terms of macroscopic stresses and thus do not directly account for crystallographic texture.

- They are all represented by analytical functions, whose forms are assumed without any detailed justification.

The most general form of this function may be written :

$$F(\sigma_{ij}) = 0 \tag{2.1}$$

where the σ_{ij} are the six components of the stress tensor expressed in the reference frame of interest. If the material is deformed plastically, the corresponding flow stresses are expressed by Eq. 2.1. If it only deforms elastically, the stress vector remains inside the surface characterized by this equation. This kind of transition between elasticity and plasticity is not quite so sharp in the case of an actual polycrystal. Should the aggregate be considered to deform plastically at the exact moment when one of its grain begins to do so, or when all its crystals are finally in the plastic state? It seems that the second assumption has received much more attention than the first in the classical approaches.

It is furthermore generally assumed that the material under consideration does not exhibit any Bauschinger effect, i.e. that

$$F(-\sigma_{ij}) = F(\sigma_{ij}) \tag{2.2}$$

Extension to the hexagonal metals is thus somewhat questionable and has not provided particularly impressive results.

A second major hypothesis regards the absence of any effect of the hydrostatic pressure. As a consequence, the yield surface is a function of the deviator stresses only, i.e.

$$F(\sigma_{11}-\sigma_{22}, \sigma_{22}-\sigma_{33}, \sigma_{33}-\sigma_{11}, \sigma_{12}, \sigma_{23}, \sigma_{31}) = 0 \tag{2.3a}$$

or, equivalently,

$$F(S_{11}-S_{22}, S_{22}-S_{33}, S_{33}-S_{11}, S_{12}, S_{23}, S_{31}) = 0 \tag{2.3b}$$

where $S_{ij} = \sigma_{ij} - (\sigma_{kk}/3)\,\delta_{ij}$ are the stress deviator components.

As pointed out by Saint-Venant in 1870 and then by Levy in 1871 and von Mises in 1913, the strain increment characteristics of a material can be deduced from the deviator stresses themselves

$$d\varepsilon_{ij} = S_{ij}\, d\lambda \tag{2.4}$$

where $d\lambda$ is a positive scalar which depends on the hardening properties. This speculative hypothesis appeared to be a particular case of the more general relation between plastic strain increments and stresses known as the normality principle or flow rule :

$$d\varepsilon_{ij} = d\lambda\, \partial F(\sigma_{ij}) / \partial\sigma_{ij} \tag{2.5}$$

where $F(\sigma_{ij})$ is the yield function corresponding to the material being considered. Equation 2.5 leads to the Saint-Venant principle when the von Mises isotropic criterion is used. Furthermore it leads to a simple geometric interpretation of the flow behaviour, i.e. the vector $\vec{d\varepsilon} = (d\varepsilon_{ij})$ is normal to the yield surface at the point (σ_{ij}), Fig. 2.1.

II.2. THE TRESCA AND VON MISES CRITERIA

Two criteria were widely used in the past to reproduce the yield behaviour of an isotropic material. The first was proposed by Tresca [18] in terms of principal stresses :

$$\sigma_I - \sigma_{III} = \sigma_0 \qquad \text{if } \sigma_I \geqslant \sigma_{II} \geqslant \sigma_{III} \tag{2.6}$$

and the second by von Mises [19] who put forward the quadratic function :

$$(\sigma_{xx}-\sigma_{yy})^2+(\sigma_{xx}-\sigma_{zz})^2+(\sigma_{yy}-\sigma_{zz})^2+6(\sigma_{xy}{}^2+\sigma_{xz}{}^2+\sigma_{yz}{}^2)=2\sigma_0{}^2 \tag{2.7}$$

Plastic deformation is assumed to occur when the maximum shear stress in the former case or the elastic energy of distortion in the latter reaches a critical value.

II.3. THE HILL 1948 CRITERION

After being processed, a material is generally anisotropic. As a consequence, the flow behaviours characterized by the Tresca and von Mises functions only provide a rough and frequently an incorrect, estimate of the plastic properties. For this reason, Hill [4] proposed in 1948 a generalization of the von Mises criterion which takes the anisotropy into partial account:

$$\begin{aligned} 2\,F(\sigma_{ij}) = {} & F\,(\sigma_{yy}-\sigma_{zz})^2+G\,(\sigma_{xx}-\sigma_{zz})^2+H\,(\sigma_{xx}-\sigma_{yy})^2 \\ & +2L\,\sigma_{yz}{}^2+2M\,\sigma_{xz}{}^2+2N\,\sigma_{xy}{}^2 = 1 \end{aligned} \tag{2.8}$$

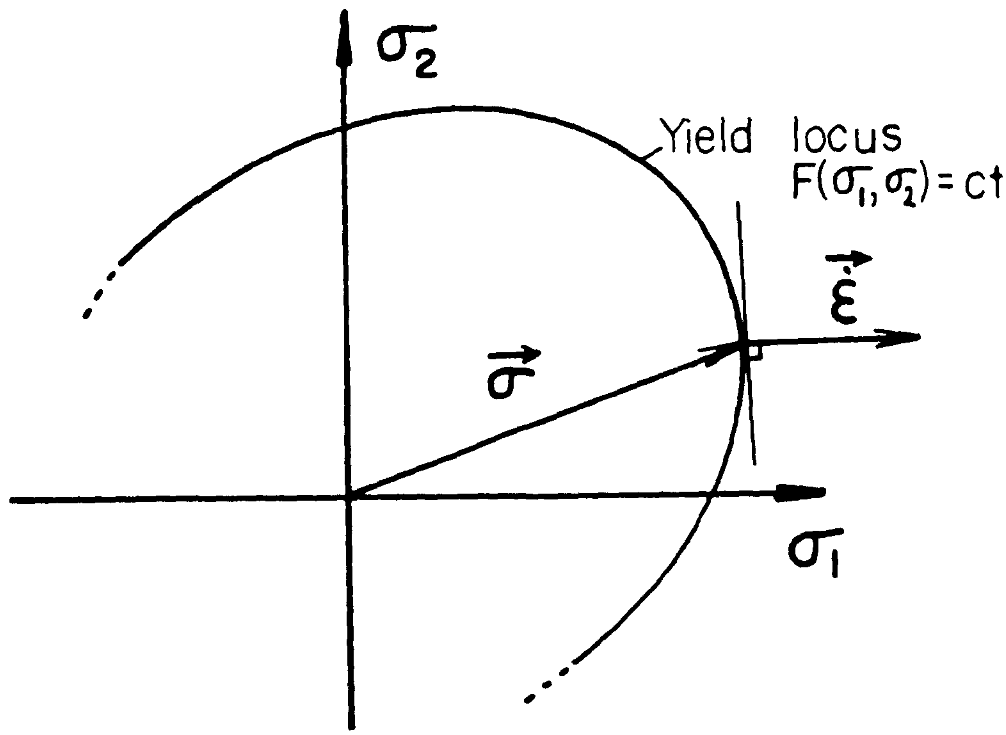

Fig. 2.1 Yield locus $F(\sigma_1, \sigma_2)=ct$ in a two-dimensional (σ_1, σ_2) stress space. The stress vector $\vec{\sigma}$ terminates on the locus and the corresponding strain rate vector $\vec{\dot{\varepsilon}}$ is normal to the yield surface at the loading point.

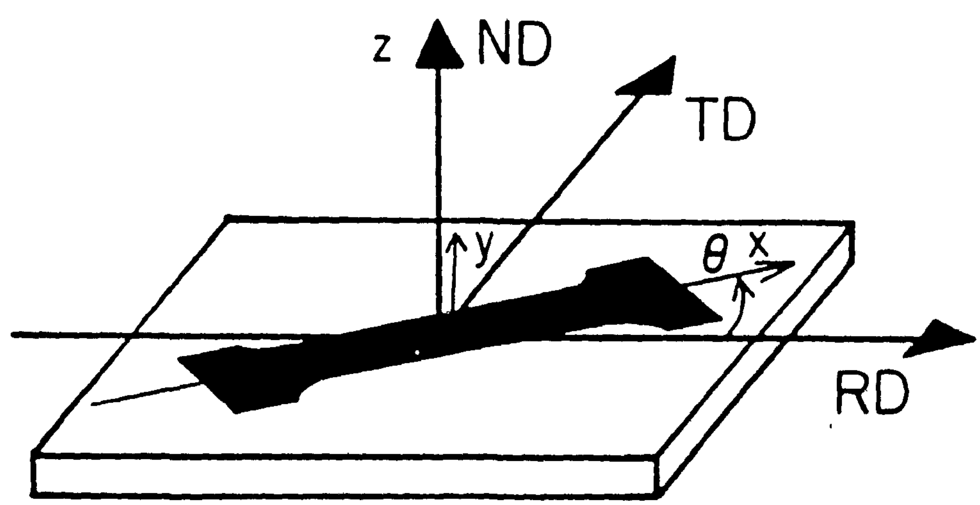

Fig. 2.2 System of coordinate axes for rolled sheet.

This criterion is restricted to materials with orthotropic physical symmetry, i.e. to those with three mutually orthogonal symmetry planes. These can generally be inferred from the symmetry of the strain path employed to produce the anisotropy. The F, G, H, L, M and N parameters characterize the current state of anisotropy and can be determined by means of six uniaxial tension or pure shear tests :

$$G + H = 1/X^2 \qquad F + H = 1/Y^2 \qquad F + G = 1/Z^2$$

$$2L = 1/R^2 \qquad 2M = 1/S^2 \qquad 2N = 1/T^2 \tag{2.9}$$

where X, Y and Z are the tensile yield stresses in the principal directions of anisotropy and R, S and T the yield stresses in shear with respect to these axes. In the case of isotropy

$$L = M = N = 3F = 3G = 3H \tag{2.10}$$

and expression 2.8 reduces to the von Mises criterion.

The Hill 1948 yield criterion has been widely used to evaluate the plastic properties of anisotropic metals. The sections that follows present a critical examination of some of its main applications.

II.3.1. YIELD STRESS $\sigma(\theta)$

The anisotropy displayed by a rolled sheet can be characterized by a set of tensile experiments carried out at different angles θ in the rolling plane (Fig. 2.2). The dependence of the yield stress on orientation can be calculated very simply from a 'reduced' (plane stress) criterion

$$(G+H)\,\sigma_x^{\,2} + (F+H)\,\sigma_y^{\,2} - 2H\,\sigma_x\sigma_y + 2N\,\sigma_{xy}^{\,2} = 1 \tag{2.11}$$

The tensile stress in the θ direction is then given by

$$\sigma(\theta) = [(G+H)\cos^4\theta + (F+H)\sin^4\theta + 2(N-H)\sin^2\theta\cos^2\theta]^{-1/2} \tag{2.12}$$

leading to

$$\begin{aligned} \sigma(0) &= (G+H)^{-1/2} \\ \sigma(90) &= (F+H)^{-1/2} \\ \text{and} \qquad \sigma(45) &= [(F+G+2N)/4]^{-1/2} \end{aligned} \tag{2.13}$$

Bramley and Mellor [20,21] applied the Hill theory to the case of steel, titanium and zinc sheets. The parameters F, G, H and N were determined experimentally and used to calculate the yield stress anisotropy, as expressed by the ratios $\sigma(0)/\sigma(90)$ and $\sigma(0)/\sigma(45)$. Since the theoretical values they derived did not seem to conform to the values expected from Equations 2.13, these were recalculated by the present author and are shown separately in Table II.1. Reasonable, although not 'perfect', agreement between the Hill analysis and the experimental observations is seen for the steels and zinc, whereas some discrepancy is observed for the titanium ; i.e. $\sigma(0)$ is greater than $\sigma(45)$ and $\sigma(90)$, while the theory predicts the reverse condition. This was attributed by the authors [20] to a difference in the rate of work hardening between the rolling and transverse directions, which cannot be accounted for by the Hill analysis.

For materials obeying power law work hardening, $\sigma = K\,\bar{\varepsilon}^n$, the ratio of the tensile flow stresses has been shown to depend on the hardening coefficient n [22-24]

$$\sigma(\theta)\,/\,\sigma(0) = [A\,/\,(G+H)^{-1/2}]^{n+1} \tag{2.14}$$

where A is the right hand side of Eq. 2.12. The predictions of the Hill quadratic criterion were nevertheless shown to diverge from the experimental observations [24] for various grades of steel.

	Steel [20]	Ti [20]	Zn [20]	Steels [21]			
				A	B	C	D
σ(0)/σ(45) theoretical present work	.951	.984	.933	.854	.886	870	.951
σ(0)/σ(45) experimental	.983	1.039	862	.953	.944	.968	.983
σ(0)/σ(90) theoretical Refs.[20,21]	.932	.874	625	.990	.980	971	.932
σ(0)/σ(90) theoretical present work	.953	.936	.644	.988	.981	973	.953
σ(0)/σ(90) experimental	.992	1.063	694	1.011	.989	1.013	.992

Table II.1. Theoretical (Eq. 2.13) and experimental (from Refs. [20] and [21]) yield stress ratios; A, B, C and D refer to the four steels investigated in Ref. [21]

Gotoh [25,26] also reported large discrepancies between Hill type calculations of yield stress anisotropy and experimental points for an Al-killed steel and for Cu-1/4H, as shown in Fig. 2.3. This is more striking in the case of the steel which displayed strong anisotropy, as expressed by an R-value varying from 1.5 to 2.4. Similar conclusions can be drawn from the work of Dillamore et al. [27] on a rimming steel.

By contrast, Svensson [28] reported very good agreement when comparing theoretical (Hill quadratic) and experimental 0.05% proof stresses in cold rolled and annealed steel and aluminum.

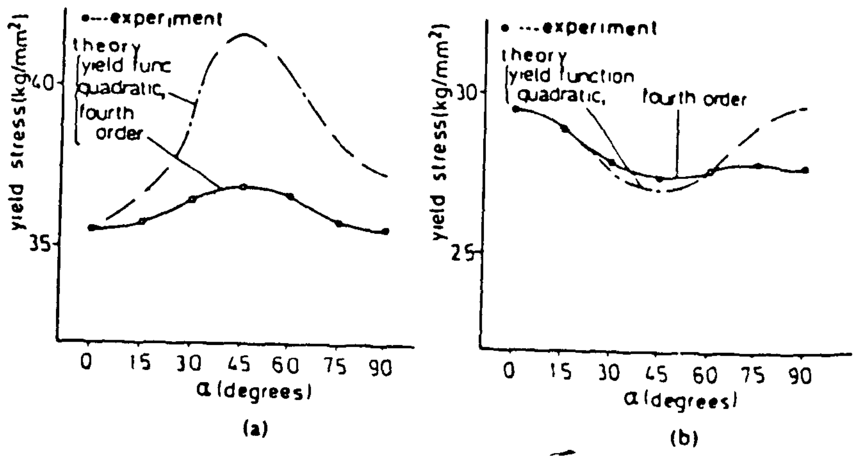

Fig. 2.3 Uniaxial yield stress curves σ(θ) for (a) an Al-killed steel and (b) Cu-1/4H. (o) experimental values; (——·——-‑) predictions based on Hill 1948 criterion; (————) Gotoh calculations (Eq. 2.61). After [25].

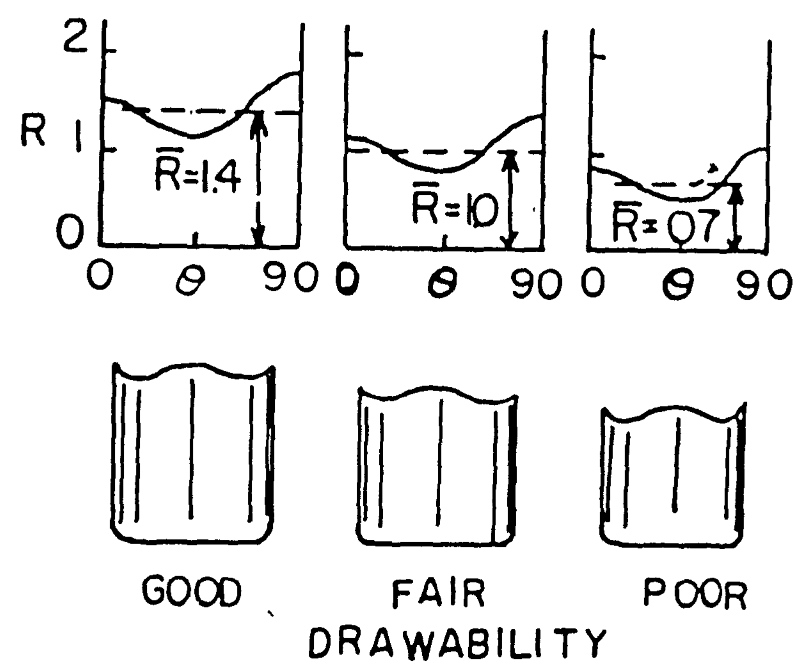

Fig. 2.4 (a) Typical variations in the R(θ) curves for low carbon steel; (b) relative sizes of the deepest cups that can be drawn from the materials with the average strain rate ratios indicated. After [31].

II.3.2. STRAIN RATE RATIO R(θ)

The anisotropy of a rolled sheet is often characterized by the strain rate ratio R(θ) [29] calculated from tensile tests carried out at various angles θ to the rolling direction (Fig. 2.2). It is defined as the ratio of the incremental strains in the width and thickness directions

$$R(\theta) = \dot{\varepsilon}_{yy} / \dot{\varepsilon}_{zz} \tag{2.15}$$

Whiteley [30] demonstrated the importance of this ratio in the evaluation of directionality in steel sheet. The R-value is readily derived from the yield function (Eq 2 11) by using the associated flow rule (Eq. 2.5). It can be shown that

$$R(\theta) = [H + (2N - F - G - 4H) \sin^2\theta \cos^2\theta] / [F \sin^2\theta + G \cos^2\theta] \tag{2 16}$$

so that

$$\begin{aligned} R(0) &= H / G \\ R(90) &= H / F \\ R(45) &= N / (F + G) - 1/2 \end{aligned} \tag{2 17}$$

and

$$R(\theta) = \frac{1 + 2[R(45)/R(0) + R(45)/R(90) - 2] \sin^2\theta \cos^2\theta}{\sin^2\theta / R(90) + \cos^2\theta / R(0)} \tag{2.18}$$

The strain rate ratio R is a measurement of the degree of anisotropic flow that occurs during drawing. The lack of drawability is in turn related to the inability of a material to resist localized thinning in the tube wall. A high R-value favors resistance to thinning and a large variation in R is related to extensive earing. Two parameters are commonly used to characterize the drawability of a sheet. The average strain rate ratio

$$\bar{R} = [R(0) + 2R(45) + R(90)] / 4 \tag{2.19}$$

is a measure of the degree of normal anisotropy and is related to the depth of draw [30]: the higher the $\bar{R}$ value, the deeper the draw, as illustrated in Fig. 2.4 [31]. By contrast, the planar strain or anisotropy ratio

$$\Delta R = [R(0) - 2R(45) + R(90)] / 2 \tag{2.20}$$

is a measure of the degree of planar anisotropy. For an isotropic material, $\bar{R} = 1$ and $\Delta R = 0$

Equation 2.18 has been widely used for assessment of the R(θ) curves pertaining to various metals. In most cases, good agreement with experimental points is reported [20,21,26,27,32-34], as shown for illustration in Fig 2 5 However, this result is not really surprising since the R(θ) curves must coincide by construction with the experimental points in the rolling, transverse and diagonal directions. More interesting conclusions can be drawn regarding the limitations of the Hill predictions when more than four ears are obtained in deep drawn cups, as shown in the next section.

II.3.3. EARING BEHAVIOUR

When a sheet of metal is deep drawn, the resulting cup very often exhibits peaks and troughs along its periphery. This inhomogeneous deformation, known as earing, originates in the crystallographic anisotropy of the workpiece [35]. As shown by Wilson and Butler [36], ears form in the rolling and transverse directions (Fig. 2.6) in the case of a material displaying a major cube component and in the diagonal directions if a rolling-type texture is present in the specimen. Little earing is observed, however, in the case of a balanced texture (see also Ref. [37]).

As discussed by Bourne and Hill [34], the positions of the ears depend on the relative values of the parameters F, G, H and N. Although their locations correspond theoretically to R(θ) maxima for uniaxial stresses applied in the

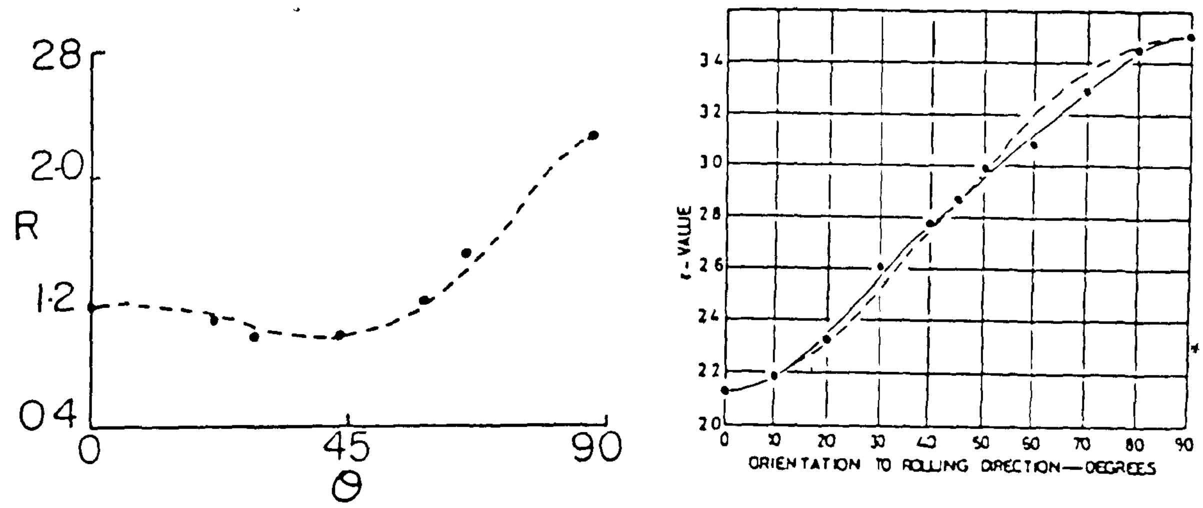

Fig. 2.5 Comparison between experimental R-values and strain rate ratio curves predicted by the Hill 1948 theory. (a) mild steel [27] and (b) zinc [20].

Fig. 2.6 Earing behaviour and maximum cup depth obtained in drawing of copper sheet. (a) "rolling-type" texture; (b) "balanced" texture and (c) "cube" texture. The arrow indicates the rolling direction in the sheet. After [36].

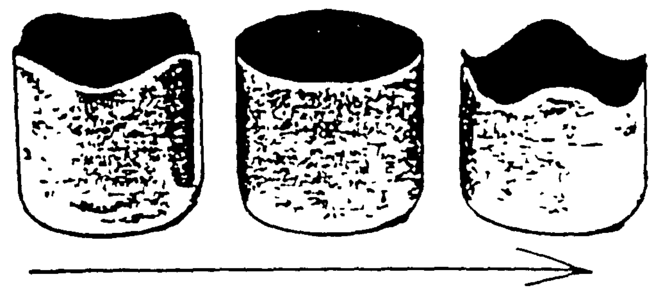

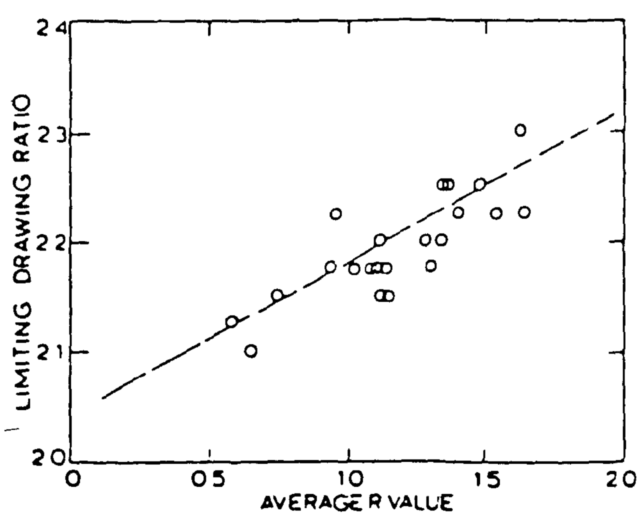

Fig. 2 7 Variation of limiting drawing ratio (LDR) with average R-value. After [30].

circumferential direction, there is experimental evidence that ears form at positions where $R(\theta)$ is maximum for a uniaxial test performed in the radial direction. For a material displaying a strong cube texture, for example, experimental R-values vary from about 1 in the $\theta = 0$ and 90° directions to about 0.1 in the diagonal ($\theta = 45^\circ$) direction [38]; this situation is consistent with the observed earing behaviour (Fig. 2.6).

Aust and Morral [33] reported that the Hill quadratic criterion predicts the right ear positions for annealed 2S aluminum. However, Bourne and Hill [34] have cited the counter example of a brass sheet in which six ears are found. In this case, the Hill quadratic criterion (Eq. 2.11) is revealed to be unsuitable, since it can only predict four maxima (corresponding to four ears) in the $R(\theta)$ curve. A cubic plastic potential would be more appropriate for this material, following the remark [34] that a homogeneous yield function of degree n can lead to the prediction of a maximum of 2n ears.

Logan [39] used a Hill type of flow criterion with planar anisotropy in FEM simulations of sheet metal formability. The calculated mean ear height was plotted versus the planar anisotropy parameter $2\Delta R/\bar{R}$ suggested by Wilson and Butler [36]. It was concluded that the Hill 1948 yield function underestimates the true earing behaviour for various degrees of anisotropy. Furthermore, it was shown that it overpredicts the amount of strain under the punch (i.e. in the biaxial region) relative to that in the flange.

II.3.4. LIMITING DRAWING RATIO (L.D.R.)

An interesting characteristic of a given material being deep drawn is the largest blank that can be successfully drawn with a given die. This property is usually quantified as the limiting drawing ratio

$$LDR = D/d \tag{2.21}$$

where D is the diameter of the largest blank successfully drawn and d is the diameter of the drawn cup. Whiteley [30] demonstrated the importance of the average strain ratio $\bar{R}$ in the assessment of a high LDR (Fig. 2.7). His analysis was based on the fact that a high $\bar{R}$-value is indicative of a high wall strength together with a low resistance to width (circumferential) strain. These two combined properties allow larger blanks to be drawn without failure. Whiteley's work was confirmed by other authors for different kinds of metals [36,40-46]. The LDR was shown [30] to be related theoretically to the ratio β of two plane strain flow stresses corresponding to $\dot{\varepsilon}_{yy} = 0$ and $\dot{\varepsilon}_{zz} = 0$:

$$ln\,(LDR) = \eta\, \beta \tag{2.22}$$

where η is an efficiency coefficient essentially associated with frictional forces; normally η $= 0.7$ to 0.8. When using the Hill anisotropic theory (Eq. 2.11), Whiteley further demonstrated that, for radial isotropy, β can be predicted quite easily to be:

$$\beta = \sqrt{(R+1)/2} \tag{2.23}$$

so that

$$LDR = exp(\, \eta \sqrt{(R+1)/2}\,) \tag{2.24}$$

As can be seen, the drawing ratio is very dependent on how well the Hill criterion approximates the shape of the yield locus for real materials, since its value is based on two flow stresses and one strain rate (normal to the yield surface) derived from the assumed locus. Furthermore, planar isotropy is assumed through the use of the $\bar{R}$-value, a condition which is more the exception than the rule. Moreover, no work hardening is considered. Under these conditions, the curve of LDR vs $\bar{R}$ expressed by Eq. 2.24 has been proved to be highly deficient. The trend generally reported is that the theoretical results obtained from the Hill theory indicate a far greater dependence on $\bar{R}$-value than actually observed in practice, as illustrated in Fig. 2.8. Furthermore, the discrepancy seems to increase with increasing $\bar{R}$ [41]. On some aluminum alloys, however, Riggs [42] has observed that a better correlation between LDR and strain ratio is obtained when the minimum instead of the average R-value is taken into consideration.

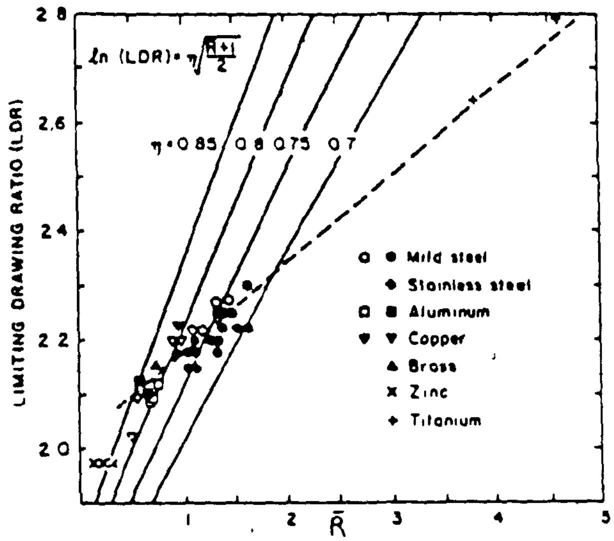

Fig. 2.8 Correlation between LDR for cylindrical flat bottom cups and average strain rate ratio. Experimental points from Refs. [30,36]. Note that the predictions based on the Hill yield surface do not fit the data. After [65].

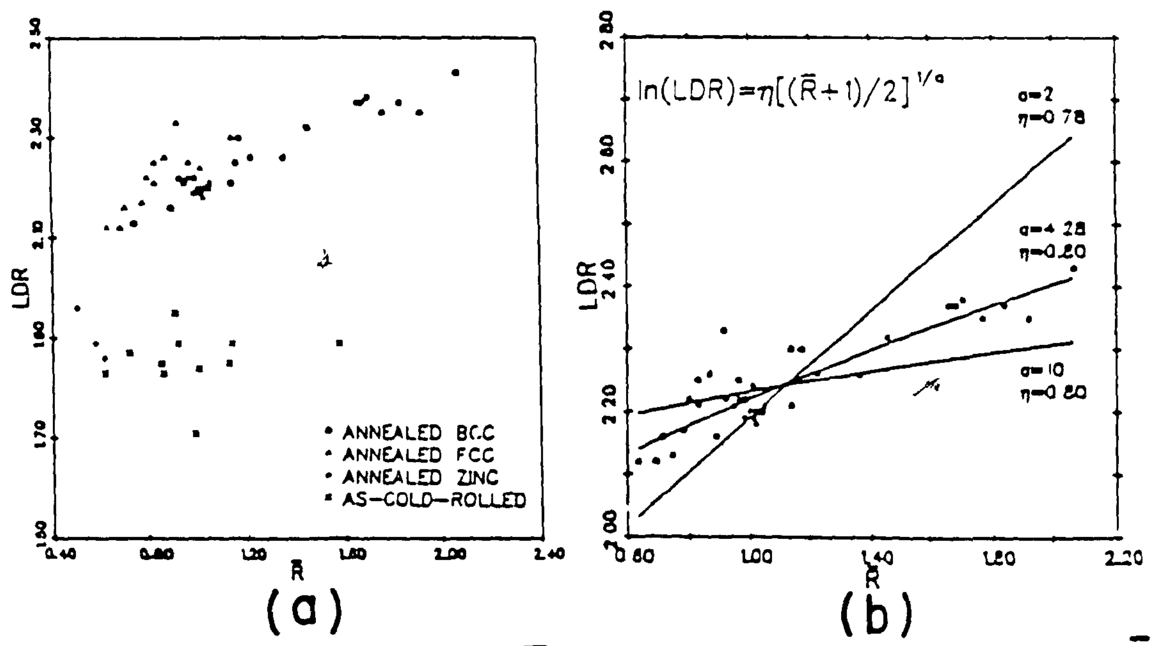

Fig. 2.9 (a) Dependence of LDR on $\bar{R}$ for various materials and (b) LDR vs. $\bar{R}$ relationship for annealed FCC and BCC metals. The full line a = 2 corresponds to the predictions based on the Hill 1948 criterion. After [40].

Meuleman [40] studied the effects of mechanical properties on the deep drawability of a selection of sheet metals, i.e. annealed BCC and FCC metals, annealed zinc, as well as some as-cold-rolled materials. His results (Fig. 2.9) show that the annealed cubic materials follow a definite trend, which is not, however, reproduced by the Hill quadratic analysis. By contrast, the drawabilities of the annealed zinc and the as-cold-rolled metals seemed to be almost independent of the average strain ratio and fell well below the predicted values.

II.3.5. WORK HARDENING CHARACTERISTICS

As discussed above, the comparison between predicted and experimental R(θ) curves is not a very sensitive test for the Hill anisotropic theory. A more realistic assessment consists of calculating the hardening characteristics of a metal following a certain deformation path (say biaxial tension) and then comparing them with those obtained along another path (say uniaxial tension).

It can be readily shown [21] from Eq. 2.11 that the biaxial stress σ_{bi} and strain ε_{bi} can be calculated from knowledge of the uniaxial behaviour :

$$\sigma_{bi} = \left[\frac{1+R(0)}{1+R(0)/R(90)}\right]^{\frac{1}{2}} \sigma_0 \qquad \varepsilon_{bi} = \left[\frac{1+R(0)/R(90)}{1+R(0)}\right]^{\frac{1}{2}} \varepsilon_0 \tag{2.25}$$

$$\sigma_{bi} = \left[\frac{1+R(90)}{1+R(90)/R(0)}\right]^{\frac{1}{2}} \sigma_{90} \qquad \varepsilon_{bi} = \left[\frac{1+R(90)/R(0)}{1+R(90)}\right]^{\frac{1}{2}} \varepsilon_{90} \tag{2.26}$$

$$\sigma_{bi} = \left[\frac{1+R}{2}\right]^{\frac{1}{2}} \sigma_{av} \qquad \varepsilon_{bi} = \left[\frac{2}{1+R}\right]^{\frac{1}{2}} \varepsilon_{av} \tag{2.27}$$

where (σ_0, ε_0) and (σ_{90}, ε_{90}) are the flow properties in the rolling and transverse directions, respectively, and (σ_{av}, ε_{av}) are taken from the stress-strain curve corresponding to the average R-value.

An interesting consequence of Eq. 2.27 is that the $\bar{R}$-value can be calculated from knowledge of the stress-strain curves determined in biaxial tension and in a uniaxial tension test carried out in the direction corresponding to $\bar{R}$ [47,48]. If these curves are fitted to the empirical expressions

$$\sigma_{bt} = A\, \varepsilon_{bt}^{\ m} \qquad (2.28)$$

$$\sigma_{av} = B\, \varepsilon_{av}^{\ n} \qquad (2.29)$$

and if it is assumed that the two hardening exponents m and n are equal, as is implicit in the Hill anisotropy theory, then from Eq. 2.27

$$R_{av} = 2\,(A\,/\,B)^{\,2/(n+1)} - 1 \qquad (2.30)$$

Bramley and Mellor [21] carried out simple tension tests in the $\theta = 0, 45$ and $90°$ directions of four stabilized steel sheets. The biaxial curves were obtained by the diaphragm method. Eqs. 2.25 to 2.27 were then employed as theoretical bases for prediction of the latter. As shown in Fig. 2.10 for one of the tested steels, good agreement is observed when the average $\bar{R}$-value is used. Similar conclusions were drawn for the other steels.

Nevertheless, these results have been contradicted by many other investigations carried out on different metals. Bramley and Mellor [20], for example, reported good agreement for titanium ($\bar{R} = 2.85$) but a very poor one for zinc sheet ($\bar{R} = 0.31$). In further studies, Woodthorpe and Pearce [49] and Pearce [50] demonstrated that a low average strain ratio ($\bar{R} < 1$) is conducive to a strong underestimate of the strain hardening behaviour in biaxial tension (Fig. 2.11a). However, better results were obtained for materials having higher R-values (Fig. 2.11b). Similar comments are applicable to the work of Ranta-Eskola [51], Horta et al. [52], Kular et al. [53] and Vial and coworkers [22,23].

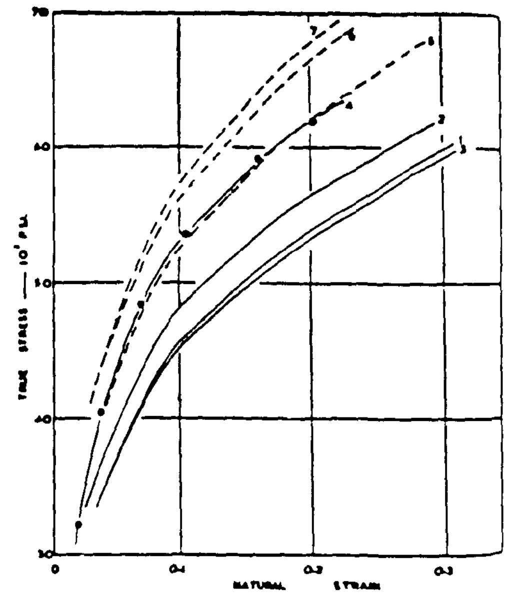

Fig. 2.10 Work-hardening characteristics for a killed steel. (1) Experimental curve, simple tension, 0° to rolling direction; (2) experimental curve, simple tension, 45° to rolling direction; (3) experimental curve, simple tension, 90° to rolling direction; (4) experimental curve, diaphragm test; (5) theoretical curve based on average R-value and corresponding work-hardening characteristics; (6) theoretical curve based on 90° tensile curve; and (7) theoretical curve based on 0° tensile curve. After [21].

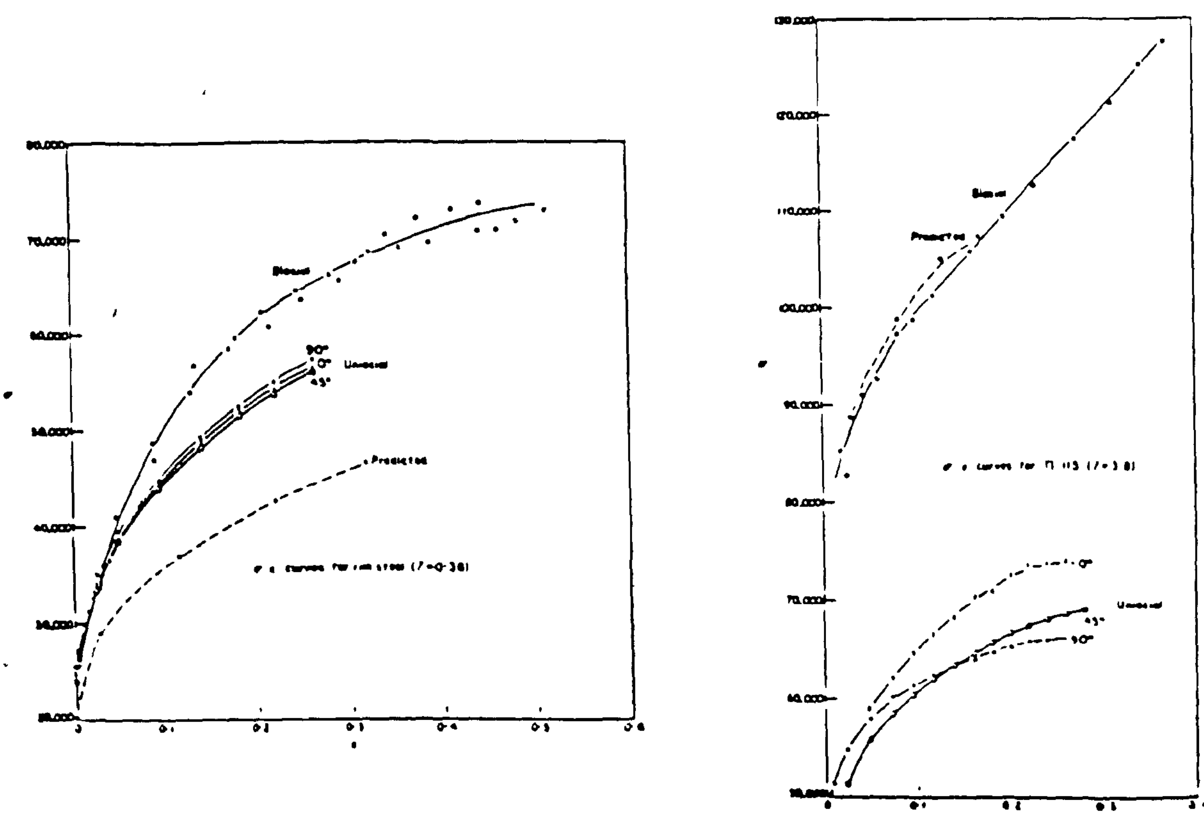

Fig. 2.11 Uniaxial and biaxial stress-strain curves for (a) an annealed rimmed steel ($\overline{R}=0.38$) and (b) annealed titanium ($\overline{R}=3.8$). After [50].

II.3.6. ANOMALOUS BEHAVIOUR

One of the interesting features of Eq. 2.27 is that the ratio $\sigma_{bi} / \sigma_{av}$ must lie on the same side of unity as the average strain ratio $\bar{R}$;

$$\bar{R} < 1 \Leftrightarrow \sigma_{bi} / \sigma_{av} \leq 1$$
$$\bar{R} \geq 1 \Leftrightarrow \sigma_{bi} / \sigma_{av} \geq 1 \qquad (2.31)$$

Woodthorpe and Pearce [49] carried out experiments on commercial purity aluminum cold rolled to different reductions. Although the corresponding $\bar{R}$-values were less than unity, all the measured $\sigma_{bi} / \sigma_{av}$ ratios were above 1, thus contradicting Eqs. 2.31. This behaviour has thus been qualified as 'anomalous'. Pearce [50] reported similar conclusions for 70/30 brass, as did Vial [22] for brass 260 : in these cases, the biaxial curves were considerably above the uniaxial ones although $\bar{R} < 1$. The theoretical and experimental $\sigma_{bi} / \sigma_{av}$ vs $\bar{R}$ curves derived by Pearce [50] are shown in Fig. 2.12. With the exception of the 'anomalous' metals mentioned above, the experimental relationship is similar in shape to the predicted one, but displaced to a higher level

It is also interesting to compare the Hill predictions expressed by Eq. 2.27 with calculations carried out on a crystallographic basis. Dillamore [54] concluded from a crystal plasticity analysis that the Hill theory approximates the biaxial/uniaxial stress ratio reasonably well for $\bar{R}$-values between 1 and 2. He furthermore demonstrated that the maximum value of $\sigma_{bi} / \overline{\sigma_{uni}}$ is 1.18; by contrast, according to Eq. 2.27, increasing the $\bar{R}$-value to infinity should lead to an infinite value of this ratio.

Logan and Hosford [55] also calculated the dependence of the biaxial/uniaxial stress ratio on the strain rate ratio $\bar{R}$ for randomly chosen rotationally symmetric mixed textures. It can be seen from Fig. 2.13 that the Hill analysis does not fit these crystallographically calculated points at all well. Similar conclusions were drawn regarding other strength ratios, i.e. the plane strain/uniaxial or plane strain/biaxial stress ratios (Fig. 2.14).

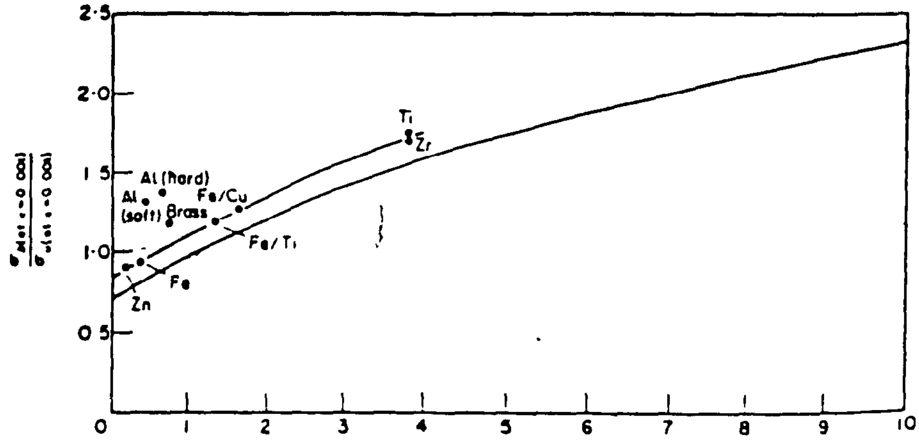

Fig. 2.12 Theoretical (Hill 1948) and exprimentally determined relationship between $\sigma_b / \overline{\sigma_u}$ and $\overline{R}$. After [50].

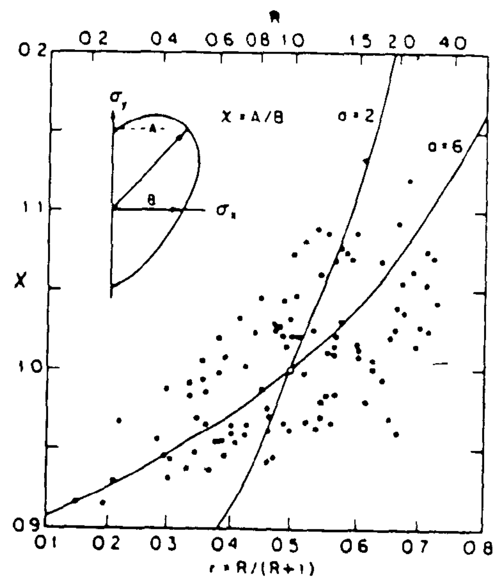

Fig. 2.13 Dependence of biaxial/uniaxial strength ratio, X , on the strain rate ratio R. Each point is a randomly chosen rotationally symmetric mixed texture. The Hill theory prediction is shown by the line a = 2 and the Hosford prediction (Eq. 2.50) by the line a = 6. After [55].

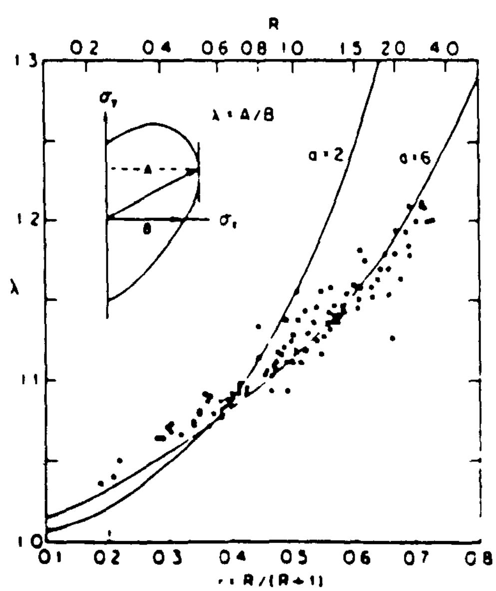

Fig. 2.14 Dependence of the plane strain $(\dot{\varepsilon}_y = 0)$/ uniaxial strength ratio, λ, on the strain rate ratio R. Each point corresponds to a randomly chosen rotationally symmetric mixed texture. The Hill theory prediction is given by the line a = 2 and the Hosford prediction (Eq. 2.50) by the line a = 6. After [55].

II.3.7. LIMIT STRAINS IN SHEET METAL

Many metal forming processes, such as stretch drawing, bulging or to a certain extent deep drawing, involve uniaxial or biaxial stretching paths. The main limitation of such deformation techniques is that fracture generally occurs at relatively low strains. For this reason, it is of interest to predict the maximum strain that can be undergone by a sheet without fracture. In principle, this critical value is the equivalent for stretching of the LDR for a drawing process.

The basis for limit strain prediction was first formulated by Marciniak and Kuczynski [56] in a well-known paper. An initial inhomogeneity in the sheet (such as a groove, see Fig. 2.15) is assumed to develop with increasing strain into a localized neck in the direction perpendicular to the largest principal stress. Their theoretical analysis made use of the Hill anisotropic criterion (Eq 2.8) applied to the cases of plane stress and planar isotropy (i.e. the R coefficient is assumed to be constant in all directions of the sheet). This leads to the reduced plastic potential

$$(R+1)\,\sigma_1^2+(R+1)\,\sigma_2^2-2R\sigma_1\sigma_2 = 2\sqrt{(2R+1)/3}\,\sigma_p^2 \qquad (2.32)$$

where σ_p denotes the equivalent yield stress for an isotropic material, and the 1 and 2 directions are those shown in Fig. 2.15. The classical flow rule (Eq. 2.5) was used to derive the strain rate characteristics corresponding to the above yield locus and the following strain hardening law was assumed

$$\sigma_p = \sigma_0\,(\varepsilon_0+\varepsilon)^n \qquad (2.33)$$

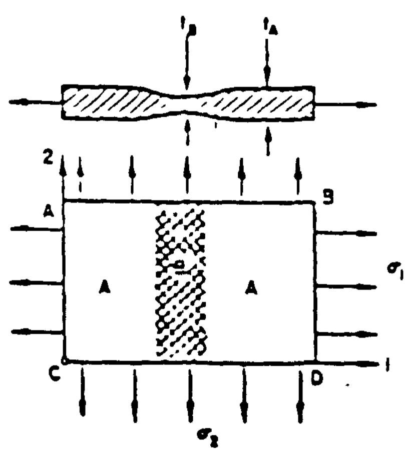

Fig. 2.15 Schematic representation of groove geometry. After [56].

In this investigation, the material properties, as expressed by the hardening coefficient n and the strain rate ratio R, as well as the loading conditions of an element of the metal, are supposed to remain unchanged during groove evolution. However, as pointed out by Sowerby and Duncan [57], this is unlikely to be true in real sheet forming operations. Marciniak and Kuczynski [56] were able to derive the stress state in the groove in this way, as well as the relative strains inside and outside the localization. The evolution of the latter quantities is illustrated in Fig. 2.16 for the case of equal biaxial tension $\sigma_2 = \sigma_1$ and for different geometric factors $t_b/t_a = f_0$ of the initial inhomogeneity. The limit strain ε^* is then defined as the maximum strain that can be attained before all the deformation is concentrated in the groove, as characterized by the points identified as C on the curves. This localization results in the loss of stability of the stretched sheet.

Marciniak's work, originally focused on biaxial loading, was extended by Sowerby and Duncan [57] to include all positive strain ratios ranging from plane strain to equal biaxial tension. They derived the principal consequences of the theory "non-mathematically" by considering the plane stress yield locus. Conclusions regarding the influence of the various material properties were drawn which are similar to those of the original paper by Marciniak and Kuczynski, as explained in more detail below.

Venter et al.[58] compared the predictions of the Marciniak analysis with the experimental limit strains obtained from the hydrostatic bulging of annealed aluminum plates. The results are presented in Fig. 2.17 as a forming limit diagram (FLD). Empirical values of the material properties were used (ε_0, n, σ_0, t_b/t_a); however, the strain rate ratio R was determined by fitting the corresponding yield surface (Eq.2.32) to experimental points, leading to a value R=1.036 (rather high for aluminum), compared to a measured Lankford coefficient R=0.54. "Encouraging agreement" was reported, although the predictions are very sensitive to all the parameters listed above.

In a further paper, Marciniak et al.[59] generalized their original work by introducing the strain rate sensitivity m and planar anisotropy, as expressed by

$$\sigma_p = \sigma_0 (\varepsilon_0 + \varepsilon)^n \dot{\varepsilon}^m \qquad (2.34)$$

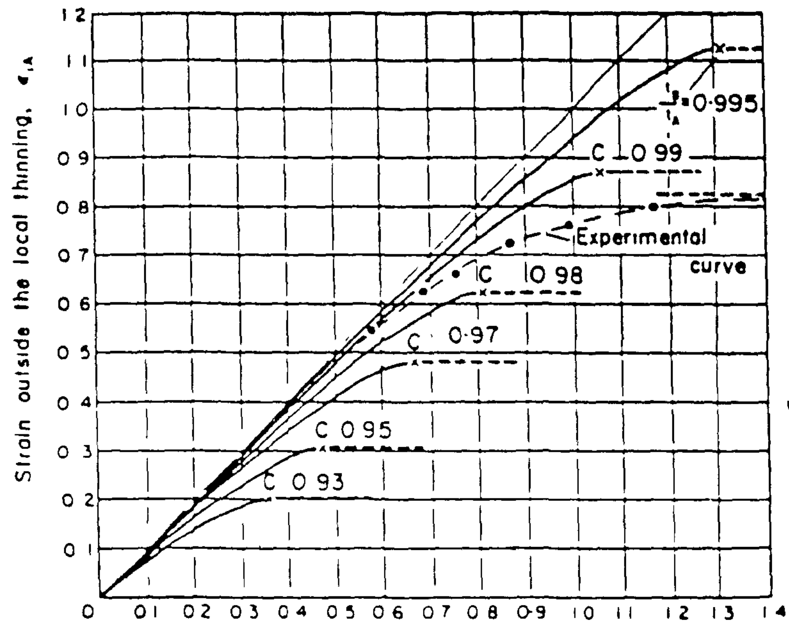

Fig. 2.16 The course of strain concentration in the groove. After [56].

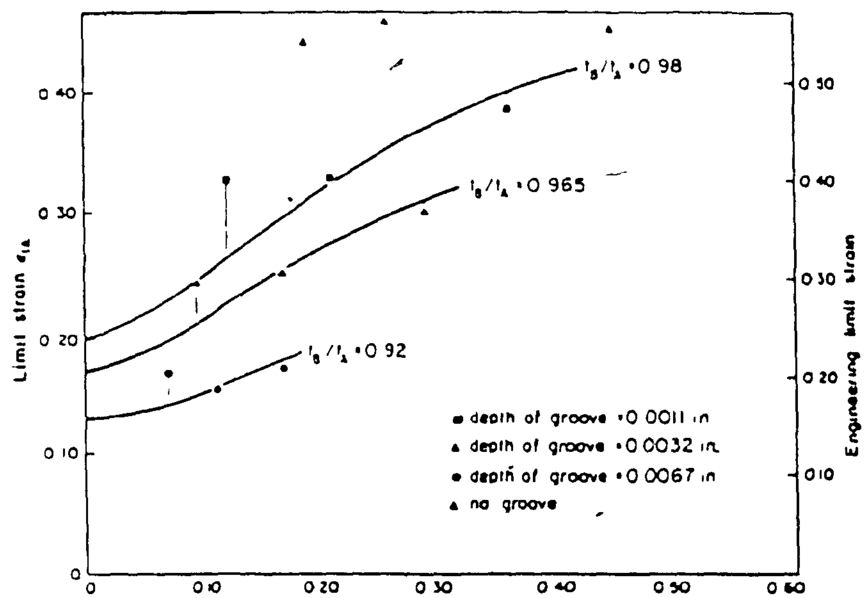

Fig. 2.17 Correlation between theoretical and experimental strain limits presented as a forming limit diagram. Experimental strains were obtained with the rolling direction transverse to the major axis of groove length. After [58].

and

$$\sigma_1^2 + \frac{R_1(1+R_2)}{R_2(1+R_1)}\sigma_2^2 - \frac{2R_1}{1+R_1}\sigma_1\sigma_2 = \sigma_p^2 \qquad (2.35)$$

where R_1 and R_2 are the strain rate ratios pertaining to the two principal directions in the sheet plane. A distinction was made between the two extreme positions of the fracture, i.e. parallel to or normal to the rolling direction, leading to an asymmetry in the FLD. The experimental results reported for steel and copper (Fig. 2.18.a-b) closely approached the theoretical curves for geometric ratios $f_0 = t_b/t_a$ of 0.99 and 0.97 or 0.98, respectively. For aluminum, however, considerable discrepancy was observed (Fig. 2.18.c).

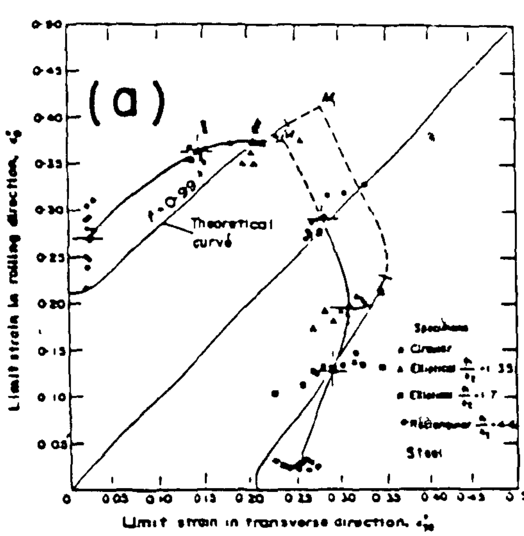

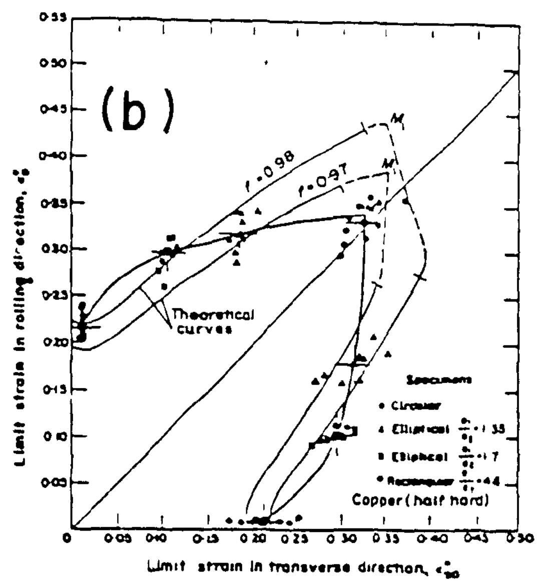

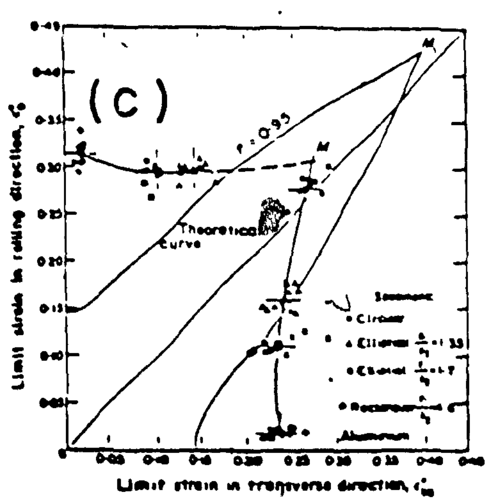

Fig. 2.18 Experimental and theoretical forming limit curves for (a) steel; (b) copper and (c) aluminum. After [59].

From the different theoretical investigations carried out on the basis of the Hill anisotropy analysis [56-62], the following trends concerning the influence of material properties on the limit strain can be summarized:

(i) The geometric (or inhomogeneity) factor $f_0 = t_b/t_a$, which is very difficult to estimate experimentally, has a very strong influence on the limit strain ε^*. The latter increases dramatically when f_0 is increased, i.e. when the inhomogeneity is made smaller A shown by Azrin and Backofen [62], f_0 is a function of the accumulated strain as well as of the ratio of the surface strains

(ii) The hardening coefficient n and strain rate sensitivity m have similar effects on the limit strain [59], which is increased when n or m is larger.

(iii) The strain rate ratio R seems to have only a secondary influence on the forming limit curve [56]. However, this predicted influence (smaller limit strains for higher R-values) still overestimates the experimental ones associated with steel sheets [61].

(iv) The initial strain ε_0 has an effect similar to that of the Lankford coefficient R.

These variations in ε^* were quantified by Marciniak and Kuczynski [56]

$$d\varepsilon^* = 7.4\, df_0 - 0.294\, dR + 1.25\, dn - 0.76\, d\varepsilon_0 \qquad (2.36)$$

where the relation expresses the departure from the 'typical' plastic properties described by $f_0 = 0.95$, $R = 1$, $n = 0.25$ and $\varepsilon_0 = 0.05$. It is of interest to note that the strain rate ratio R has opposite influences on stretching and drawing : an increase in R leads to better drawability but concurrently to a deterioration in the behaviour during extension. Stretch forming thus requires a material having high n and low R values.

II.3.8. YIELD SURFACES

Experimental yield surfaces :

The approximate validity of the Hill anisotropy theory can be verified by comparing the yield surfaces predicted by this analysis with experimental loci. In this way, the plane strain and biaxial behaviours of a workpiece can, for example, be readily visualized.

Only a few experimental yield surfaces have been determined 'completely'. Completely here means that more than the five conventional loading conditions shown in Fig. 2.19 have been examined. Five points in the principal stress plane appear in fact to be enough to estimate the yield locus, as they are sufficient to determine the *size* of the locus. However, there is a great deal of indeterminacy concerning the *shape* of the yield surface, which is closely linked to the strain rate behaviour of the material. The Hill quadratic criterion obviously predicts a smooth yield locus, which will fit the yield stress data reasonably well. The question then remains : what about the strain rates? It is clear that much more data are required regarding the experimental surfaces, in particular their local inclinations, i.e. the values of the strain rate components.

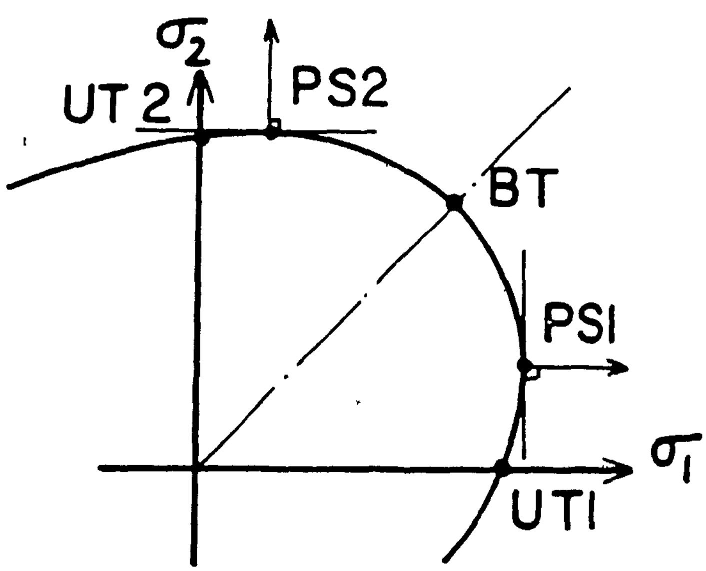

Fig. 2.19 Schematic representation of various loading points on a two-dimensional locus: uniaxial tension in the (UT1, $\sigma_2=0$) and (UT2, $\sigma_1=0$) directions; biaxial (BT, $\sigma_1=\sigma_2$) and plane strain (PS1, $\dot{\varepsilon}_2=0$, and PS2, $\dot{\varepsilon}_1=0$) tension.

In 1971, Dillamore et al.[27] carried out experiments on stabilized stainless steels using combination of axial loading and internal pressure. One of the loci obtained in this way is displayed in Fig. 2.20a. As noted by the authors, these experimental yield surfaces cannot be fitted by an expression of the form proposed by Hill, but require at least a sixth power equation in the stresses. Similar loading conditions (biaxial loading under internal pressure and simultaneous axial tension or compression) were used by Althoff and Wincierz [63] for yield locus measurements of annealed copper and aluminum. The specimens tested were prepared so as to exhibit rather sharp textures. As shown in Fig. 2.20b, the yield surface of copper tubes with a (001)[110] sheet orientation displays rounded corners and flat edges, a geometry which cannot be accommodated by a Hill quadratic criterion (Fig 2.20c). These are better duplicated by crystallographic calculations [63]. However, the experimental yield locus pertaining to recrystallized aluminum tubes is more rounded (Fig. 2.20d) and may be fitted by an analytic function of the Hill type (Eq. 2.11 or 2.32). From this work, it can be deduced that the classical continuum approach does not seem to fit the yielding behaviour of highly textured metals.

In an investigation of copper and aluminum single crystals, Grzesik [64] found good agreement between experimental and crystallographic yield loci. Nevertheless, the lack of values in the uniaxial directions due to his use of the Knoop hardness test renders any comparison with analytic yield functions difficult, if not questionable.

Vial et al. [22,23] measured the uniaxial tension, uniaxial (through thickness) compression, balanced biaxial tension (bulge test) and plane strain compression properties of sheets of various metals (steel, Al, Cu and brass). It was shown that the Hill 1948 criterion is not able to give a good fit to the plastic behaviour of all the samples tested (Fig. 2.21). Its inability to reproduce both the plane strain and biaxial behaviours was partially overcome by the use of more sophisticated criteria, as discussed in section II.4. Similar conclusions were reached by Benferrah [65] regarding the behaviour of cold rolled Al sheet. Also of interest is the investigation carried out by Stout et al. [66] who studied systematically the behaviour of 1100 aluminum from yield to large strains (>1.0). Their measured (back extrapolated) yield stresses diverge from the von

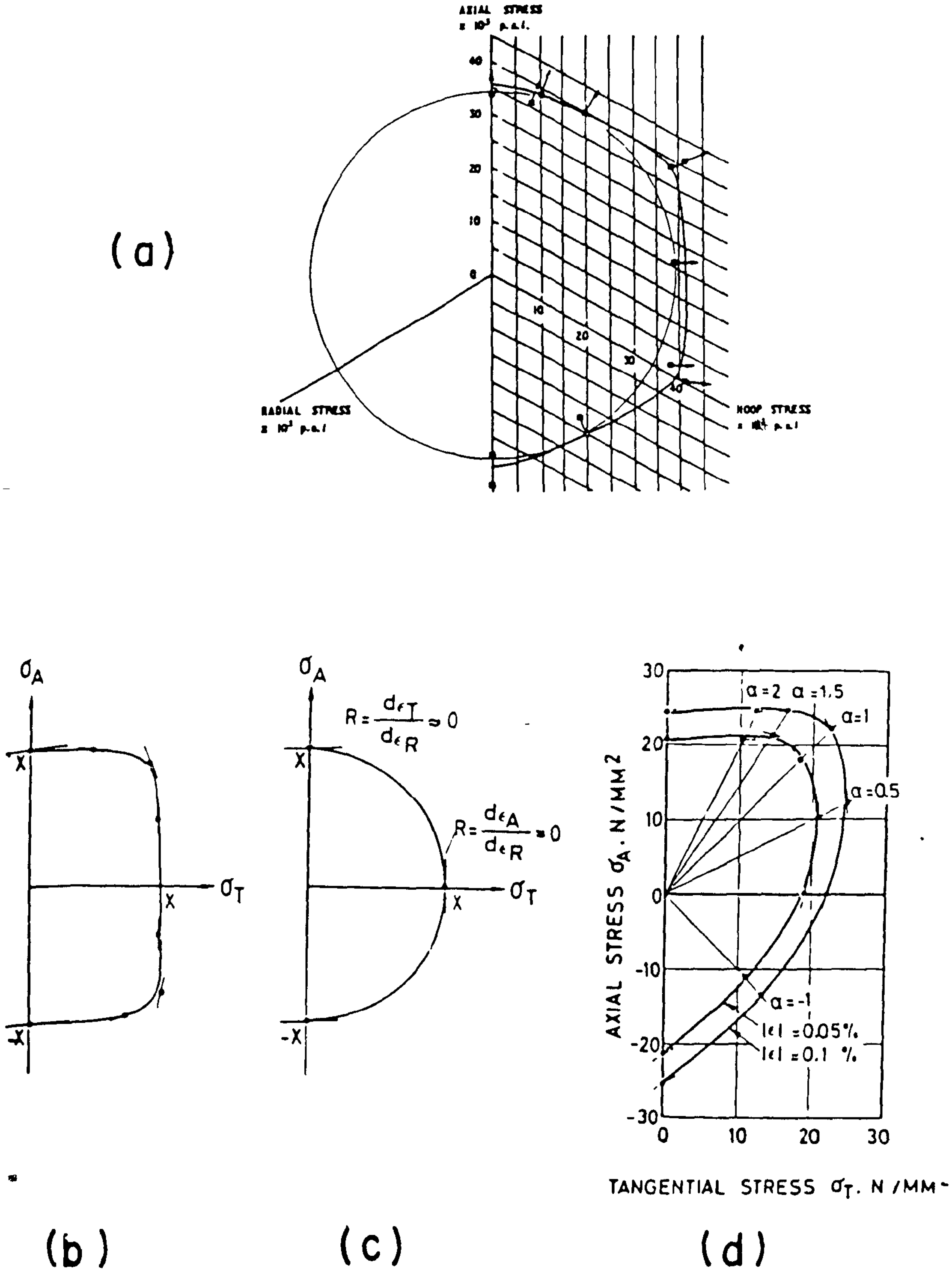

Fig. 2.20 (a) Yield locus plotted in the π-plane for a mild steel. The arrows, indicating the externally directed normal to the yield locus, are determined from strain rate ratio measurements. After [27]. (b) Experimental locus corresponding to a (001)[110] texture. After [63]. (c) Hill 1948 prediction based on yield strength measurement and R = 0 for a {100}<011> texture. After [63]. (d) Measured yield locus for a recrystallized aluminum tube. After [63].

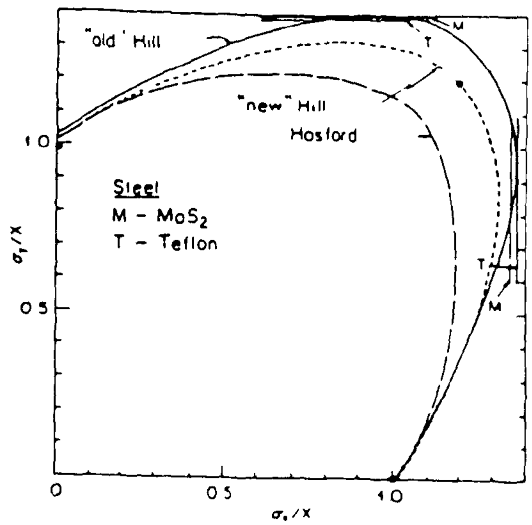

(a)

(b)

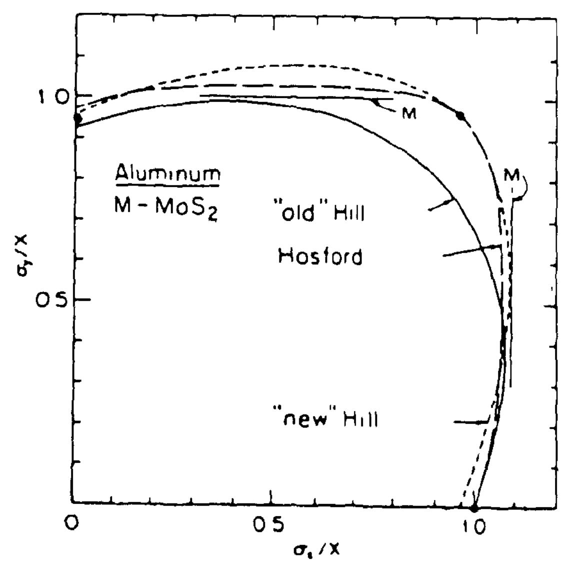

Fig. 2.21 Comparison of experimental data with predicted yield loci normalized by uniaxial tension, X. Experimental data are indicated by solid points and by horizontal and vertical tangents obtained from plane strain tests. The Hill 1948 predictions are referred to as Hill "old" criterion. (a) steel and (b) aluminum. After [22,23].

Mises locus and are better approximated by the theory of polycrystal plasticity [67].

Calculated yield surfaces :

Polycrystal yield surfaces can also be calculated by various crystallographic approaches, as explained in more detail in chapter III. These methods are based on the Taylor/Bishop and Hill theory [1,2,6] of polycrystal plasticity, according to which the overall yield locus is calculated as an average over the reoriented single crystal loci. Canova et al.[11] used a modified version of this analysis (i.e. the relaxed constraints (RC) method of texture prediction) to calculate the grain orientation distribution after a given deformation This calculated distribution was used to plot some yield locus projections, an example of which is shown in Fig. 2.22. Although the vertices and edges displayed by these surfaces are probably too sharp when compared with experimental loci (because the textures predicted by the RC model are too pronounced), it is evident that the overall shape cannot be reproduced by some quadratic function.

Similar comments can be made with regard to the use of experimental (instead of calculated) orientation distributions (OD's). Bunge [10,68], Da C. Viana et al. [38,69] and van Houtte [70] have all employed OD facilities to determine the yield loci of deformed metals. The surfaces obtained in this way by the Bishop and Hill (or modified Bishop and Hill) method display smoother shapes than the ones of Canova et al.[11] (see Fig. 2.23). However, the presence of some flat regions still renders the Hill quadratic criterion unsuitable.

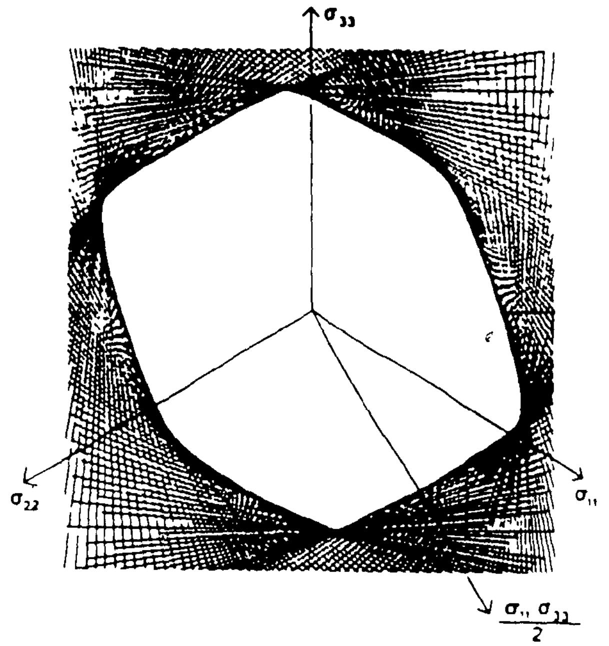

Fig. 2.22 π-plane representation of a calculated FCC yield surface after a rolling reduction of $\varepsilon_{33} = -2$. After [11].

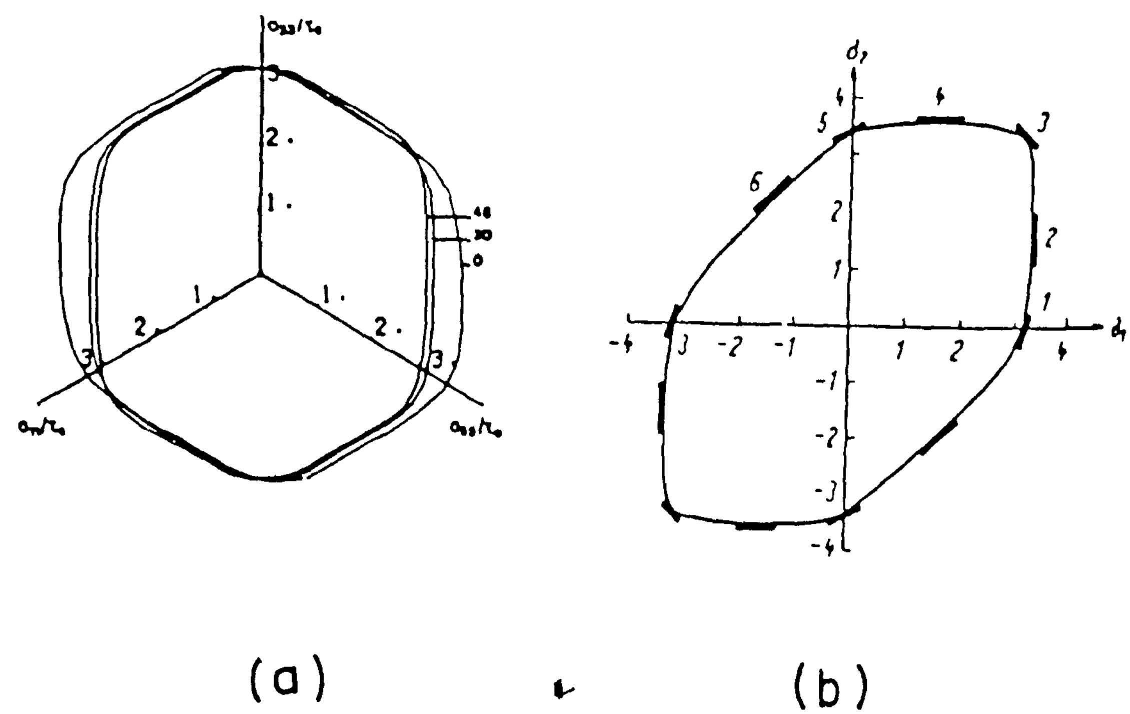

Fig. 2.23 (a) π-plane representation of the FCC theoretical yield surface corresponding to a copper rolling texture. The texture data were taken from a CODF representation. The three angles $\theta = 0$, 30 and 45° pertain to the angle between the 1-axis and the rolling direction. After [70]. (b) Yield locus calculated from CODF data for a 90% cold rolled copper sheet. After [10].

II.4. OTHER YIELD CRITERIA

During the last decade, some new yield criteria have been introduced in order to overcome some of the deficiencies observed in the original Hill (1948) analysis, as reviewed above. The general properties of such functions remain unchanged; i.e. they are expressed in terms of macroscopic stresses, the Bauschinger effect is not taken into account, the hydrostatic pressure is not considered to influence yielding and the parameters of the yield function are determined experimentally. These new criteria will be classified into four groups : those of (i) Hill 1979, (ii) Hosford, (iii) Bassani and (iv) some miscellaneous yield surfaces proposed in the literature.

II.4.1. Hill 1979 yield function

Following the work of Woodthorpe and Pearce [49] on the anomalous behaviour of aluminum, Hill in 1979 [71] (and prior to this date in private communication) put forward a new non-quadratic yield function for orthotropic metals

$$\begin{aligned} f|\sigma_2-\sigma_3|^m + g|\sigma_3-\sigma_1|^m + h|\sigma_1-\sigma_2|^m + a|2\sigma_1-\sigma_2-\sigma_3|^m \\ + b|2\sigma_2-\sigma_1-\sigma_3|^m + c|2\sigma_3-\sigma_2-\sigma_1|^m = \sigma^m \end{aligned} \tag{2.37}$$

Here the σ_i are principal components and m is an exponent which can be a non-integer. When m=2, Eq. 2.37 returns to the form of Eq. 2.8. Eight parameters have to be determined experimentally, i.e. a, b, c, f, g, h, m and σ. As noted by Hosford [24], this general form recognizes the possibility of planar anisotropy. However, it cannot be used for loading conditions which involve shear relative to the 1, 2 and 3 principal axes of anisotropy. If in-plane isotropy is assumed, then the criterion is valid; i.e. shear stress terms are not necessary since the 1 and 2 axes may be oriented in any direction in the sheet.

By applying the normality rule and assuming in-plane isotropy, Hill [71] calculated the biaxial/uniaxial stress and strain rate ratios as a function of the locus parameters

$$\sigma_b/\sigma_u = [\tfrac{1}{2}(1+R)(1+\frac{(2^{m-1}-2)(a-c)}{a+2^{m-2}c+f})]^{-1/m} \tag{2.38}$$

$$R = [(2^{m-1}+2)a-c+h]/[(2^{m-1}-1)a+2c+f] \tag{2.39}$$

For practical use, truncated forms for planar isotropy and plane stress conditions ($\sigma_3 = 0$) were derived with the following coefficients

(i) a = b = 0, f = g, h = 0

$$c|\sigma_1+\sigma_2|^m + f(|\sigma_1|^m + |\sigma_2|^m) = \sigma^m \tag{2.40}$$

(ii) a = b, c = 0, f = g = 0

$$a(|2\sigma_1-\sigma_2|^m + |2\sigma_2-\sigma_1|^m) + h|\sigma_1-\sigma_2|^m = \sigma^m \tag{2.41}$$

(iii) a = b, c = 0, f = g, h = 0

$$a(|2\sigma_1-\sigma_2|^m + |2\sigma_2-\sigma_1|^m) + f(|\sigma_1|^m + |\sigma_2|^m) = \sigma^m \tag{2.42}$$

(iv) a = b = 0, f = g = 0

$$c|\sigma_1+\sigma_2|^m + h|\sigma_1-\sigma_2|^m = \sigma^m \tag{2.43}$$

However, if exception is made for the work of Kobayashi et al. [72] and Dodd and Caddell [73], only case (iv) has been investigated experimentally to any degree [22-24,55,60,74-78]. The advantage of these Hill criteria is that they provide greater flexibility than does the earlier 1948 version. The shape of the yield locus can be changed by considering different exponents m, leading to differences in the R-value predictions (Eq. 2.39).

Dodd and Caddell [73] studied the relation between the parameter R and the exponent m which is required to encompass the anomalous behaviour [49]. The four cases derived by Hill (Eqs. 2.40 to 2.43) were considered, but only under the simplified assumption of planar isotropy. For a given ratio $\sigma_b/\sigma_u > 1$, the limit curve m(R) was calculated using Eq. 2.38. It was shown that case (iii) requires special attention since its use is limited to a minimum value of R. Apart from this restriction, Dodd and Caddell [73] showed that the exponent m can be bounded as the Lankford coefficient R varies. Reporting also the strain rate ratio results obtained from Refs. [49,60,74], they stated that cases (i) to (iii) require m values greater than 2 to predict anomalous behaviour, whereas case (iv) induces m exponents less than 2 (see Table II.2).

Similar results were obtained by Kobayashi et al. [72], who derived the stress-strain relations for plane-strain compression, as expressed by the ratio σ(plane strain)/σ(uniaxial). One of the problems involved in the equivalence between the two tests (as in the case of the biaxial vs uniaxial relationship) is to define the generalized stress and strain increments. As proposed by Mellor and Parmar [78], these can be calculated by considering the equivalence of the plastic work : the work per unit volume should be the same when derived from the stress-strain behaviours of the two tests under consideration.

R	m	Reference	Material
0.6	1.47	49	Aluminum
0.5	1.38	49	Aluminum
0.44	1.5	60	Rimming Steel
0.72	1.8	60	Soft Aluminum
0.63	1.7	74	Soft Aluminum
0.86	1.8	74	70/30 Brass

Table II.2. Experimental values of R and m (from Ref. [73])

If $$\sigma_u = K_u \varepsilon_u^{n_u} \tag{2.44}$$

and $$\sigma_p = K_p \varepsilon_p^{n_p} \tag{2.45}$$

then the equality $w_u = w_p$ implies that

$$K_u \varepsilon_u^{n_u+1} / (n_u + 1) = K_p \varepsilon_p^{n_p+1} / (n_p + 1) \tag{2.46}$$

so that

$$\varepsilon_p = [\frac{K_u (n_p + 1)}{K_p (n_u + 1)} \varepsilon_u^{nu+1}]^{1/(np+1)} \tag{2 47}$$

Similar relations were derived for the biaxial case. The plane strain stress σ_p is then calculated as follows :

$$\sigma_p = \sigma_u (\sigma_p / \sigma_u) = K_u (\sigma_p / \sigma_u)^{n+1} \varepsilon_p^{n_p} \tag{2.48}$$

where ε_p is given by Eq. 2.47 and σ_p / σ_u is obtained theoretically from the yield surface (Eqs. 2.37) and the normality rule.

Using the experimental results of Vial et al. [23] on Al, Cu and brass, Kobayashi et al. [72] reported m-values (fitted from data obtained at a strain $\varepsilon = 0.1$) in the range 1.717 to 1.743 for case (iv) of the Hill equation and above 2 when the other reduced criteria are employed. The reverse results were obtained for an Al-killed steel. Except for the latter example, the correlation between the calculated and experimental true stress-true strain curves was reasonable, as shown in Fig. 2.24. The slight discrepancies observed were attributed to the observed dependence of the exponent m on strain as well as to the questionable assumption of in-plane isotropy : the R-values given by Vial [23] vary from 1.47 to 2.32 for the steel and are in the range [0.45, 0.87] for the copper sheet, for example.

As discussed above, the most commonly used Hill 1979 criterion corresponds to case (iv), Eq. 2.43. When expressed in terms of R (planar isotropy), this gives

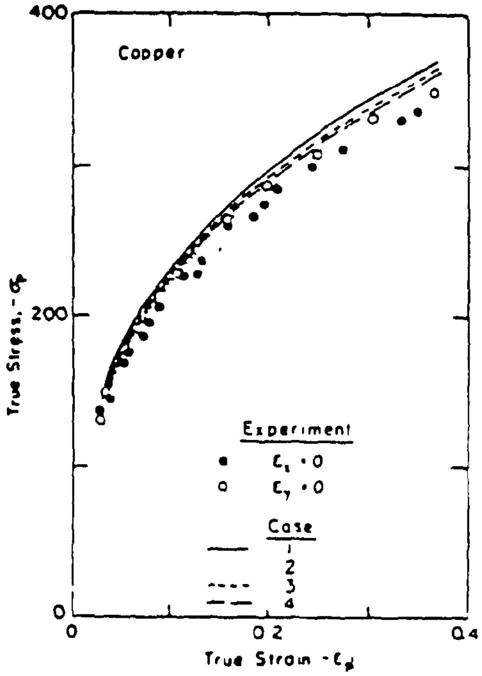

Fig. 2.24 Plane strain compression results comparing predictions vs. experiment for Cu. Cases (1) to (4) refer to predictions obtained from Eqs. 2.40 to 2.43, respectively. After [72].

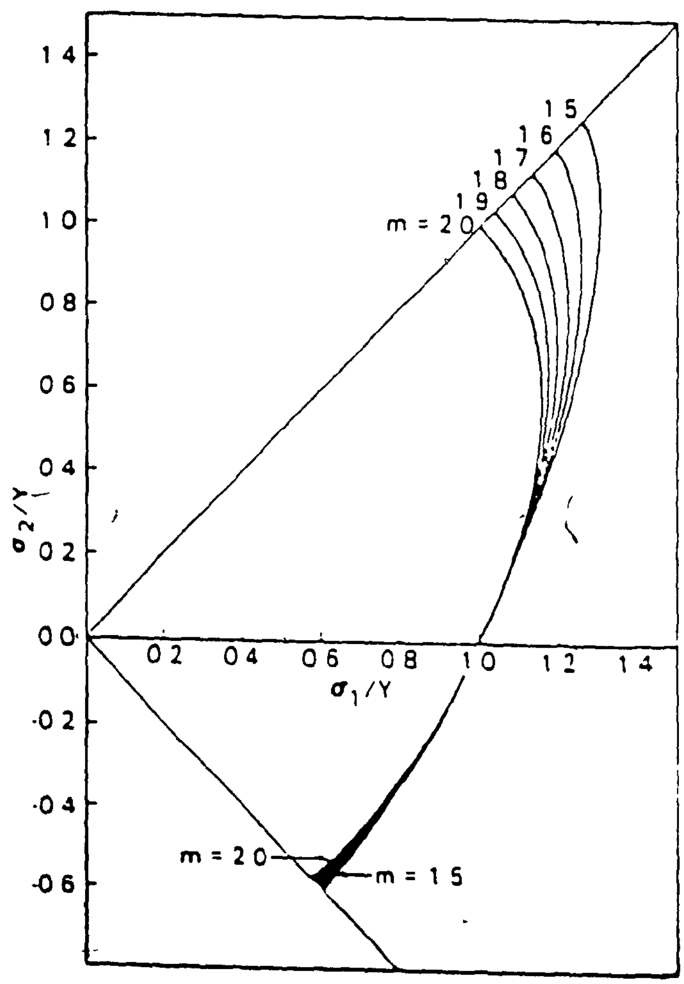

Fig. 2.25 Yield loci based on Hill 1979 yield criterion (case (iv), Eq. 2.49) for R = 1.0. After [78].

$$(1+2R)|\sigma_1-\sigma_2|^m + |\sigma_1+\sigma_2|^m = 2(1+R)\,\sigma_u^{\,m} \tag{2.49}$$

Such a potential is of particular interest for materials with strain rate ratios less than unity, since their plastic properties are not well reproduced by the quadratic function of Eq. 2.8. The influence of the exponent m on the shape of the yield locus is shown in Fig. 2.25. As can be seen, a decrease in m results in an increase in the biaxial and plane strain stresses. Mellor and Parmar [78] used the experimental work of Taghvaipour et al. [79] to determine the flow curves in simple and biaxial tension, employing Eq. 2.38 applied to case (iv). As illustrated in Fig. 2.26 for a steel, the use of an exponent $m=1.5$ gives a satisfactory fit to the biaxial stress-strain curve, despite the low R-value (0.44). In the case of aluminum ($R=0.72$), $m=1.8$ is best.

This 'experimentally' determined m-value was used by Parmar and Mellor [60] for the prediction of limit strains. The Marciniak-Kuczynski model [56] described in section II.3.7 was used, and the principle of the equivalence of plastic work was assumed. The influence of m on the forming limit calculated in this way is shown in Fig. 2.27. It can be appreciated that the use of an exponent $m=1.8$ instead of 2 in the yield criterion reduces dramatically the limit strain in aluminum near balanced biaxial tension. This is of particular interest when the experimental points of Marciniak et al. [59], reported in Fig. 2.18c, are examined, as these are overestimated by the Hill 1948 function. However, it must be borne in mind that the effect of m (as well as of R) on limit strain is probably less than that predicted by the Marciniak model. Thus, care is required in the conclusions drawn from studies of the critical influence of the various parameters included in this kind of model.

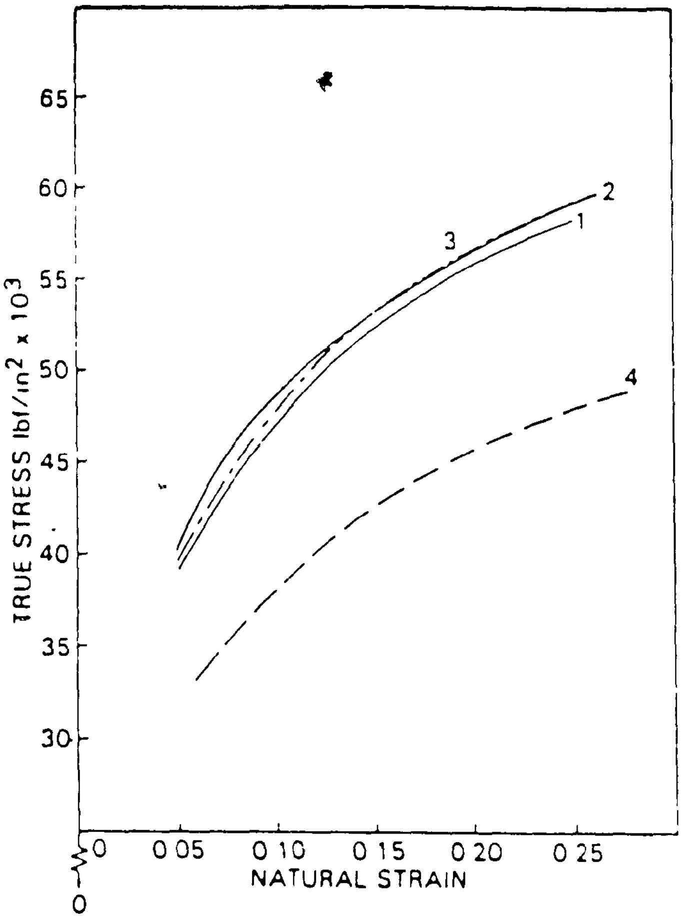

Fig. 2.26 Estimation of m-value from work-hardening characteristics in simple and biaxial tension for a particular steel ($\bar{R} = 0.44$). (1) experimental curve, simple tension, based on average of curves along 0, 45 and 90° to rolling direction; (2) experimental curve, diaphragm test; (3) balanced biaxial tension curve predicted from curve (1), based on Eq. 2.49 with m = 1.5; and (4) balanced biaxial tension curve predicted from curve (1), based on average R-value and Hill 1948 criterion. After [78].

Fig. 2.27 Theoretical forming limit curves showing the influence of the index m (Eq. 2.49). After [60].

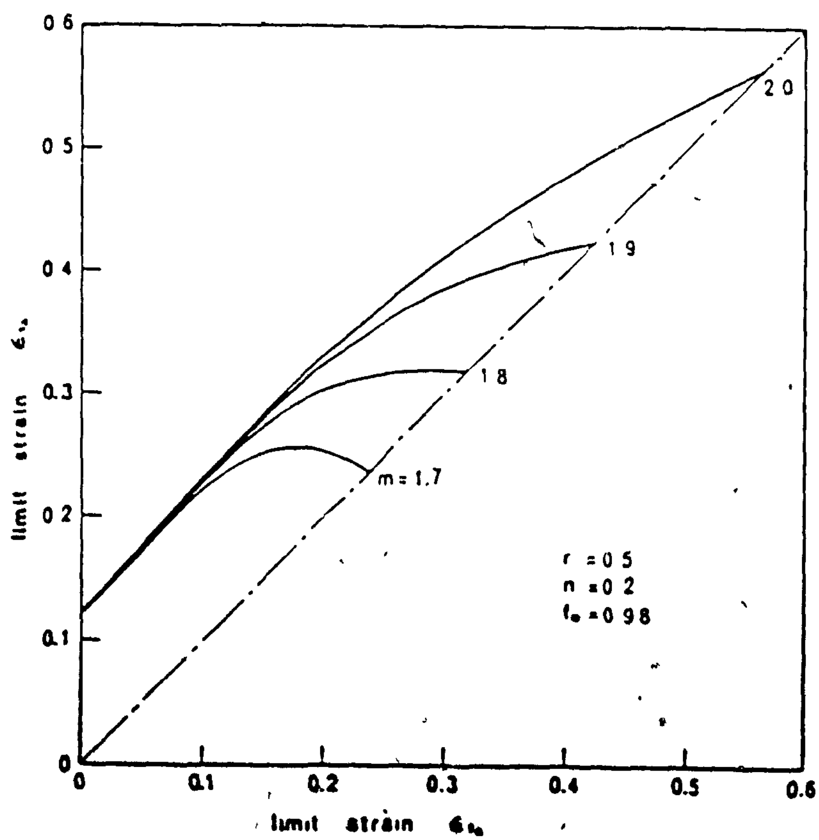

II.4.2. Hosford criteria

Hosford and coworkers [8,23,24,41,43,55,75,80] have carried out many theoretical and experimental investigations on sheet anisotropy. Some of them were focused on a comparison between the predictions obtained from continuum and crystallographic methods of analysis. Their basic technique consists of the generation of textures with rotational symmetry about an (hkl) direction normal to the sheet, averaging the Taylor factor M vs R curves for the individual orientations, and then calculating the R-value (by determining the minimum of the $\overline{M}$ vs R locus), as well as some stress ratios of interest. Both the Taylor/Bishop and Hill [1,6] crystallographic approach based on $\{111\}<1\bar{1}0>$ or $\{110\}<1\bar{1}1>$ slip [8,41,75,81] and the Piehler technique [9] founded on $<111>$-pencil glide [55] were employed in these studies in order to calculate the various parameters of interest (M, R, σ_b/σ_u, LDR,...)

As already discussed in section II.3, the Hill 1948 theory predicts a greater dependence of LDR on R than observed experimentally, underestimates the biaxial flow stress for $R<1$ and overestimates the plane strain strength for $R>0.5$[41]. To overcome these difficulties, Hosford considered a generalized anisotropic yield criterion which appears to be a particular case of the Hill 1979 function (Eq. 2.37) :

$$|\sigma_x|^a + |\sigma_y|^a + R\,|\sigma_x - \sigma_y|^a = (1+R)\,Y^a \tag{2.50}$$

This criterion was used [55,75] to evaluate theoretically some stress ratios corresponding to biaxial tension, uniaxial tension and plane strain compression. In contrast to the Hill case (iv) function, Eq. 2.50 is not able to explain the "anomalous" behaviour reported by Woodthorpe and Pearce [49]. When compared to the crystallographic calculations for FCC or BCC metals (with $\{111\}<1\bar{1}0>$ or $\{110\}<1\bar{1}1>$ slip), it was shown [75] that the best fit corresponds to an exponent $a=8$ to 10 in Eq. 2.50. When compared with the predictions obtained with the $<111>$ pencil glide assumption [55], a similar continuum criterion proved to give good agreement with an exponent a near 6 (see Fig. 2.14). The same value was obtained when fitting to the calculated isotropic yield locus for a randomly oriented material. However, it was not known how well these upper-bound calculations are able to represent the yielding behaviour of actual materials.

In that spirit, a very interesting experimental investigation was carried out by Vial et al. [22,23]. Two main questions were asked, namely :

(i) How can stress-strain curves under complex loading paths be predicted from simple uniaxial tension tests and strain rate ratios ?

(ii) Which yield criterion best fits the experimental data ?

For that purpose, the three functions expressed by Eqs. 2.11 (Hill quadratic), 2.49 (Hill 1979) and 2.50 (Hosford 1979) were employed, but the first and third equations were somewhat modified to take account of a certain degree of planar anisotropy.

$$R\sigma_y^2 + P\sigma_x^2 + RP(\sigma_x - \sigma_y)^2 = P(R+1)\,\sigma^2 \tag{2.51}$$

$$R\,|\sigma_y|^a + P\,|\sigma_x|^a + RP\,|\sigma_x - \sigma_y|^a = P(R+1)\,\sigma^a \tag{2.52}$$

Here R and P represent the strain rate ratios in the rolling and transverse directions, respectively. The exponent a was equal to 6 for FCC and 8 for BCC metals. In Eq. 2.49, the exponent m was fitted to the experimental observations. Four sheet metals with quite different R-values and hardening behaviours, were tested, i.e. Al, Cu, brass and an Al-killed steel. From the comparison between the experimental and theoretical biaxial/uniaxial tension curves and plane strain data, it was concluded that no single criterion can provide the best prediction for all the materials investigated. This is also illustrated in Fig. 2.21, where it can be seen that the "old" Hill, "new" Hill and Hosford criteria give sequential good fits to the experimental yield loci.

In a recent paper [24], Hosford reviewed briefly the effect of the different flow criteria on the prediction of the yield stress ratio $\sigma(\theta)/\sigma(0)$ (see section II.3.1). The latter is overestimated by the Hill 1948 analysis. The introduction of shear terms in his own function (Eq. 2.52) proved to be inconsistent since it led to an obligatory exponent $a=2$, whereas much larger values are intended.

To overcome this difficulty, it was proposed that the yield function should be expressed in the principal stress axes, i.e.

$$R_2 |\sigma_1|^a + R_1 |\sigma_2|^a + R_1 R_2 |\sigma_1 - \sigma_2|^a = R_2 (R_1 + 1) Y_1^a \tag{2.53}$$

This is formally the same function as Eq. 2.52, but is expressed in different axes. Applying this yield criterion to different directions θ and assuming power law work hardening $\sigma = K\bar{\varepsilon}^n$, it was shown that

$$\sigma(90) / \sigma(0) = [\, R(90)(R(0)+1) / R(0)(R(90)+1)\,]^{n+1/a} \tag{2.54}$$

$$\sigma(45) / \sigma(0) = [\, 2R(90)(R(0)+1) / (R(0)+R(90))(1+R(45))\,]^{n+1/a} \tag{2.55}$$

The experimental data displayed in Fig. 2.28 indicate the necessity of a high exponent near 8 in the Hosford criterion in order to reproduce the $\sigma(\theta)/\sigma(0)$ variations for $\theta = 45$ and 90°.

Clearly, all the data reported by the Hosford team are better reproduced by high exponents (6 or 8) when using Eq. 2.50 or Eq. 2.52. This is in apparent contradiction with the results obtained with the Hill 1979 criterion (case (iv)), from which the best exponent seem to lie in the range [1.6,2.0].

More recently, it was shown by Dodd and Caddell [73] that different versions of the Hill 1979 function can lead to completely different exponents m, some of which can accommodate the anomalous behaviour. For example, case (iii) (Eq. 2.42) leads to m-values as high as 5 or 7 for a material exhibiting a strain rate ratio of around 0.4. By contrast, for case (iv) (Eq. 2.43), the corresponding exponent is in the range [1.3, 1.5]. Furthermore, it is easily shown that, for R-values less than unity, the biaxial vs uniaxial behaviour (σ_b/σ_u) is a decreasing function of m in the Hill locus (Eq. 2.49), but an increasing function of the exponent a in the Hosford criterion (Eq. 2.50). Thus, the above apparent contradiction may be due simply to the difference in the type of standard considered.

Fig. 2.28 Experimental flow stress ratios σ_{90}/σ_0 and σ_{45}/σ_0 compared with parameters for predicting these ratios (Eqs. 2.54 and 2.55, R = R(0), Q = R(45) and P = R(90)). Data are for various grades of steel. After [24].

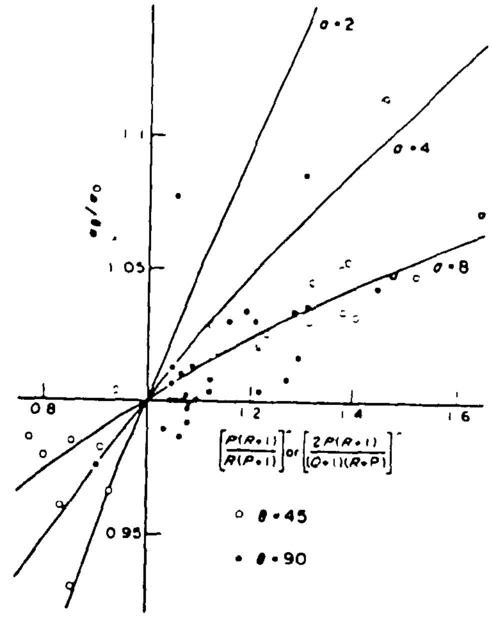

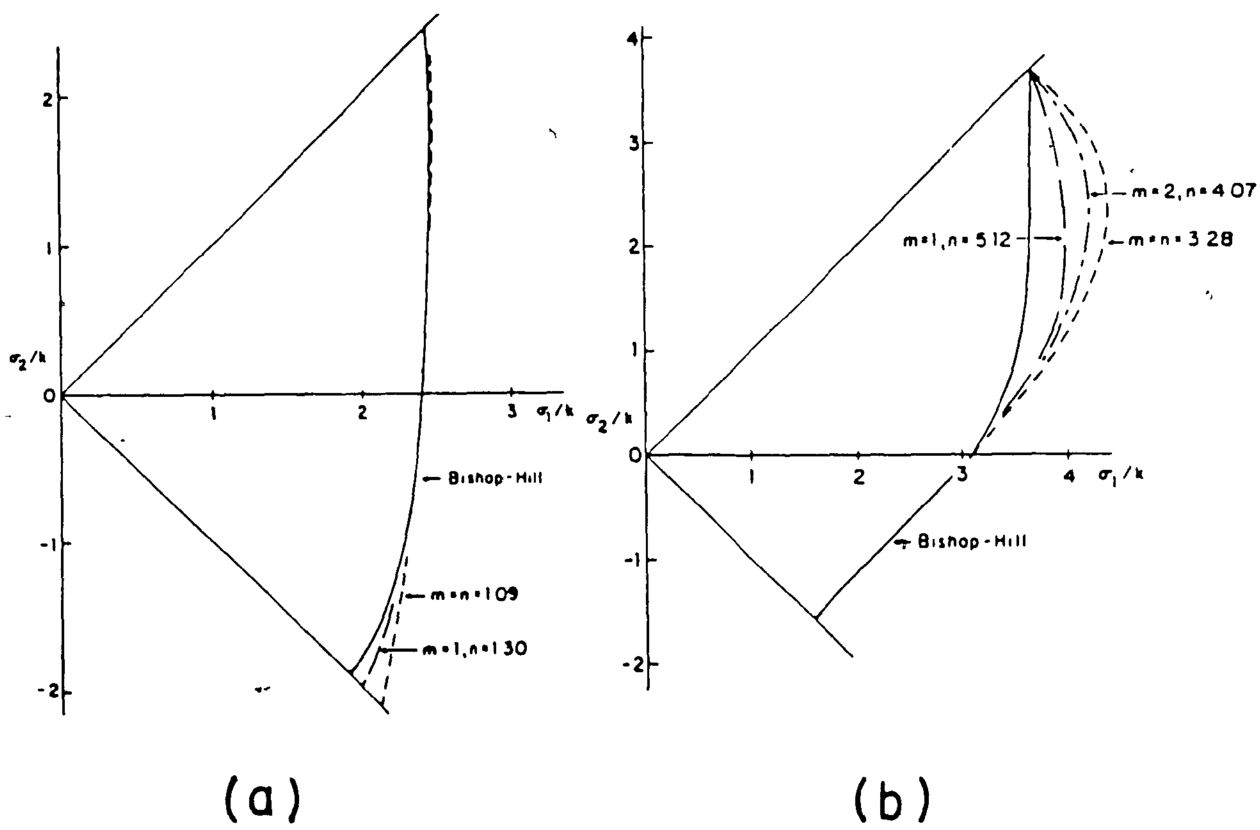

Fig. 2.29 Yield loci for (a) [100] ideal texture, R = 0.092 and (b) [110] ideal texture, R = 7.3. After [76,77].

II.4.3. Bassani criterion

Bassani [76,77] has also characterized the yielding behaviour of metals with transversely isotropic plastic properties. His approach was similar to the one adopted, more or less at the same time, by the Hosford group: namely, the fitting of continuum yield functions to crystallographically calculated loci.

His study was restricted to ideal transversely isotropic textures as specified by their Miller indices [hkl]. In such a case, all the crystals of the aggregate have an <hkl> crystallographic direction parallel to the 3-axis of transverse isotropy. The crystallographic calculations were carried out using a classical Bishop and Hill method for restricted $\{111\}<1\bar{1}0>$ or $\{110\}<1\bar{1}1>$ slip. Both the envelope construction and stress averaging techniques [82] were used for this purpose. The results obtained for the [100] and [110] ideal textures are shown in Fig. 2.29.

A new continuum function was introduced by Bassani to fit these loci :

$$\left| \frac{\sigma_1 + \sigma_2}{2\sigma_b} \right|^n + \left| \frac{\sigma_1 - \sigma_2}{2\tau} \right|^m = 1 \tag{2.56}$$

which was found to be flexible enough to incorporate the behaviour of a wide range of transversely isotropic textures. Note the presence of two different exponents in this criterion, which have to be greater than or equal to one for convexity requirements. The strain rate ratio R is expressed by

$$R = \frac{1}{2}\left[\frac{m}{2} \left(\frac{\sigma_u}{2\tau} \right)^m \left(\frac{2\sigma_b}{\sigma_u} \right)^n - 1 \right] \tag{2.57}$$

so that Eq. 2.56 can be written

$$|\sigma_1 + \sigma_2|^n + (n/m)(1+2R)\,\sigma_u^{n-m}\,|\sigma_1 - \sigma_2|^m = \sigma_u^n\,[1 + (n/m)(1+2R)] \tag{2.58}$$

This reduces to the Hill 1979 criterion (Eq. 2.49) when n = m. The relationship between R, σ_u and σ_b derived from this function is thus

$$\sigma_b / \sigma_u = \tfrac{1}{2}[\, 1 + (n/m)(1 + 2R)\,]^{1/n} \tag{2.59}$$

which can incorporate the 'anomalous' behaviour. Three of the four parameters (σ_b, σ_u and R) were fitted to the data of the Bishop and Hill yield surfaces. m was equated to 1, 2 or n for convexity purposes ($m \geqslant 1$). In this way, the two classes of loci (crystallographic and continuum) coincide in the uniaxial and biaxial directions, and their slopes for uniaxial loading are identical, as illustrated in Fig. 2.29. The best fit was found to correspond to m = 1 with n-values varying in the range [1.3, 5.6] for the different textures investigated. Even though such criteria are not homogeneous in the stresses, they appear to be of greater flexibility than the Hill 1979 function.

Another set of textures was investigated by Bassani [76], namely the orthotropic textures, such as the one produced by rolling. Planar isotropy was also assumed. In this case, an ideal orthotropic rolling texture (hkl) [uvw] was defined as one comprised of equal percentages of (hkl) [uvw], ($\bar{h}$kl) [$\bar{u}$vw], (h$\bar{k}$l) [u$\bar{v}$w] and (hk$\bar{l}$) [uv$\bar{w}$] (because of symmetry requirements). Bishop and Hill calculations were carried out for single textures and combinations of ideal orientations (Fig. 2.30). These loci were then approximated by a family of orthotropic yield loci

$$C_1 |\sigma_1 + \sigma_2|^n + C_2 |\sigma_1 - \sigma_2| + C_3 (\sigma_1 - 2\sigma_2)^2 + C_4 (\sigma_2 - 2\sigma_1)^2 = 1 \tag{2.60}$$

The necessary five parameters were fitted to the calculated (crystallographic) values of σ_{u_1}, σ_{u_2}, R_1, R_2 and σ_b, so that the corresponding yield stresses and slopes coincide for both the crystallographic and continuum loci. However, such functions, for a particular ratio σ_2 / σ_1, have generally more than one solution in the stresses, some of them violating the convexity requirements. In the examples investigated [76], only one of the yield surfaces was found to be convex for each case. The locus predictions made in this way are presented in Fig. 2.30, from which a reasonable agreement is observed. Nevertheless, it is not known how well functions such as Eq. 2.60 are able to represent a wide range of plastic behaviours. It can be objected also that too many parameters are necessary for practical use : the more coefficients (and hence the more complicated the yield function), the better the results, but at the cost of a loss in simplicity.

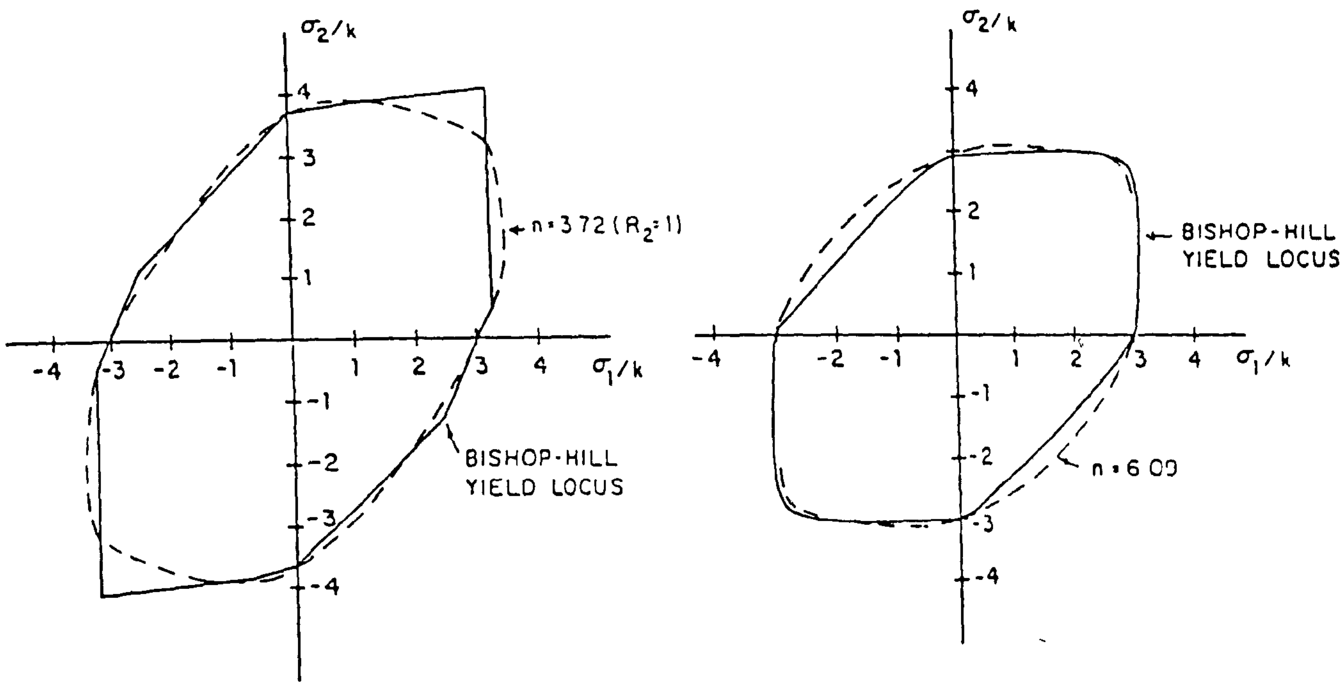

Fig. 2.30 (a) $\{110\}\langle 1\bar{1}2\rangle$ ideal orthotropic texture and (b) 40% $\{100\}\langle 001\rangle$ + 20% $\{213\}\langle 47\bar{5}\rangle$ + 10% $\{112\}\langle 1\bar{1}0\rangle$ + 10% $\{112\}\langle 11\bar{1}\rangle$ + 20% isotropic texture. Broken line : phenomenological yield function of Eq. 2.60 After [76].

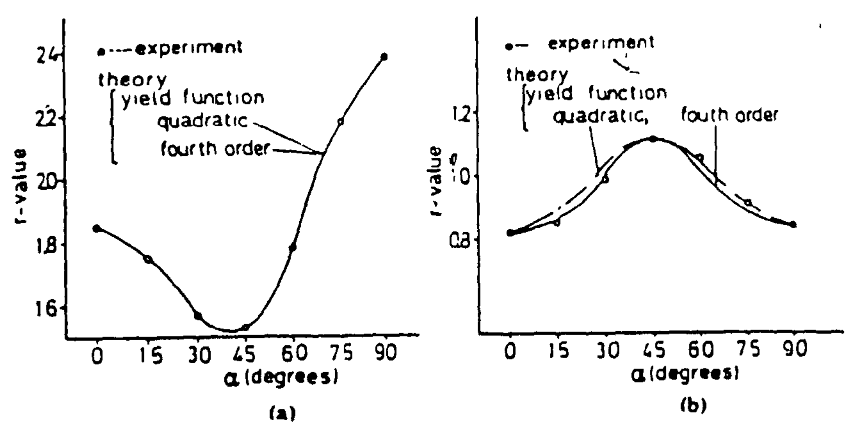

Fig. 2.31 Experimental and theoretical R-values for (a) an Al-killed steel and (b) Cu-1/4H. (o) experimental values; (——- - ——- - —) Hill 1948 predictions and (————) Gotoh calculations. After [25].

II.4.4. Other yield behaviour descriptions

Gotoh criterion

After a statement of some of the disadvantages of the Hill quadratic yield function, Gotoh [26] proposed a fourth order criterion which includes nine parameters

$$f = A_1\sigma_x^4 + A_2\sigma_x^3\sigma_y + A_3\sigma_x^2\sigma_y^2 + A_4\sigma_x\sigma_y^3 + A_5\sigma_y^4 + (A_6\sigma_x^2 + A_7\sigma_x\sigma_y + A_8\sigma_y^2)\,\tau_{xy}^2 + A_9\,\tau_{xy}^4 \qquad (2.61)$$

The expressions of the strain rate and stress ratios derived from Eq. 2.61 depend on the A_i coefficients, as is the case for the type of ear formation. Gotoh determined the range of variation of his function parameters so as to be able to reproduce the occurrence of 0, 2, 4, 6 or 8 ears in drawn cups (as shown by Bourne and Hill [34], a polynomial yield locus of degree n can predict a maximum of 2n ears). All the information required for the determination of the A_i's is given by a series of 4 uniaxial tests at $\theta = 0$, 22.5, 45 and 90° as well as by a biaxial (or plane-strain) tension experiment. In this way, the theoretical and experimental $R(\theta)$ and $\sigma(\theta)$ curves coincide at the four directions θ mentioned above.

In a further paper [25], an investigation was carried out on a commercial Al-killed steel and on Cu-1/4H sheets in order to verify the validity of such fourth order criteria. The results obtained for the $R(\theta)$ and $\sigma(\theta)$ curves are shown in Figs. 2.31 and 2.3, from which it can be seen that a much better fit is produced by the Gotoh criterion rather than with the Hill quadratic function. This is however not surprising since the A_i parameters were chosen so as to permit the predicted yield stress curve to pass through the four experimental points.

Shih and Lee criterion

An interesting extension of Hill's formulation for anisotropic plasticity was carried out by Shih and Lee [83]. The proposed yield function

$$F = M_{ij}(\sigma_i - \alpha_i)(\sigma_j - \alpha_j) - k^2 = 0 \tag{2.62}$$

has the following characteristics :

(i) F is a quadratic criterion involving linear terms in the principal stresses.

(ii) the M_{ij} coefficients describe the dependence of yield stress on orientation ("distortion" of the yield surface)

(iii) the α_i parameters describe the strength differential between tensile and compressive behaviour (Bauschinger effect)

(iv) k quantifies the size of the locus.

These parameters were all determined from uniaxial tension and compression tests carried out along the principal axes under the assumption of orthotropy. The Shih and Lee formulation proved to give good agreement with experiment for the yield strength and yield locus calculation (Fig. 2.32) for HCP metals. However, the R-value predictions were somewhat less convincing and only a reasonable consistency with the experimental points was reported.

Benferrah criterion

In an experimental study of the development of anisotropy during the cold rolling of aluminum sheet, Benferrah [65] was confronted with the anomalous behaviour reported in [2]; the Hill quadratic locus was found to diverge from the experimental one in the biaxial region (Fig. 2.33). The use of the generalized 1979 criterion to overcome this difficulty led to an average experimental exponent m=1.7 in Eq. 2.49. However, because of the planar anisotropy observed, a somewhat modified Hill type criterion was proposed

$$|F\sigma_1 + G\sigma_2|^m + H|\sigma_1 - \sigma_2|^m + 2N\sigma_{12}^m = 1 \tag{2.63}$$

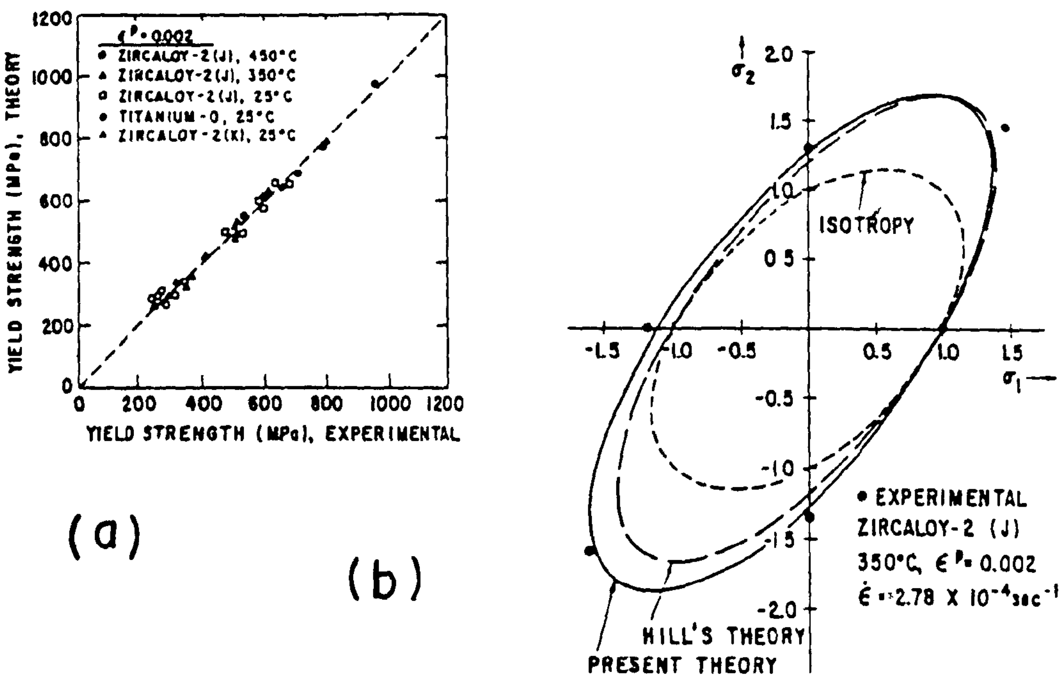

Fig. 2.32 (a) Comparison of calculated (based on Shih and Lee [83] formulation) and experimental yield stresses for different materials. (b) Plane stress yield loci based on the Shih and Lee [83] theory, Hill's theory and isotropy as compared to experimental data for Zircaloy-2 tested at 350°C.

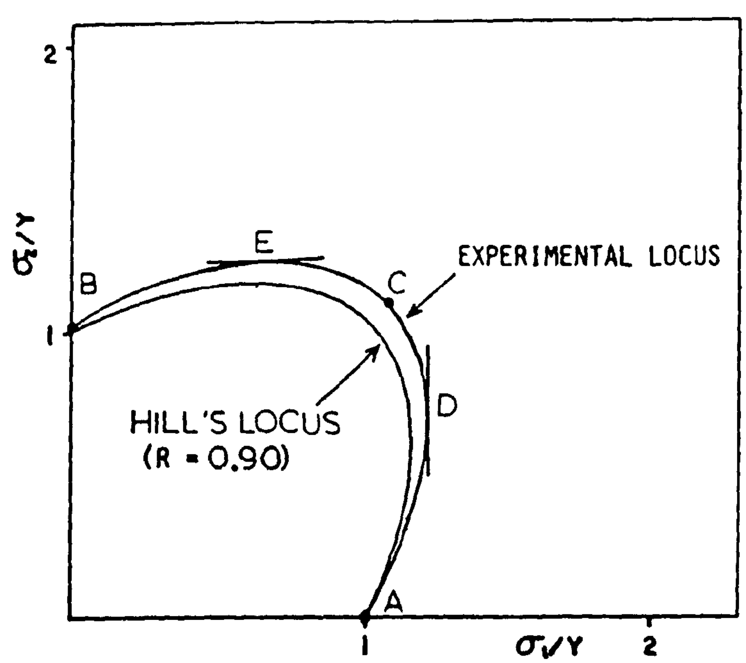

Fig. 2.33 Theoretical Hill 1948 and experimental yield loci for a cold rolled Al sheet. After [65].

This criterion does not violate the condition of the non-influence of the hydrostatic pressure, since the first term on the L.H. side of Eq. 2.63 can be thought to come from a more general criterion involving $|(F+G)\sigma_3 - F\sigma_1 - G\sigma_2|^m$. Although no evidence of the reliability of such a function has been demonstrated, it has the advantage of taking into account the in-plane anisotropy often observed in rolled and annealed materials.

II.5. CONCLUSIONS AND SUMMARY

As illustrated by all the examples given above, the correlation between theory and experiment is relatively poor. No single criterion is able to reproduce the behaviour of a wide range of metals and to fit an extensive variety of plastic properties. In fact, most of the characteristics reviewed are strongly dependent on how well the assumed criterion approximates the shape of the real locus. Continuum quadratic or non-quadratic yield functions are thought to be unable to characterize the complete shape and size of actual yield surfaces.

The properties predicted by the classical criteria used in the literature (Hill 1948, Hill 1979, Hosford 1979, Bassani and Gotoh functions) are summarized in Table II.3. The blanks correspond to situations which, to our knowledge, have not been investigated. The interested reader is referred to the following review papers for more information : Hosford and Backofen [8], Backofen [82], Sowerby and Johnson [84], Hosford and Caddell [80], Mellor and Parmar [78], Blickwede [31], Sowerby [85], Mellor [86,87] and Hosford [81].

TABLE II.3

	Hill 1948	Hill 1979	Hosford 1979	Bassani	Gotoh
Yield stress ratio	variations overestimated	–	better than Hill 1948 with a = 8	–	very good
Strain rate ratio R(θ)	good	–	–	–	very good
Earing behaviour	underestimated maxi. no of ears:4	–	–	–	right no of ears with adequate parameters
LDR vs. R	greater dependence than observed	better than Hill 1948 with m < 2	good in certain cases	–	–
Biaxial work hardening character.	underestimated for R < 1 overestimated for R > 1	better than Hill 1948 with m < 2	good in certain cases	–	–
Anomalous behaviour	not predicted	predicted with m ∈]1,2[	not predicted	predicted	predicted
Limit strains	too large dependence on R	rather good for R < 1 and m < 2	–	–	–
Yield surfaces	too smooth irregular predictions	irregular predictions	good agreement with B&H calc. with a = 6 (BCC) and a = 8 (FCC)	reasonable approximation of B&H loci Possibility of corners	–
General comments	best with mat. having R∉]1,2[or planar isotropy	adjustable exp. m m varies with strain	high exp. (6 to 8) compared to m < 2 for Hill 1979	2 exp. n and m with m = 1,2 or n(adjustable and greater than 2)	9 adjustable parameters

CHAPTER III

CRYSTALLOGRAPHIC YIELD SURFACES OF PERFECT AND DISORIENTED SINGLE CRYSTALS

III.1. DESCRIPTION OF THE SINGLE CRYSTAL YIELD SURFACE

The yield surface of a 'perfect' cubic single crystal is well known. It is derived from knowledge of the activated slip systems*. More precisely, if the slip plane is represented by {hkl} and the slip direction by <uvw>, then the shear stress acting on the {hkl}<uvw> system is

$$\tau = b_i \sigma_{ij} n_j \tag{3.1}$$

where σ_{ij} is the state of stress and b_i and n_j are the normalized components of the slip direction and slip plane normal, respectively. On the assumption that the $\{111\}<1\bar{1}0>$ family of slip systems is dominant in FCC metals (or equivalently that the $\{110\}<1\bar{1}1>$ systems dominate in BCC metals), Bishop and Hill [1, 6] demonstrated that the yield surface is a polyhedron in stress space with 56 vertices and 24 faces. Each of the latter is associated with one of the 24 $\{111\}<1\bar{1}0>$ possible slip systems and is characterized by Eq. 3.1. When the stress vector terminates on a face, slip occurs on the corresponding system; when it intersects an edge, the two to six adjacent systems are activated; finally, when it intersects a vertex, the adjoining 6 or 8 systems can be activated.

* This chapter is based substantially on Ref. [88].

Similar polyhedra can be constructed by assuming that other slip systems operate as well, e.g. the {112}<11$\bar{1}$> in BCC metals [89]. However, such models are more complex because the different sets of systems generally have different critical resolved shear stresses associated with them.

III.2. ANALYTIC REPRESENTATION OF THE SCATTER OBSERVED IN EXPERIMENTAL POLE FIGURES

A given polycrystal cannot be realistically described by the superposition of discrete ideal orientations since a spread is generally observed around the various texture components detected experimentally. An example is presented in Fig. 3.1 for an Al sheet containing a cube texture taken from the work of Lucke et al. [90] (see also Rose and Stuwe [91] and Althoff and Wincierz [63]). Similar conclusions can be drawn regarding melt-grown single crystals, in which a scatter of around 2° has been reported for Al and Cu single crystals grown by the Bridgman technique [64]. In coarse grained crystals deformed by rolling [92, 93], this can increase up to 5°. Furthermore, Van Houtte [94] and Lucke et al. [90] have reported still larger misorientations (e.g. 10 to 15°) in rolled polycrystals.

For computational purposes, it is useful to represent such an orientation spread by means of a gaussian distribution. Although not entirely realistic physically, the scatter is generally assumed to have rotational symmetry about the <100> axes, which leads to simplifications in subsequent calculation. This approach was adopted by Bunge [16], who proposed the following function for the distribution density of a particular orientation **g** :

$$f(g) = f(g_0)\, exp\,(\, -\omega^2 \,/\, \omega_0^2\,) \tag{3.2}$$

Here ω is the rotation angle responsible for the spread, and ω_0 is the scatter width, both of which are defined in more detail below.

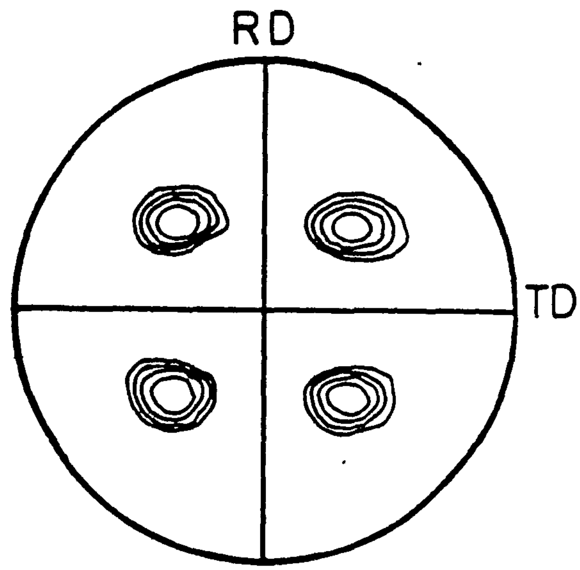

Fig. 3.1 {111} pole figures of high purity cube textured annealed aluminum. From Ref. [90].

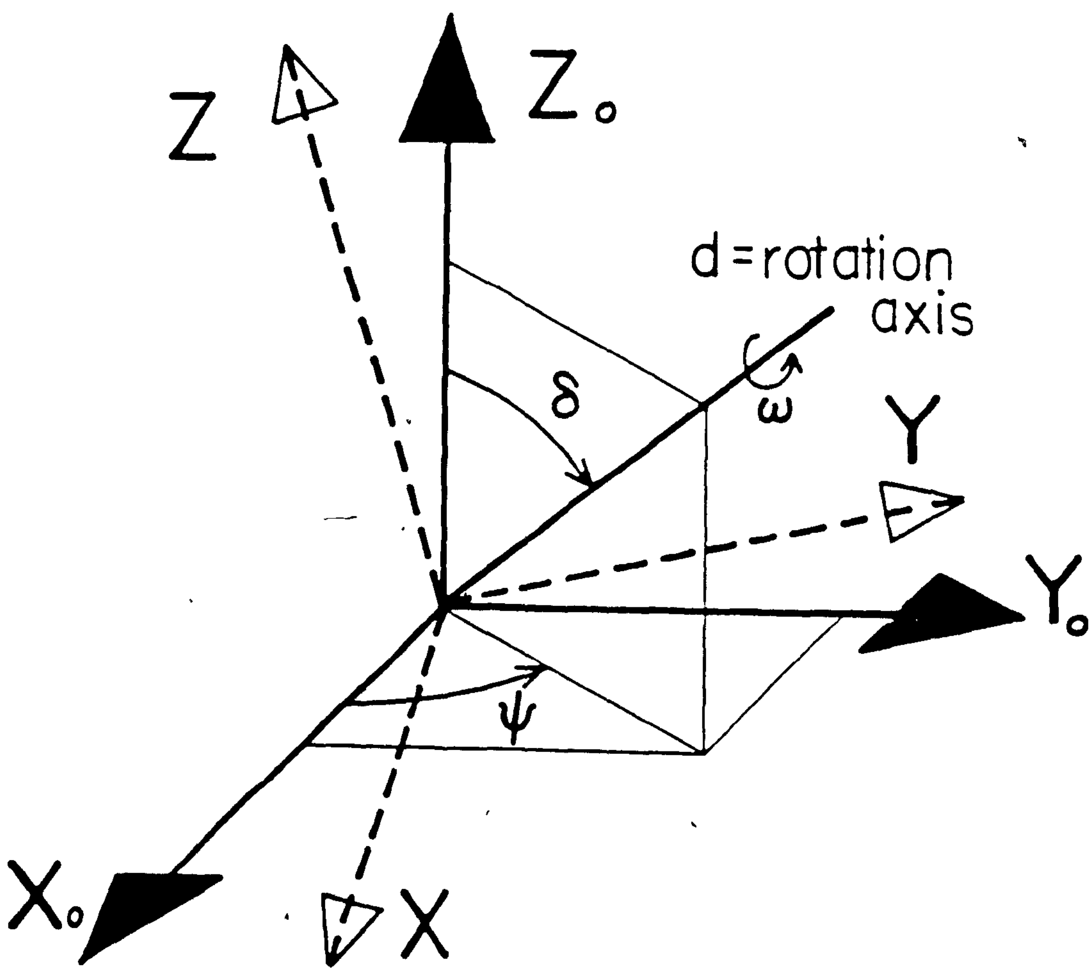

Fig. 3.2 Representation of the orientation difference between two grains by the rotation axis d (referred to in terms of the angles δ and ψ) and the angle of rotation ω about this axis.

Let us consider two different orthogonal reference systems : (C_0) associated with the <100> axes of the ideal orientation g_0, and (C) associated with the <100> axes of each disoriented crystal g. In the present case, the C_0 axes coincide with the sample axes, which provide the reference system with respect to which the strain rate tensor is defined. It is always possible to go from the first to the second orthogonal system by a single rotation ω about a specific axis of rotation d. The orientation of this axis can be characterized by the spherical coordinates δ, ψ (Fig. 3.2), so that the orientation of grain g is in turn specified by the three angles (δ, ψ, ω). These angles should not be confused with the Euler angles which are also associated with the orientation of grain g, but which are less useful for the present purpose. The transformation matrix for passage from the (C_0) to the (C) axes as well as the relation between the two sets of angles are given in Appendix III.1.

A rotationally symmetric gaussian distribution of misorientation ω_0 about the ideal orientation g_0 can thus be generated by randomizing :

(i) the position of the rotation axis (i.e. by setting up random values of cos δ and ψ according to uniform distributions in the ranges [0,1] and [0,2π]); and

(ii) the rotation angle ω itself, according to the gaussian probability distribution specified below:

$$p(\omega) = p(\omega_0)\, exp\left(-\tfrac{1}{2}(\omega/\omega_0)^2 \right) \tag{3.3}$$

Figures 3.3a to 3.3f show the evolution of {100} pole figures corresponding to a series of gaussian distributions of increasing scatter width ω_0. For this purpose, 200 orientations were used with scatter widths ω_0 = 0, 5, 10, 15, 20 and 45°. It should be noted that this definition of the scatter width differs from the one used in the metallurgical literature (Eq. 3.1), but is consistent with the notation generally employed in statistics. The {111} pole figures pertaining to ω_0 = 5, 10 and 15° are shown in Figs. 3.4a to 3.4c. This representation, with lines of equal intensity, should be compared with the experimental pole figures of Fig. 3.1, from which it can be seen that the experimental scatter width is about 10°.

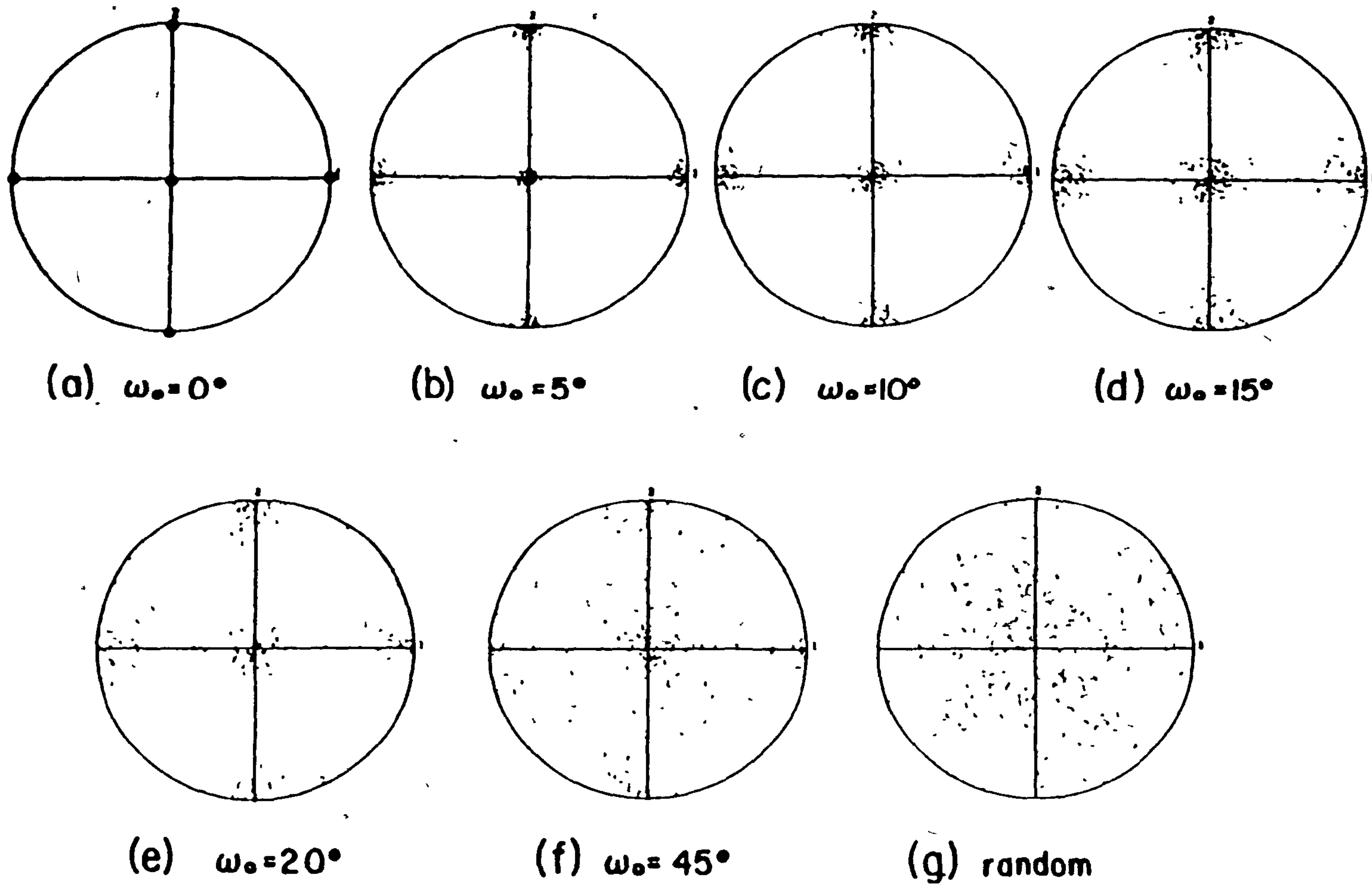

Fig. 3.3 {100} pole figures corresponding to a series of gaussian distributions of increasing scatter width ω_0. (a) $\omega_0 = 0°$ (single crystal), (b-f) $\omega_0 = 5°$, $10°$, $15°$, $20°$, $45°$, (g) random.

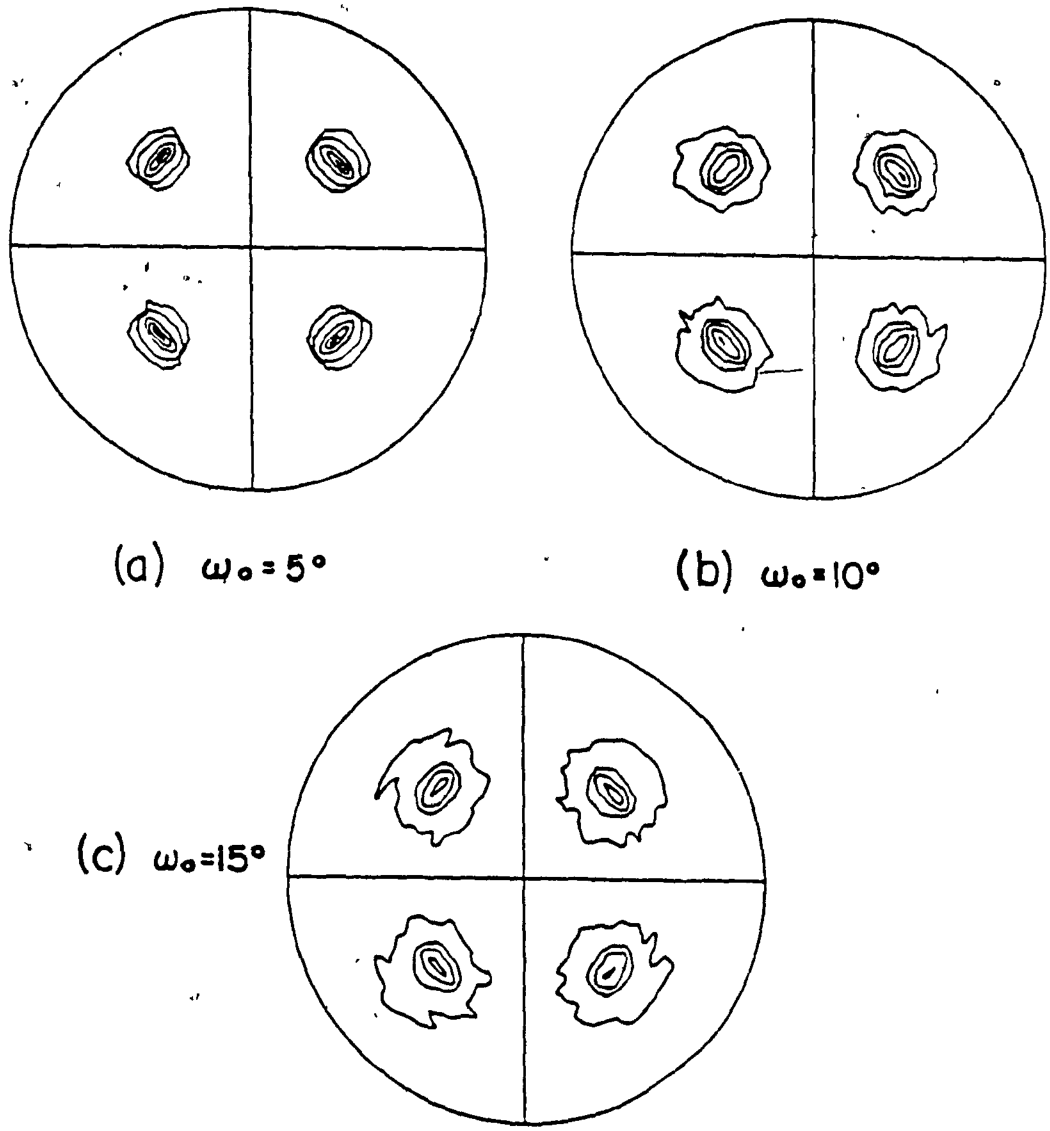

Fig. 3.4 {111} pole figures using contour lines corresponding to gaussian distributions of increasing scatter widths : (a) $\omega_0 = 5°$ (b) $\omega_0 = 10°$ and (c) $\omega_0 = 15°$. Plotting subroutine from Ref. [98].

The random orientations were generated by employing the following elementary volume [16,95] :

$$dg = (1/\pi^2)\, \sin^2(\omega/2)\, d\omega\, d(\cos\delta)\, d\psi \qquad (3.4)$$

An example of the distribution obtained in this way is given in Fig. 3.3g.

III.3. CALCULATION OF THE POLYCRYSTAL YIELD SURFACE - TAYLOR MODEL

In the present investigation, the Taylor uniform strain assumption [2] as well as the Bishop and Hill maximum work principle [1] were employed and applied to each crystallite of the various representative polycrystals described above. The relevant corner or edge of the single crystal yield locus is the one for which the rate of plastic work per unit volume:

$$\dot{W} = S_{ij}{}^{g}\, \dot{\varepsilon}_{ij}{}^{g} \qquad (3.5)$$

attains a maximum value. In the above equation, $S_{ij}{}^{g}$ and $\dot{\varepsilon}_{ij}{}^{g}$ are the components of the deviator stress and strain rate tensors associated with each grain.

The yield locus of the polycrystal as a whole was then calculated from the averages of the power terms associated with the individual grains [11,76,77], as given by :

$$\overline{\dot{W}} = S_{ij}\, \dot{\varepsilon}_{ij} = \overline{S_{ij}{}^{g}\, \dot{\varepsilon}_{ij}{}^{g}} = \overline{S_{ij}{}^{g}}\, \dot{\varepsilon}_{ij} \qquad i,j = 1,2,3 \qquad (3.6)$$

for all $\dot{\varepsilon}_{ij}$. Here use is made of the Taylor assumption $\dot{\varepsilon}_{ij}{}^{g} = \dot{\varepsilon}_{ij}$, where $\dot{\varepsilon}_{ij}$ and S_{ij} refer to the polycrystal, summation over repeated indices is indicated, and the bars denote averaging over the single crystal orientations being considered. For all $\dot{\varepsilon}_{ij}$, expression 3.6 defines a set of hyperplanes in stress space, the inner envelope of which characterizes the yield surface. As the power dissipated is a scalar quantity, this computation only gives the distance from the origin to the tangent hyperplane representing each particular strain rate (see Fig. 3.5) and not the stress component itself.

Because of the lack of influence of the hydrostatic pressure on the yield stress, there are only five independent components of the stress tensor, and the yield surface can therefore be represented in terms of five, as opposed to six, dimensions. In carrying out this simplification, there is nevertheless some freedom of choice regarding the representation of the stress components in the reduced stress space. Kocks et al.[96], for example, selected the sets :

$$\vec{S} = (S_\iota) = ((S_{11} - S_{22})/2, 3S_{33}/2, S_{23}, S_{31}, S_{12}) \tag{3.7}$$

$$\vec{\dot{\varepsilon}} = (\dot{\varepsilon}_\iota) = (\dot{\varepsilon}_{11} - \dot{\varepsilon}_{22}, \dot{\varepsilon}_{33}, 2\dot{\varepsilon}_{23}, 2\dot{\varepsilon}_{31}, 2\dot{\varepsilon}_{12}) \tag{3.8}$$

for their stress and strain rate vectors. Canova et al.[11] have shown that, as long as the $\vec{S}$ and $\vec{\dot{\varepsilon}}$ vectors are work-conjugate (i.e. if $S_{ij}\,\dot{\varepsilon}_{ij} = S_k\,\dot{\varepsilon}_k$), the normality rule is satisfied in the respective five-dimensional space. However, as a result of the differences in scaling between the various stress and strain rate components, care is required when plotting or deriving yield surface sections because of the normalizations that are required. To simplify the plotting procedure, the following modified notation* is therefore proposed :

$$\vec{S} = (S_\iota) = ((S_{22} - S_{11})/\sqrt{2}, \sqrt{3/2}\,S_{33}, \sqrt{2}\,S_{23}, \sqrt{2}\,S_{31}, \sqrt{2}\,S_{12}) \tag{3.9}$$

$$\vec{\dot{\varepsilon}} = (\dot{\varepsilon}_\iota) = ((\dot{\varepsilon}_{22} - \dot{\varepsilon}_{11})/\sqrt{2}, \sqrt{3/2}\,\dot{\varepsilon}_{33}, \sqrt{2}\,\dot{\varepsilon}_{23}, \sqrt{2}\,\dot{\varepsilon}_{31}, \sqrt{2}\,\dot{\varepsilon}_{12}) \tag{3.10}$$

---

* Van Houtte [97] has independently derived a similar type of space, differing only in the definitions of the two unit vectors in the π-plane (Van Houtte's axes are rotated clockwise by 15° with respect to the ones used here). Any rotated reference system in this particular subspace will in fact lead to such an improved representation as long as the condition $S_k\,\dot{\varepsilon}_k = S_{ij}\,\dot{\varepsilon}_{ij}$ is respected.

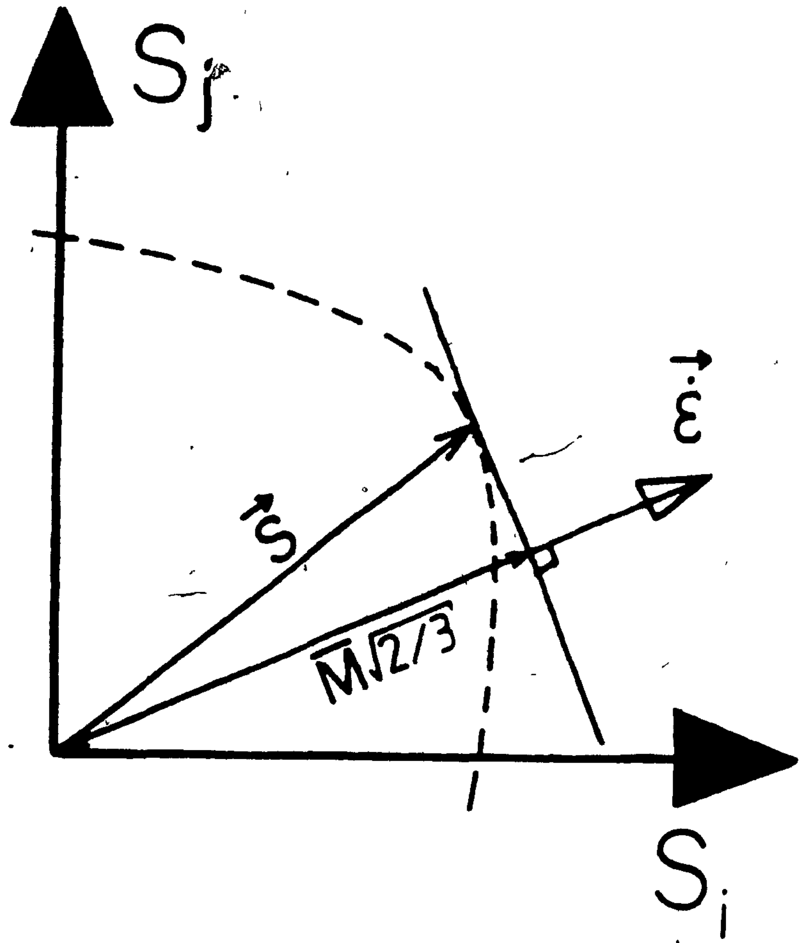

Fig. 3.5 The mean Taylor factor $\overline{M}$, averaged over all the grains, is proportional to the distance from the origin to the tangent hyperplane associated with a particular applied strain rate. The broken line represents the projection of the yield surface onto two dimensions defined as the inner envelope of all the hyperplanes.

Note that, as these vectors are work conjugate, the normality rule continues to apply, and that, unlike earlier reference frames, the present one is orthonormal: the five base vectors defining the five dimensional stress or strain rate space have the same length. The derivations of the transformation matrix, as well as of the unit vectors used in this work, are given in Appendix III.2**.

The hyperplanes defined by Eq. 3.6 can be represented by :

$$S_\iota \dot{\varepsilon}_\iota = \overline{S_\iota{}^g}\, \dot{\varepsilon}_\iota \qquad \iota = 1 \text{ to } 5 \tag{3.11}$$

For each grain, the stress vector ($S_\iota{}^g$) is calculated using the maximum work principle or equivalently the flow rule: i.e. the prescribed strain rate vector ($\dot{\varepsilon}_i$) is taken as normal to the yield surface associated with the single crystal being considered at the point $S_\iota{}^g$.

In this way, a section [11] of the locus in the π-plane ($S_3 = S_4 = S_5 = 0$), for example, is characterized by the inner envelope of the lines

$$S_1\dot{\varepsilon}_1 + S_2\dot{\varepsilon}_2 = \overline{S_1{}^g}\dot{\varepsilon}_1 + \overline{S_2{}^g}\dot{\varepsilon}_2 + \overline{S_3{}^g}\dot{\varepsilon}_3 + \overline{S_4{}^g}\dot{\varepsilon}_4 + \overline{S_5{}^g}\dot{\varepsilon}_5 \tag{3.12}$$

The four ratios $\dot{\varepsilon}_2/\dot{\varepsilon}_1$, $\dot{\varepsilon}_3/\dot{\varepsilon}_1$, $\dot{\varepsilon}_4/\dot{\varepsilon}_1$ and $\dot{\varepsilon}_5/\dot{\varepsilon}_1$ thus have to be varied for the complete description of such a two dimensional section.

By contrast, the projection onto the π-plane ($\dot{\varepsilon}_3 = \dot{\varepsilon}_4 = \dot{\varepsilon}_5 = 0$) is given by the envelope of another set of lines specified by

$$S_1\dot{\varepsilon}_1 + S_2\dot{\varepsilon}_2 = \overline{S_1{}^g}\dot{\varepsilon}_1 + \overline{S_2{}^g}\dot{\varepsilon}_2 \tag{3.13}$$

for all $\dot{\varepsilon}_1$ and $\dot{\varepsilon}_2$.

** It should be noted that, with the present five-dimensional notation, the von Mises equivalent strain rate is defined as $\dot{\varepsilon}_{eq} = (\frac{2}{3}\dot{\varepsilon}_{ij}\dot{\varepsilon}_{ij})^{\frac{1}{2}} = (\frac{2}{3}\dot{\varepsilon}_i\dot{\varepsilon}_i)^{\frac{1}{2}}$ so that the equivalent stress is given by $\sigma_{eq} = W / \dot{\varepsilon}_{eq} = \sigma_{ij}\, \dot{\varepsilon}_{ij} / \dot{\varepsilon}_{eq}$. By contrast, when the Kocks et al. notation (Eq. 3.8) is used, the von Mises equivalent strain rate is given by $\dot{\varepsilon}_{eq} = (\frac{1}{3}\dot{\varepsilon}_1{}^2 + \dot{\varepsilon}_2{}^2 + (\dot{\varepsilon}_3{}^2 + \dot{\varepsilon}_4{}^2 + \dot{\varepsilon}_5{}^2)/6)^{\frac{1}{2}}$.

It is readily seen that the projection leads to much simpler computations because only the ratio $\dot{\varepsilon}_2/\dot{\varepsilon}_1$ needs to be varied in order to define the operative stress vector. The determination of S_i^g from a section necessitates instead the 'sweeping' of strain rate space with up to four parameters.

The envelope method described above is only valid under the Taylor uniform strain assumption and can only lead, from a practical point of view, to two dimensional projections of the polycrystal yield surface.

The two dimensional subspaces presented below were prepared with the aid of the 'equilibrated' components described above, which lead directly to π-plane and other stress space projections of suitable shape. Because of the orthotropic symmetry, the different subspaces used in this work (π-plane and shear stress planes) are 'closed' in terms of the definitions of Canova and coworkers [11] and the hyperplanes defined by Eq. 3.11 describe projections of the yield surface which coincide with its sections. Thus, in each subspace, the distance from the origin to the tangent is $\overline{M}\sqrt{2/3}$, where $\overline{M}$ is the mean Taylor factor defined by $\overline{M} = \overline{\dot{W}}/\tau_c\ \dot{\varepsilon}_{eq}$. Here τ_c is the critical resolved shear stress and $\dot{\varepsilon}_{eq}$ is the conventional equivalent strain rate.

III.4. YIELD SURFACE INTERSECTIONS FOR CUBE TEXTURED POLYCRYSTALS

Two types of yield surface intersections were prepared by the method described above : (i) the π-plane (S_{11}, S_{22}, S_{33}) cross-section (Fig. 3.6); and (ii) that containing two of the shear stress axes (S_{ij}, S_{ik}) and therefore passing through the origin (Fig. 3.7). For this purpose, the minimum number of grains required for an acceptable representation of the yield surface was first determined. This was done by calculating the dependence of the mean Taylor factor along three loading directions in the π-plane (plane strain, $\dot{\varepsilon}_2 = 0$; uniaxial tension along the 1 direction $\dot{\varepsilon}_2 = \dot{\varepsilon}_1/\sqrt{3}$; and plane strain, $\dot{\varepsilon}_2 = \dot{\varepsilon}_1\sqrt{3}$) on the number of grains under consideration for the random and gaussian (scatter width $\omega_0 = 10°$) cases. As illustrated in Table III.1, about 800 crystallites are required to attain representativity for the random material, whereas 400 grains are sufficient for a good approximation of the behaviour of the textured samples (which only contain a single texture component, of course).

Orientation of the grains	Number of grains	Taylor factor $\overline{M}$		
		$\dot{\varepsilon}_2 = 0$	$\dot{\varepsilon}_2 = \dot{\varepsilon}_1/\sqrt{3}$	$\dot{\varepsilon}_2 = \dot{\varepsilon}_1 \sqrt{3}$
random	200 400 800	2.820 2.861 2.893	2.999 3.042 3.062	2.831 2.860 2.861
gaussian scatter width $\omega_0 = 10°$	200 400 800	2.336 2.347 2.349	2.421 2.424 2.424	2.367 2.360 2.359

Table III.1. Dependence of the mean Taylor factor $\overline{M}$ on the number of grains along three loading directions $\dot{\varepsilon}_2 = 0$ (plane strain), $\dot{\varepsilon}_2 = \dot{\varepsilon}_1 / \sqrt{3}$ (simple tension) and $\dot{\varepsilon}_2 = \dot{\varepsilon}_1 \sqrt{3}$ (plane strain).

The evolution of yield surface shape in the π-plane with increasing scatter width is presented in Fig. 3.6. The initial form of the yield surface is the well-known single crystal hexagon which corresponds to a scatter width $\omega_0 = 0°$. The hexagon becomes more and more rounded as ω_0 is increased to 5 and then to 10°; it then remains relatively circular in the interval $10° < \omega_0 < 20°$, and thus corresponds fairly well to the Hill quadratic yield criterion (with cubic symmetry) in this interval. For scatter widths above 20°, flattened faces appear once again, separated by rounded vertices; finally, as the random distribution is approached, the 'rounded Tresca' shape first found by Bishop and Hill [6] becomes evident.

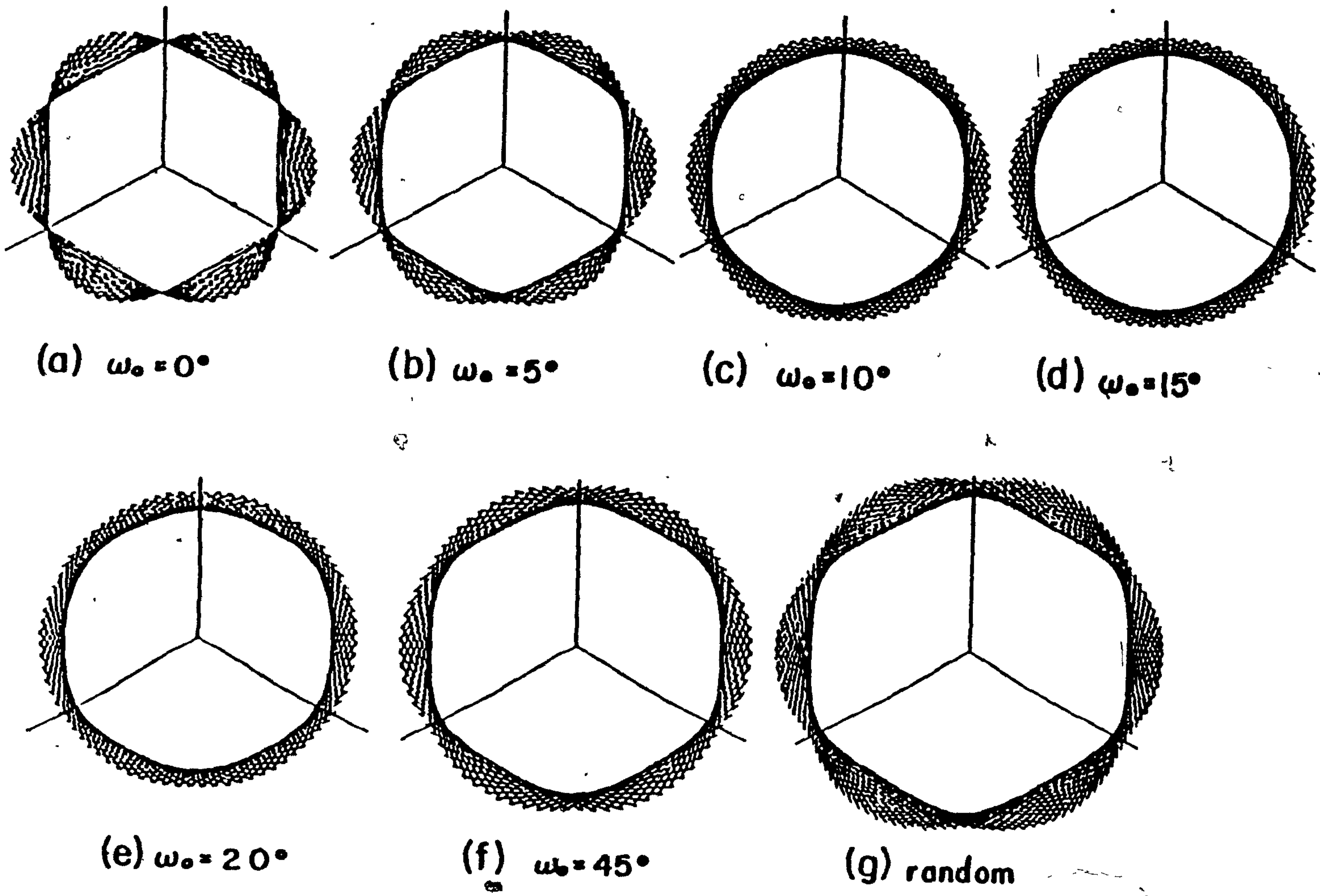

Fig. 3.6 π-plane sections of the polycrystal yield surface corresponding to increasing scatter widths : (a-f) $\omega_0 = 0, 5, 10, 15, 20, 45°$; (g) random distribution.

These shape changes find a ready explanation in the evolution of the mean Taylor factor as ω_0 is increased, which is different for uniaxial and plane strain deformation [98]. In uniaxial tests, $\overline{M}$ decreases from 2.45 at $\omega_0=0°$ to about 2.42 in the range $7.5°<\omega_0<10°$, finally tending to 3.07 in the random configuration (Fig. 3.8). By contrast, in the plane strain case, $\overline{M}$ increases regularly from 2.12 at $\omega_0=0°$ to a value of 2.85 in the random polycrystal. Thus the π-plane cross section has the same approximately hexagonal shape when the ratio $\overline{M}$ (uniaxial tension)/ $\overline{M}$ (plane strain) = 1.07 (e.g. at $\omega_0=5°$ and in the random polycrystal, see Fig. 3.8), but conversely is roughly circular when this ratio has a value of about 1.02, i.e. in the range $12.5°<\omega_0<17.5°$.

The evolution of the shear plane cross section is somewhat different (Fig. 3.7). Although it begins with a clearly defined polyhedron for $\omega_0=0°$, which is a square in this case, progress towards a circular shape is much slower, and the latter is only attained when the polycrystals are randomly orientated. It is of particular interest that the yield surface still exhibits a relatively angular form in this subspace when the scatter widths are in the range commonly observed experimentally (i.e. $\omega_0=7.5$ to 15°). The somewhat rounded vertices in these cases are associated with loading in pure or simple shear on planes normal to (and in directions parallel to) two of the <100> axes.

It should be noted that the two types of cross section illustrated above only give partial information on the shape of the yield locus as a whole. This is because they show the shape in the vicinity of only 12 of the 56 Bishop and Hill vertices, i.e. the 6 π-plane vertices of the normal stress type (type A in the Kocks [99] classification) and the 6 C type vertices in the three perpendicular shear stress planes passing through the origin. Thus Figs. 3.6 and 3.7 do not throw any light on locus shape in the vicinity of the 44 other vertices (i.e. near the 8, 24 and 12 corners of the B, D and E types).

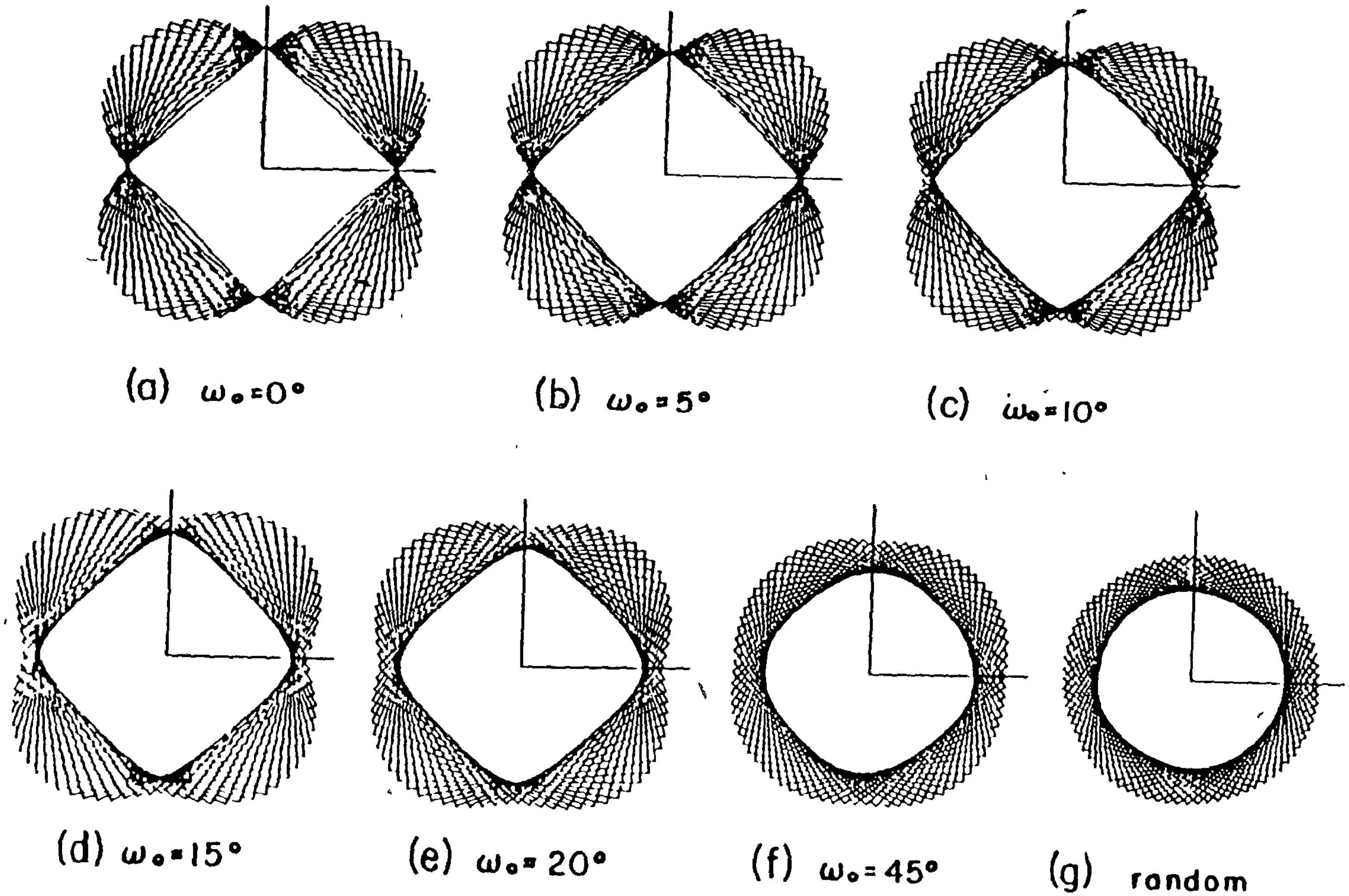

Fig. 3.7 Shear plane sections of the polycrystal yield surface corresponding to increasing scatter widths : (a-f) $\omega_0 = 0, 5, 10, 15, 20, 45°$; (g) random distribution.

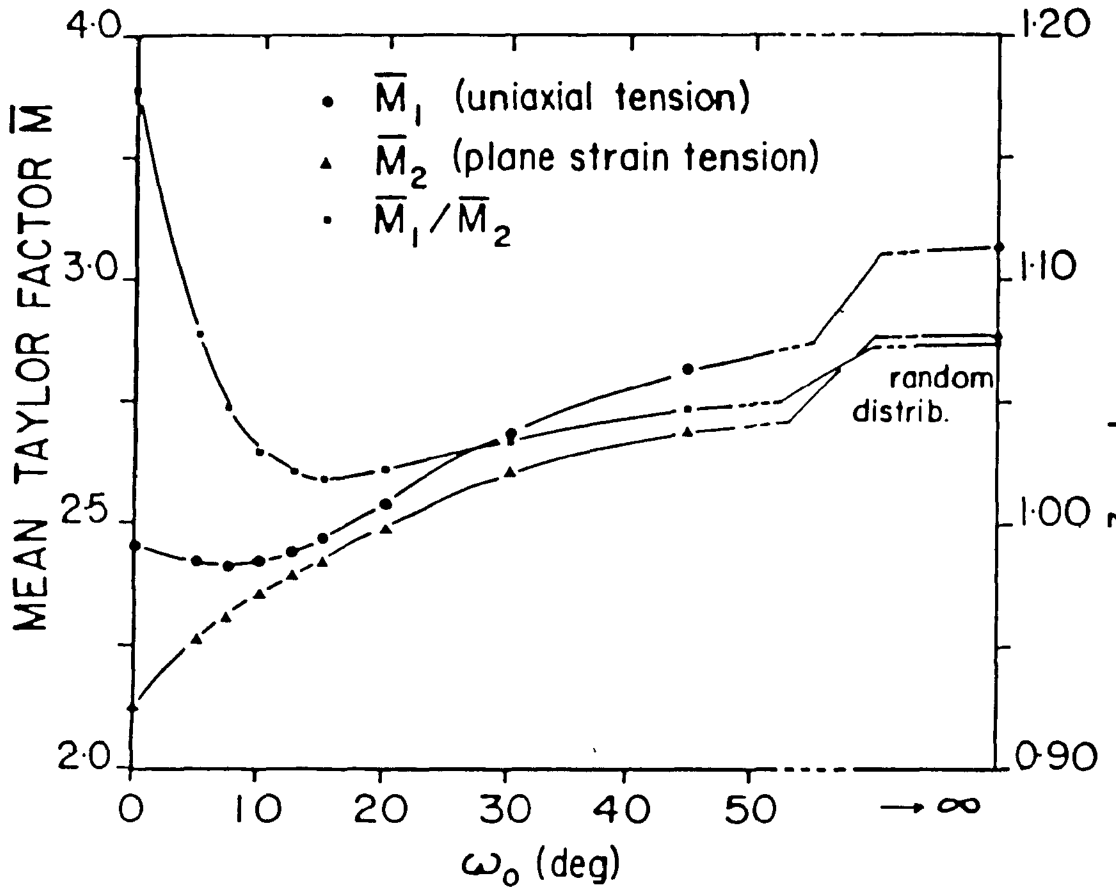

Fig. 3.8 Dependence of the mean Taylor factor $\overline{M}$ on scatter width ω_0. For each value of ω_0, $\overline{M}$ was calculated for a set of 400 grains. (•) $\overline{M_1}$ (uniaxial tension); (▲) $\overline{M_2}$ (plane strain tension); (■) ratio $\overline{M_1}/\overline{M_2}$. After [98].

III.5. DEGREE OF ANISOTROPY

As shown in Ref. [88], the yield locus of an isotropic material must be circular in any two-dimensional shear stress space (and for any reference frame). Fig. 3.7 clearly shows that this necessary condition is fulfilled by the random polycrystal. Thus the shear stress cross-sections provide direct evidence for the anisotropic nature of a given material. The degree of plastic anisotropy which results from the application of a normal stress cannot be judged with the same ease, however, from the π-plane sections presented in Fig. 3.6. This is because the section of the yield surface associated with the isotropic (random) material is not circular, whereas the nearly circular yield loci presented above (e.g. for scatter widths of 10 to 15°) are, by contrast, not identified with planar isotropy. Thus the shape of the π-plane yield locus is not of direct utility for an evaluation of the degree of anisotropy present in these materials*. Two measures which are by their nature more useful for this purpose are the dependencies on orientation of the 'uniaxial' yield stress and of the transverse strain rate ratio or Lankford coefficient.

The usual experimental test for the determination of both the yield stress and the strain rate ratio can be described by the following stress and strain rate tensors:

$$\underset{\sim}{\sigma} = \begin{bmatrix} ? & 0 & 0 \\ 0 & 0 & 0 \\ 0 & 0 & 0 \end{bmatrix} \qquad and \qquad \underset{\sim}{\dot{\varepsilon}} = \begin{bmatrix} \dot{\varepsilon}_{11} & ? & ? \\ ? & ? & ? \\ ? & ? & ? \end{bmatrix} \tag{3.15}$$

Here the reference axes are those of the sample, $\dot{\varepsilon}_{11}$ is imposed and the remaining strain rate components are unknown. Note, however, that for the

* Some of the conditions affecting the possible shapes of the π-plane loci pertaining to both cubic and isotropic materials are discussed in Ref. [88].

present cube texture, as for rolled (or orthotropic) materials more generally, the Z axis or normal direction (Fig. 2.2) is an axis of mirror symmetry. As a result, prescribing $\sigma_{13}=0$ is equivalent to the condition $\dot{\varepsilon}_{13}=0$, and likewise for σ_{23} and $\dot{\varepsilon}_{23}$. Thus the strain rate tensor can be simplified to give:

$$\dot{\underset{\sim}{\varepsilon}} = \begin{bmatrix} \dot{\varepsilon}_{11} & ? & 0 \\ ? & ? & 0 \\ 0 & 0 & ? \end{bmatrix} \tag{3.16}$$

In anisotropic materials, the condition $\sigma_{12}=0$ generally implies that $\dot{\varepsilon}_{12}\neq 0$. Consequently, the tensors described by Eqs. 3.15 and 3.16 are rigorously valid only for long samples (because of the constraints due to the shoulders in short samples).

The yield stress $\sigma_{11}(\theta)$ and strain rate ratio $R(\theta)$ pertaining to such a 'true' uniaxial tensile test carried out on a sample oriented along the θ direction (Fig. 2.2) can in principle be calculated from average polycrystalline yield surface data as follows. A Taylor approach is generally used in which strain rate directions are imposed on the polycrystal as well as on its constituent grains. However, it can be seen from Eq. 3.16 that two degrees of freedom are left in defining these directions, i.e. $\dot{\varepsilon}_{33}$ (or $\dot{\varepsilon}_{22}$) and $\dot{\varepsilon}_{12}$. The yield surface section ($\sigma_{12}=\sigma_{13}=\sigma_{23}=0$) is thus completely determined by the inner envelope of the hyperplanes:

$$S_1\dot{\varepsilon}_1 + S_2\dot{\varepsilon}_2 = \overline{\dot{W}} = \overline{S_1}\dot{\varepsilon}_1 + \overline{S_2}\dot{\varepsilon}_2 + \overline{S_5}\dot{\varepsilon}_5 \tag{3.17}$$

when expressed in the five dimensional notation of Eqs. 3.9 and 3.10 for all directions $\vec{\dot{\varepsilon}}$. It is evident that the necessary variation of both the $\dot{\varepsilon}_2/\dot{\varepsilon}_1$ and $\dot{\varepsilon}_5/\dot{\varepsilon}_1$ ratios would lead to extensive computation; for this reason the following simpler method, used in Refs. [11] and [16], was employed.

In this case the tensile test is specified by the following stress and strain rate components:

$$\underset{\sim}{\sigma} = \begin{bmatrix} ? & ? & ? \\ ? & 0 & ? \\ ? & ? & 0 \end{bmatrix} \qquad \text{and} \qquad \underset{\sim}{\dot{\varepsilon}} = \begin{bmatrix} \dot{\varepsilon}_{11} & 0 & 0 \\ 0 & ? & 0 \\ 0 & 0 & ? \end{bmatrix} \tag{3.18}$$

Here $\dot{\varepsilon}_{11}$ is imposed, $\dot{\varepsilon}_{22}$ and $\dot{\varepsilon}_{33}$ are unknown, and the nul values of the shear strain rates can be associated with non prescribed (and generally non-zero) values of the corresponding S_{ij}. The latter are considered to be induced by the shoulders or grips. Since the normal direction is an axis of mirror symmetry (see above), the conditions $\sigma_{13}=0$ and $\sigma_{23}=0$ can be additionally specified, leading to :

$$\underset{\sim}{\sigma} = \begin{bmatrix} ? & ? & 0 \\ ? & 0 & 0 \\ 0 & 0 & 0 \end{bmatrix} \tag{3.19}$$

Note that the condition $\sigma_{12}\neq 0$ cannot be fulfilled at the free surface of the specimen, so that Eq. 3.19 only applies to the interior of the specimen. It can be seen from the strain rate tensor specified by Eq. 3.18 that only one degree of freedom is left since $\dot{\varepsilon}_{12}=0$. The calculation of yield surfaces is greatly simplified in this way. Under these conditions, the locus projection $\mathcal{P}$ in the π-plane (see Fig. 3.9) is readily determined for a given grain distribution (i.e. a given value of $\overline{\dot{W}}$) by the inner envelope of the hyperplanes

$$S_1\dot{\varepsilon}_1 + S_2\dot{\varepsilon}_2 = \overline{\dot{W}} = \overline{S_1}\dot{\varepsilon}_1 + \overline{S_2}\dot{\varepsilon}_2 \tag{3.20}$$

when varying just the ratio $\dot{\varepsilon}_2/\dot{\varepsilon}_1$. The yield stress $\sigma_{11}(\theta)$ is then deduced from the locus obtained in this way and the strain rate ratio $R(\theta)$ from the tangent to the surface at the loading point P_0(see Fig. 3.9).

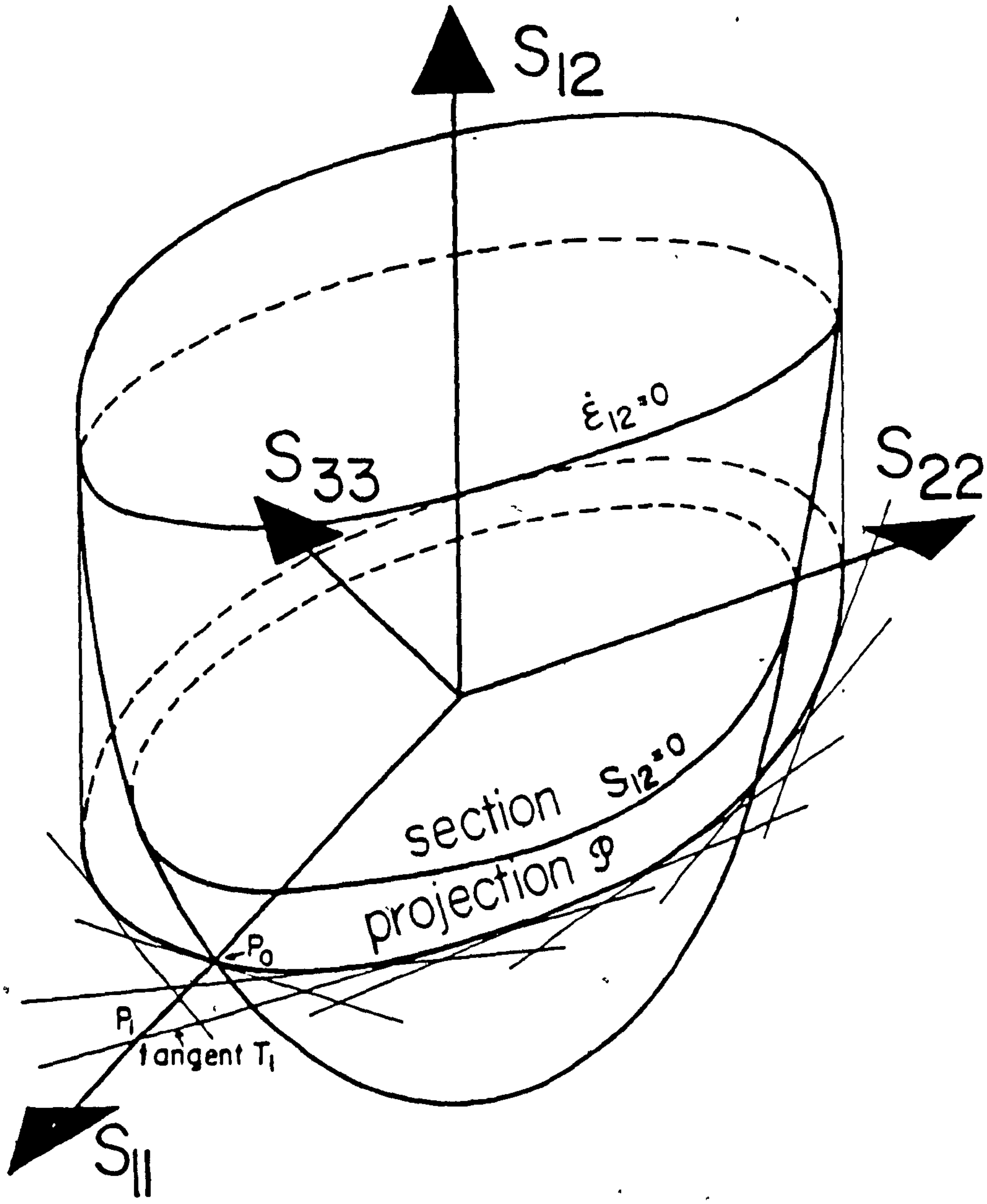

Fig. 3.9 Determination of the yield strength as well as the plastic strain rate ratio from the (π, S_{12}) section of the yield surface. $\mathcal{P}$ is the projection on the π-plane of this three-dimensional yield surface and P_0 is the projection of the loading point. The yield strength is determined from the distance OP_0 and the strain rate ratio from the tangent to the projection $\mathcal{P}$ at the point P_0.

Figure 3.10a shows the dependence on scatter width of the $\sigma_{11}(\theta)/\sigma_{11}(0)$ curves obtained with the yield surface projections ($\dot{\varepsilon}_{12}=0$). Note that $\sigma_{11}(\theta)$ is constant for the random distribution, which is a requirement for isotropy, but a property that is not evident from the π-plane yield locus for this material. The fairly smooth dependence of the single crystal flow stress is also of interest. This contains two cusps, which do not, however, violate the normality rule regarding the yield surface itself. The cusps disappear when the scatter width is increased. For the range $\omega_0=10$ to $20°$, which is of interest from a practical point of view, it can be seen that the $\sigma_{11}(\theta)/\sigma_{11}(0)$ plot has a generally undulating shape.

The dependence on orientation θ of the strain rate ratio

$$R(\theta) = \dot{\varepsilon}_{22}(\theta)/\dot{\varepsilon}_{33}(\theta) = (\sqrt{3}\,\dot{\varepsilon}_1(\theta)/\dot{\varepsilon}_2(\theta) - 1)/2 \qquad (3.21)$$

was calculated for the same type of tensile test as employed for the yield stress ratio dependencies presented above. Here the ratio $-\dot{\varepsilon}_1/\dot{\varepsilon}_2$ is the slope of the tangent at the loading point P_0 which is part of the projection $\mathcal{P}$ described above. The R(θ) curves are illustrated as a function of increasing scatter width in Fig. 3.10b.

It should be noted that, whereas the yield stress ratio was determined with reasonable accuracy using only 400 orientations, calculation of the strain rate ratio requires a larger number of grains (600), particularly when the π-plane cross-section exhibits fairly sharp curvature near the S_{11} axis. The latter description applies to small scatter widths ($\omega_0<7.5°$), and to θ values close to the symmetry axes of the material. Under these conditions, as well as for a random distribution, the R(θ) values obtained in this study involve errors of up to ±10%.

It is evident from Fig. 3.10 that, whereas the single crystal yield stress ratio exhibits two cusps, which are linked to changes of vertex, the strain rate ratio varies smoothly at the same values of θ. It displays instead an approximately parabolic shape in the central region, with singular points in the rolling and

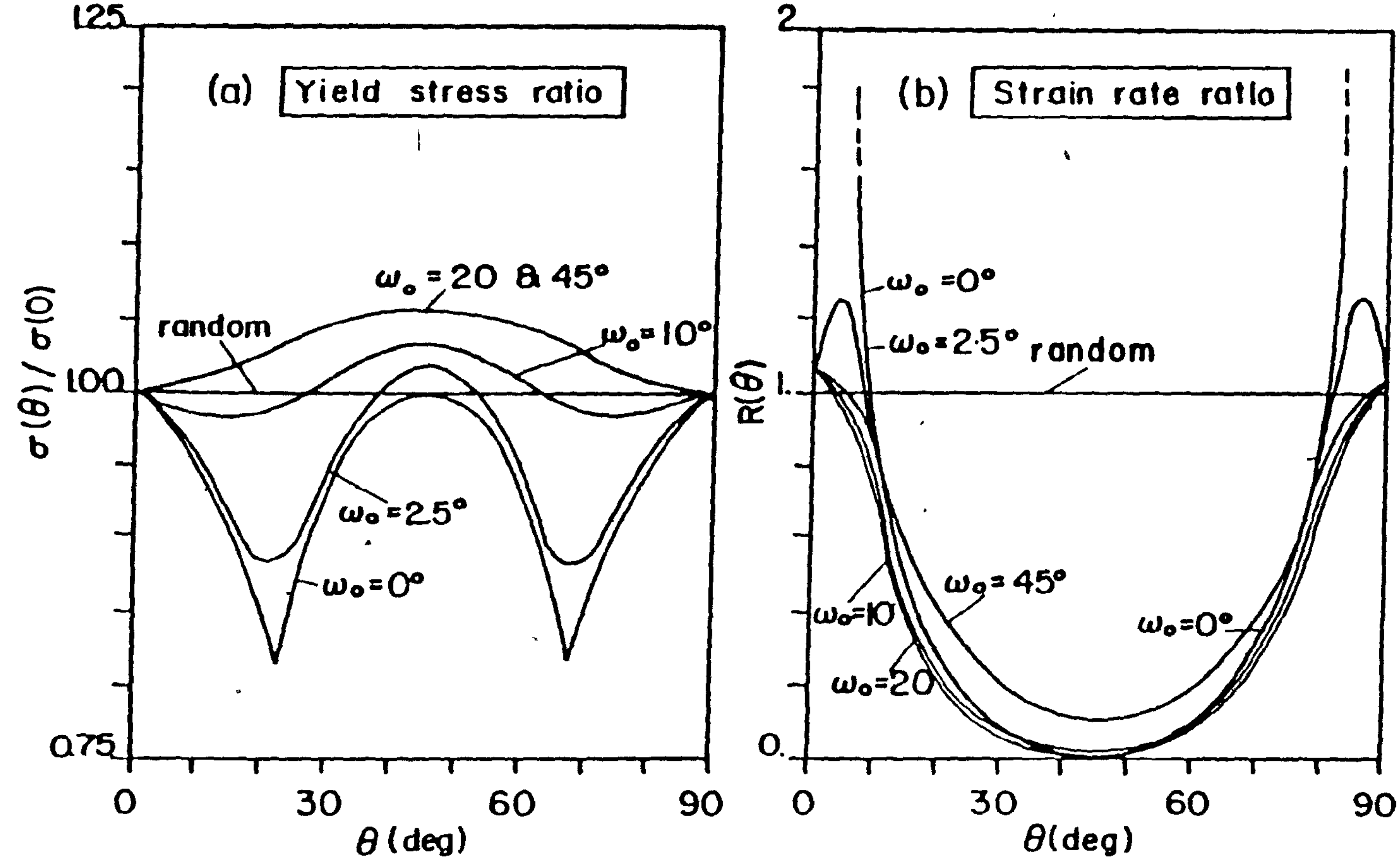

Fig. 3.10 (a) Yield stress ratio $\sigma(\theta)/\sigma(0)$ and (b) strain rate ratio $R(\theta)$ vs. loading direction θ in the plane of the sheet for the present grain distributions.

transverse directions. On increasing the scatter width, the discontinuities disappear and the shape of the central part of the curve is essentially unchanged, even for a scatter width of 45°. This is essentially due to the strong anisotropy displayed (over the whole range of scatter levels) by the shear plane sections (see Fig. 3.8a-f). By contrast, when the orientations are fully randomized, the ratio changes dramatically and adopts a constant value of 1, as required. The large difference between the flow behaviours of random and $\omega_0 = 45°$ samples is of particular interest.

The large variations in R value with θ associated with scatter widths in the 'realistic' range 10 to 20° display the qualitative features expected from the literature [38]. By contrast, $R(\theta)$ curves for low scatter widths (see Fig. 3.10b) are in apparent contradiction with experimental investigations carried out on single crystals. The cups drawn from crystals of {100}<001> orientation have four ears [35], whereas eight ears of unequal size are predicted for the single ($\omega_0 = 0°$) and near single ($\omega_0 = 2.5°$) crystals of Fig. 3.10b. At this point it must be recalled that the texture itself changes during deep drawing [114], modifying the anisotropy of the testpiece. Hence a drawn single crystal will no longer retain its unique and precise starting orientation, but will instead increase its 'spread' and perhaps contain some secondary texture components as well. For this reason, the crystallographic predictions based on higher misorientations (e.g. $\omega_0 > 10°$) are probably more suitable for comparison with experimental single crystal observations, as in this case four ears are predicted.

III.6. ANALYTICAL REPRESENTATION OF THE YIELD SURFACES PERTAINING TO 'PERFECT' AND 'DISORIENTED' SINGLE CRYSTALS

III.6.1. Single crystal case

It is now of interest to quantify the evolution of the single crystal locus with increasing misorientation. For this purpose, a five dimensional representation of the classical Bishop and Hill polyhedron will first be given, and then extended to the case of disoriented crystals.

As described above, the yield surface of a cubic single crystal displaying $\{111\}<1\bar{1}0>$ or $\{110\}<1\bar{1}1>$ slip is a polyhedron in stress space, with 24 faces and 56 vertices. These faces are characterized by Eq. 3.1. When these equations are expressed in terms of the components S_i (referred to the crystal $<100>$ axes, Eq. 3.9), it is readily shown that

$$\begin{cases} |2S_1| + |S_3| + |S_4| = \sqrt{2} \\ |S_1 - \sqrt{3}S_2| + |S_4| + |S_5| = \sqrt{2} \\ |S_1 + \sqrt{3}S_2| + |S_3| + |S_5| = \sqrt{2} \end{cases} \tag{3.22}$$

The single crystal locus is defined as the inner envelope of these planes. This is of particular interest when a section of the polyhedron referred to particular axes (say the specimen axes) is desired. In this case, the stress deviator components $S_{i(C)}$ have to be expressed in terms of the $S_{i(S)}$ values in this new reference frame

$$S_{i(C)} = Q_{ij}\, S_{j(S)} \tag{3.23}$$

The matrix Q employed for this purpose characterizes the position of the crystal axes with respect to the specimen axes. For a grain having its $<hkl>$ and $<uvw>$ directions parallel to the normal and rolling directions of a sheet, respectively, Q is given by

$$Q = \begin{bmatrix} (r_1^2 - r_2^2 + u_2^2 - u_1^2)/2 & \sqrt{3}(u_3^2 - r_3^2)/2 & u_2u_3 - r_2r_3 & u_1u_3 - r_1r_3 & u_1u_2 - r_1r_2 \\ \sqrt{3}(n_2^2 - n_1^2)/2 & (3n_3^2 - 1)/2 & \sqrt{3}n_2n_3 & \sqrt{3}n_1n_3 & \sqrt{3}n_1n_2 \\ u_2n_2 - u_1n_1 & \sqrt{3}u_3n_3 & u_2n_3 + u_3n_2 & u_1n_3 + u_3n_1 & u_1n_2 + u_2n_1 \\ r_2n_2 - r_1n_1 & \sqrt{3}r_3n_3 & r_2n_3 + r_3n_2 & r_1n_3 + r_3n_1 & r_1n_2 + r_2n_1 \\ u_2r_2 - u_1r_1 & \sqrt{3}u_3r_3 & u_2r_3 + u_3r_2 & u_1r_3 + u_3r_1 & u_1r_2 + u_2r_1 \end{bmatrix} \tag{3.24}$$

where $n_1 = h/\sqrt{h^2+k^2+l^2}$, $n_2 = k/\sqrt{h^2+k^2+l^2}$, $n_3 = l/\sqrt{h^2+k^2+l^2}$

$r_1 = u/\sqrt{u^2+v^2+w^2}$, $r_2 = v/\sqrt{u^2+v^2+w^2}$, $r_3 = w/\sqrt{u^2+v^2+w^2}$

$u = n \times r$

Eqs. 3.22 can thus be expressed in terms of macroscopic stress components, from which any section in stress space is easily derived. An example of such a calculation is shown in Fig. 3.11 for the cube {100}<001> component.

III.6.2. Case of a disoriented crystal

As the misorientation around an ideal orientation is increased, it has been shown (Figs. 3.6 and 3.8) that the shape as well as the size of the corresponding yield surface both vary. An attempt to quantify these variations has been made, which consists of calculating the evolution of specific points on the locus with increasing scatter width ω_0. These points were chosen to be half the vertices (28) and half the mid-points of the faces (12) of the polyhedron (because of the symmetry).

In order to carry out this calculation in a simple way, a Taylor approach was used in which some strain rate directions are prescribed to the disoriented ideal orientation. Forty (28 + 12) such vectors were selected as follows:

(i) 12 correspond to the normals to the faces of the single crystal polyhedron;

(ii) the 28 others are the central 'normals' to the yield surface at the vertices. Given that a vertex is defined as the intersection of 6 or 8 planes, each such normal can be taken as the average over the 6 or 8 corresponding vectors. When these 40 strain rate directions are applied, the corresponding stress vectors can be calculated using the normality rule and then averaged over the crystal distribution. The angles ψ between the stress vectors calculated in this way and the ones associated with the single crystal were also determined : this gives an estimate of the progressive distortion of the locus as the misorientation is increased.

The positions of the vertices and mid-points of the faces, as well as of the 'quasi' vertices and of the mid-points of the 'quasi' faces, are given in Tables III.2. and III.3 for the $\omega_0 = 0°$ (single crystal) and $\omega_0 = 15°$ grain distributions,

Fig. 3.11 π-plane cross-sections of the yield surface corresponding to a cube textured sheet. The perfect hexagon pertaining to a single crystal ($\omega_0 = 0°$) is derived from Eqs. 3.22 or from Eqs. 3.25 with $n = \infty$. The rounded hexagon corresponds to a cube texture with a spread $\omega_0 = 7.5°$ and has been calculated from Eqs. 3.25 with $n = 8.75$.

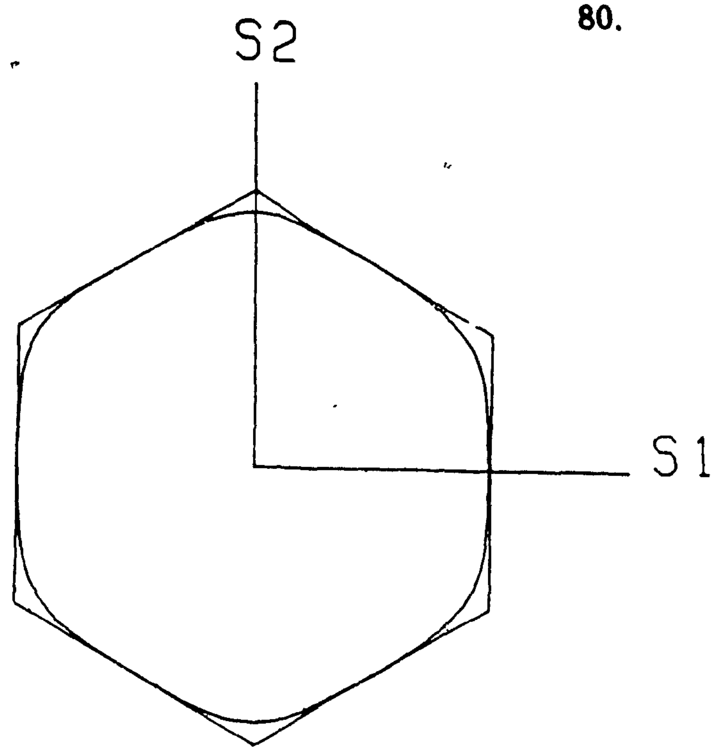

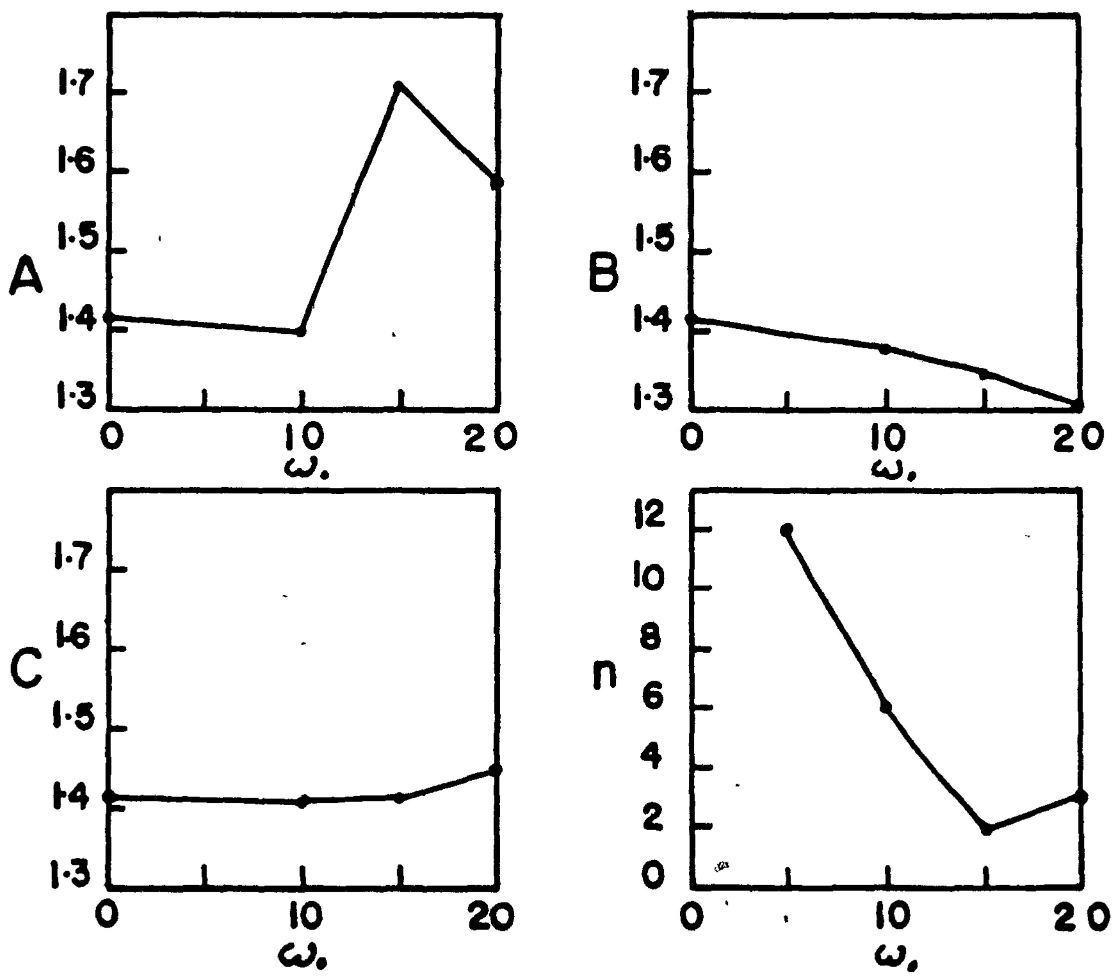

Fig. 3.12 Dependence of the coefficients A, B, C (normalized by $\sqrt{6}\,\tau_c$) and n on the gaussian spread ω_0.

Table III.2. Positions of the vertices (types A, B, C, D and E) and of the midpoints of the faces in the 5-dimensional stress space of Eq. (3.9). Case of the Bishop and Hill polyhedron ($\omega_0 = 0°$). Stress units $= \sqrt{6}\,\tau_c$

Type	Vertex	S1	S2	S3	S4	S5	$\lVert S \rVert$
A	1	0	$-2/\sqrt{6}$	0	0	0	$\sqrt{2/3}$
	2	$1/\sqrt{2}$	$1/\sqrt{6}$	0	0	0	
	3	$-1/\sqrt{2}$	$1/\sqrt{6}$	0	0	0	
C	4	0	0	$\sqrt{2}$	0	0	$\sqrt{2}$
	5	0	0	0	$\sqrt{2}$	0	
	6	0	0	0	0	$\sqrt{2}$	
E	7	$-1/2\sqrt{2}$	$-3/2\sqrt{6}$	0	$1/\sqrt{2}$	0	1
	8	$-1/2\sqrt{2}$	$-3/2\sqrt{6}$	0	$-1/\sqrt{2}$	0	
	9	$-1/2\sqrt{2}$	$3/2\sqrt{6}$	$1/\sqrt{2}$	0	0	
	10	$-1/2\sqrt{2}$	$3/2\sqrt{6}$	$-1/\sqrt{2}$	0	0	
	11	$1/\sqrt{2}$	0	0	0	$1/\sqrt{2}$	
	12	$1/\sqrt{2}$	0	0	0	$-1/\sqrt{2}$	
D	13	$1/2\sqrt{2}$	$-1/2\sqrt{6}$	$1/\sqrt{2}$	0	$1/\sqrt{2}$	$\sqrt{7/6}$
	14	$1/2\sqrt{2}$	$-1/2\sqrt{6}$	$-1/\sqrt{2}$	0	$1/\sqrt{2}$	
	15	$1/2\sqrt{2}$	$-1/2\sqrt{6}$	$1/\sqrt{2}$	0	$-1/\sqrt{2}$	
	16	$1/2\sqrt{2}$	$-1/2\sqrt{6}$	$-1/\sqrt{2}$	0	$-1/\sqrt{2}$	
	17	$-1/2\sqrt{2}$	$-1/2\sqrt{6}$	0	$1/\sqrt{2}$	$1/\sqrt{2}$	
	18	$-1/2\sqrt{2}$	$-1/2\sqrt{6}$	0	$-1/\sqrt{2}$	$1/\sqrt{2}$	
	19	$-1/2\sqrt{2}$	$-1/2\sqrt{6}$	0	$1/\sqrt{2}$	$-1/\sqrt{2}$	
	20	$-1/2\sqrt{2}$	$-1/2\sqrt{6}$	0	$-1/\sqrt{2}$	$-1/\sqrt{2}$	
	21	0	$1/\sqrt{6}$	$1/\sqrt{2}$	$1/\sqrt{2}$	0	
	22	0	$1/\sqrt{6}$	$-1/\sqrt{2}$	$1/\sqrt{2}$	0	
	23	0	$1/\sqrt{6}$	$1/\sqrt{2}$	$-1/\sqrt{2}$	0	
	24	0	$1/\sqrt{6}$	$-1/\sqrt{2}$	$-1/\sqrt{2}$	0	
B	25	0	0	$1/\sqrt{2}$	$1/\sqrt{2}$	$-1/\sqrt{2}$	$\sqrt{3/2}$
	26	0	0	$1/\sqrt{2}$	$-1/\sqrt{2}$	$1/\sqrt{2}$	
	27	0	0	$-1/\sqrt{2}$	$1/\sqrt{2}$	$1/\sqrt{2}$	
	28	0	0	$1/\sqrt{2}$	$1/\sqrt{2}$	$1/\sqrt{2}$	
Faces	29	0	0	0	$-1/\sqrt{2}$	$1/\sqrt{2}$	1
	30	0	0	$1/\sqrt{2}$	0	$-1/\sqrt{2}$	
	31	0	0	$-1/\sqrt{2}$	$1/\sqrt{2}$	0	
	32	0	0	0	$1/\sqrt{2}$	$1/\sqrt{2}$	
	33	0	0	$-1/\sqrt{2}$	0	$-1/\sqrt{2}$	
	34	0	0	$1/\sqrt{2}$	$-1/\sqrt{2}$	0	
	35	0	0	0	$1/\sqrt{2}$	$-1/\sqrt{2}$	
	36	0	0	$1/\sqrt{2}$	0	$1/\sqrt{2}$	
	37	0	0	$-1/\sqrt{2}$	$-1/\sqrt{2}$	0	
	38	0	0	0	$-1/\sqrt{2}$	$-1/\sqrt{2}$	
	39	0	0	$-1/\sqrt{2}$	0	$1/\sqrt{2}$	
	40	0	0	$1/\sqrt{2}$	$1/\sqrt{2}$	0	

Table III.3. Positions of the vertices and the mid-points of the faces in the 5-dimensional stress space of Eq. 3.9. Ψ is the angle between the stress vector of interest and the corresponding one associated with the Bishop and Hill polyhedron. Disoriented yield surface corresponding to $\omega_0 = 15°$.

Type	Vertex	S1	S2	S3	S4	S5	‖S‖	Ψ(deg)
A	1	0.005	−0.823	0.015	0.008	0.005	0.824	1.28
	2	0.706	0.423	−0.006	0.001	0.003	0.823	1.04
	3	−0.703	0.426	0.000	−0.002	−0.003	0.822	1.24
C	4	0.012	−0.023	1.322	0.018	0.013	1.322	1.48
	5	−0.015	−0.023	−0.013	1.322	0.013	1.322	1.43
	6	−0.021	−0.003	−0.010	−0.009	1.324	1.326	1.09
E	7	−0.322	−0.548	−0.015	0.806	0.001	1.026	6.80
	8	−0.314	−0.542	0.002	−0.796	−0.014	1.013	6.85
	9	−0.312	0.535	0.805	0.015	0.006	1.016	7.48
	10	−0.321	0.542	−0.813	−0.007	−0.012	1.029	7.28
	11	0.628	0.010	−0.016	−0.005	0.790	1.009	6.61
	12	0.628	−0.002	0.008	0.013	−0.811	1.026	7.30
D	13	0.310	−0.202	0.713	0.086	0.699	1.068	5.13
	14	0.315	−0.177	−0.683	−0.075	0.726	1.063	4.93
	15	0.346	−0.191	0.699	−0.059	−0.697	1.065	3.23
	16	0.325	−0.175	−0.710	0.078	−0.705	1.070	4.66
	17	−0.328	−0.196	0.063	0.712	0.694	1.067	3.66
	18	−0.337	−0.171	−0.075	−0.683	0.723	1.067	4.67
	19	−0.307	−0.191	−0.085	0.701	−0.716	1.068	5.21
	20	−0.300	−0.185	0.082	−0.704	−0.714	1.067	5.29
	21	−0.002	0.370	0.699	0.703	0.084	1.062	4.86
	22	−0.014	0.370	−0.711	0.696	−0.076	1.064	4.57
	23	0.010	0.380	0.701	−0.699	−0.078	1.064	4.41
	24	0.001	0.400	−0.693	−0.703	0.071	1.068	3.84
B	25	0.016	−0.022	0.667	0.676	−0.667	1.161	1.39
	26	−0.003	0.005	0.678	−0.661	0.681	1.166	0.80
	27	−0.020	−0.003	−0.685	0.664	0.668	1.165	1.26
	28	−0.014	−0.018	0.656	0.677	0.686	1.166	1.55
Faces	29	0.068	−0.089	0.018	−0.686	0.736	1.012	6.74
	30	0.070	0.099	0.681	−0.025	−0.736	1.010	7.38
	31	−0.116	−0.009	−0.690	0.743	0.005	1.021	6.88
	32	0.051	−0.117	0.008	0.718	0.699	1.010	7.31
	33	0.055	0.114	−0.690	−0.043	−0.740	1.020	7.79
	34	−0.121	0.009	0.695	−0.713	0.026	1.004	7.14
	35	0.069	−0.116	0.019	0.675	−0.749	1.018	8.25
	36	0.041	0.109	0.749	0.020	0.671	1.012	7.40
	37	−0.125	0.014	−0.699	−0.713	0.021	1.006	7.30
	38	0.066	−0.107	−0.007	−0.743	−0.677	1.013	7.62
	39	0.062	0.087	−0.718	−0.011	0.715	1.019	6.05
	40	−0.121	−0.012	0.696	0.722	0.024	1.011	7.12

respectively. It can be seen that the A, B and C vertices evolve isotropically when the scatter width is increased, as expressed by low values of the angle ψ. This is not surprising since these corners belong to "closed" subspaces, as defined by Canova et al. [11].

In a manner analogous to the one employed for the case of the perfect single crystal, the equation of the yield surface pertaining to the disoriented grain can be expressed as the inner envelope of the four loci

$$\begin{cases} |2S_1/C| + |S_3/B| + |S_4/B| = 1 \\ |(S_1 - \sqrt{3}S_2)/C| + |S_4/B| + |S_5/B| = 1 \\ |(S_1 + \sqrt{3}S_2)/C| + |S_3/B| + |S_5/B| = 1 \\ |2S_1|^n + |S_1 - \sqrt{3}S_2|^n + |S_1 + \sqrt{3}S_2|^n = A^n \end{cases} \tag{3.25}$$

Here A, B, C and n depend on the misorientation ω_0 and $A = \frac{1}{2}(2+2^n)^{1/n}C$. For the perfect crystal ($\omega_0 = 0°$), $A = B = C = \sqrt{2}$ and $n = \infty$. The fourth expression in Eq. 3.25 has been added to take into account the evolution of the shape of the locus in the π-plane (S_1, S_2) : the exponent n equals 2 for $\omega_0 = 15°$, since the π-plane section is almost circular (Fig. 3.6). It is to be noted that the slightly rounded faces and vertices observed in the shear stress plane (Fig. 3.8) for typical scatter widths $\omega_0 < 20°$ has not been considered here The evolution of the A, B, C and n parameters is shown in Fig. 3.12 as a function of ω_0. The yield locus of a polycrystal displaying a strong cube component ($\omega_0 = 7.5°$) calculated using Eq. 3.25 is also illustrated in Fig. 3.11. It should be noted that this method permits an estimate to be made of the yielding behaviour of highly textured aggregates, by the use of only one ideal orientation (together with the components required by the symmetry). When many texture components are present in a given material, the corresponding loci can be readily combined, as shown in more detail in chapter V.

III.7. SUMMARY

Idealized cube textures were set up which (i) are rotationally symmetric, and in which (ii) the misorientation angle obeys a gaussian distribution of scatter width increasing from 0° (single crystal) to 45°. Crystallographic yield surfaces were calculated for these textures, leading to the following conclusions:

(1) The five dimensional form of the yield surface can be given an improved representation by employing the following 'equilibrated' deviator stress and strain rate 'vectors' :

$$\vec{S} = (S_i) = ((S_{22} - S_{11})/\sqrt{2}, \sqrt{3/2}\, S_{33}, \sqrt{2}\, S_{23}, \sqrt{2}\, S_{31}, \sqrt{2}\, S_{12})$$
$$\vec{\dot{\varepsilon}} = (\dot{\varepsilon}_i) = ((\dot{\varepsilon}_{22} - \dot{\varepsilon}_{11})/\sqrt{2}, \sqrt{3/2}\, \dot{\varepsilon}_{33}, \sqrt{2}\, \dot{\varepsilon}_{23}, \sqrt{2}\, \dot{\varepsilon}_{31}, \sqrt{2}\, \dot{\varepsilon}_{12})$$

This representation has the advantage over earlier notations that it leads directly to the two dimensional cross sections of the yield surface.

(2) As the scatter width of the idealized cube texture is increased, the yield surface cross-sections in shear stress space gradually evolve from a square form (single crystal) to a circular one (when the orientations are fully random) For the scatter widths of 5 to 20° commonly found experimentally, the three-dimensional yield locus remains distinctly angular Thus materials of cubic symmetry can be readily distinguished from isotropic materials (with spherical yield loci) in this subspace

(3) As the scatter width of the idealized cube texture is increased, the yield surface cross sections in the π-plane gradually evolve from a hexagonal form (single crystal) to a nearly circular one (when the scatter widths are in the range 12.5 to 17.5°), to a rounded hexagonal form once again (when the orientations are fully random). Thus analytical descriptions such as the quadratic yield criterion of Hill can give a good approximation of the yielding behaviour in this subspace for scatter widths of 15°±2.5°. Because the same rounded hexagonal form is observed at 6° (for the idealized cubic materials), as well as for the fully randomized samples, materials of cubic symmetry cannot be distinguished from fully isotropic ones in this subspace.

(4) Because the degree of planar anisotropy cannot be readily evaluated from the shape of the π-plane yield locus alone, it is more useful to represent the directionality in stress properties in terms of the yield stress and strain rate

ratios. These are highly anisotropic for the single crystal, become slightly less 'lobed' as the scatter width is increased, but only adopt constant values when the orientations are fully random. By these measures, samples with a scatter width of 6°, as well as random materials (both of which have π-plane cross-sections of identical shape) display distinctly different degrees of plastic anisotropy, essentially because of the changing contributions made by their shear properties as the scatter width is increased.

(5) Analytical representations of the yield surfaces pertaining to 'perfect' and 'disoriented' single crystals have been proposed. Sections of the loci corresponding to highly textured polycrystals can be readily assessed using these functions. As the texture of an aggregate can be decomposed into a finite number of disoriented ideal orientations (each with a specific volume fraction and scatter width), the overall yielding behaviour can be derived in a semi-analytic manner from suitable combinations of the individual yield surfaces.

CHAPTER IV

THE CONTINUUM MECHANICS OF TEXTURED POLYCRYSTALS : BASIC METHOD

The CMTP (continuum mechanics of textured polycrystals) method was developed so as to permit the anisotropy of textured polycrystals to be described in a simple way. It has the advantage that it involves a straightforward analytical representation of the yield surface, and that the yield locus is spatially oriented with respect to the ideal orientation of interest rather than with respect to the symmetry axes of the workpiece. In this way, the direct link between texture and anisotropy is made explicit rather than implicit.

In the original work of Montheillet et al. [5], the quadratic yield criterion proposed by Hill [4]:

$$F(S) = f(S_{yy}-S_{zz})^2 + g(S_{zz}-S_{xx})^2 + h(S_{xx}-S_{yy})^2 + 2l\,S_{yz}^2 + 2m\,S_{zx}^2 + 2n\,S_{xy}^2 = 1 \tag{4.1}$$

was assumed to give a good approximation of the Bishop and Hill single crystal yield surface. As explained in more detail below, the six parameters f, g, h, l, m and n (which reduce to two for cubic symmetry) are adjusted so that they give a best fit to the Bishop and Hill polyhedron. A question regarding the fitting process can be asked by the reader at this point : what kind of information is lost when the single crystal polyhedron is approximated by a smooth yield locus of the present type? In terms of the yield stresses, the loss is probably not too important as long as the assumed function does not significantly over- or underestimate the distance from the origin of the various vertices of the polyhedron. In terms of the strain rate characteristics, however, (which are given by the normals to the yield surface) the assumption is more questionable and can be thought to give rise to possibly undesirable errors in plastic properties such as the strain rate ratios. Fortunately, the crystallographic calculations of the yield surface for a disoriented single crystal presented in Chapter III give a partial justification of the CMTP assumption : i.e. a crystal with a spread of around 15° has a circular yield locus in the normal stress plane. Nevertheless, the extent to which the shape of the yield surface is faithfully reproduced in other types of stress space remains to be assessed critically.

IV.1. PRINCIPLES OF THE CMTP METHOD

The calculations carried out on the disoriented single crystals clearly lead to the following comments. For typical experimental scatter widths (5 to 15°), the yield surface does not exhibit any vertices in the π-plane (Fig. 3.6) : it has a smooth rounded shape. In consequence, it could be well approximated by a near quadratic continuum yield function. A Hill type locus, as will be seen below, gives a quasi-perfect fit in this particular subspace. However, one has to keep in mind that the shear stress cross section shown in Fig. 3.7 does exhibit some rather sharp vertices. Thus it can be expected that a good representation could only be obtained by means of an analytical function with an exponent of low value, that is near 1.4.

The above remarks indicate that the crystallographic locus of a disoriented single crystal can at least be approximated by a continuum yield function without the loss of an unacceptable amount of information regarding the size and shape (stress and strain rate characteristics, respectively) of the yield surface.

In the CMTP method (originally proposed by Montheillet et al. [5] for the quadratic case) a yield function of the Hill type :

$$\begin{aligned} F(S) = \alpha\,(|S_{11}-S_{22}|^n + |S_{22}-S_{33}|^n + |S_{33}-S_{11}|^n)\,/\,(\sqrt{6}\,\tau_c)^n \\ +2\,\beta\,(|S_{12}|^m + |S_{23}|^m + |S_{31}|^m)\,/\,(\sqrt{6}\,\tau_c)^m = 1 \end{aligned} \tag{4.2}$$

is assumed to represent the yielding behaviour of a highly textured fcc or bcc polycrystal containing a dispersion of orientations about a single ideal orientation. In this expression, the S_{ij} are the components of the deviator stress tensor $\underset{\sim}{S}$ referred to the <100> axes of the ideal orientation; α and β are two coefficients to be determined (see section IV.1.1); τ_c is the critical resolved shear stress; and n and m are two exponents equal to or greater than 1. This condition arises from convexity requirements , as shown in Appendix IV.1.

At this point it is important to underline the two main features of the CMTP method , as opposed to the traditional continuum methods :

(i) The principal axes of anisotropy are chosen to coincide with the <100> axes of the texture component of interest (rather than with those of the specimen);

(ii) The values of the yield function coefficients α and β are determined from crystallographic (as opposed to mechanical) considerations.

IV.1.1. Evaluation of the coefficients α and β of the yield function

In the CMTP method, α and β are adjusted so that a 'best' fit is obtained between the yield function of Eq. 4.2 and the crystallographic yield surface for fcc or bcc disoriented single crystals displaying $\{111\}<1\bar{1}0>$ or $\{110\}<1\bar{1}1>$ slip, respectively. The fitting process is carried out by minimizing the root mean square distance Σ between some specific points of the crystallographically calculated locus and the continuum yield surface taken along the radii leading to the points considered (see Fig.4.1).

Some freedom regarding the choice of the crystallographic yield locus as well as the points to be considered is available. One possibility consists of minimizing the Σ associated with the vertices of the Bishop and Hill polyhedron. An alternative, more complicated method is to carry out the fitting process by considering both the 'rounded' vertices as well as the faces of the loci calculated above for the different scatter widths.

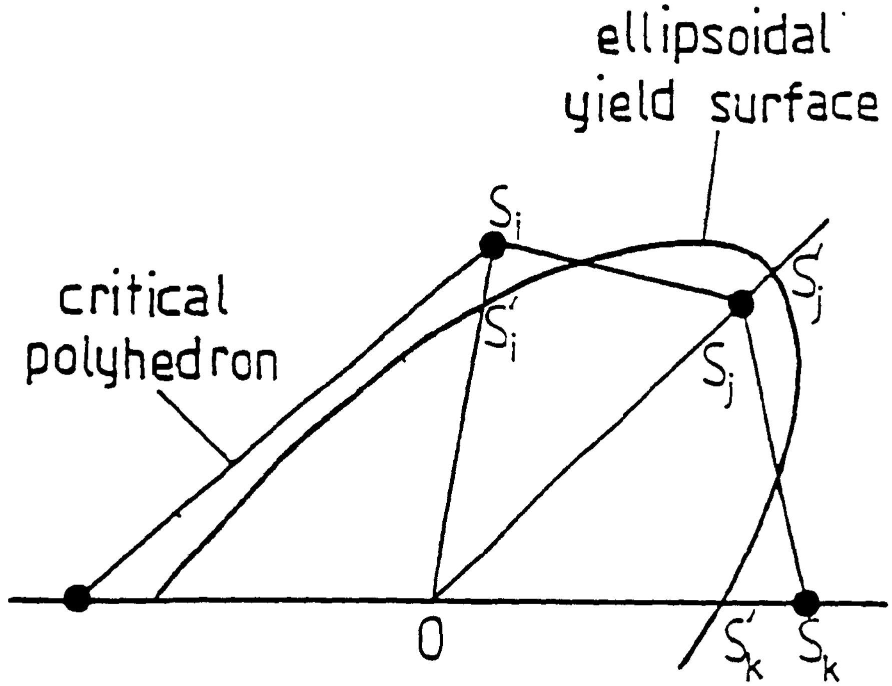

Fig. 4.1 Two-dimensional section of the five dimensional crystallographic yield surface (schematic). The three vertices S_i, S_j and S_k of the critical polyhedron should be compared with the points S_i', S_j' and S_k' of the ellipsoidal yield surface to which they correspond. In the fitting procedure for the determination of α and β, the sum of the squares $|S_i S_i'|^2$ is minimized.

Once different sets of N vectors $\overrightarrow{OS_i}$ in the five dimensional stress space have been selected, the root mean square distance Σ can be calculated in the following way. If S'_i is defined as the intersection of OS_i with the yield function $F(S, \alpha, \beta) = 1$ given by Eq. 4.2 (see Fig.4.1), then

$$\Sigma = \sum_{i=1}^{N} (\overrightarrow{S_i S'_i})^2 \tag{4.3}$$

i.e.

$$\Sigma = \sum_{i=1}^{N} (\lambda_i - 1)\overrightarrow{OS}_i^2 \tag{4.4}$$

where λ_i is defined by

$$\overrightarrow{OS'}_i = \lambda_i \overrightarrow{OS}_i = (\lambda_i S_{1i}, \quad , \lambda_i S_{5i}) \tag{4.5}$$

Since (S'_i) belongs to the yield function $F(S, \alpha, \beta) = 1$, λ_i can be calculated by solving the equation :

$$F(\lambda_i S_{1i}, \; .., \lambda_i S_{5i}, \alpha, \beta) = 1 \tag{4.6}$$

Using Eqs. 4.2 in conjunction with the 5-dimensional notation of Eq. 3.9 :

$$\begin{aligned} &|\lambda_i|^n \alpha\, 2^{-n/2} [\, |2S_{1i}|^n + |S_{1i} - \sqrt{3}S_{2i}|^n + |S_{1i} + \sqrt{3}S_{2i}|^n \,] \\ &+ |\lambda_i|^m \beta\, 2^{1-m/2} [\, |S_{3i}|^m + |S_{4i}|^m + |S_{5i}|^m \,] - 1 = 0 \end{aligned} \tag{4.7}$$

For a given set of vectors $\overrightarrow{OS_i}$ and for given exponents n and m, α and β are calculated so as to minimize the distance Σ. Tables IV.1 to IV.3 show the results obtained with different sets of vectors $\overrightarrow{OS_i}$.

In Table IV.1, the two exponents n and m of the yield function were assumed to be equal and the fitting process was carried out using the vertices of the Bishop and Hill polyhedron. The minimum of the Σ values is obtained with an exponent $n = m = 1.6$. This indicates that the 'best' fit between the single crystal polyhedron and the Hill type yield function with one exponent is obtained for $n = 1.6$, $\alpha = 0.46$ and $\beta = 0.51$. It is to be noted that the quadratic criterion used primarily by Montheillet et al. [5], also leads to a good approximation of the yield surface. It is also of interest that a perfect fit ($\Sigma = 0$) with respect to the vertices is obtained in normal stress space with $\alpha = 1/2$, whatever the exponent n; by contrast, when solely the shear stresses are taken into consideration, a perfect fit corresponds to the values $\beta = 1/2$ and an exponent $n = 1.6$.

n	α	β	Σ
1.0	0.37	0.39	1.168
1.4	0.42	0.46	0.085
1.6	0.46	0.51	0.030
1.7	0.47	0.54	0.041
1.8	0.49	0.57	0.065
2.0	0.52	0.64	0.138
2.2	0.55	0.72	0.223
2.5	0.59	0.88	0.352
3.0	0.63	1.24	0.537
4.0	0.64	2.49	0.784
6.0	0.65	9.38	1.009
12.0	0.68	416.	1.202

Table IV.1. Dependence on exponent n of the coefficients α and β in the CMTP yield criterion. The root mean square distance Σ indicates the quality of the overall fit, which is best for $n = 1.6$

ω_0	n	α	β	Σ
0°	1.6	0.46	0.51	0.030
10°	1.6	0.47	0.53	0.024
15°	1.7	0.46	0.56	0.015
20°	1.7	0.45	0.60	0.009

Table IV.2. Dependence on scatter width ω_0 of the coefficients α and β and the exponent n when the CMTP method is based on the 'disoriented' single crystal. For each value of ω_0, α, β and n were optimized so as to minimize the root mean square distance Σ.

ω_0	n	m	α	β	Σ
0°	3.0	1.4	0.47	0.58	0.366
15°	2.6	1.5	0.49	0.62	0.213
15°	1.7	1.7	0.43	0.68	0.280

Table IV.3. Dependence on scatter width ω_0 of the coefficients α and β and the exponents n and m when the CMTP method is based on the 'disoriented' single crystal. For each value of ω_0, α, β, n and m were optimized so as to minimize the root mean square distance Σ.

In Table IV.2, the minimization of Σ was carried out using the 'vertices' calculated for various grain distributions (Table III.3) and the one exponent (n=m) yield function of Eq. 4.2. The minimum Σ-value was obtained with the exponent $n=1.6$ for the cases $\omega_0=0°$ (single crystal) and $\omega_0=10°$, and with $n=1.7$ for higher spreads, i.e. $\omega_0=15$ and 20°.

In Table IV.3, the same type of fitting process was carried out using both the 'vertices' as well as the mid-points of the faces of the disoriented yield surface (Tables III.2 and 3). Two different exponents n and m were considered in Eq. 4.7. The introduction of these extra points (mid-points of the faces) led to an improvement in the fit of the locus. Only the two grain distributions corresponding to $\omega_0=0°$ and $\omega_0=15°$ were treated. The difference in the two parameters n and m ($n=2.6$ and $m=1.5$ for $\omega_0=15°$) finds a ready explanation in the discrepancy observed in the normal and shear stress behaviours of Figs. 3.6 and 3.7. The higher values of Σ reported in Table IV.3 compared to the ones shown in Tables IV.1 and IV.2 are readily explained by the introduction of the mid-points of the faces. If the two exponents are equated to give $n=m=1.7$, for example, it is found that $\alpha=0.43$, $\beta=0.68$ and $\Sigma=0.280$, so that the condition $n\neq m$, for which $\Sigma=0.213$, provides an improvement in the fit (see Table IV.3).

IV.1.2. Yield surface cross-sections

The yield loci established by the first method (Table IV.1) are illustrated in Figs. 4.2 and 4.3 in terms of their π-plane and shear plane intersections,

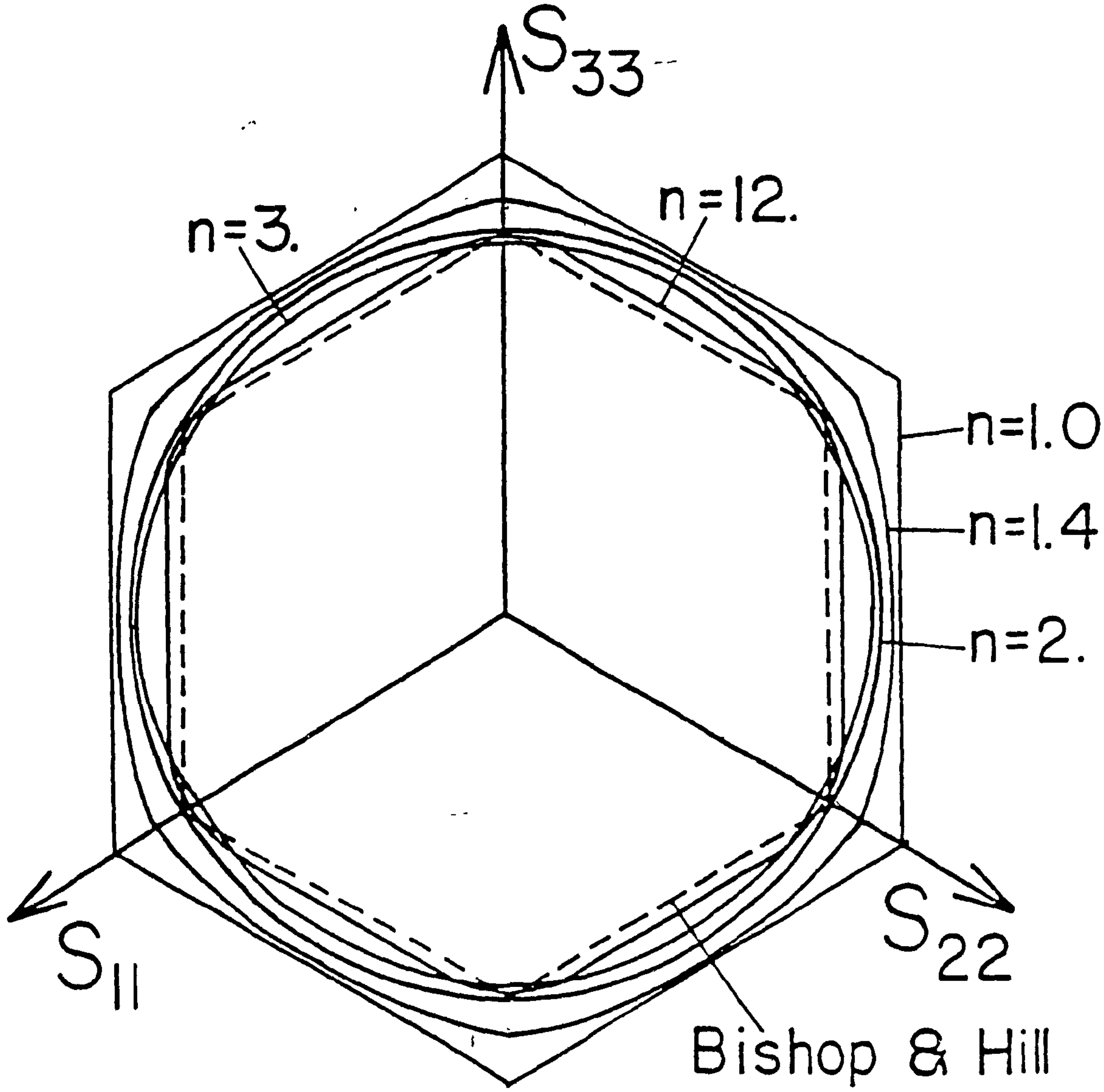

Fig. 4.2 π-plane sections of the Bishop and Hill polyhedron (broken line) and the generalized CMTP yield surfaces for five values of the exponent n.

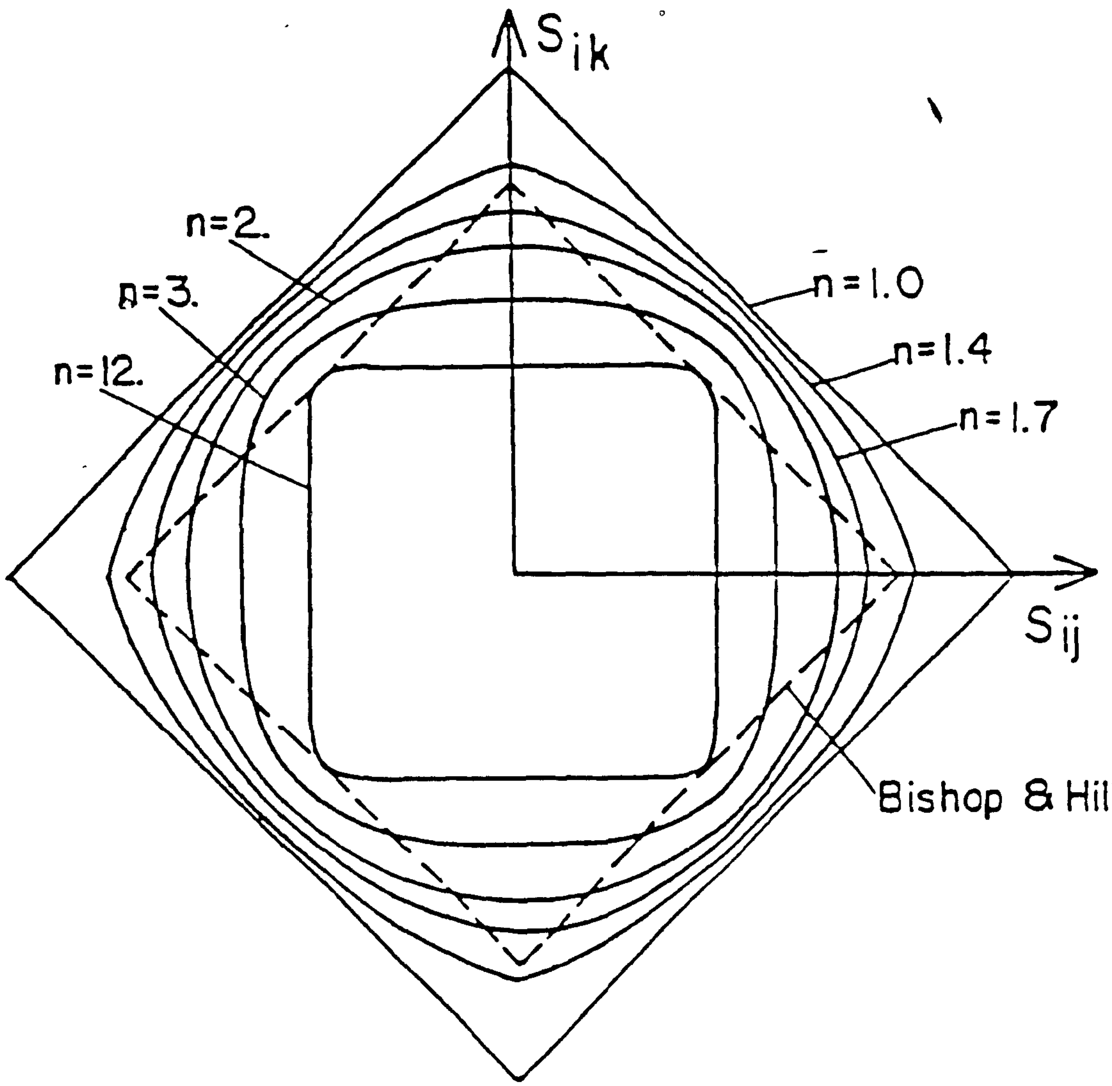

Fig. 4.3 Shear plane sections of the Bishop and Hill polyhedron (broken line) and the generalized CMTP yield surfaces for six values of the exponent n.

respectively. It can be seen from Fig. 4.2 (which corresponds to the fit to the Bishop and Hill polyhedron) that the π-plane section of the CMTP yield surface evolves from a hexagonal shape to a circular one as the exponent n is increased from 1 to 2. As n is further increased in the range 2 to 12, flat edges and rounded vertices begin to appear, until finally a rounded hexagon is seen at $n = 12$. In the shear planes (S_{ij}, S_{ik}) (Fig. 4.3), a somewhat similar behaviour is observed. In this case, the yield surface cross-section is a square when $n = 1$, becomes circular for the quadratic case ($n = 2$), and evolves towards a square again as n approaches 12, but inclined at 45° to the original one. It should be noted that the effect of increasing n in the π-plane cross-section of Fig. 4.2 (hexagon → circle → hexagon) is qualitatively similar to that of increasing the scatter width shown in Fig. 3.6. Similar remarks apply to the shear plane cross-sections (Fig. 3.7), except that the effect of increasing the scatter width is fully represented by n-values in the range $1 \leqslant n \leqslant 2$

Some further information regarding the extent of convergence and divergence displayed by the CMTP and crystallographic yield surfaces may be gained from the shear cross-sections taken at some distance from the origin. This can be done by setting $S_{12} + S_{13} + S_{23} = K$, and then representing the cross-sections in a manner analogous to that employed for the deviator stresses in the π-plane. We refer to this cross-section here as the π'-plane (which is not a closed subspace, although the three-dimensional subspace (S_{12}, S_{13}, S_{23}) is closed), in which the coordinates are ($S_{12} - K/3$, $S_{13} - K/3$, $S_{23} - K/3$). For purposes of illustration, cross-sections corresponding to $n = 2$ and $n = 1.7$ have been prepared and are presented in Figs. 4.4a and 4.4b, respectively, for three values of K ($K = 0$, 0.5 and 1.0). It should be noted that the Bishop and Hill vertices of the B type [99] (<111> tension or compression) are located on the $K = 0.5$ section and that these are reasonably well simulated by both continuum yield surfaces ($n = 1.7$ and $n = 2.0$). By contrast, the yield corners of the C-type ({100}<010> shear), which are on the $K = 1.0$ section, are better circumscribed by the $n = 1.7$ than the $n = 2.0$ representation. It thus appears that, whereas the quadratic yield surface is easier to use (e.g. the normality rule can be readily applied analytically), a non-quadratic yield function with an exponent of 1.7 provides a closer approximation in this particular subspace to the ones calculated from crystallographic considerations.

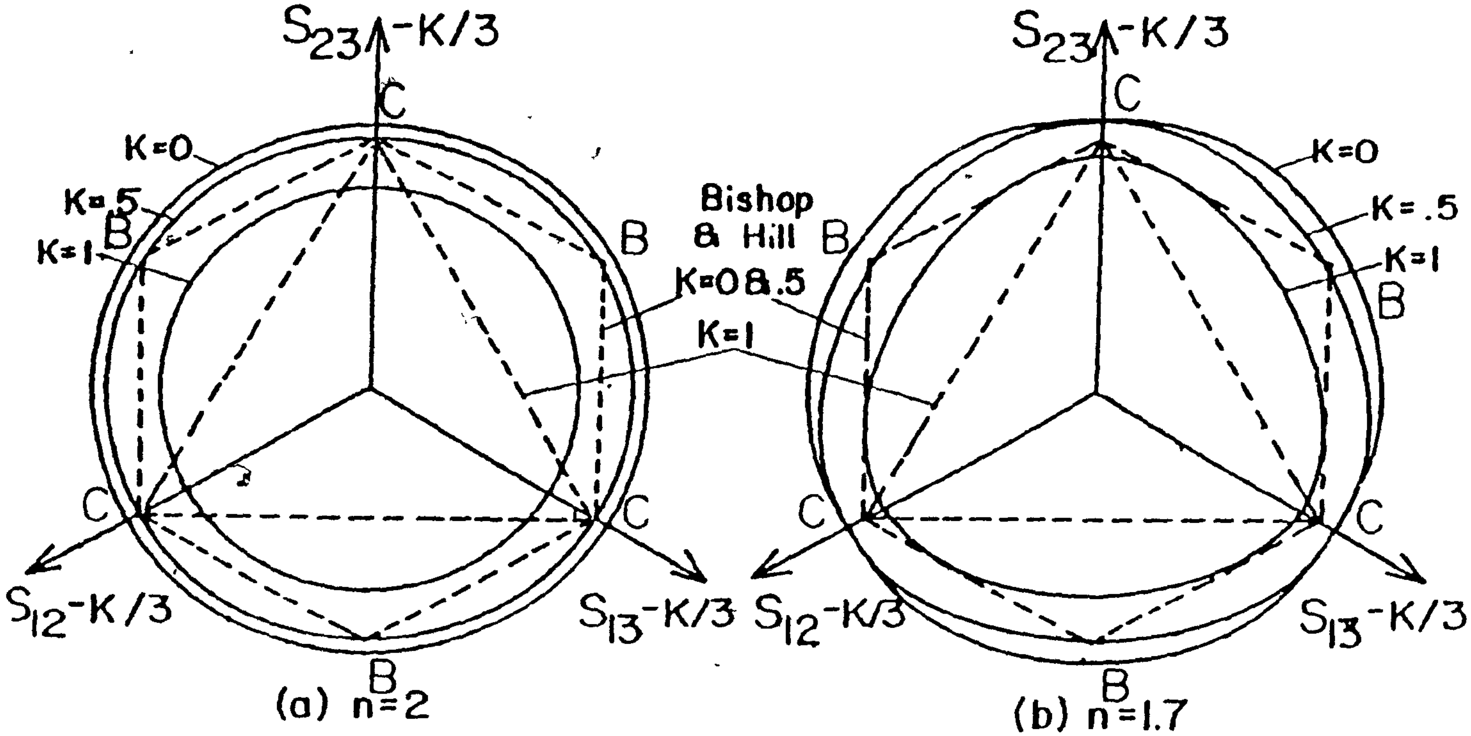

Fig. 4.4 Intersections of the Bishop and Hill polyhedron (broken line) and the CMTP locus with the planes $S_{12}+S_{23}+S_{31}=K$ for $K=0$, 0.5 and 1. (a) $n=2$ (b) $n=1.7$.

We now examine the differences in the extent to which the five classes of single crystal vertices [99] are suitably fitted by the various sets of coefficients n, α and β listed in Table IV.1 (and interpolated values when necessary). For example, the six A type vertices corresponding to <100> tension or compression are best fitted by the yield locus with the exponent n=2.1; by contrast, the eight B type corners (<111> tension or compression) are better circumscribed when n = 1.8. The six C type vertices in turn, which correspond to {100}<001> shear, lie close to the yield surface with an exponent n=1.6. Finally, n values of 1.5 and 3.5, respectively, are in the best agreement with the 24 D (<100> tension or compression + {100}<011> shear) and 12 E ({100}<010> shear + {110}<110> shear) type vertices.

Thus, depending on the sharpness of the texture present and on the type of loading encountered (which determines the class of vertex that is the most frequently activated), different values of the yield locus exponent are likely to lead to the most precise results.

When 'inhomogeneous' functions are considered ($n \neq m$), such as those referred to in Table IV.3, similar shapes of the loci are obtained, but with a somewhat different size, in the two subspaces investigated (π-plane and shear stress plane).

As a result of these computations, the following conclusions pertaining to the choice of the exponents n and m as well as the parameters α and β can be drawn :

. The 'best' fit between the Bishop and Hill polyhedron and a one exponent yield surface of the Hill type is obtained with $n=1.6$, $\alpha=0.46$ and $\beta=0.51$.

. A good estimate is also given by a quadratic criterion with $n=2$, $\alpha=0.52$ and $\beta=0.64$; the latter is easier to manipulate for analytical calculations.

. A further significant improvement is obtained when two different exponents are considered and when both the 'rounded' vertices and mid-points of the faces corresponding to the disoriented single crystal are taken into account. In this case, the best fit corresponds to $n=2.6$, $m=1.5$, $\alpha=0.49$ and $\beta=0.62$.

IV.1.3. Different types of continuum yield surfaces

In this study, different types of continuum or semi-continuum yield functions were used, which were assumed to give a good representation of the locus of a single or disoriented single crystal. The simplest of these is the Hill quadratic yield function [4], which can be written :

$$\alpha\,[\,(S_{11}-S_{22})^2+(S_{11}-S_{33})^2+(S_{22}-S_{33})^2\,]\,+2\beta\,[\,S_{12}^2+S_{13}^2+S_{23}^2\,] = 1 \tag{4.8}$$

or

$$\alpha/2\,[\,(2S_1)^2+(S_1-\sqrt{3}S_2)^2+(S_1+\sqrt{3}S_2)^2\,]\,+\beta\,[\,S_3^2+S_4^2+S_5^2\,] = 1 \tag{4.9}$$

when using Eq.3.9.

This expression, when developed, reduces to a very simple one:

$$3\,\alpha\,(S_1^2+S_2^2)\,+\,\beta\,(S_3^2+S_4^2+S_5^2) = 1 \tag{4.10}$$

As shown above, $\alpha=0.52$ and $\beta=0.64$.

As will be demonstrated in paragraph IV,2, this simple function permits the plastic properties of samples containing several different texture components to be derived in a straightforward manner.

The second type of locus used is the Hill non-quadratic function [71] with a single exponent :

$$\alpha\,[\,|S_{11}-S_{22}|^n+|S_{11}-S_{33}|^n+|S_{22}-S_{33}|^n\,]\,+2\beta\,[\,|S_{12}|^n+|S_{13}|^n+|S_{23}|^n\,] = 1$$

$$\text{or}\quad \alpha\,2^{-n/2}\,[\,|2S_1|^n+|S_1-\sqrt{3}S_2|^n+|S_1+\sqrt{3}S_2|^n\,] \tag{4.11}$$

$$+\,\beta\,2^{1-n/2}\,[\,|S_3|^n+|S_4|^n+|S_5|^n\,] = 1$$

The coefficients α and β pertaining to the above two criteria are given in Table IV.1 as a function of the exponent n. Although more accurate, the generalization of the quadratic case involves longer and more complicated calculations, especially when the normality principle has to be inverted, i.e. when stress components have to be derived from knowledge of the strain rate components. This criterion will be referred to as the "new" Hill criterion.

The yet more complex (in terms of computations) Hill yield function with two different exponents (Eq. 4.2) was also investigated. It will be referred to as the Hill "two-exponent" criterion.

Other yield functions based on the Bishop and Hill locus were also used in this work. Recalling that slip occurs on the {111} $<1\bar{1}0>$ or {110} $<1\bar{1}1>$ systems in the fcc and bcc metals, respectively, it was shown by Bishop and Hill [28] that the condition for slip can be written :

$$\begin{cases} A \pm G \pm H = \pm\sqrt{6}\,\tau_c \\ B \pm F \pm H = \pm\sqrt{6}\,\tau_c \\ C \pm F \pm G = \pm\sqrt{6}\,\tau_c \end{cases} \tag{4.12}$$

where $A=\sigma_{22}-\sigma_{33}$, $B=\sigma_{33}-\sigma_{11}$, $C=\sigma_{11}-\sigma_{22}$, $F=\sigma_{23}$, $G=\sigma_{31}$, $H=\sigma_{12}$ and τ_c is the critical resolved shear stress.

When written in the five dimensional notation of Eq.3.9, this leads to :

$$\begin{cases} |2S_1|+|S_3|+|S_4| = \sqrt{2} \\ |S_1-\sqrt{3}S_2|+|S_4|+|S_5| = \sqrt{2} \\ |S_1+\sqrt{3}S_2|+|S_3|+|S_5| = \sqrt{2} \end{cases} \tag{4.13}$$

where the stress deviator components are normalized by $\sqrt{6}\,\tau_c$.

The single crystal yield surface is then given by the inner envelope of these three polyhedra and can thus be expressed by means of the two relations :

$$F(S) = [\,|2S_1|+|S_3|+|S_4|-\sqrt{2}\,]\ [\,|S_1-\sqrt{3}S_2|+|S_4|+|S_5|-\sqrt{2}\,]$$
$$[\,|S_1+\sqrt{3}S_2|+|S_3|+|S_4|-\sqrt{2}\,] = 0 \qquad (4.14)$$

and $S_1^2 + S_2^2 + S_3^2 + S_4^2 + S_5^2$ *minimum*

for a given stress direction.

It is interesting to note that development of Eq.4.14 produces .

$$(1/\sqrt{2})\,[\,|2S_1|+|S_1+\sqrt{3}S_2|+|S_1-\sqrt{3}S_2|\,] + (2/\sqrt{2})\,[\,|S_3|+|S_4|+|S_5|\,] -1$$
$$+ \text{terms}\,(S_i^3, S_i^2S_j, S_iS_jS_k, S_i^2, S_iS_j) = 0 \qquad (4.15)$$

The first two terms look familiar : they have exactly the same form as the Hill criterion (Eq.4.2), with an exponent n = 1, however, and $\alpha = \beta = 1/\sqrt{2}$. They thus represent a kind of 'partial' development of the Bishop and Hill criterion involving only the linear terms.

One could also take into consideration only the squared terms in order to obtain another analytic yield function which represents another partial development of the Bishop and Hill criterion. Finally, if the stresses are raised to a power n, the following type of equation is obtained .

$$\alpha\,[\,|2S_1|^n|S_1-\sqrt{3}S_2|^n+|2S_1|^n|S_1+\sqrt{3}S_2|^n+|S_1-\sqrt{3}S_2|^n|S_1+\sqrt{3}S_2|^n\,]$$
$$+\beta\,[\,(|S_3|^n+|S_4|^n)(|S_4|^n+|S_5|^n)+(|S_3|^n+|S_4|^n)(|S_3|^n+|S_5|^n) \qquad (4.16)$$
$$+(|S_4|^n+|S_5|^n)(|S_3|^n+|S_5|^n)\,] + \gamma\,[\,|2S_1|^n(|S_3|^n+|S_4|^n+2|S_5|^n)$$
$$+|S_1-\sqrt{3}S_2|^n(2|S_3|^n+|S_4|^n+|S_5|^n)+|S_1+\sqrt{3}S_2|^n(|S_3|^n+2|S_4|^n+|S_5|^n)\,] = 1$$

When n = 1 and $\alpha = \beta = \gamma = 1/2$, the squared terms of Eq. 4.15 are found. When n = 2, the expression reduces to :

$$9\alpha(S_1^2+S_2^2)^2+\beta\,[\,(S_3^2+S_4^2+S_5^2)^2+S_3^2S_4^2+S_3^2S_5^2+S_4^2S_5^2\,]$$
$$+\gamma\,[\,S_3^2(7S_1^2+9S_2^2-2\sqrt{3}S_1S_2)+S_4^2(7S_1^2+9S_2^2+2\sqrt{3}S_1S_2)$$
$$+S_5^2(10S_1^2+6S_2^2)\,] = 1 \qquad (4.17a)$$

which is a quartic yield function. The coefficients α, β and γ were calculated using the same method as for the Hill criteria described above and it was found that $\alpha=0.205$ and $\beta=\gamma=0.305$. If the condition $\gamma=0$ is now prescribed in order to avoid the presence of mixed stress terms (i.e. normal x shear stresses), then the fitting process leads to $\alpha=0.40$ and $\beta=0.48$. These two new criteria (i.e. $n=2$ with $\gamma\neq0$ and $n=2$ with $\gamma=0$) will be referred to as PL1 and PL2, respectively.

Two other criteria were derived in a similar way :

$$9\alpha(S_1{}^2+S_2{}^2)^2+\beta(S_3{}^2+S_4{}^2+S_5{}^2)^2 = 1 \tag{4.17b}$$

and

$$3\alpha(S_1{}^2+S_2{}^2)+\beta(S_3{}^2+S_4{}^2+S_5{}^2)+\gamma(|S_3S_4|+|S_3S_5|+|S_4S_5|) = 1 \tag{4.17c}$$

identified here as PL3 ($\alpha=0.38$ and $\beta=0.59$) and PL4 ($\alpha=0.54$, $\beta=0.60$ and $\gamma=0.20$), respectively.

IV.2 THE PREDICTION OF PLASTIC PROPERTIES

In this section, the manner in which plastic properties can be predicted from texture data is considered. Only the Hill "one-exponent" function is treated for simplicity, whereas most of the analytical results were obtained with the simpler "quadratic" criterion.

It is assumed that the crystallographic texture of a given material is known in terms of sets of Miller indices {hkl}<uvw> or Euler angles (see Appendix III.1). These data can be obtained experimentally from X-ray diffraction measurements, which lead to pole figures and eventually to CODF (crystallite orientation distribution function) data [16]. They can also be calculated theoretically : the full constraint (FC) and relaxed constraint (RC) methods of texture prediction have proved their ability to reproduce experimental pole figures satisfactorily [98, 100-102]. However, they generally predict textures which are too sharp when compared to experiment and do not reproduce the differences observed between materials such as Al and Cu.

The basic information needed for the CMTP method can be summed up as follows :

(i) a set of ideal orientations (Miller indices or Euler angles) into which the polycrystalline texture has been decomposed;

(ii) the volume fraction of each of these ideal orientations, as well as the spread around them, if possible;

(iii) the volume fraction of the random component (i.e. of the "background" generally observed in pole figures).

Two sets of axes need to be considered :

(a) the specimen axes (S), i.e. those in which the experiment (tension, torsion,...) is carried out for the measurement of the plastic properties of interest;

(b) the crystal axes (C), i.e. the <100> directions of the ideal orientation under discussion. The CMTP function $F(\underset{\sim}{S}) = 1$ (see paragraph 4.2.2) is taken to represent the yield surface of this crystal.

The material under investigation is assumed to be submitted to arbitrary stress and strain rate tensors, which are expressed in the axes of the specimen :

$$\underset{\sim}{\sigma}(S) = (\sigma_{ij}(S)) \quad \text{and} \quad \underset{\sim}{\dot{\varepsilon}}(S) = (\dot{\varepsilon}_{ij}(S)) \tag{4.18}$$

Here the prescribed σ_{ij} components correspond to non-prescribed $\dot{\varepsilon}_{ij}$ values and vice versa. For example, in the case of a uniaxial tensile test, the only unknown σ_{ij} is the tensile stress σ_{11} (the other σ_{ij}'s are prescribed to be zero); the corresponding strain rate component $\dot{\varepsilon}_{11}$ is by contrast the only fixed component of the tensor $\underset{\sim}{\dot{\varepsilon}}$ (S).

IV.2.1. Plastic anisotropy induced by a single ideal orientation

Actual materials usually exhibit more than one ideal orientation. However, it is of interest to see the influence each texture component {hkl}<uvw> can have on the plastic properties. In the section that follows, tensor analysis is used to derive these stress and strain rate characteristics. The equivalent vector technique will be employed in the next section, for comparison purposes.

<u>First case - Prescribed strain rate tensor.</u>

Here the material is considered to be submitted to the following arbitrary strain rate tensor, which is prescribed in the axes of the specimen (S) :

$$\dot{\underset{\sim}{\varepsilon}}_{(S)} = (\dot{\varepsilon}_{ij\,(S)}) \tag{4.19}$$

Using the crystallographic {hkl} plane and <uvw> direction, the orientation of the specimen axes (S) can be deduced with respect to that of the crystal (C) axes through a transformation matrix P whose coefficients depend only on the Miller indices. To derive the deviator stress tensor $\underset{\sim}{S}$ in the (S) coordinate system, $\dot{\underset{\sim}{\varepsilon}}_{(S)}$ must first be converted into the (C) representation :

$$\dot{\underset{\sim}{\varepsilon}}_{(C)} = P\,\dot{\underset{\sim}{\varepsilon}}_{(S)}\,\tilde{P} \tag{4.20}$$

Here $\tilde{P}$ is the transpose of P. $\underset{\sim}{S}_{(C)}$ is then obtained from the CMTP yield criterion and the normality principle :

$$\dot{\underset{\sim}{\varepsilon}}_{(C)} = \dot{\lambda}\,\partial F / \partial \underset{\sim}{S}_{(C)} \tag{4.21}$$

where $\dot{\lambda}$ is a positive scalar (it should be noted that the differentiations involving S_{ij} and S_{ji} must be carried out separately). This leads to :

$$\left\{\begin{array}{l}
\dot{\varepsilon}_{xx} = \dot{\lambda}\, \alpha\, n \left[\dfrac{|S_{xx}-S_{yy}|^{n}}{S_{xx}-S_{yy}} + \dfrac{|S_{xx}-S_{zz}|^{n}}{S_{xx}-S_{zz}} \right] \\[2ex]
\dot{\varepsilon}_{yy} = \dot{\lambda}\, \alpha\, n \left[- \dfrac{|S_{xx}-S_{yy}|^{n}}{S_{xx}-S_{yy}} + \dfrac{|S_{yy}-S_{zz}|^{n}}{S_{yy}-S_{zz}} \right] \\[2ex]
\dot{\varepsilon}_{zz} = \dot{\lambda}\, \alpha\, n \left[- \dfrac{|S_{xx}-S_{zz}|^{n}}{S_{xx}-S_{zz}} - \dfrac{|S_{yy}-S_{zz}|^{n}}{S_{yy}-S_{zz}} \right] \\[2ex]
\dot{\varepsilon}_{xy} = \dot{\lambda}\, \beta\, m \dfrac{|S_{xy}|^{m}}{S_{xy}} \\[2ex]
\dot{\varepsilon}_{yz} = \dot{\lambda}\, \beta\, m \dfrac{|S_{yz}|^{m}}{S_{yz}} \\[2ex]
\dot{\varepsilon}_{xz} = \dot{\lambda}\, \beta\, m \dfrac{|S_{xz}|^{m}}{S_{xz}}
\end{array}\right. \tag{4.22}$$

where the $\dot{\varepsilon}_{ij}$ and S_{ij} are expressed in the crystal axes. The stresses themselves can then be derived when inverting these expressions. For a non-quadratic function (n and $m \neq 2$), this is done numerically, as shown in Appendix IV.2. However, for the quadratic case, a complete analytic calculation can be carried out. It is readily shown that

$$\dot{\underset{\sim}{\varepsilon}}(C) = \dot{\lambda} \begin{bmatrix} 3S_{xx} & 4S_{xy}/3 & 4S_{xz}/3 \\ 4S_{xy}/3 & 3S_{yy} & 4S_{yz}/3 \\ 4S_{xz}/3 & 4S_{yz}/3 & 3S_{zz} \end{bmatrix} \tag{4.23}$$

and that

$$\underset{\sim}{S}(C) = 1/\dot{\lambda} \begin{bmatrix} \dot{\varepsilon}_{xx}/3 & 3\dot{\varepsilon}_{xy}/4 & 3\dot{\varepsilon}_{xz}/4 \\ 3\dot{\varepsilon}_{xy}/4 & \dot{\varepsilon}_{yy}/3 & 3\dot{\varepsilon}_{yz}/4 \\ 3\dot{\varepsilon}_{xz}/4 & 3\dot{\varepsilon}_{yz}/4 & \dot{\varepsilon}_{zz}/3 \end{bmatrix} \tag{4.24}$$

Finally, since it can be demonstrated that $\dot{\lambda} = \dot{W}/2$, where $\dot{W} = \underset{\sim}{S}.\dot{\underset{\sim}{\varepsilon}}$ is the power dissipated per unit volume, the desired stress tensor $\underset{\sim}{S}_{(S)}$ can be readily deduced by transforming $\underset{\sim}{S}_{(C)}$ onto the (S) axes :

$$\underset{\sim}{S}_{(S)} = \tilde{P}\,\underset{\sim}{S}_{(C)}\,P \qquad (4.25)$$

The stresses themselves can in turn be derived from the boundary conditions regarding the hydrostatic pressure at the surface of the workpiece.

The plastic anisotropy of strongly textured cubic polycrystals displaying a single ideal orientation can be predicted in this way with relative ease.

The quadratic theory was applied to the case of the fixed end torsion test by Montheillet et al. [5]. The developed axial stress σ_{zz} was of particular interest. It was demonstrated that the latter is associated with specific texture components, as well as with small rotations of these components about the radius of the specimen away from the nominal ideal orientation. The predicted axial stress vs. crystallographic texture relationships were in good agreement with experimental observations relating to the torsion of Al, Cu and α-Fe over a wide range of temperatures, strains and strain rates. The analysis is extended here to the case of the free end torsion test [103].

In this case, the strain rate tensor is specified by

$$\dot{\underset{\sim}{\varepsilon}}_{(S)} = \begin{bmatrix} -\dot{\eta}/2 & 0 & 0 \\ 0 & -\dot{\eta}/2 & \dot{\varepsilon} \\ 0 & \dot{\varepsilon} & \dot{\eta} \end{bmatrix} \qquad (4.26)$$

where $2\dot{\varepsilon}$ is the applied torsional strain rate and $\dot{\eta}$ is the induced rate of change of the specimen length. The specimen axes (S) = (r, θ, z) are shown in Fig. 4.5. If {hkl} is the crystallographic plane parallel to the shear plane (r, θ) and <uvw> is the crystallographic direction near the shear direction θ, then the transformation matrix P from the specimen to the crystal axes is

$$P = \begin{bmatrix} r_1 & u_1 & n_1 \\ r_2 & u_2 & n_2 \\ r_3 & u_3 & n_3 \end{bmatrix} \tag{4.27}$$

where $u_1 = u / \sqrt{u^2+v^2+w^2}$, $u_2 = v / \sqrt{u^2+v^2+w^2}$, $u_3 = w / \sqrt{u^2+v^2+w^2}$

$n_1 = h / \sqrt{h^2+k^2+l^2}$, $n_2 = k / \sqrt{h^2+k^2+l^2}$, $n_3 = l / \sqrt{h^2+k^2+l^2}$

$r = u \times n$

Following the method described above, and employing the quadratic yield criterion, it is readily shown that

$$\begin{cases} S_{rr(S)} = \dot{\eta} / 2\dot{\lambda} [-1/6\alpha - 3(1/\beta - 1/3\alpha)/2 \, r_\iota^2 n_\iota^2] - \dot{\varepsilon} / \dot{\lambda} (1/\beta - 1/3\alpha) \, r_\iota^2 n_\iota u_\iota \\ S_{\theta\theta(S)} = \dot{\eta} / 2\dot{\lambda} [-1/6\alpha - 3(1/\beta - 1/3\alpha)/2 \, u_\iota^2 n_\iota^2] - \dot{\varepsilon} / \dot{\lambda} (1/\beta - 1/3\alpha) u_\iota^3 n_\iota \\ S_{zz(S)} = \dot{\eta} / 2\dot{\lambda} [-1/6\alpha - 3(1/\beta - 1/3\alpha)/2 \, n_\iota^4] - \dot{\varepsilon} / \dot{\lambda} (1/\beta - 1/3\alpha) \, u_\iota n_\iota^3 \\ S_{r\theta(S)} = -\dot{\eta} / 2\dot{\lambda} [3(1/\beta - 1/3\alpha)/2 \, r_\iota n_\iota^2 u_\iota] - \dot{\varepsilon} / \dot{\lambda} (1/\beta - 1/3\alpha) \, r_\iota n_\iota u_\iota^2 \\ S_{rz(S)} = -\dot{\eta} / 2\dot{\lambda} [3(1/\beta - 1/3\alpha)/2 \, r_\iota n_\iota^3] - \dot{\varepsilon} / \dot{\lambda} (1/\beta - 1/3\alpha) \, r_\iota u_\iota n_\iota^2 \\ S_{\theta z(S)} = -\dot{\eta} / 2\dot{\lambda} [3(1/\beta - 1/3\alpha)/2 \, u_\iota n_\iota^3] \\ \qquad\qquad - \dot{\varepsilon} / \dot{\lambda} (1/\beta - 1/3\alpha) [u_\iota^2 n_\iota^2 - 1/2\beta(1/\beta - 1/3\alpha)] \end{cases} \tag{4.28}$$

$$\text{with } \dot{\lambda} = \dot{W}/2 = \{ 3\dot{\eta}^2/8 [3/2\beta - 1/6\alpha - 3(1/\beta - 1/3\alpha)/2 \, n_\iota^4] + \dot{\varepsilon}^2 [1/2\beta - (1/\beta - 1/3\alpha) \, u_\iota^2 n_\iota^2] - \dot{\eta}\dot{\varepsilon} \, 3/2 (1/\beta - 1/3\alpha) \, u_\iota n_\iota^3 \}^{1/2} \tag{4.29}$$

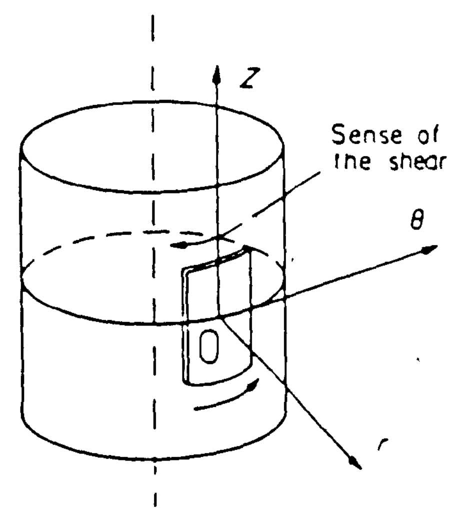

Fig. 4.5 System of coordinate axes in torsion testing.

The boundary conditions imposed on the sample are concerned with the free end ($\sigma_{zz}=0$) and free surface ($\sigma_{rr}=0$), leading to $S_{rr}=S_{zz}$ (deviator stresses). It is thus readily deduced that

$$\dot{\eta}/\dot{\varepsilon} = -4/3\,(u_i n_i r_i^{\,2} - u_i n_i^{\,3})\,/\,(n_i^{\,2} r_i^{\,2} - n_i^{\,4} + 1/\beta/(1/\beta - 1/3\alpha)) \tag{4.30}$$

which expresses the rate of length change per unit torsional strain rate which is induced by the presence of a given ideal orientation. For an isotropic medium, $\beta=3\alpha$, so that $\dot{\eta}=0$.

The link between the fixed end and free end torsion tests can now be made explicit. This is done by calculating the ratio of the rate of length change $\dot{\eta}$ ($\sigma_{zz}=0$, free end) to the axial stress σ_{zz}($\eta=0$, fixed end). Using Eqs. 4.28, it is found that

$$\frac{\dot{\eta}(\sigma_{zz}=0)}{\sigma_{zz}(\eta=0)} = -\frac{4}{3}\,\frac{\left(\frac{1}{2\beta}-\left(\frac{1}{\beta}-\frac{1}{3\alpha}\right)u_i^2 n_i^2\right)}{\frac{1}{\beta}+\left(\frac{1}{\beta}-\frac{1}{3\alpha}\right)\left(n_i^2 r_i^2-n_i^4\right)}\,|\dot{\varepsilon}| \tag{4.31}$$

For all the ideal orientations investigated, the RHS term of Eq. 4.31 is negative, leading to the following conclusions :

	Fixed end torsion	Free end torsion
$\sigma_{zz}<0$	compression	lengthening
$\sigma_{zz}>0$	tension	shortening
$\sigma_{zz}=0$	no axial effect	no length change

This is in complete agreement with the intuitive comment that a compressive force should correspond to the lengthening of the sample, and vice versa. These predictions will be compared with experimental observations in Chapter V.

<u>Second case - Prescribed stress tensor - Strain rate ratio R(θ)</u>

The plastic anisotropy of a sheet can be characterized in terms of the so-called R-value. Following Lankford et al.[29], we define the strain rate ratio

$R(\theta)$ pertaining to a direction inclined at an angle θ to the rolling direction (Fig. 2.2) as

$$R(\theta) = \dot{\varepsilon}_{yy}(\theta) / \dot{\varepsilon}_{zz}(\theta) \tag{4.32}$$

where $\dot{\varepsilon}_{yy}$ and $\dot{\varepsilon}_{zz}$ are the width and thickness strain rates experienced by a tensile sample which was oriented and is being pulled along the θ direction.

In the literature, different strain levels have been employed for the measurement of $R(\theta)$. For example, Semiatin et al.[104] carried out tensile tests to elongations of 18%, Goodman and Hu [105] and Helias and coworkers [106] adopted a strain of 15%, whereas Truszkowski and Jarominek [107] measured $R(\theta)$ at the limit of uniform elongation as well as at zero elongation (obtained by back extrapolating the $R(\theta)$ vs. $\dot{\varepsilon}_{xx}$ relation determined over a range of strains). In a similar manner, Stickels and Mould [108] made their measurements at maximum load. Unfortunately, the lack of a standard procedure for determining the Lankford coefficient leads to difficulties when the observations of different workers are compared. As a result, when the other sources of error are taken into consideration, there remains an uncertainty of as much as 10 to 20% in the published values of this ratio for a given state of material.

During the tensile test employed for the determination of R, the form of the stress tensor is prescribed :

$$\underset{\sim}{\sigma}_{(xyz)} = \begin{bmatrix} \sigma_{xx} & 0 & 0 \\ 0 & 0 & 0 \\ 0 & 0 & 0 \end{bmatrix} \tag{4.33}$$

although the value of σ_{xx} is generally not known.

The $\underset{\sim}{\sigma}_{(C)}$ tensor with respect to the crystal axes can then be deduced from the developed $\underset{\sim}{\sigma}_{(xyz)}$ tensor and the experimentally determined ideal orientation. $\dot{\underset{\sim}{\varepsilon}}_{(C)}$ is derived next from the CMTP criterion and the normality principle, after which $\dot{\underset{\sim}{\varepsilon}}_{(xyz)}$ is obtained by transforming $\dot{\underset{\sim}{\varepsilon}}_{(C)}$ onto the specimen axes. The detailed calculation is presented in Appendix IV.3 for the quadratic case and leads to :

$$R(\theta)=\frac{\dot{\varepsilon}_{yy}}{\dot{\varepsilon}_{xx}}=\frac{\frac{1}{4}\Sigma(u_i^4+r_i^4-2u_i^2r_i^2)\sin^2 2\theta+\Sigma(u_i^2r_i^2)\cos^2 2\theta+\frac{1}{2}\Sigma(r_iu_i^3-u_ir_i^3)\sin 4\theta-\frac{3}{5}}{\Sigma(r_i^2n_i^2)\cos^2\theta+\Sigma(u_i^2n_i^2)\sin^2\theta+\Sigma(r_iu_in_i^2)\sin 2\theta-\frac{3}{5}} \tag{4.34}$$

where the parameters r_i, u_i, n_i ($i=1,2,3$) are the components of the specimen axis vectors (RD, TD, ND) along the (C) axes and the summations over the index i are extended from 1 to 3. The stress parameter σ_{xx} is also easily derived:

$$\sigma_{xx}(\theta) = [\, 5/6\, \Sigma\, (\, r_i \cos\theta + u_i \sin\theta\,)^4 + 1/6\,]^{-1/2} \tag{4.35}$$

as is the yield strength ratio :

$$\sigma_{xx}(\theta)/\sigma_{xx}(0) = [\, \frac{5\Sigma(r_i^4)+1}{5\,\Sigma(r_i\cos\theta+u_i\sin\theta)^4+1}\,]^{\frac{1}{2}} \tag{4.36}$$

<u>Symmetry considerations</u> :

In rolling, the deformation path is such that the texture normally has three planes of symmetry, viz. the planes normal to ND, TD and RD, respectively (Fig. 2.2). The strain rate ratio must also obey these symmetry conditions, the last two of which lead to :

$$R(-\theta) = R(\theta) \tag{4.37}$$

$$R(\Pi-\theta) = R(\theta) \tag{4.38}$$

It is evident from the form of Eq. 4.34 that relations 4.37 and 4.38 cannot be satisfied for an arbitrary ideal orientation. However, the symmetry requirement can be met by recognizing [109] that an ideal orientation described by the set of Miller indices {hkl}<uvw> generally consists of as many as four distinct orientations {hkl}<uvw>, $\{\bar{h}\bar{k}\bar{l}\}$<uvw>, {hkl}$<\bar{u}\bar{v}\bar{w}>$ and $\{\bar{h}\bar{k}\bar{l}\}<\bar{u}\bar{v}\bar{w}>$. As shown on the pole figure of Fig. 4.6, each of the last three orientations can be deduced from the first by a suitable symmetry operation. Nevertheless, orientations of maximum symmetry, such as {100}<001>, {100}<011>, {110}<001> and $\{110\}<1\bar{1}0>$, are completely described by a single set of poles; orientations with intermediate symmetry, such as

$\{110\}<1\bar{1}2>$ and $\{112\}<11\bar{1}>$, require two sets of poles; whereas orientations of minimum symmetry, e.g. $\{123\}<63\bar{4}>$ require the maximum of four equivalent sets, see Fig. 4.7. As a result, in the most general case, the R-value must be calculated by taking a weighted (0.25) average over the four equivalent sets :

$$R(\theta) = \frac{\dot{\varepsilon}_{yy}(\{hkl\}<uvw>)+\dot{\varepsilon}_{yy}(\{\bar{h}\bar{k}\bar{l}\}<uvw>)+\dot{\varepsilon}_{yy}(\{hkl\}<\bar{u}\bar{v}\bar{w}>)+\dot{\varepsilon}_{yy}(\{\bar{h}\bar{k}\bar{l}\}<\bar{u}\bar{v}\bar{w}>)}{\dot{\varepsilon}_{zz}(\{hkl\}<uvw>)+\dot{\varepsilon}_{zz}(\{\bar{h}\bar{k}\bar{l}\}<uvw>)+\dot{\varepsilon}_{zz}(\{hkl\}<\bar{u}\bar{v}\bar{w}>)+\dot{\varepsilon}_{zz}(\{\bar{h}\bar{k}\bar{l}\}<\bar{u}\bar{v}\bar{w}>)} \tag{4.39}$$

which leads to :

$$R(\theta) = \frac{\frac{1}{4}\,\Sigma\,(u_i^4+r_i^4-2\,u_i^2 r_i^2)\sin^2(2\theta)+\Sigma\,(u_i^2 r_i^2)\cos^2(2\theta)-\frac{3}{5}}{\Sigma\,(r_i^2 n_i^2)\cos^2\theta+\Sigma\,(u_i^2 n_i^2)\sin^2\theta-\frac{3}{5}} \tag{4.40}$$

A similar procedure must be employed to satisfy symmetry conditions 4.37 and 4.38 for the yield strength ratio, Eq. 4.36.

It should be noted that this averaging procedure does not correspond to a classical Taylor model and is presented here for its ease of use. It will be discussed in more detail in Chapter VI. A more realistic averaging technique, such as that of Taylor, leads to comparable results. However, this comment only applies to the quadratic or near quadratic yield criteria, which are by nature smooth.

The strain rate $R(\theta)$ and yield strength $\sigma(\theta)/\sigma(0)$ ratio predictions obtained in this way for the commonly observed ideal orientations will be presented in section V. These will concern the Hill quadratic and non-quadratic functions applied to the textures present in cubic metals.

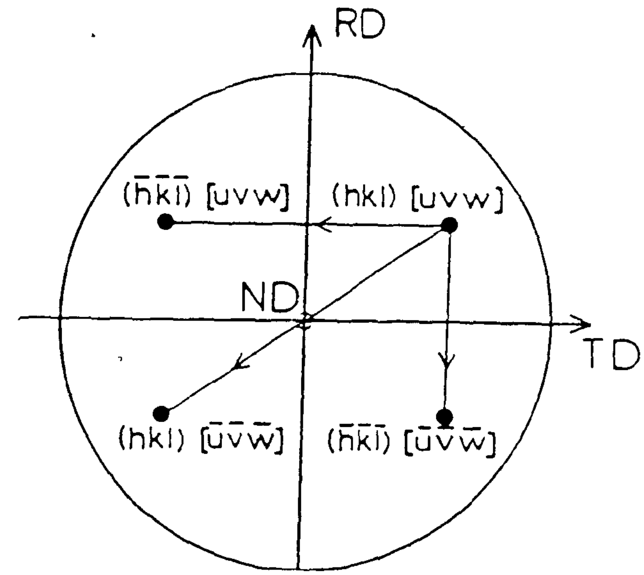

Fig. 4.6 Relative positions of the four orientations $\{hkl\}<uvw>$, $\{\bar{h}\bar{k}\bar{l}\}<uvw>$, $\{hkl\}<\bar{u}\bar{v}\bar{w}>$ and $\{\bar{h}\bar{k}\bar{l}\}<\bar{u}\bar{v}\bar{w}>$ on a pole figure for a rolled material.

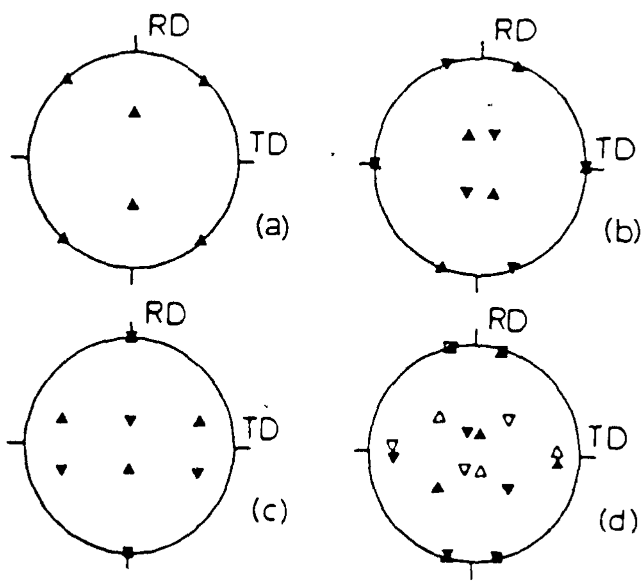

Fig. 4.7 {111} pole figures for the ideal orientations known as : (a) Goss $\{110\}<001>$; (b) Bs $\{110\}<1\bar{1}2>$; (c) Cu $\{112\}<11\bar{1}>$; (d) S $\{123\}<63\bar{4}>$.

IV.2.2. Plastic anisotropy of textured polycrystals

Deformed aggregates of actual materials usually exhibit more than one ideal orientation. Their plastic properties must therefore be calculated as some particular average over the distribution of grains (or orientations). For this purpose, it is necessary to define the interactions between the individual grains. Sachs [3] took the view that all the grains are subjected to the same macroscopic stress 'direction' (the magnitude of the stress components may differ, however). This assumption does not allow for any accommodation between individual crystals, nor does it permit stress equilibrium to be attained; thus it is not conducive to a satisfactory description of real metals. At the other extreme, Taylor [2] assumed that all the grains deform at the same macroscopic strain rate. The latter approach leads to the better agreement between prediction of the plastic properties and experimental observations. More recently, some mixed boundary condition methods have been proposed in which only a part of the macroscopic strain rate tensor is prescribed, together with the complementary stress components These models, known as the 'relaxed constraint' [98, 100-102] and 'continuous constraint' [110] methods, are intermediate between the Sachs and Taylor approaches. They involve considerations of the change in shape of the grains during deformation, as a result of which some of the conditions regarding the shear components associated with the grain 'edges' can be relaxed.

Only the two extreme deformation models (i.e. Taylor and Sachs) are employed here; they can be considered to indicate the two limits for the effects of grain interaction.

For simplicity, the section that follows will be restricted to the evaluation of R(θ) in rolled sheet. As mentioned above, the strain rate ratio R(θ) is measured in a uniaxial tension test carried out along a direction inclined at an angle θ to the rolling direction (Fig.2.2). It is defined as the ratio of the width to thickness strain rates (Eq. 4.32).

<u>Taylor model</u>

In order to apply the Taylor model, in which all the grains undergo the same strain as the polycrystal, it is useful to characterize the tensile test as follows

$$\underset{\sim}{\sigma}_{(xyz)} = \begin{bmatrix} \sigma_{11} & \sigma_{12} & 0 \\ \sigma_{12} & 0 & 0 \\ 0 & 0 & 0 \end{bmatrix} \qquad \underset{\sim}{\dot{\varepsilon}}_{(xyz)} = \begin{bmatrix} \dot{\varepsilon}_{11} & 0 & 0 \\ 0 & \dot{\varepsilon}_{22} & 0 \\ 0 & 0 & \dot{\varepsilon}_{33} \end{bmatrix} \tag{4 41}$$

This is the condition usually employed when crystallographic Taylor/Bishop and Hill calculations are carried out [11, 16]. However, the possible non-zero value of the shear stress σ_{12} is in contradiction with the boundary condition $\sigma_{12}=0$ related to the free surface of the specimen. Thus Eqs. 4 41 only apply to the interior of the sample. When expressed in terms of vectors and deviator stresses, these relations become :

$$\vec{S}_{(xyz)} = \begin{vmatrix} S_1 \\ S_2 = S_1/\sqrt{3} \\ 0 \\ 0 \\ S_5 \end{vmatrix} \qquad \vec{\dot{\varepsilon}}_{(xyz)} = \begin{vmatrix} \dot{\varepsilon}_1 \\ \dot{\varepsilon}_2 \\ 0 \\ 0 \\ 0 \end{vmatrix} \tag{4 42}$$

The strain rate vector must now be transformed into the crystal axes

$$\dot{\varepsilon}_{i\,(C)} = Q_{ji}\,\dot{\varepsilon}_{j\,(xyz)} \qquad j = 1,2 \tag{4.43}$$

The matrix Q employed for this purpose is given by :

$$Q = \begin{bmatrix} \cos 2\theta & 0 & 0 & 0 & -\sin 2\theta \\ 0 & 1 & 0 & 0 & 0 \\ 0 & 0 & \cos\theta & -\sin\theta & 0 \\ 0 & 0 & \sin\theta & \cos\theta & 0 \\ \sin 2\theta & 0 & 0 & 0 & \cos 2\theta \end{bmatrix} \cdot Q_0 \tag{4.44}$$

where Q_0 is given by Eq. 3.24 and corresponds to $Q(\theta = 0)$. In order to derive the stress components $S_{i\,(C)}$, the normality rule is applied :

$$\dot{\varepsilon}_{i(C)} = \dot{\lambda}\, \partial F(S_j) / \partial S_{i(C)} \qquad i = 1 \text{ to } 5 \tag{4.45}$$

where F is the CMTP yield function, for example Eq. 4.2. For simplicity, only the case of the Hill quadratic (n = 2) yield surface is considered, since a non-integer criterion renders the inversion of the normality rule more difficult (see Appendix IV.2).

Setting the exponent n in the Hill locus equal to two, the strain rate components can be readily deduced

$$\dot{\varepsilon}_{i(C)} = \dot{\lambda}\, A_i\, S_{i(C)} \qquad i = 1 \text{ to } 5 \tag{4.46}$$

with $A_1 = A_2 = 6\alpha$ and $A_3 = A_4 = A_5 = 2\beta$. This leads, equivalently, to

$$S_{i(C)} = \dot{\varepsilon}_{i(C)} / \dot{\lambda} A_i = Q_{ji}\, \dot{\varepsilon}_{j(xyz)} / \dot{\lambda} A_i \qquad i = 1 \text{ to } 5 \tag{4.47}$$

and then to

$$S_{k(xyz)} = Q_{ki} [\, Q_{ji}\, \dot{\varepsilon}_{j(xyz)} / \dot{\lambda} A_i\,] \qquad k = 1 \text{ to } 5 \tag{4.48}$$

Since the function being considered is homogeneous and of degree 2 in the stresses, $\dot{\lambda}$ can be calculated as follows :

$$\dot{W} = S_{i(C)}\, \dot{\varepsilon}_{i(C)} = \dot{\lambda}\, S_{i(C)}\, \partial F(S_j) / \partial S_{i(C)} = 2\dot{\lambda} \tag{4.49}$$

Thus $\quad \dot{\lambda} = S_{i(C)}\, \dot{\varepsilon}_{i(C)} / 2 = S_{k(xyz)}\, \dot{\varepsilon}_{k(xyz)} / 2 \qquad (4.50)$

and $\quad \dot{\lambda} = \dot{\varepsilon}_{k(xyz)}\, Q_{ki} [\, Q_{ji}\, \dot{\varepsilon}_{j(xyz)} / 2\dot{\lambda} A_i\,]$

or $\quad \dot{\lambda} = \{ \dot{\varepsilon}_{k(xyz)}\, Q_{ki} [\, Q_{ji}\, \dot{\varepsilon}_{j(xyz)} / A_i\,] / 2 \}^{1/2} \qquad (4.51)$

When more than one ideal orientation is present, the deviator stress components (Eq. 4.48) are averaged on a volume fraction basis.

The yield stress as well as the strain rate ratio R(θ) can now be calculated as follows : the ratio $\dot{\varepsilon}_1/\dot{\varepsilon}_2$ in Eq. 4.42 is varied until the loading direction $S_{2(xyz)}/S_{1(xyz)} = 1/\sqrt{3}$ derived from Eq. 4.48 is reached. Under these conditions, the complete stress vector is determined (i.e. the yield stress σ_{11} and the shear stress σ_{12}) and the R-value is given in turn by

$$R(\theta) = \dot{\varepsilon}_{yy} / \dot{\varepsilon}_{zz} = (\sqrt{3}\,\dot{\varepsilon}_1 / \dot{\varepsilon}_2 - 1)/2 \tag{4.52}$$

<u>Sachs model</u>

In the case of the Sachs model, the uniaxial tensile test can be characterized in the normal way by the following stress and strain rate tensors :

$$\underset{\sim}{\sigma}_{(xyz)} = \begin{bmatrix} \sigma_{11} & 0 & 0 \\ 0 & 0 & 0 \\ 0 & 0 & 0 \end{bmatrix} \qquad \underset{\sim}{\dot{\varepsilon}}_{(xyz)} = \begin{bmatrix} \dot{\varepsilon}_{11} & \dot{\varepsilon}_{12} & 0 \\ \dot{\varepsilon}_{12} & \dot{\varepsilon}_{22} & 0 \\ 0 & 0 & \dot{\varepsilon}_{33} \end{bmatrix} \tag{4.53}$$

Here the stress direction is imposed on the polycrystal, but not the value of σ_{11} itself. By contrast, $\dot{\varepsilon}_{11}$ is prescribed and $\dot{\varepsilon}_{22}$, $\dot{\varepsilon}_{33} = -\dot{\varepsilon}_{11} - \dot{\varepsilon}_{22}$ and $\dot{\varepsilon}_{12}$ are unknown. The possible non-zero value of $\dot{\varepsilon}_{12}$ (corresponding to the condition $\sigma_{12} = 0$) makes the tensors strictly valid only for long samples. In the five dimensional notation of Eq. 3.9, the deviator stress and strain rate vectors are .

$$\overrightarrow{S}_{(xyz)} = \left| \begin{array}{l} S_1 \\ S_2 = S_1/\sqrt{3} \\ 0 \\ 0 \\ 0 \end{array} \right. \qquad \overrightarrow{\dot{\varepsilon}}_{(xyz)} = \left| \begin{array}{l} \dot{\varepsilon}_1 \\ \dot{\varepsilon}_2 \\ 0 \\ 0 \\ \dot{\varepsilon}_5 \end{array} \right. \tag{4.54}$$

When using this kind of vector, the Taylor deformation model is difficult to apply because both of the strain rate ratios $\dot{\varepsilon}_2 / \dot{\varepsilon}_1$ and $\dot{\varepsilon}_5 / \dot{\varepsilon}_1$ need to be varied simultaneously (see section III.3), leading to extensive computations. By contrast, the Sachs approach can be readily employed in the following way.

First the stress direction S_2 / S_1 is imposed on each grain of the polycrystal with the specimen axes oriented along the θ direction. If the ideal orientation of the grain is {hkl}<uvw>, then the stress vector can be transformed into the crystal axes by means of the matrix $\tilde{Q}$, which is the transpose of Q (Eq. 4.44). In this way

$$\vec{S}_{(C)} = \tilde{Q}\,\vec{S}_{(xyz)} \tag{4.55}$$

so that

$$S_{i(C)} / S_{1(xyz)} = Q(1,i) + Q(2,i)\, S_{2(xyz)} / S_{1(xyz)} \tag{4.56}$$

Since the vector $\vec{S}_{(C)}$ must terminate at the yield surface specified by Eq 4.2, the following relation applies ·

$$\begin{aligned} S_{1(xyz)} = \{ & \alpha\, 2^{-n/2} [\, |2S_{1(C)} / S_{1(xyz)}|^{n} + |(S_{1(C)} + \sqrt{3} S_{2(C)}) / S_{1(xyz)}|^{n} \\ & + |(S_{1(C)} - \sqrt{3} S_{2(C)}) / S_{1(xyz)}|^{n} + 2\beta 2^{-n/2} [\, |S_{3(C)} / S_{1(xyz)}|^{n} \\ & + |S_{4(C)} / S_{1(xyz)}|^{n} + |S_{5(C)} / S_{1(xyz)}|^{n} \,] \}^{-1/n} \end{aligned} \tag{4.57}$$

When more than one ideal orientation is present, the $S_{1(xyz)}$ values associated with each of them have to be averaged on a volume fraction basis

Thus, the tangent to the overall polycrystal yield surface can be calculated by prescribing three different stress ratios $S_2/S_1 = 1/\sqrt{3}$, $1/(\sqrt{3}-0.01)$ and $1/(\sqrt{3}+0.01)$, fitting a suitable polynomial, and then evaluating the R-value in the θ direction by means of the normality rule.

Both the Taylor and Sachs deformation models will be used in Section V for derivation of the strain rate and yield stress ratios pertaining to rolled and recrystallized metals.

IV.3. PREDICTION OF MACROSCOPIC YIELD SURFACES

One of the objectives of the CMTP method is the derivation of macroscopic yield surfaces from knowledge of the polycrystalline texture. The following sequence is used for this purpose:

(i) The yield surface of a disoriented crystal is assumed to be represented by a CMTP yield function of one of the types described in section IV.1.2.

(ii) For each ideal orientation, this yield surface is reoriented into the testpiece axes by means of the texture information.

(iii) The loci reoriented in this way for the various grains of the aggregate are averaged (on a volume fraction basis) using a suitable deformation model (Taylor, Sachs or intermediate techniques), leading to the overall macroscopic surface.

If the yield function is given by $F(S_{i\,(C)}) = 1$ in the crystal <100> axes, it can be readily expressed in the specimen (S) reference frame by means of the matrix Q (Eq. 3.17). This leads to

$$F(\,Q_{ji}\,S_{j\,(S)}\,) = 1 \tag{4.58}$$

which is the equation of the yield surface in the specimen axes pertaining to a single texture component. When dealing with more than one ideal orientation, these loci are combined :

(i) at constant strain rate ratio (Fig. 4.8a). In this case, all the grains are subjected to the same strain rate as the polycrystal (Taylor model); or

(ii) at constant stress ratio (Fig. 4.8b). The same stress direction is prescribed to each crystal (Sachs technique).

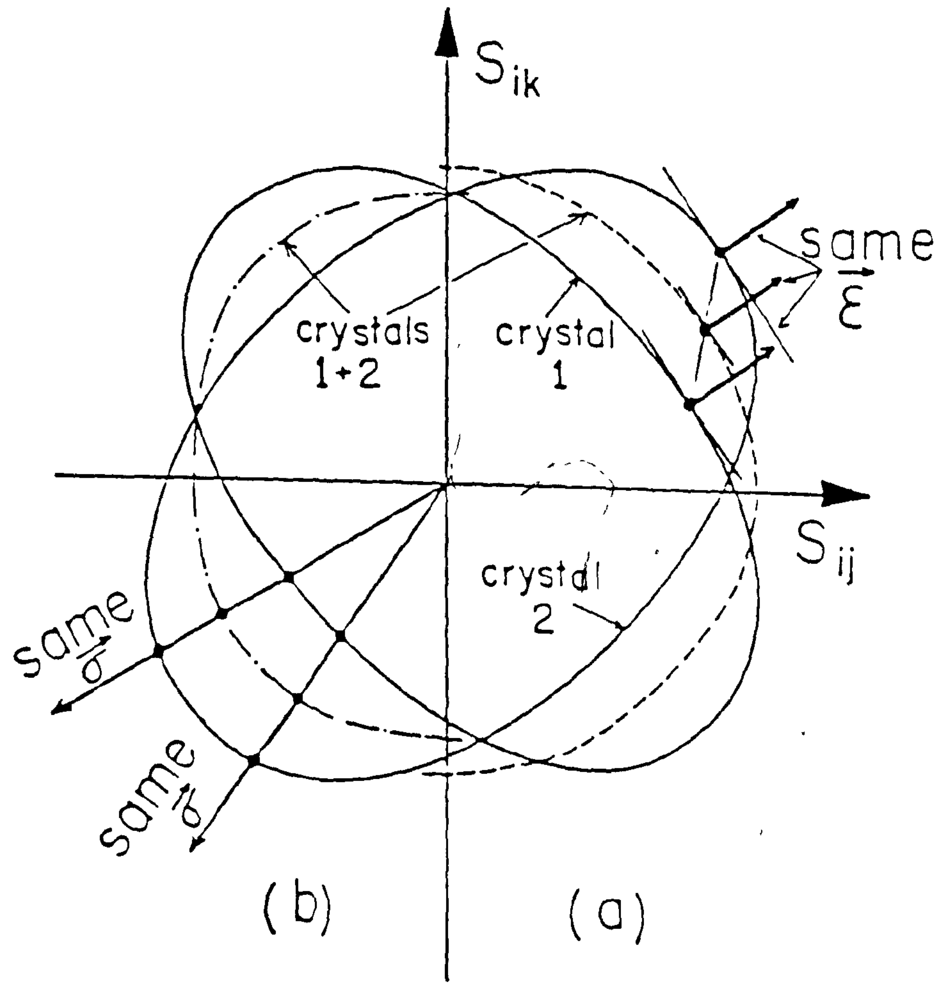

Fig. 4.8 (a) Combination of two yield surfaces by the Taylor method The crystals associated with each of the loci strain at the same rate as the polycrystal.

(b) Combination of two yield surfaces by the Sachs method. The crystals associated with each of the loci experience the same stress direction as the polycrystal.

In each case, the strain rate or stress ratio has to sweep the subspace of interest (shear stress plane, normal stress or π-plane, etc...) by increments, which can be varied depending on the desired accuracy of the polycrystalline locus. Three-dimensional loci are theoretically accessible. However, the necessary two dimensional sweeping (a direction in three dimensional space is characterized by two parameters) renders the computations unrealistically lengthy [111]. For this reason, only planar cross sections of the yield surfaces were calculated in this study, as discussed in Chapter VI.

IV.4. CONTRIBUTION FROM THE RANDOMLY ORIENTED GRAINS

A polycrystalline texture very often cannot be realistically represented by only a finite number of disoriented texture components. As much as 10 to 20% of the grains can remain randomly oriented in many deformed materials, as characterized by the more or less uniform 'background' observed in pole figures. For the present analysis, it is necessary to incorporate the effect of this random background by means of an analytic function representing the yield surface of a random polycrystal.

If the crystallographic loci of Figs. 3.6g and 3.7g (random aggregate) are compared to the continuum surfaces of Figs. 4.2 and 4.3, respectively, the following comments can be made :

(i) In the shear stress plane (S_i, S_j) (i, j=3, 4, 5), the yield locus of a randomly oriented polycrystal can be represented by a quadratic function

$$S_i^2 + S_j^2 = Y_1^2 \qquad i,j=3,4,5 \tag{4.59}$$

(ii) in the π-plane (S_1, S_2), the shape of the crystallographic surface suggests a representation of the form

$$|2S_1|^n + |S_1 - \sqrt{3}S_2|^n + |S_1 + \sqrt{3}S_2|^n = Y_2^n \tag{4.60}$$

Let us first derive the three parameters n, Y_1 and Y_2 . It is well known [6] that the Taylor factors in uniaxial and plane strain tension for a random aggregate are respectively $M_T = 3.06$ and $M_{PST} = 2.86$. This has been confirmed by our calculations (Table III.1). The coefficients n and Y_2 of Eq. 4.60 can be estimated from these two values. Defining the Taylor factor [6] as

$$M = \dot{W} / \bar{\dot{\varepsilon}} \tau_c \tag{4.61}$$

and using the normality rule (Eq. 4.45) at a specific point (S_{i_0}) together with the definition of the equivalent strain rate

$$\bar{\dot{\varepsilon}} = (2/3 \, \dot{\varepsilon}_i \dot{\varepsilon}_i)^{1/2} \tag{4.62}$$

it is readily shown that

$$M(S_{i0}) = \sqrt{\frac{3}{2}} \frac{1}{\tau_c} [\frac{\partial F}{\partial S_i} (S_{i0}) S_{i0}] / [\frac{\partial F}{\partial S_i} (S_{i0})^2]^{\frac{1}{2}} \tag{4.63}$$

Furthermore, if the yield function $F(S_i) = \text{constant} = c$ is homogeneous and of degree n

$$\partial F / \partial S_i (S_j) S_j = n \; c \tag{4.64}$$

leading to

$$M(S_{i0}) = \sqrt{\frac{3}{2}} \frac{1}{\tau_c} n c / [\frac{\partial F}{\partial S_i} (S_{i0})^2]^{\frac{1}{2}} \tag{4.65}$$

Applying this relation to the yield criterion of Eq. 4.60, it is seen that :

for uniaxial tension : $$M_T = \sqrt{3} \, 2^{-1/n} Y_2 / \sqrt{6} \tau_c \tag{4.66}$$

for plane strain tension : $$M_{PST} = 3 (2 + 2^n)^{-1/n} Y_2 / \sqrt{6} \tau_c \tag{4.67}$$

Consequently $$M_{PST} / \sqrt{3} M_T = (1 + 2^{n-1})^{-1/n} \tag{4.68}$$

Substituting for $M_T = 3.06$ and $M_{PST} = 2.86$, it is found that

$$n \approx 9 \tag{4.69}$$

and
$$Y_2 = 1\ 908\sqrt{6}\,\tau_c \tag{4.70}$$

The parameter Y_1 can now be derived by considering some symmetry properties. For this purpose, let us define two sets of axes :

(i) (S_0), in which the π-plane section of the locus pertaining to a random aggregate is given by Eq. 4.60; and

(ii) (S), derived from (S_0) by a matrix Q (Eq. 3.17). By choosing Q in a suitable way ($r_1 = \cos\theta, r_2 = \sin\theta, r_3 = 0, u_1 = -\sin\theta, u_2 = \cos\theta, u_3 = 0, n_1 = n_2 = 0, n_3 = 1$) it can be shown that

$$\begin{cases} S_1 = S_1^0 \cos 2\theta - S_5^0 \sin 2\theta \\ S_2 = S_2^0 \\ S_3 = S_3^0 \cos\theta - S_4^0 \sin\theta \\ S_4 = S_3^0 \sin\theta + S_4^0 \cos\theta \\ S_5 = S_1^0 \sin 2\theta + S_5^0 \cos 2\theta \end{cases} \tag{4.71}$$

From the definition of isotropy, the yield locus in the π-plane, referred to the (S) axes, is given by :

$$\begin{cases} S_3 = S_4 = S_5 = 0 \\ |2S_1|^n + |S_1 - \sqrt{3}S_2|^n + |S_1 + \sqrt{3}S_2|^n = Y_2^{\ n} \end{cases} \tag{4.72}$$

which leads (with $\theta = \pi/4$) to

$$\begin{cases} S_3^0 = S_4^0 = S_1^0 = 0 \\ |2S_5^0|^n + |S_5^0 - \sqrt{3}S_2^0|^n + |S_5^0 + \sqrt{3}S_2^0|^n = Y_2^{\ n} \end{cases} \tag{4.73}$$

This proves the strict equivalence between S_1 and S_5 (and by symmetry S_3 and S_4), i.e. the Taylor factors in plane strain tension and pure shear are identical for the random grain distribution. Applying Eq. 4.65 to the yield criterion of Eq. 4.59, it is seen that

$$Y_1 = M_{PST} / 3\sqrt{6}\tau_c = 0\ 953\sqrt{6}\tau_c \tag{4.74}$$

Furthermore, as shown by Canova et al [11], any of the coordinate axes can be taken as an ∞-fold axis : it therefore appears that the yield surface pertaining to a random aggregate is a sphere in the subspace (S_1, S_3, S_4, S_5).

The locus corresponding to a random polycrystal can thus be described in different subspaces by the following two functions :

<u>Plane (S_2, S_i)</u> i = 1, 3, 4, 5

$$|2S_i|^n + |S_i - \sqrt{3}S_2|^n + |S_i + \sqrt{3}S_2|^n = Y_2{}^n \tag{4.75}$$
$$\text{with } n = 9 \text{ and } Y_2 = 1\ 908\sqrt{6}\tau_c$$

<u>Subspace (S_1, S_3, S_4, S_5)</u>

$$S_1{}^2 + S_3{}^2 + S_4{}^2 + S_5{}^2 = Y_1{}^2 \tag{4.76}$$
$$\text{with } Y_1 = 0.953\sqrt{6}\tau_c$$

A comparison between the π-plane and shear stress plane cross-sections calculated by both the Taylor/Bishop and Hill and the present models is carried out in Fig. 4.9.

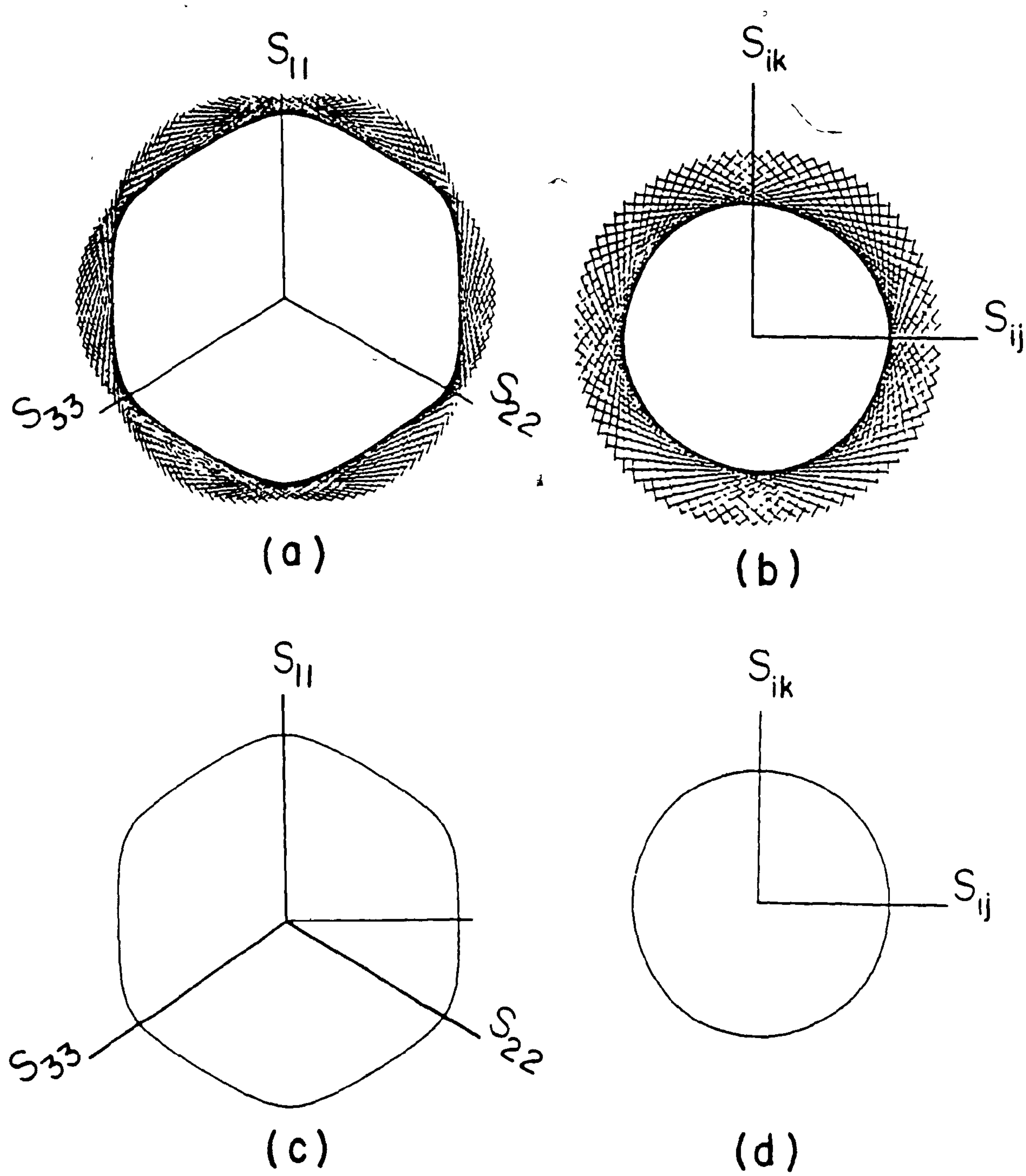

Fig. 4.9 (a-b) Crystallographic yield surface cross-sections associated with a random polycrystal. (a) π-plane; (b) shear stress plane section.

(c-d) Continuum yield surface cross-sections associated with Eqs. 4.75 and 4.76, respectively. (c) π-plane; (d) shear stress plane section.

CHAPTER V

YIELD SURFACES AND PLASTIC PROPERTIES - RESULTS -

In this chapter are reported most of the results obtained by the crystallographic and CMTP methods. In the first section, attention is focussed on the influence of each common experimental ideal orientation on the yield locus of rolled sheet and on its plastic (strain rate) properties. In the second section, the present predictions are extended to polycrystalline textures and compared with experimental data published in the literature.

V.1. YIELD SURFACES AND PLASTIC PROPERTIES FOR COMMONLY OBSERVED IDEAL ORIENTATIONS

V.1.1. Principal ideal orientations observed in rolled or annealed sheets

BCC metals - Rolled BCC metals, such as plain carbon steels, commonly exhibit the $\{111\}<1\bar{1}0>$ and $\{111\}<11\bar{2}>$ components [108, 109, 115-120]. After annealing, two further components, the $\{100\}<011>$ and $\{112\}<1\bar{1}0>$, are generally reported [106, 109, 115]. The above ideal orientations, together with others that are less frequently cited, are collected for reference in Table V.1. An example of a typical experimental texture is reproduced in Fig. 5.1a.

FCC metals - The rolling textures observed in the FCC metals depend on both the stacking fault energy and the homologous temperature. The principal components in the high stacking fault energy metals are $\{112\}<11\bar{1}>$ (the Cu texture), $\{123\}<63\bar{4}>$ (the S component) and $\{110\}<1\bar{1}2>$ (the brass or Bs texture), whereas the $\{110\}<1\bar{1}2>$ (Bs) and $\{110\}<001>$ (Goss) are the most intense in the low stacking fault energy metals [14, 15, 109, 121]. Annealing leads to the appearance of the cube texture $\{100\}<001>$ [14]. These

Metals and characteristics	Textures	Ref.
bcc metals	{100}<011>, {112}<1$\bar{1}$0> {111}<1$\bar{1}$0>, {111}<11$\bar{2}$>	109, 115, 116
Low carbon steel, $\varepsilon_r = 0.96$	{111}<1$\bar{1}$0>, {111}<11$\bar{2}$> {100}<011>	117
Steel	major component {111}<1$\bar{1}$0>	116, 117, 119
Steel 0.2%C	{100}<011>, {112}<1$\bar{1}$0>	120
Al-killed low carbon steel, $\varepsilon_r = 0.64$ at room temp.	{111}<1$\bar{1}$0>, {111}<11$\bar{2}$> {554}<22$\bar{5}$>	108
Al-killed low carbon steel Rimmed steel $\varepsilon_r = 0.95$, annealed at 870°C $\varepsilon_r = 0.99$, annealed at 870°C $\varepsilon_r = 0.99$, annealed at 1090°C	{111}<1$\bar{1}$0> {411}<14$\bar{8}$> {100}<012> {100}<011>, {111}<11$\bar{2}$>	106

Table V.1. Principal ideal orientations observed in rolled or annealed bcc sheet. ε_r is expressed in terms of reduction in height.

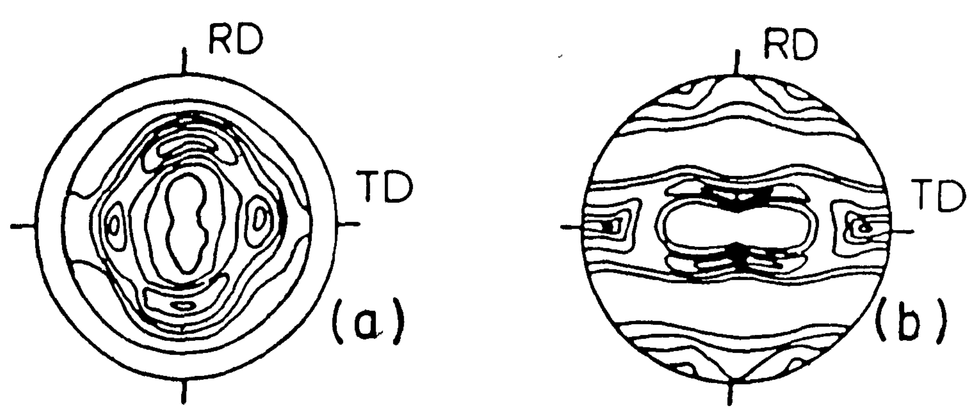

Fig.5.1 (a) Typical {100} pole figure for rolled steel. After [108]. (b) Typical {111} pole figure for rolled FCC metals. After [116].

Metals and characteristics	Textures	Ref.
fcc metals	$\{112\}\langle 11\bar{1}\rangle$, $\{18\ 24\ 51\}\langle 32\bar{2}\rangle$, $\{8\ 12\ 23\}\langle 73\bar{4}\rangle$, $\{135\}\langle 21\bar{1}\rangle$, $\{20\ 35\ 64\}\langle 94\bar{5}\rangle$, $\{146\}\langle 21\bar{1}\rangle$	116, 154, 155
fcc metals high stacking fault energy low stacking fault energy	$\{112\}\langle 11\bar{1}\rangle$, $\{123\}\langle 41\bar{2}\rangle$, $\{110\}\langle 1\bar{1}2\rangle$ $\{110\}\langle 1\bar{1}2\rangle$, $\{110\}\langle 001\rangle$	109
Brass, $\varepsilon_r = 0.96$, room temperature	$\{110\}\langle 1\bar{1}2\rangle$, minor $\{110\}\langle 001\rangle$	116 156
α-brass, $\varepsilon_r = 0.90$, room temperature	$\{110\}\langle 1\bar{1}2\rangle$, $\{123\}\langle 41\bar{2}\rangle$, $\{111\}\langle 1\bar{1}0\rangle$	15
α-brass, annealed 30mn at 350°C	$\{111\}\langle 11\bar{2}\rangle$, $\{110\}\langle 0\bar{1}1\rangle$, $\{110\}\langle 1\bar{1}2\rangle$	14
Al, $\varepsilon_r = 0.96$ at room temperature	$\{146\}\langle 21\bar{1}\rangle$	157
Al, $\varepsilon_r = 0.80$ at room temperature	$\{110\}\langle 1\bar{1}2\rangle$, $\{311\}\langle \bar{1}12\rangle$	32
Al and Cu, $\varepsilon_r > 0.99$	$\{110\}\langle 1\bar{1}2\rangle$	116, 156, 158
Cu	$\{110\}\langle 1\bar{1}2\rangle$, $\{112\}\langle 11\bar{1}\rangle$	116, 159
Cu	$\{135\}\langle 21\bar{1}\rangle$, $\{110\}\langle 1\bar{1}2\rangle$, $\{112\}\langle 11\bar{1}\rangle$	116, 160
Cu, $\varepsilon_r = 0.96$ at room temperature	$\{123\}\langle 41\bar{2}\rangle$, $\{110\}\langle 1\bar{1}2\rangle$, $\{112\}\langle 11\bar{1}\rangle$	116, 157
Cu, $\varepsilon_r = 0.90$ at room temperature	$\{112\}\langle 11\bar{1}\rangle$, $\{123\}\langle 41\bar{2}\rangle$, $\{110\}\langle 1\bar{1}2\rangle$	15
Cu, annealed 30mn at 350°C	$\{100\}\langle 001\rangle$, minor $\{100\}\langle 011\rangle$	14
Gilding metal, $\varepsilon_r = 0.90$ at room temperature	$\{110\}\langle 1\bar{1}2\rangle$, $\{123\}\langle 41\bar{2}\rangle$, $\{111\}\langle 1\bar{1}0\rangle$	15

Table V.2. Principal ideal orientations observed in rolled or annealed fcc sheet. ε_r is expressed in terms of reduction in height.

components, and others less frequently cited, are listed in Table V.2 and a typical experimental texture is reproduced in Fig. 5.1b.

V.1.2. Strain rate and yield strength ratios predicted by the CMTP method for selected ideal orientations.

The strain rate $R(\theta)$ as well as yield strength $\sigma(\theta)/\sigma(0)$ ratios predicted by the CMTP method are now presented for the main ideal orientations observed experimentally. The two types of experiment represented by Eqs. 4.41 (not strictly uniaxial tensile test) and 4.53 (uniaxial tensile test) will be considered in turn to describe the tension test carried out to measure the R-values. The former will be used in conjunction with the uniform strain (Taylor) model, whereas the latter with the uniform stress direction (Sachs) assumption.

In Fig. 5.2, $R(\theta)$ predictions are illustrated for the following orientations : $\{100\}\langle 001\rangle$ (cube), $\{100\}\langle 011\rangle$, $\{100\}\langle 012\rangle$, $\{110\}\langle 001\rangle$ (Goss), $\{110\}\langle 1\bar{1}2\rangle$ (Bs), $\{111\}\langle 1\bar{1}0\rangle$, $\{111\}\langle 11\bar{2}\rangle$, $\{112\}\langle 1\bar{1}0\rangle$, $\{112\}\langle 11\bar{1}\rangle$ (Cu), $\{123\}\langle 41\bar{2}\rangle$, $\{123\}\langle 63\bar{4}\rangle$ (S) and $\{554\}\langle 22\bar{5}\rangle$. Separate sets of predictions are given in Figs. 5.2a to 5.2d for the CMTP Hill quadratic, CMTP Hill n = 1.7, CMTP PL4 and crystallographic yield surfaces, respectively. By ideal orientation, we refer here to a group of *four* sets of Miller indices, as discussed in the previous chapter. The full and dashed lines in Figs. 5.2a to 5.2d represent the predictions obtained by the Taylor and Sachs models, respectively.

It is immediately apparent that the two types of predictions do not differ significantly for most of the cases when the continuum yield functions are involved (Figs. 5.2a to 5.2c). This can be readily explained by the relatively smooth contours of such yield loci; as a result, when the rounded continuum surfaces associated with the four sets of Miller indices are combined, whether at constant stress ratio (Sachs) or at constant strain rate ratio (Taylor), similar overall yielding characteristics are obtained. Nevertheless, as the yield locus becomes more angular (PL4 function, Fig. 5.2c), the difference between the Taylor and Sachs approaches is increased, i.e. there is a stronger dependence of the strain rate characteristics on the stress state and small variations in the

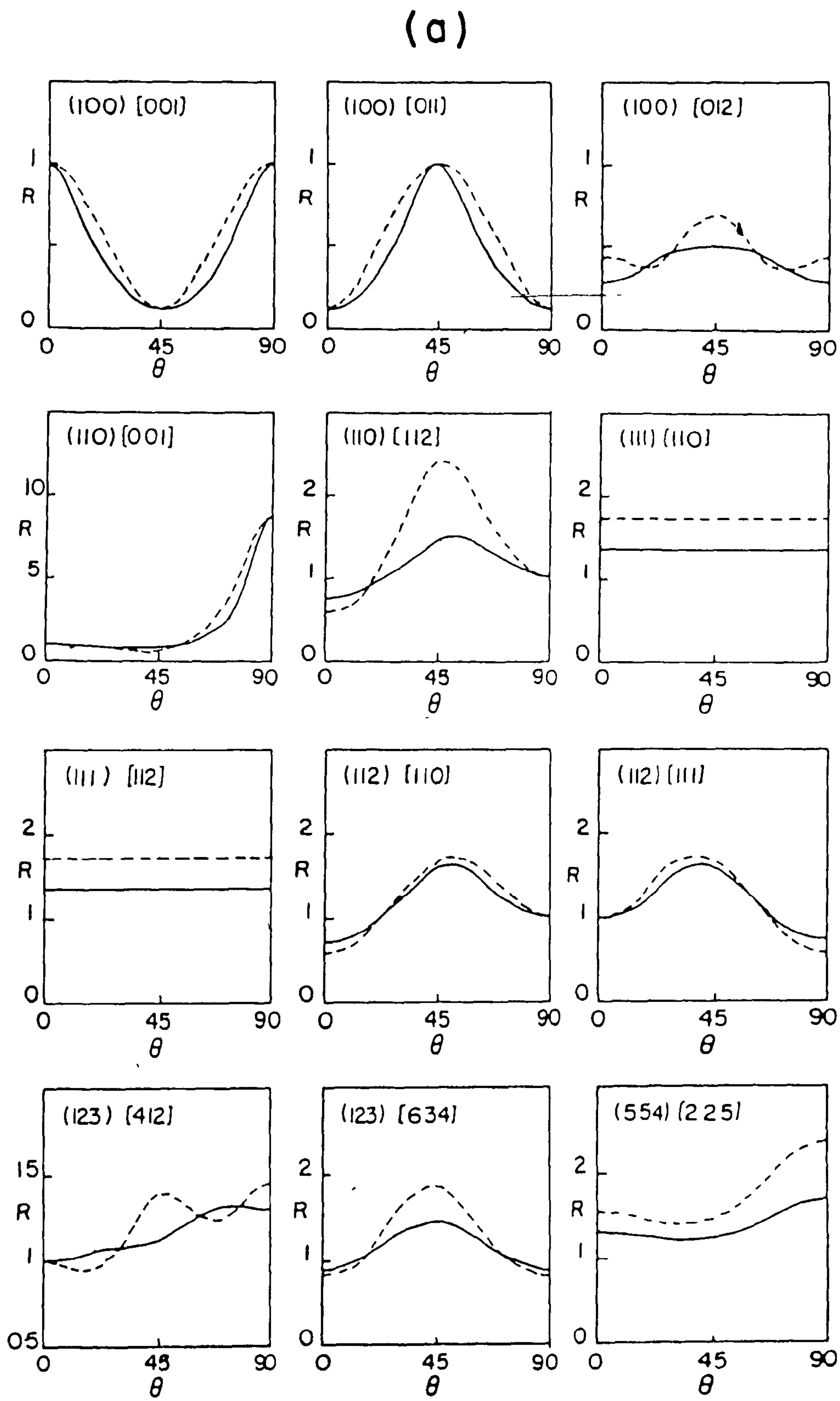

Fig.5.2 Values of R(θ) predicted by the CMTP method for common ideal orientations. The symmetry requirements of the rolling process are taken into account. (——) Taylor uniform strain assumption; (– – – –) Sachs model. (a) CMTP n = 2; (b) CMTP n = 1.7; (c) CMTP PL4 criterion and; (d) crystallographic (Bishop and Hill) approach.

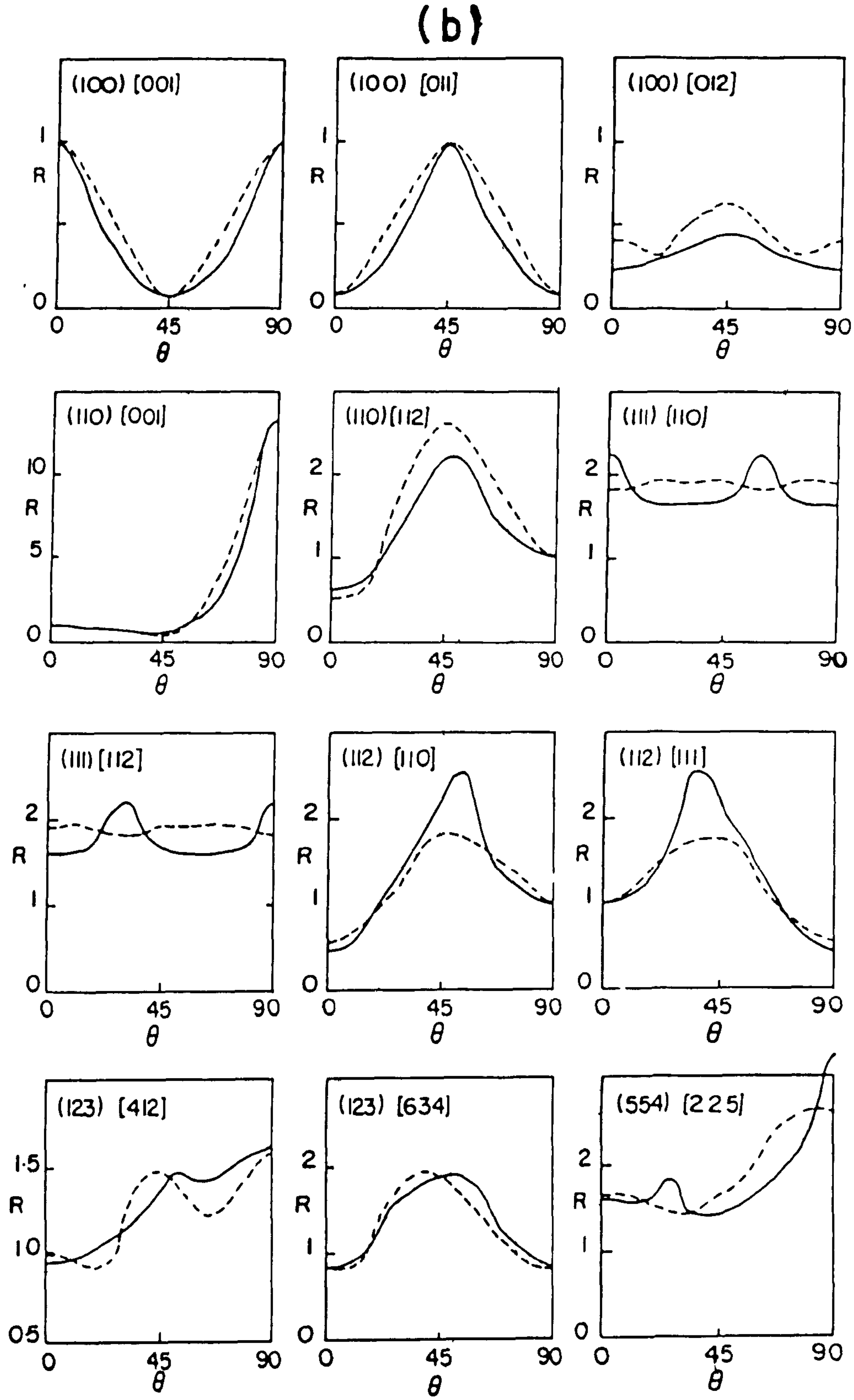

Fig.5.2 Values of R(θ) predicted by the CMTP method for common ideal orientations. The symmetry requirements of the rolling process are taken into account. (——) Taylor uniform strain assumption; (– – – –) Sachs model. (a) CMTP n = 2; (b) CMTP n = 1.7; (c) CMTP PL4 criterion and; (d) crystallographic (Bishop and Hill) approach.

(c)

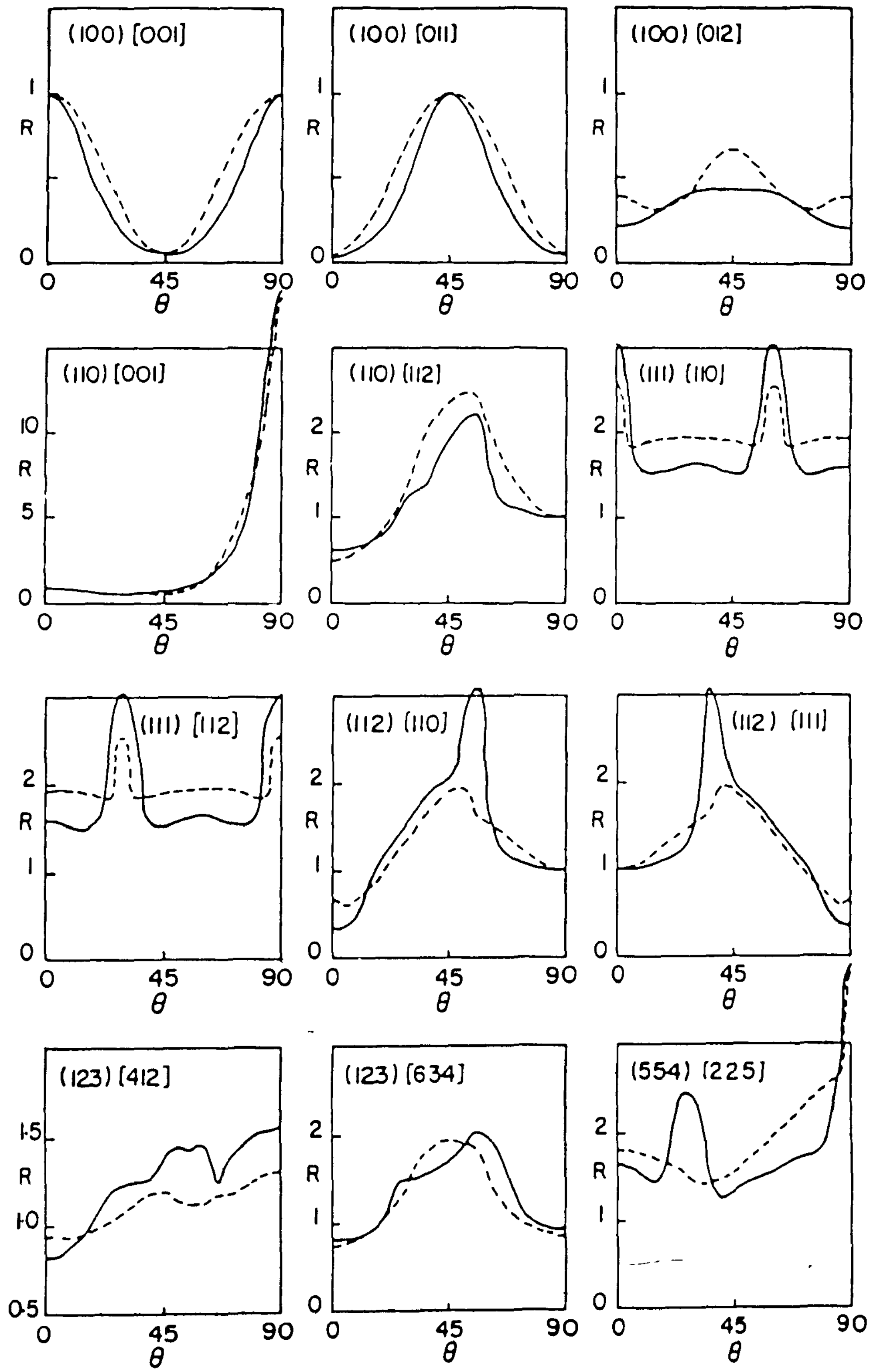

Fig.5.2 Values of R(θ) predicted by the CMTP method for common ideal orientations. The symmetry requirements of the rolling process are taken into account. (——) Taylor uniform strain assumption; (– – – –) Sachs model. (a) CMTP n = 2; (b) CMTP n = 1.7; (c) CMTP PL4 criterion and; (d) crystallographic (Bishop and Hill) approach.

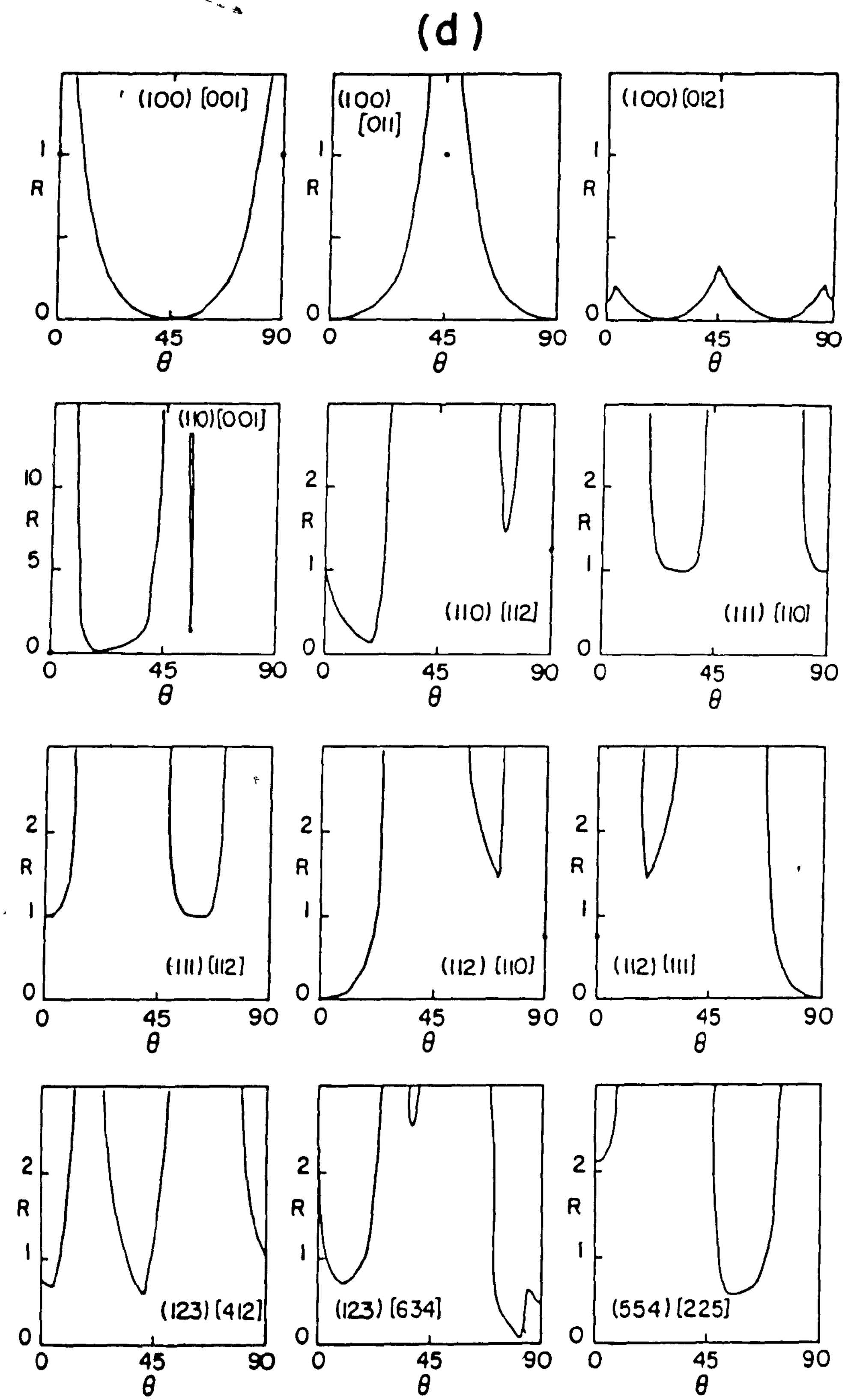

Fig.5.2 Values of R(θ) predicted by the CMTP method for common ideal orientations. The symmetry requirements of the rolling process are taken into account. (——) Taylor uniform strain assumption; (– – – –) Sachs model. (a) CMTP n = 2; (b) CMTP n = 1.7; (c) CMTP PL4 criterion and; (d) crystallographic (Bishop and Hill) approach.

applied stress induce large variations in the strain rate ratio. The strain rate vs stress relationship becomes even more sensitive in the Bishop and Hill model, for which the R-coefficient often attains an infinite and therefore unreasonable value (Fig. 5.2d). This comment is expected to remain valid when calculations are carried out on polycrystalline materials displaying a combination of texture components.

Several features of the dependence of strain rate ratio on ideal orientation are worth noting. These are highlighted below by comparing the Taylor and Sachs predictions obtained from the CMTP $n = 1.7$ criterion with experimental data.

Cube component {100}<001> - All the continuum functions investigated predict a large dependence of R on angle θ for this component. A value of 1 is found in the rolling and transverse directions, whereas the diagonal ($\theta = 45°$) tensile test is characterized by a low expected R-value near 0.1. These predictions are in very good agreement with the experimental data reported by Viana et al. [38] on a very strong cube textured copper sheet (Fig 5.3a).

{100}<011> component - Similar comments can be made for this ideal orientation as it is simply the cube component rotated by $\theta = 45°$ around the normal to the sheet plane. Experimental measurements reported by Parnière and Roesch [122] on iron single crystal sheets led to $R(0) = 0.05$, $R(45) = 1.00$ and $R(90) = 0.04$. These values are also consistent with the CMTP predictions (Fig. 5.3b).

{100}<012> component - This unique orientation is produced experimentally in cold rolled and annealed low carbon steel sheets [106]. As shown in Fig. 5.3c, the CMTP predictions obtained with the $n = 1.7$ criterion (as well as with the other continuum functions, see Fig. 5.2) are in good agreement with the experimental points.

Goss component {110}<001> - The general shape of the $R(\theta)$ curve is again similar for the various continuum yield criteria (Fig. 5.2); a high R-value is obtained in the transverse direction, indicative of a high resistance to thinning. Parnière and Roesch [122] reported values of up to 32 at $\theta = 80°$ for iron single

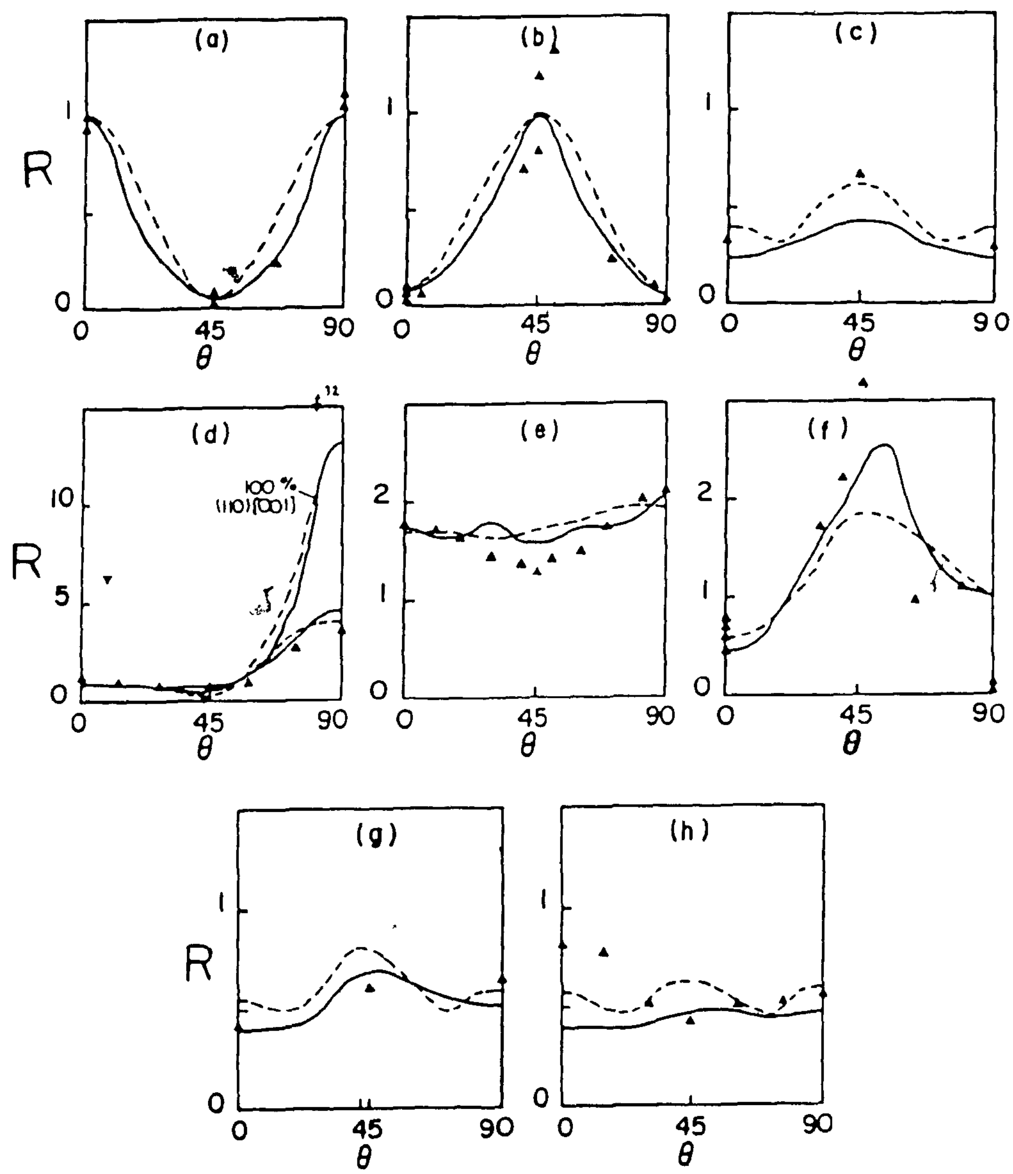

Fig.5.3 Comparison of CMTP predictions ((———) Taylor and (– – – –) Sachs models) and experimental data (▲) for various metals displaying the texture components indicated. The predictions are based on the CMTP n = 1.7 criterion -

(a) copper with a strong $\{100\}\langle 001\rangle$ texture; data from Ref. [38].
(b) iron single crystal sheet - $\{100\}\langle 011\rangle$ orientation; data from Ref. [122].
(c) cold rolled and annealed low C steel - $\{100\}\langle 012\rangle$ orientation; data from Ref. [106].
(d) iron single crystal sheet - $\{110\}\langle 001\rangle$ orientation; data (▼) from Ref. [122]; cold rolled steel sheet : 70% $\{110\}\langle 001\rangle$ + 20% $\{211\}\langle 0\bar{1}1\rangle$ + 10% random components; data (▲) from Ref. [123].
(e) cold rolled and annealed low C steel : 60% $\{111\}\langle uvw\rangle$ + 30% $\{554\}\langle 22\bar{5}\rangle$ + 10% random orientations; data from Ref. [106].
(f) iron single crystal sheet : $\{112\}\langle 1\bar{1}0\rangle$ orientation; data from Ref. [122].
(g) cold rolled and annealed low C steel : $\{411\}\langle 14\bar{8}\rangle$ orientation; data from Ref. [106].
(h) cold rolled steel sheet : $\{511\}\langle 14\bar{9}\rangle$ orientation; data from Ref. [123].

crystals. By contrast, the results of Ito and coworkers [123] fall well below the CMTP predictions (Fig. 5.3d), the best agreement being obtained with the n = 2 criterion, Fig. 5.2a. As their data pertain to a steel having only 70 or 80% of its grains in the Goss orientation, better agreement is observed if the CMTP calculation is modified to include a more realistic distribution of grain orientations : e.g. 70% {110}<001> + 20% {211}<0$\bar{1}$1> +10% random, see Fig. 5.3d.

<u>{111}<uvw> component</u> - This type of texture has been shown experimentally to increase the drawability of steel sheet [124] because it entails the presence of a high average $\overline{R}$-value together with a low planar anisotropy ratio ΔR. These requirements are consistent with the CMTP predictions obtained from the Sachs and to a lesser degree the Taylor models The conditions for optimum drawability as predicted by the CMTP method are discussed in more detail in section V.1.3. Comparison with the R-values corresponding to a cold rolled and annealed low C steel containing a strong {111}<uvw> texture together with the {554}<22$\bar{5}$> component [106] shows that the CMTP method slightly underestimates the variation of R with θ (Fig. 5.3e).

<u>{112}<1$\bar{1}$0> component</u> - The study by Parnière and Roesch [122] of iron single crystal sheets having orientations near the {112}<1$\bar{1}$0> led to experimental R-values of around 0.65 in the rolling direction, between 2 and 3 in the diagonal direction and between 0 and 1 in the transverse direction. These trends are well reproduced by the CMTP predictions (the Taylor results are best), as illustrated in Fig. 5.3f, especially when it is taken into account that the experimental R-values refer to single crystals, which are considerably more anisotropic than highly textured aggregates.

<u>{411}<14$\bar{8}$> component</u> - Fig. 5.3g shows some experimental R data reported by Elias et al. [106] for a low C steel displaying a strong {411}<14$\bar{8}$> texture. The CMTP predictions are in good agreement with the measured values.

<u>{511}<14$\bar{9}$> component</u> - The texture and R-value results of Ito and coworkers [123] pertaining to a cold rolled steel sheet can be used in a similar manner. In this case, the continuum predictions based on the observed strong {511}<14$\bar{9}$> texture underestimate the experimental R-values near the rolling direction

(Fig. 5.3h). However, they predict the overall magnitude of R with reasonable accuracy. Note also the difference in measured R-coefficient between the dependences of Figs. 5.3g and 5.3h, which correspond to similar orientations. This underlines the errors (up to 10 or 20%) that characterize the measurement of strain rate ratio. This is accentuated by the lack of a standard procedure for determining the Lankford coefficient, which leads to additional difficulties when the observations of different workers are being compared: i.e. different strain levels are frequently employed for the definition of R-value.

<u>FCC rolling texture (Bs, Cu and S components)</u> - The Bs, Cu and S ideal orientations are the most commonly observed components in rolled FCC metals. They form the so-called 'rolling tube' in the CODF representation. As can be seen from Fig. 5.4a [125], such a combination of orientations leads to ears at 45°, the presence of which is consistent with our continuum calculations. The relative absence of ears (R = ct) (Fig. 5.4b) can be ensured by balancing these components against another which promotes ear formation at $\theta = 0°$ and 90°. This is done industrially [125] by introducing appropriate quantities of the recrystallization (cube) texture (Fig. 5.4c), whose $R(\theta)$ peaks and troughs are also well reproduced by the CMTP predictions (Fig. 5.2).

<u>BCC rolling texture</u> - The $\{111\}<11\bar{2}>$ and $\{554\}<22\bar{5}>$ orientations commonly appear together in rolled steel sheets. They are very close on a pole figure (Fig. 5.5a) and thus are rather difficult to distinguish. However, it appears from our calculations (see Fig. 5.2) that distinct flow behaviours are predicted for these two orientations, especially when the Hill quadratic criterion (Fig. 5.2a) is used. This underlines the importance of being able to determine with accuracy the presence of the various ideal orientations as well as their respective weights, as can be done with the CODF (crystallite orientation distribution function) method of texture representation. It is also of interest that the PL4 yield function predicts less divergence in the properties of these two close orientations. The experimental R-values reported for a steel [126] having around 50% of $\{554\}<22\bar{5}>$ and 50% of $\{111\}<uvw>$ are compared with the CMTP predictions ($n = 1.7$) for this material in Fig. 5.5b.

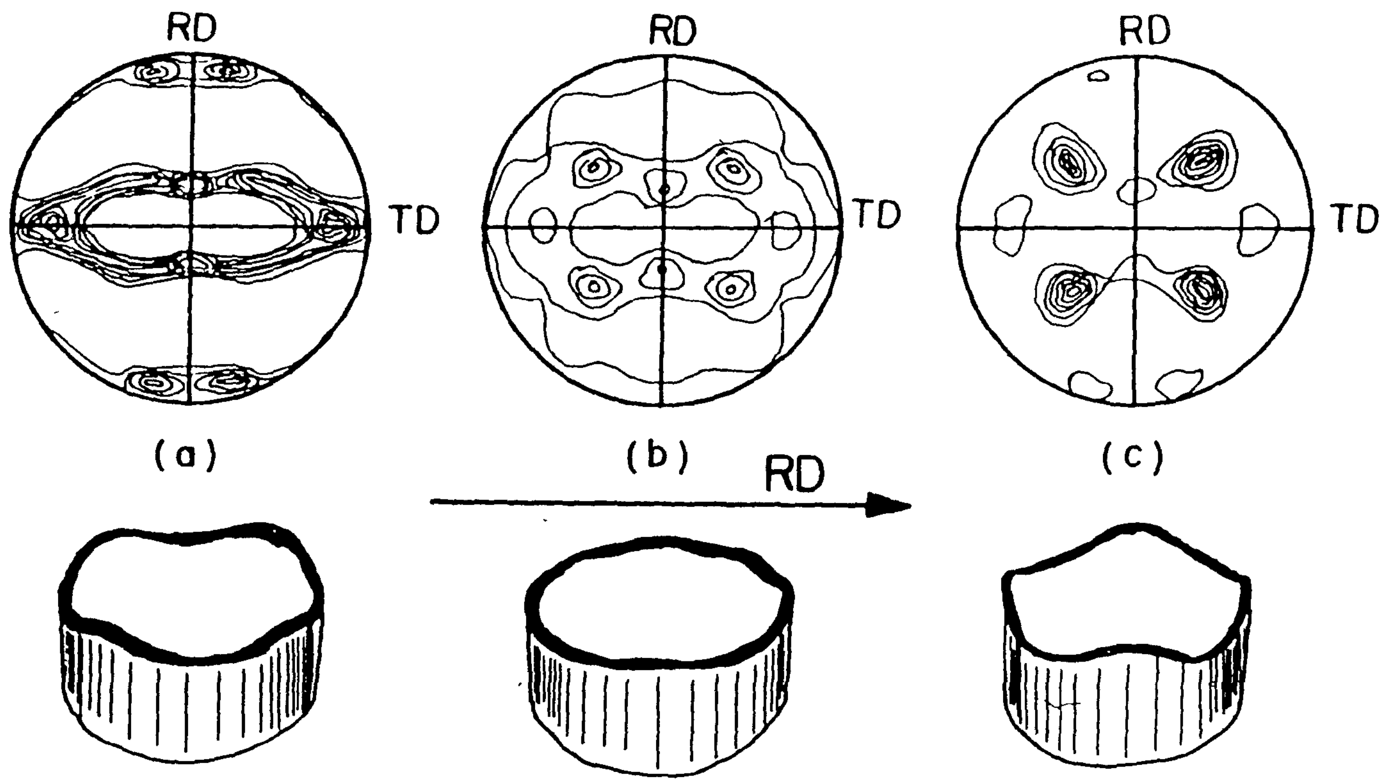

Fig.5.4 Earing in aluminum deep drawn cups as related to their textures ({111} pole figures).

(a) strong cold rolling "tube" texture associated with earing at 45°;

(b) "balanced" eight ear texture with small ear amplitude;

(c) strong cube texture associated with earing at 0 and 90°. Adapted from Ref. [125].

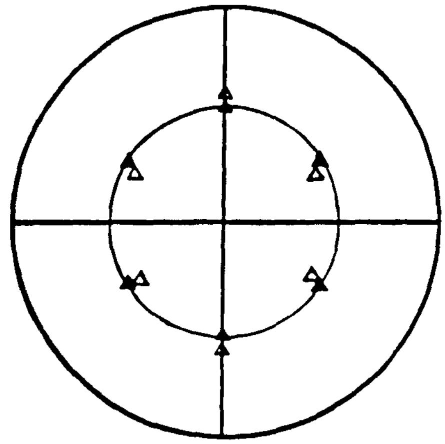

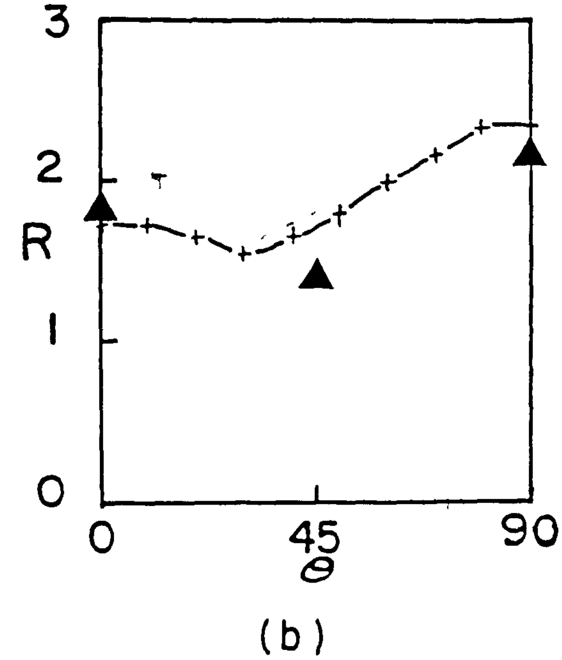

Fig.5.5 (a) {100} pole figure for the {111}<11$\bar{2}$> (▲) and {554}<22$\bar{5}$> (△) orientations.

(b) CMTP (Taylor n=1.7) predictions for a steel containing 50% {554}<22$\bar{5}$> + 25% {111}<1$\bar{1}$0> and 25% {111}<11$\bar{2}$>. Experimental data (▲) from Ref. [126].

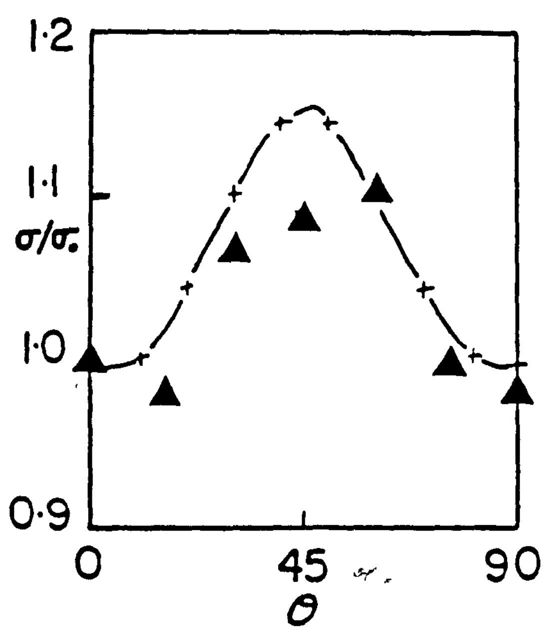

Fig.5.6 CMTP predictions for the yield strength ratio σ(θ)/σ(0) of cube textured copper sheet containing 80% {100}<001> + 20% {100}<011>. Experimental data (▲) from Ref. [14].

Finally, it should be mentioned that the predicted yield strength ratios $\sigma(\theta)/\sigma(0)$ are also consistent with experimental data reported in the literature, as illustrated in Fig. 5.6 for an annealed sheet of cube textured copper [14]. Nevertheless, the predictions seem to slightly overestimate the yield strength ratio in the diagonal direction.

V.1.3. Optimum drawability

As discussed in section II.3.2., the drawability of a metal sheet can be quantified in terms of the $\overline{R}$ and ΔR parameters (Eqs. 2.19 and 2.20). The drawability is strongly influenced by the crystallographic texture [124, 127-129] and it has been shown [124] that, in the case of a steel sheet, the former is enhanced by the presence of a $\{111\}<1\bar{1}0>$ type texture. A high $\overline{R}$ in conjunction with a low ΔR is desirable since they lead to a deeper draw and to less earing, respectively.

Although the $\overline{R}$ and ΔR coefficients have been generally expressed by Eqs. 2.19 and 2.20, somewhat different definitions will be used here, following the work of Meuleman [40]. This modification is related to the observation that a material exhibiting R(0) = 0.5, R(45) = 1.0 and R(90) = 1.5 has the same $\overline{R}$ and ΔR values as a sheet with planar isotropy and R = ct = 1. More rigorous definitions can be given as follows :

$$\overline{R} = \frac{2}{\pi}\int_0^{\pi/2} R(\theta)\, d\theta \tag{5.1}$$

$$\Delta R = \frac{2}{\pi}\int_0^{\pi/2} |\, \overline{R} - R(\theta)\, |\, d\theta \tag{5.2}$$

The latter equation has the advantage of giving a true indication of the extent of planar anisotropy. Furthermore, Eq. 5.1 gives a true average value of the strain rate ratio, even in the case of six or eight ears. A possible development of these expressions leads to, for example :

$$\bar{R} = [\, R(0) + 2R(5) + \quad + 2R(45) + \quad + 2R(85) + R(90) \,] / 36 \tag{5.3}$$

$$\Delta R = [\, |\bar{R} - R(0)| + 2|\bar{R} - R(5)| + \quad . + 2|\bar{R} - R(45)| + \\ + 2|\bar{R} - R(85)| + |\bar{R} - R(90)| \,] / 36 \tag{5.4}$$

These are the equations which were used in our calculations.

In order to determine the texture components which should lead to optimum drawability, random ideal orientations were generated by means of three randomly chosen Euler angles. For each component derived in this way (plus the three symmetrical components mentioned earlier), $\bar{R}$ and ΔR were calculated using the Taylor model. The results are displayed on Fricke diagrams [129] which provide a simple way of plotting ideal orientations, Figs. 5.7 and 5.8.

The CMTP quadratic criterion ($n=2$, $\alpha=0.52$ and $\beta=0.64$) was used in Fig. 5.7 to calculate the average $\bar{R}$ and planar ΔR strain rate ratios. Only the orientations which lead to $\bar{R}>1.35$ together with $\Delta R<0.2$ were retained. No orientation was found to fulfill the more severe condition $\bar{R}>1.40$ and $\Delta R<0.2$. It can be seen from this diagram that optimum drawability is obtained when the crystallographic plane (111) lies in the plane of the sheet, whatever the crystallographic direction (which must lie between the (110) and (112) positions). The calculations also indicate that no other texture component can provide the same combination of properties. This prediction provides quantitative confirmation of the observation which is well known empirically [124]. Similar results were obtained with the new Hill criterion ($n \simeq 1.7$, $\alpha=0.47$ and $\beta=0.54$).

Identical predictions are shown in Fig. 5.8 , which were obtained with the PL4 yield function. In this case, however, the imposed conditions were somewhat more severe : $\bar{R}>1.5$ and $\Delta R<0.2$. The conclusions are the same as those reported for the Hill quadratic criterion, i.e. a {111}<uvw> texture favors the drawability. However, the larger R-values obtained with the PL4 yield function (compared to the $n=2$ locus) can be associated with predictions of

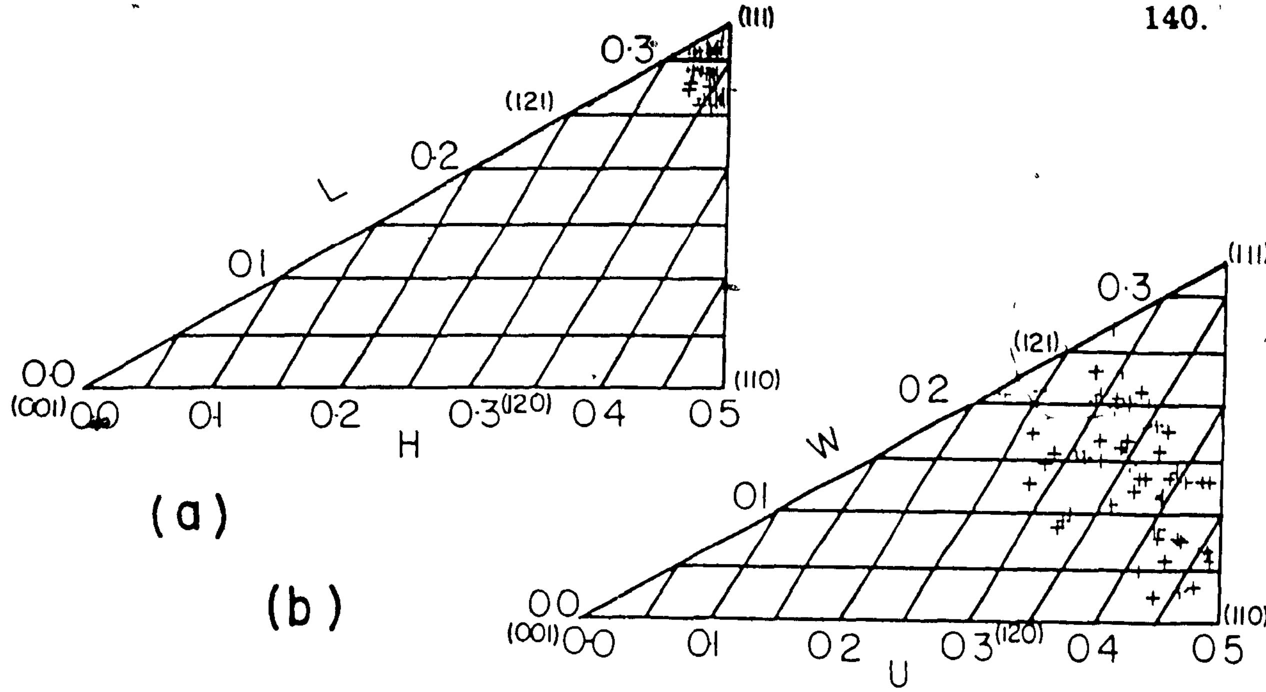

Fig.5.7 Orientations leading to $\bar{R} > 1.35$ together with $\Delta R < 0.2$ as calculated by the CMTP n = 2 criterion. The crystallographic planes (a) and directions (b) associated with these orientatiohs are plotted on Fricke [129] diagrams.

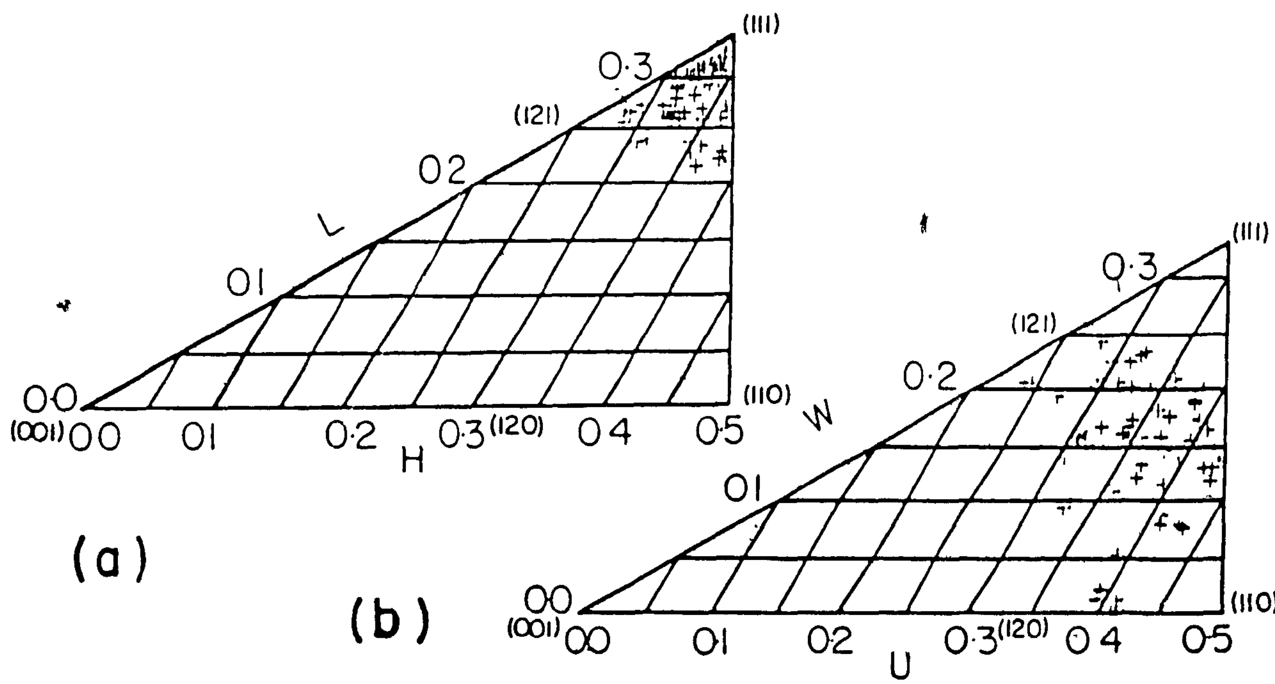

Fig.5.8 Orientations leading to $\bar{R} > 1.50$ together with $\Delta R < 0.2$ as calculated by the CMTP PL4 criterion. The crystallographic planes (a) and directions (b) of these orientations are plotted on Fricke [129] diagrams.

a deeper draw and are closer to the experimental measurements reported in the literature ($\bar{R}_{max} \approx 2$).

By contrast, calculations carried out with the PL3 yield function (Eq. 4.17b) lead to the prediction that the presence of both the (111) and (112) planes will improve drawability. The latter result is not, however, confirmed experimentally. Furthermore the R-values attained with the PL3 criterion are relatively small (maximum of around 1.2).

Since no method was found which permits the application of the Taylor model to the PL1 and PL2 (Eq. 4.17a) functions (because of the problems associated with inversion of the normality rule), only the Sachs approach was used in this case. When such a combination is employed over the four sets of Miller indices $\pm\{hkl\}\pm\langle uvw\rangle$, all the yield functions investigated ($n=2$, $n=1.7$, PL 1, 2, 3 and 4 functions) lead to the necessary $\{111\}\langle uvw\rangle$ texture for optimum drawability.

It was also of interest to investigate the influence of the different experimental ideal orientations on drawability. This is illustrated in Table V.3 for the $n=2$ and PL4 yield functions. it can be seen that the drawability requirements ($\bar{R}$ maximum and ΔR minimum) are best satisfied by the $\{111\}\langle 1\bar{1}0\rangle$ and $\{111\}\langle 11\bar{2}\rangle$ components (observed only in BCC materials) and to a lesser degree by the $\{123\}\langle 41\bar{2}\rangle$ orientation. By contrast, the common FCC deformation and annealing textures (Bs, Cu, Cube, Goss and S) are all intrinsically unsuitable for deep drawing applications. The Goss component, for example, is expected to give rise to a very deep draw (associated with a high $\bar{R}$-value) but concurrently to highly developed ears (associated with a high ΔR-value).

V.1.4. Anomalous behaviour

As already discussed in section II.3.6, the so-called 'anomalous behaviour' refers to a material simultaneously displaying the two properties

Texture component	$\bar{R}$		ΔR	
	n = 2	PL4	n = 2	PL4
$\{100\}\langle 001\rangle$ (cube)	0.461	0.408	0.270	0.288
$\{100\}\langle 011\rangle$	0.461	0.408	0.270	0.288
$\{100\}\langle 012\rangle$	0.403	0.339	0.070	0.073
$\{110\}\langle 001\rangle$ (Goss)	1.943	2.873	1.501	3.041
$\{110\}\langle 1\bar{1}2\rangle$ (Bs)	1.159	1.240	0.219	0.386
$\{111\}\langle 1\bar{1}0\rangle$	1.365	1.814	0	0.357
$\{111\}\langle 11\bar{2}\rangle$	1.365	1.814	0	0.357
$\{112\}\langle 1\bar{1}0\rangle$	1.199	1.400	0.255	0.551
$\{112\}\langle 11\bar{1}\rangle$ (Cu)	1.199	1.400	0.255	0.551
$\{123\}\langle 41\bar{2}\rangle$	1.159	1.263	0.105	0.179
$\{123\}\langle 63\bar{4}\rangle$ (S)	1.157	1.357	0.182	0.372
$\{146\}\langle 21\bar{1}\rangle$	1.085	1.195	0.188	0.358
$\{554\}\langle 22\bar{5}\rangle$	1.365	1.805	0.131	0.389

Table V.3. Average $\bar{R}$ and planar ΔR strain rate ratios (Eqs.5.3 and 5.4) for the main ideal orientations, taking into account the symmetry requirements of Fig. 4.6. $\bar{R}$ and ΔR are calculated from the n = 2 and PL4 yield functions.

$$\overline{R} < 1 \tag{5.5}$$

and
$$\sigma_b / \overline{\sigma_u} > 1 \tag{5.6}$$

These experimental values are in contradiction with the predictions of the classical Hill macroscopic theory which indicates that $\overline{R}$ and $\sigma_b/\overline{\sigma_u}$ should lie on the same side of unity. It is therefore of interest to see if the various CMTP criteria, which are more soundly based from a crystallographic point of view, can explain this anomaly.

A procedure was used which is similar to the one described in the previous section; i.e. random orientations were generated and $\overline{R}$ and $\sigma_b/\overline{\sigma_u}$ values were calculated according to the uniform strain rate model. The Hill quadratic, PL3 and PL4 functions were used for this purpose. For ease of reference, the $\sigma_b/\overline{\sigma_u}$ vs $\overline{R}$ curves predicted by the classical Hill approach ($\sigma_b/\overline{\sigma_u} = (2(1+\overline{R}))^{1/m}/2$ from Eq. 2.49) are reported in Fig. 5.9 together with some experimental measurements. The computational results obtained with the Hill quadratic criterion are shown in Fig. 5.10. It can be seen that such a yield function does not allow for any anomalous behaviour. Furthermore, the calculated points ($\sigma_b/\overline{\sigma_u}$, $\overline{R}$) fall close to the m = 2.0 curve of Fig. 5.9.

When the PL3 function is used (Fig. 5.11a), a less extended $\sigma_b/\overline{\sigma_u}$ vs $\overline{R}$ relationship is observed; in this case, all the simulated orientations lead to R in the range [0.45, 1.2]. However, some of the data can indeed account for the anomalous behaviour, $\overline{R}<1$ and $\sigma_b/\overline{\sigma_u}>1$. They are plotted on a Fricke [129] diagram, Fig. 5.11b, and correspond to orientations having their crystallographic planes near the (011) or (012) planes.

When the PL4 criterion is used, Figs. 5.12a and 5.12b, a smoother and more dispersed version of the $\sigma_b/\overline{\sigma_u}$ vs $\overline{R}$ curve is obtained. It falls just below the m = 1.7 plot of Fig. 5.9. The orientations leading to the anomalous behaviour are shown in Fig. 5.12b and are all concentrated near the (012) plane. This supports the Bishop and Hill calculations carried out by Bassani [76,77] on ideal transversely isotropic textures, as shown in Fig. 5.13.

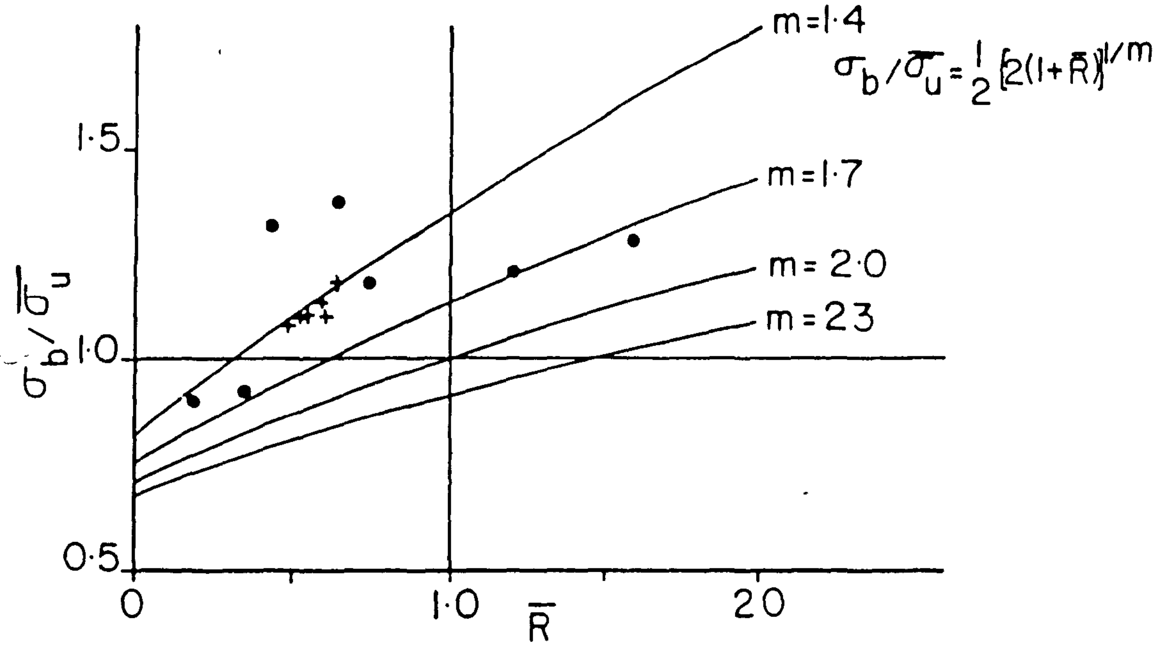

Fig.5.9 Ratio of the biaxial over the average uniaxial yield stress vs $\bar{R}$ as predicted by the Hill non-quadratic yield criterion (Eq. 2.49) for various exponents m. Experimental values from Pearce [50] (●) and Woodthorpe and Pearce [49] (+).

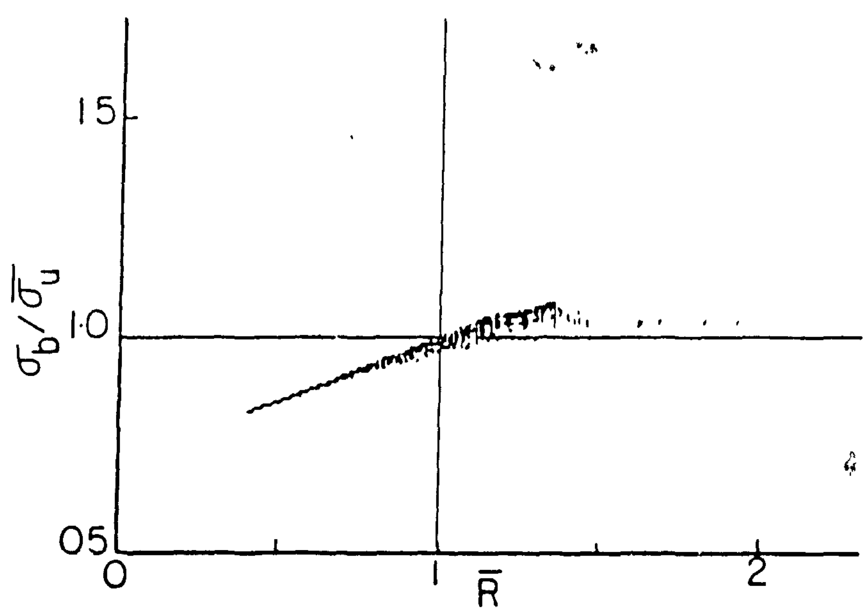

Fig.5.10 Ratio of the biaxial over the average uniaxial yield stress vs $\bar{R}$ as predicted by the CMTP n = 2 criterion for randomly generated orientations.

(a)

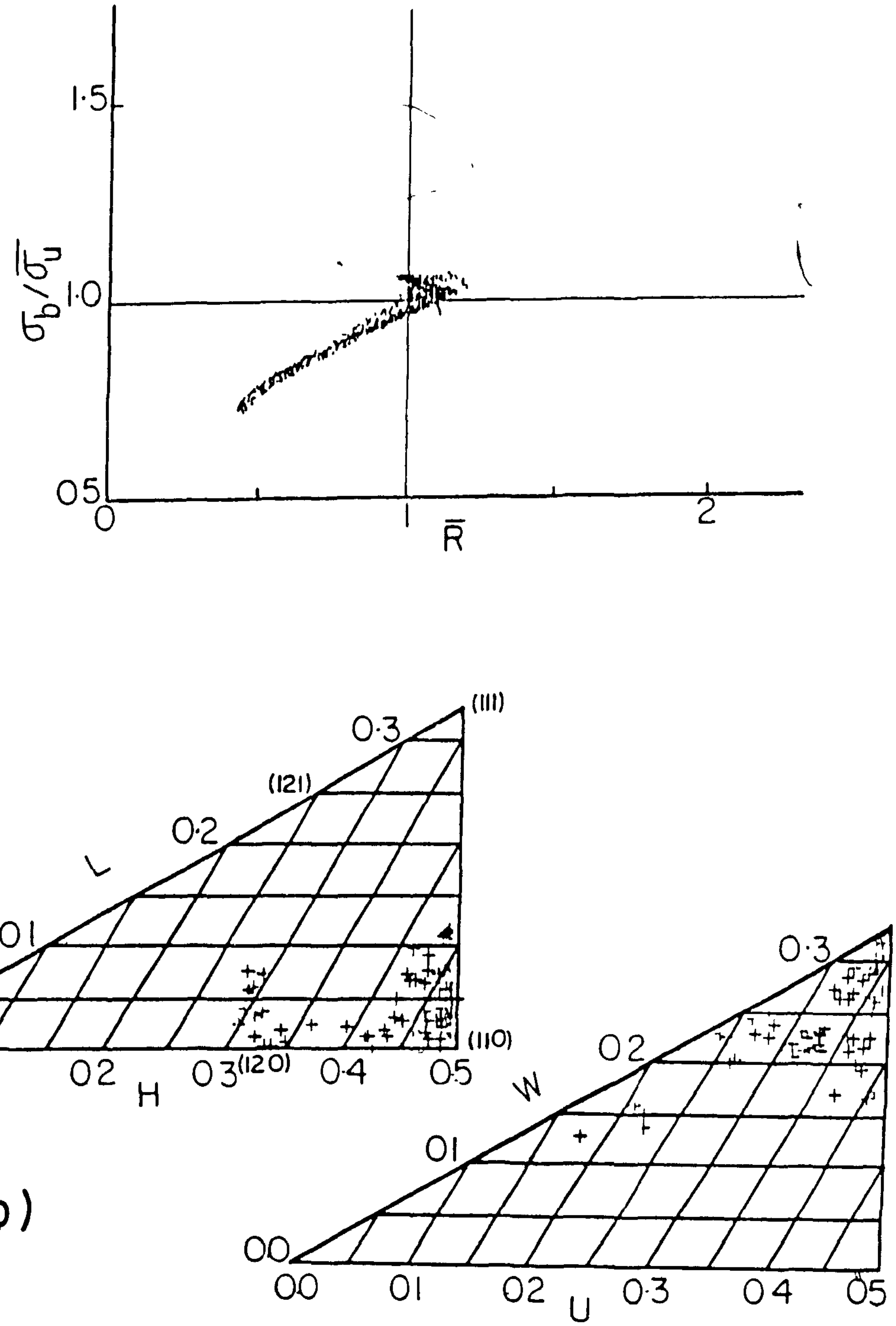

(b)

Fig.5.11 (a) Ratio of the biaxial over the average uniaxial yield stress vs $\overline{R}$ as predicted by the CMTP PL3 criterion for randomly generated orientations.

(b) Crystallographic planes and directions of the orientations leading to $\sigma_b/\overline{\sigma_u} > 1$ together with $\overline{R} < 1$ as predicted by the CMTP PL3 criterion.

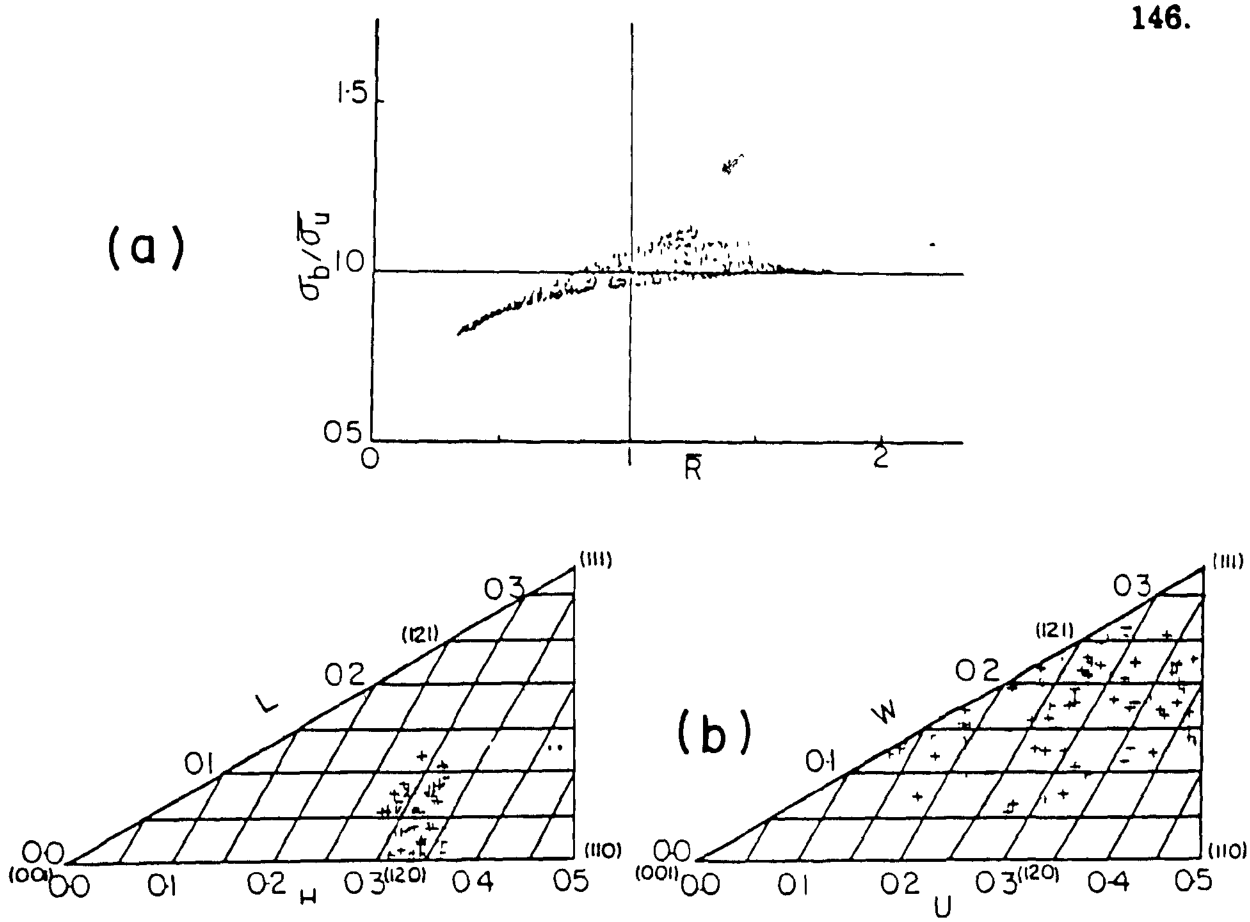

Fig.5.12 (a) Ratio of the biaxial over the average uniaxial yield stress vs $\overline{R}$ as predicted by the CMTP PL4 criterion for randomly generated orientations.

(b) Crystallographic planes and directions of the orientations leading to $\sigma_b/\overline{\sigma_u} > 1$ together with $\overline{R} < 1$ as predicted by the CMTP PL4 criterion.

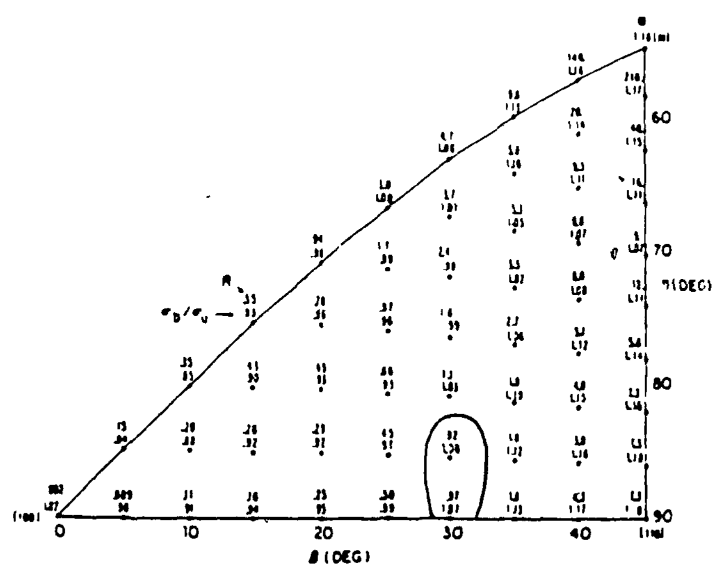

Fig.5.13 **R-values (top number in pair) and $\sigma_{(biaxial)}/\sigma_{(uniaxial)}$ for ideal transversely isotropic textures, as calculated by the crystallographic (Bishop and Hill) model. Each point on the spherical triangle designates an ideal transversely isotropic texture [76,77].**

It should be noted that, to the author's knowledge, no experimental evidence of the textures leading to the anomalous behaviour has been reported in the literature. Thus the present predictions regarding the role of the (012) component remain to be confirmed.

It must also be stated that, although the continuum functions investigated here allow for the anomalous behaviour, they do not reproduce the high σ_b/σ_u values (near 1.3 or 1.4 with $\overline{R} < 1$) reported by Pearce [50] on aluminum. It is of course possible that some *combination* of texture components would lead to such an ensemble of properties.

V.1.5. Axial stresses and length changes in torsion testing

Several papers have been published [91, 130-133] dealing with the axial stresses developed and length changes taking place during torsion testing. The most complete study was carried out by Montheillet and coworkers [133], in which the axial forces induced and the textures developed during fixed end tests were determined for polycrystalline samples of Al, Cu and α-Fe over the temperature ranges 20 to 400, 500 and 800°C, respectively. Depending on the temperature and strain range, the experimental ideal orientations were observed to be rotated about the radial axis either parallel to, or in the sense opposite to, that of the shear. From the evolution of the inclinations with respect to the sample axes, the signs (tension or compression) and magnitudes of the axial stresses were predicted by the CMTP quadratic method and found to be in good agreement with those observed [5].

The length changes reported [91, 130, 131] during the free end torsion testing of metals are not normally correlated with the textures developed. However, the link between the plastic anisotropy and the preferred orientations can also be made explicit by means of the CMTP method, as shown in section IV.2.1. The approach described permits the deviator stress components S_{ij} with respect to the specimen axes to be determined as linear functions of the axial strain rate $\dot{\eta}$ and $\dot{\gamma} = 2\dot{\varepsilon}_{\theta z}$. By means of suitable boundary conditions ($\sigma_{zz} = 0$ for the free end and $\sigma_{rr} = 0$ at the surface), $\dot{\eta}$ and $\dot{\gamma}$ can be linked analytically (Eq. 4.30). Thus $\dot{\eta}$ can be positive, negative or zero; its sign and relative magnitude depend on (i) the particular texture component developed in the material; and (ii) the degree of asymmetry (or inclination) of the relevant ideal orientation with respect to the axial (z) and tangential (θ) directions of the specimen. As an illustration, the CMTP quadratic predictions for the {100}<0vw> texture (i.e. {100} plane parallel to the shear plane of the specimen and <0vw> direction parallel to the shear direction) are shown in Fig. 5.14 [103], together with the experimental data and calculations of Rose and Stuwe [91] relating to the twisting of copper at room temperature. The agreement is reasonable, particularly when it is recognized that a 100% volume fraction of the {100}<0vw> component was employed in the present calculation, whereas the experimental fraction was likely to be somewhat lower.

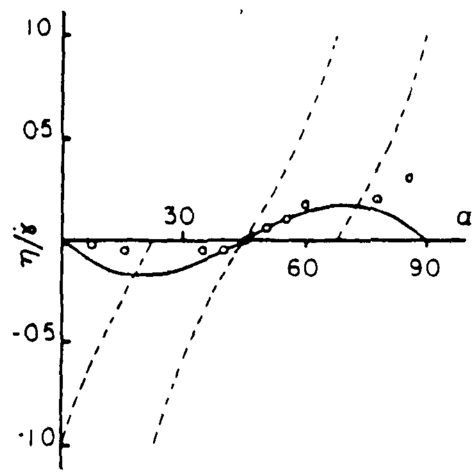

Fig.5.14 Ratio of the elongation strain rate ($\dot{\eta}$) to the torsion or shear strain rate ($\dot{\gamma}$) as a function of the angle α between the (100) and tangential directions for different ideal orientations. (———) CMTP prediction, n = 2; (o) experimental data and (– – – –) theoretical calculations of Ref. [91].

V.1.6. Yield surface prediction

Yield surface cross-sections were calculated following the method described in section IV.3 with the various CMTP functions studied. The experimental results used for comparison purposes are taken from the work of Althoff and Wincierz [63]. Their investigation included three sets of annealed copper tubular specimens having a {001}<100>, {001}<110> or {001}<730> texture (here {hkl} refers to the radial and <uvw> to the axial directions, respectively) and one set of aluminum specimens with a pronounced {112}<$1\bar{1}0$> texture. The experimental points are displayed as solid points in Figs. 5.15 to 5.18. All the yield surfaces (of the uniform strain type) have been normalized to the uniaxial tensile stress in the tangential direction.

Bishop and Hill surfaces (Figs. 5.15a to 5.18a) - As can be seen, the agreement between calculated and experimental surfaces is relatively good for the {100}<001>, {001}<110> and {001}<730> components. Nevertheless, the vertices predicted seem to be too sharp when compared to the apparently more rounded zones of the experimental loci. In the case of the {112}<$1\bar{1}0$> texture, the shape of the experimental yield surface reported by Althoff and Wincierz [63] is better approximated by the Sachs model. It should be added that the first three orientations studied were associated with very small spreads (around $\omega_0 \approx 5°$), whereas the {112}<$1\bar{1}0$> component appears to be more dispersed ($\omega_0 \approx$ 10 to 15°). This suggests that such crystallographic calculations are more appropriate for very strong textures, where the polycrystal can be identified as a 'quasi' single crystal.

Hill quadratic surface (Fig. 5.15b to 5.18b, Eq. 4.9) - As expected from the form of Eq. 4.9, which has to be reoriented for the different ideal orientations of interest, the loci obtained have elliptical shapes. Thus, the rounded corners and flats edges observed in the case of the three above-mentioned components cannot be reproduced in an accurate way, although the general symmetry of the surface is maintained. By contrast, for the locus corresponding to the {112}<$1\bar{1}0$> texture (Fig. 5.18b), an almost perfect fit is obtained. The latter orientation displays a higher experimental scatter (around 10 to 15°) than the cube texture (around 5°). The CMTP $n=2$ function thus seems to be again more suitable for orientations displaying conventional scatter.

CMTP $n=1.4$ surface (Fig. 5.15c to 5.18c, Eq. 4.11) - In this case, much less smooth surfaces are obtained. Good agreement is observed for the cube and {100}<011> textures, which have low experimental scatters. For the

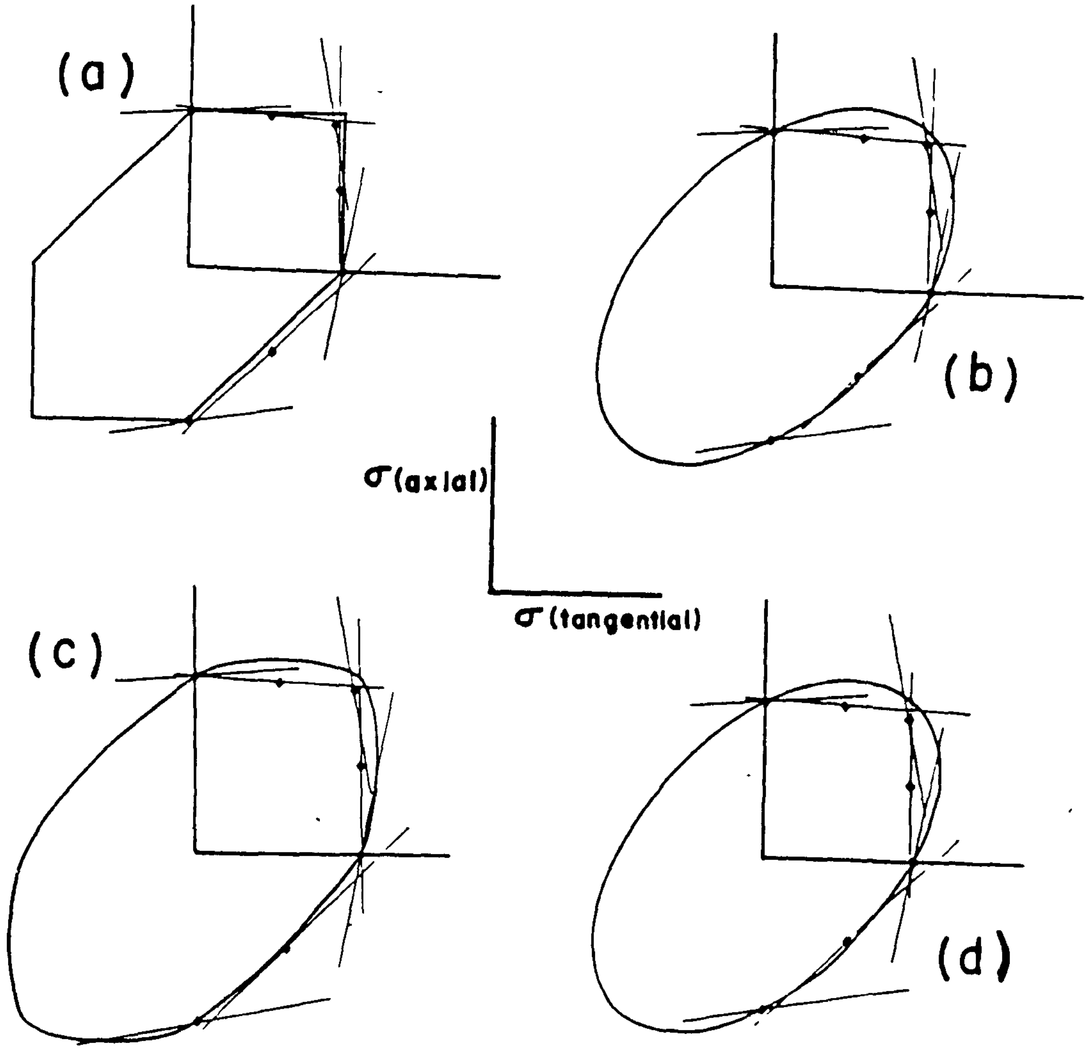

Fig.5.15 Comparison between the experimental ($\sigma_{(tangential)}$,$\sigma_{(axial)}$) yield surface cross-sections of Althoff and Wincierz [63] and the present theoretical predictions for a strong cube texture {100}<001> (orientation spread $\omega_0 \approx 5°$) normalized by the uniaxial tangential yield stress. The Sachs and Taylor models are in this case equivalent. Note that the experimental data are represented by squares and lines for the stress and strain rate characteristics, respectively.

(a) crystallographic (Bishop and Hill) model

(b) CMTP predictions, n = 2

(c) CMTP predictions, n = 1.4

(d) CMTP predictions, PL4 criterion.

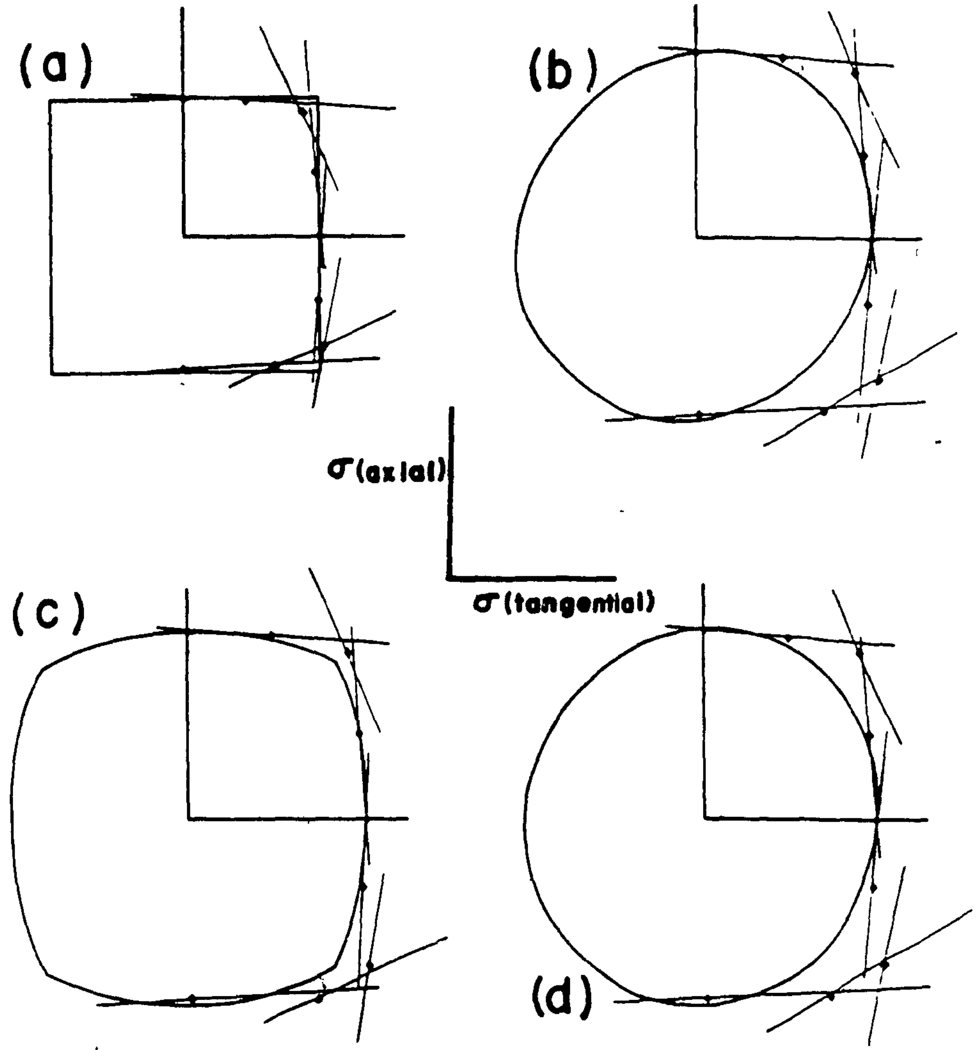

Fig.5.16 Comparison between the experimental ($\sigma_{(tangential)}, \sigma_{(axial)}$) yield surface cross-sections of Althoff and Wincierz [63] and the present theoretical predictions for a strong {100}<011> texture (orientation spread $\omega_0 \approx 5°$) normalized by the uniaxial tangential yield stress. The Sachs and Taylor models are in this case equivalent. Note that the experimental data are represented by squares and lines for the stress and strain rate characteristics, respectively.

(a) crystallographic (Bishop and Hill) model
(b) CMTP predictions, $n = 2$
(c) CMTP predictions, $n = 1.4$
(d) CMTP predictions, PL4 criterion.

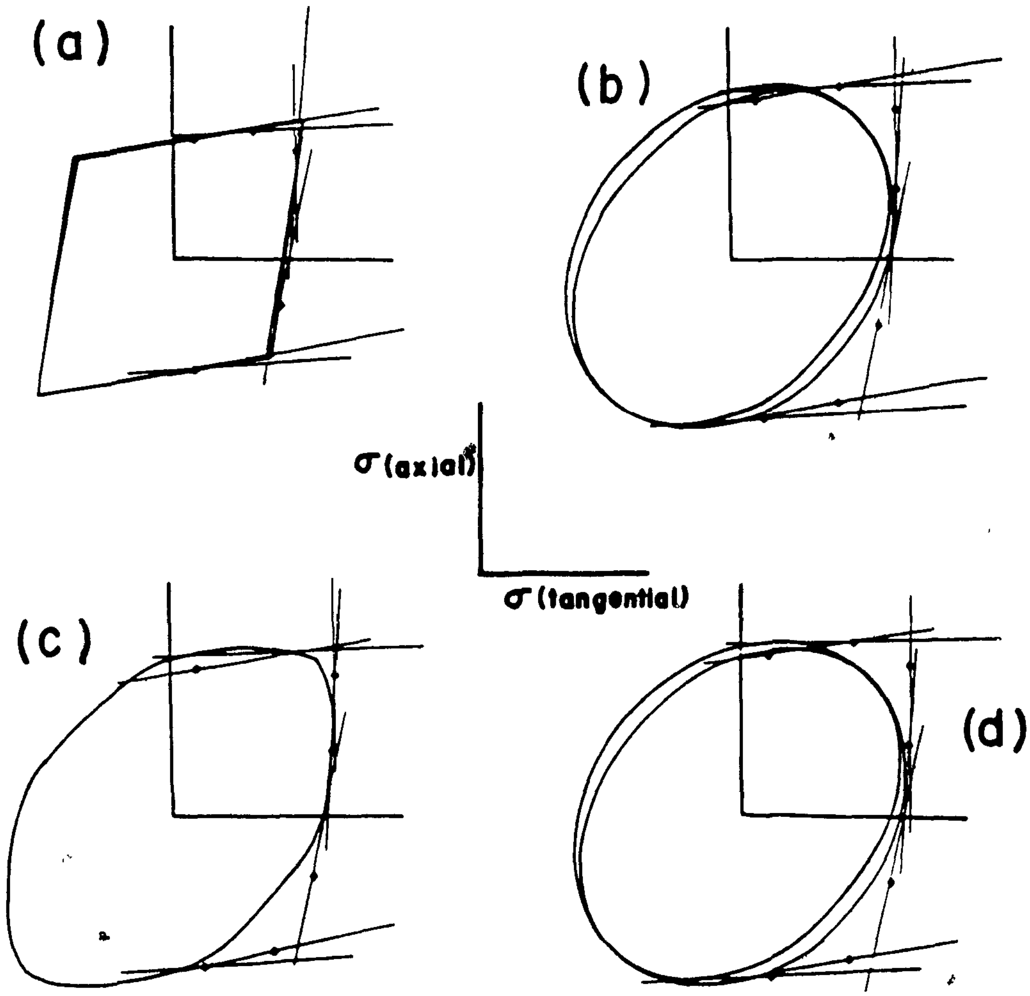

Fig.5.17 Comparison between the experimental ($\sigma_{(tangential)}, \sigma_{(axial)}$) yield surface cross-sections of Althoff and Wincierz [63] and the present theoretical predictions for a strong {001}<370> texture (orientation spread $\omega_0 \approx 5°$) normalized by the uniaxial tangential yield stress. The Sachs and Taylor calculations are displayed as inner and outer loci, respectively. Note that the experimental data are represented by squares and lines for the stress and strain rate characteristics, respectively.

(a) crystallographic (Bishop and Hill) model

(b) CMTP predictions, n = 2

(c) CMTP predictions, n = 1.4

(d) CMTP predictions, PL4 criterion.

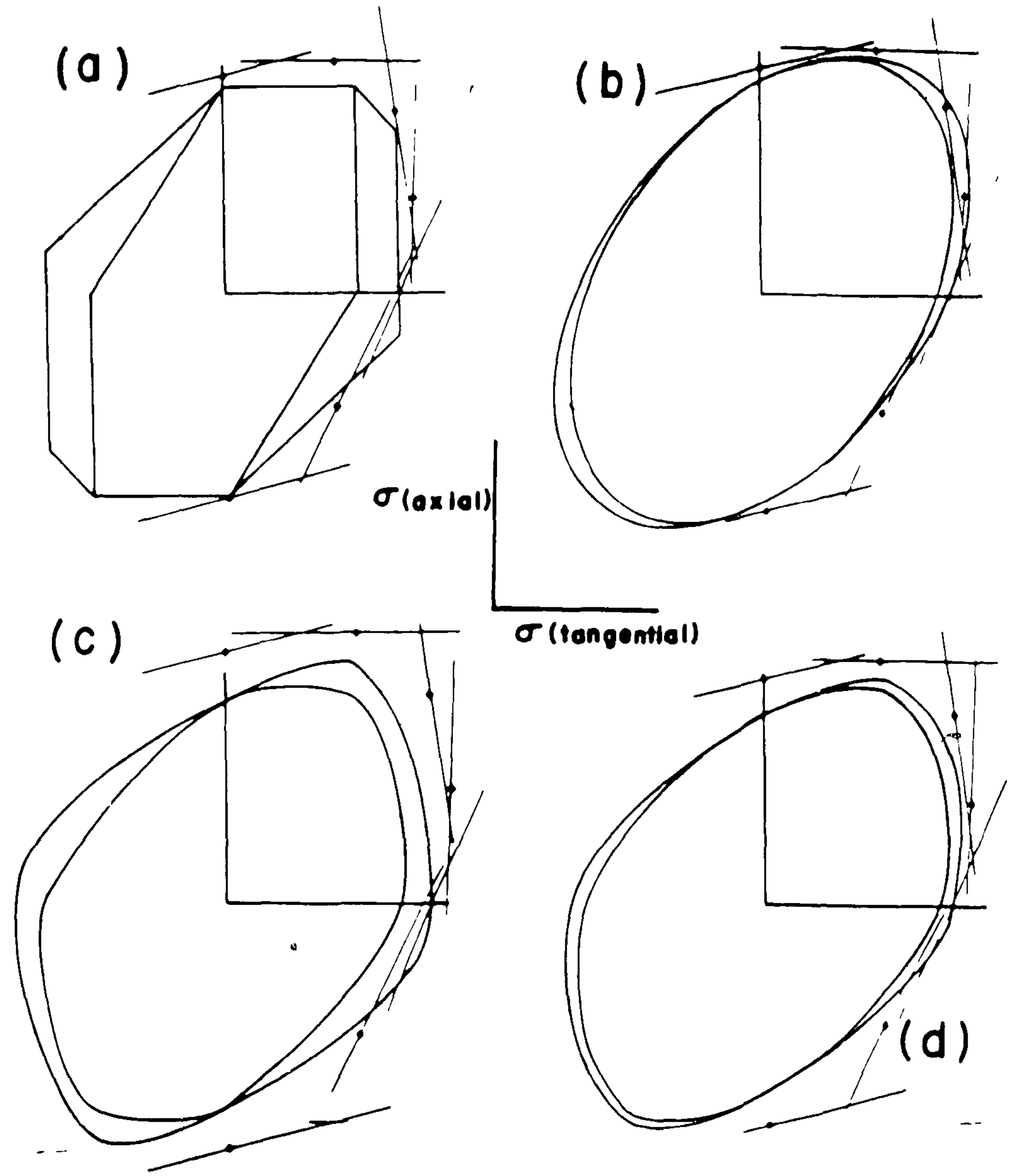

Fig 5.18 Comparison between the experimental ($\sigma_{(tangential)}$,$\sigma_{(axial)}$) yield surface cross-sections of Althoff and Wincierz [63] and the present theoretical predictions for a {112}<$1\bar{1}0$> texture (orientation spread $\omega_0 = 10$ to 15°) normalized by the uniaxial tangential yield stress. The Sachs and Taylor calculations are displayed as inner and outer loci, respectively. Note that the experimental data are represented by squares and lines for the stress and strain rate characteristics, respectively.

(a) crystallographic (Bishop and Hill) model

(b) CMTP predictions, n = 2

(c) CMTP predictions, n = 1.4

(d) CMTP predictions, PL4 criterion.

$\{001\}<730>$ orientation, the curve predicted by the CMTP method approaches the one corresponding to the cube component and underestimates the "pure shear" behaviour ($\sigma_{(axial)} = -\sigma_{(tangential)}$). Finally, the $\{112\}<1\bar{1}0>$ experimental locus does not seem to be well reproduced by either a Taylor or a Sachs model. Both of these underestimate the plane strain ($\dot{\varepsilon}_{(axial)} = 0$ and $\dot{\varepsilon}_{(tangential)} = 0$) vs uniaxial behaviours as well as the ratio of the uniaxial stresses $\sigma_{u(tangential)}/\sigma_{u(axial)}$.

<u>PL4 function</u> (Fig. 5.15d to 5.18d, Eq. 4.17c) - This function has a form similar to that of the Hill quadratic criterion except for some complementary shear components (see Eqs. 4.9 and 4.17) The predictions are thus similar in the case of the three (100) type components. For the $\{112\}<1\bar{1}0>$ orientation, however, the additional shear terms produce a less regular form. The agreement with the experimental points is acceptable, but the plane strain ($\dot{\varepsilon}_{(tangential)} = 0$) vs uniaxial behaviour as well as the uniaxial stress ratio cited above are underestimated.

<u>PL1 and PL2 functions</u> (Eq. 4.17a) - These predictions are not reported here. In both cases, the yield surfaces are smooth and comparable to those obtained with the n=2 or PL4 criterion. However, for the $\{100\}<011>$ component, the PL2 function predicts a rounded square shape rotated 45° (about the radial direction) away from the experimental locus, and is thus in disagreement with it.

As can be seen, no unique surface, whether crystallographic or continuum, is able to predict the whole range of experimental yield loci. Nevertheless, some general trends can be discerned :

- The Bishop and Hill method predicts the shape of the yield surfaces corresponding to highly textured polycrystals (with scatters ω_0 less than 5°) very well.

- The quadratic (or near quadratic) CMTP locus as well as the PL4 function give reasonable fits to yield surfaces corresponding to more scattered orientations, i.e. with spreads of around 15°.

- It seems that there is a relationship between the spread ω_0 and the exponent n in the Hill type of function (Eq. 4.11). A lower exponent ($n = 1.4$, for example) leads to a better approximation of the locus pertaining to highly textured aggregates (e.g. $\omega_0 = 5°$, Figs. 5.15c and 5.16c), whereas an exponent $n = 2$ is more appropriate for more dispersed orientations (e.g. $\omega_0 = 10$ to $15°$, Fig. 5.18b)

- For typical experimental scatters (around 10 to 15°), the best compromise seems to be attained by a Hill type of criterion with an exponent n between 1 4 and 2.0 (say $n = 1.7$) or by the PL4 function (the latter leading to much easier computations).

At this point, it is worth noting that such comparisons between theoretical and experimental two-dimensional surfaces only provide an incomplete assessment of the validity of one method or another A more faithful test would consist of a comparison of the plastic behaviours (which are related to the size and shape of the overall five-dimensional yield locus) in different directions of the workpiece. These can include the strain rate or stress ratios, the biaxial vs uniaxial behaviour, length changes or axial stresses in torsion testing etc..., as shown previously.

V.2. PLASTIC PROPERTIES AND YIELD SURFACES FOR TEXTURED POLYCRYSTALS

In this section, the results of the CMTP predictions for the ideal orientations presented above are generalized to the case of more complex polycrystalline textures in FCC and BCC metals. The first step in this study requires the accurate determination of the distribution of grain orientations in the sample. This can be done approximately by looking at the experimental pole figures and deducing the principal ideal orientations that are present together with their respective volume fractions [134]. This, of course, only leads to a first approximation of the real grain distribution. However, as long as the CMTP yield functions already take into account the scatter around a given texture component observed experimentally, such an estimate may be sufficient for many purposes, as will be seen below. For use of the crystallographic model, more accurate representation of the polycrystalline texture is necessary; in this case, the Bishop and Hill polyhedron represents the yield surface of a 'perfect' single crystal without any misorientation. The complete information needed can be provided by a CODF (crystallite orientation distribution function) analysis (see for example Ref. [16]) which gives the probability that a crystal has a given orientation. The many applications of this method to various kinds of metals (FCC, BCC, HCP...) have proved its ability to give a good representation of the true grain distribution.

In this study, the CMTP calculations were carried out using the decomposition of polycrystalline textures into a finite number (1 to 9 plus the symmetrical components, i.e. 4 to 36) of ideal orientations. For the crystallographic (Bishop and Hill) model, the distribution of the crystals was simulated from CODF data, which were generally found in the form of (i) texture component; (ii) scatter width; and (iii) volume fraction.

V.2.1. Typical rolling and recrystallization textures

V.2.1.1. *Experimental observations*

<u>FCC metals</u> - The sheets of copper and α-brass investigated by Hirsch and coworkers [12] were tested by these authors in three different states : (i) as-rolled (R), (ii) annealed to a partially recrystallized state (P) and (iii) annealed to a fully recrystallized state (F). For ease of reference, their experimental (111) pole figures are reproduced in Fig. 5.19 for the Cu, Cu-5%Zn and Cu-20%Zn metal sheets. The effect of increasing the Zn content and the annealing time (a few minutes for the partially recrystallized and 30 minutes for the fully recrystallized states, respectively) is well illustrated in these pole figures. The typical rolling textures (copper-, transition- and Bs-type) and recrystallization textures (cube component with twins, mixed texture and Bs-type) are seen in the first and third rows of Fig. 5.19, respectively. As expected, the partially recrystallized state leads to an intermediate, and therefore balanced, texture.

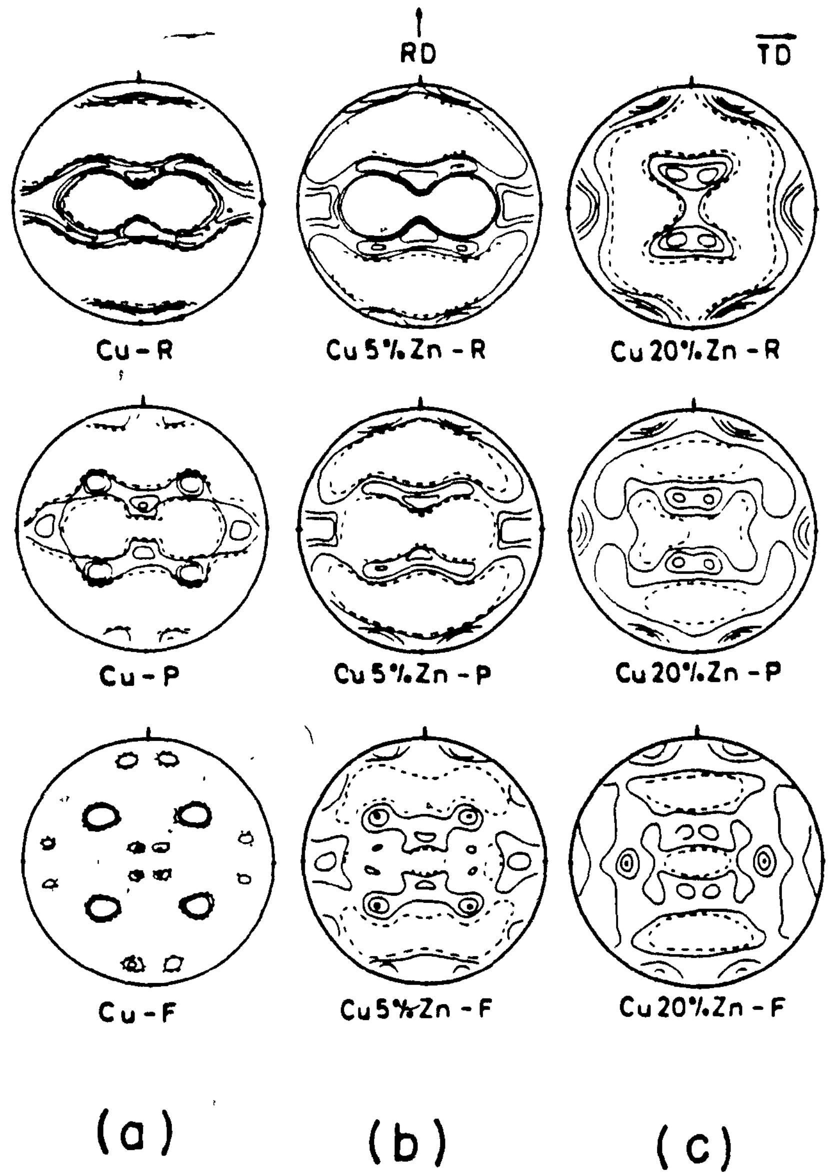

Fig.5.19 Experimental {111} pole figures for rolled and recrystallized sheets. After Hirsch et al. [12]. "R" - as rolled ; "P" - partially recrystallized; and "F" - fully recrystallized materials. (a) Cu; (b) Cu-5%zn; and (c) Cu-20%Zn.

The quantitative analysis based on the published CODF data [12] is reported in Table V.4.

BCC metals - In Fig. 5.20, some typical pole figures are reported for Al-killed and rimmed mild steels, taken from the work of Parnière [135]. These display the classical (111) type texture ($\{111\}<1\bar{1}0>$ and/or $\{111\}<11\bar{2}>$ components), together with some $\{554\}<22\bar{5}>$ and to a lesser degree some of the $\{100\}<011>$ and $\{310\}<001>$ orientations. A detailed ODF analysis was unfortunately not available for these steels. The various texture components present were thus derived only approximately, directly from the pole figures, by taking account of the intensity levels. They are listed in Table V.5.

V.2.1.2. *Texture simulation*

The pole figures shown in Figs. 5.21 and 5.22 were reconstructed (and not predicted) from the texture data pertaining to Figs. 5.19 and 5.20. This operation was carried out in order to check whether the ideal orientation / scatter width / volume fraction method leads to a reasonably faithful reproduction of the experimental distribution of grain orientations in each material. For the copper/brass series, the quantitative analysis of Hirsch et al. [12] reported in Table V.4 was used. Good agreement with the experimental pole figures (Fig. 5.19) is observed. In the case of the rolled steels, the simplified estimates of the ideal orientations, together with their volume fractions and scatter widths, also appear to simulate the experimental pole figures of Fig. 5.20 quite well.

V.2.2. Prediction of polycrystalline yield surfaces

Yield surface cross-sections were calculated for the various grain distributions considered in the previous section. These were performed for both Taylor and Sachs conditions (see Fig. 4.8), and by both the crystallographic as well as the continuum methods.

Texture component	Cu			Cu-5%Zn			Cu-20%Zn		
	(R)	(P)	(F)	(R)	(P)	(F)	(R)	(P)	(F)
Bs-$\{011\}\langle 2\bar{1}1\rangle$	21.5	9.7	–	29.3	27.4	6.25	64.9	32.5	5.9
Cu-$\{112\}\langle 11\bar{1}\rangle$	29.1	7.9	–	19.4	10.7	–	–	–	–
S-$\{123\}\langle 63\bar{4}\rangle$	47.3	22.5	4.3	36.5	43.9	20.6	–	–	–
Goss-$\{011\}\langle 100\rangle$	–	–	–	4.1	2.4	5.8	17.1	14.6	7.5
$\{236\}\langle 38\bar{5}\rangle$	–	–	–	–	–	–	–	48.9	72.7
Cube-$\{100\}\langle 001\rangle$	–	29.7	44.0	–	2.0	7.8	–	–	–
$\{122\}\langle 2\bar{2}1\rangle$	–	17.7	22.1	–	–	–	–	–	–
$\{437\}\langle 18\bar{4}\rangle$ + $\{148\}\langle 74\bar{4}\rangle$ + $\{418\}\langle 74\bar{4}\rangle$	–	–	23.3	–	–	20.8	–	–	–
$\{527\}\langle 12\ 5\ \overline{10}\rangle$ $\{625\}\langle 7\ 9\ \overline{12}\rangle$	–	–	–	–	–	34.1	–	–	–

Table V.4. Volume fractions (%) of the main texture components observed in Cu, Cu-5%Zn and Cu-20%Zn : (R) = rolled; (P) = partially recrystallized; (F) = fully recrystallized. From Ref. [12].

Texture component	Rimmed steel	Al-killed steel
$\{111\}\langle 1\bar{1}0\rangle$	46	54
$\{111\}\langle 11\bar{2}\rangle$	8	16
$\{554\}\langle 22\bar{5}\rangle$	23	30
$\{100\}\langle 011\rangle$	8	0
$\{310\}\langle 001\rangle$	15	0

Table V.5. Volume fractions (%) of the main texture components observed in two grades of steel as estimated from the pole figures of Ref. [135].

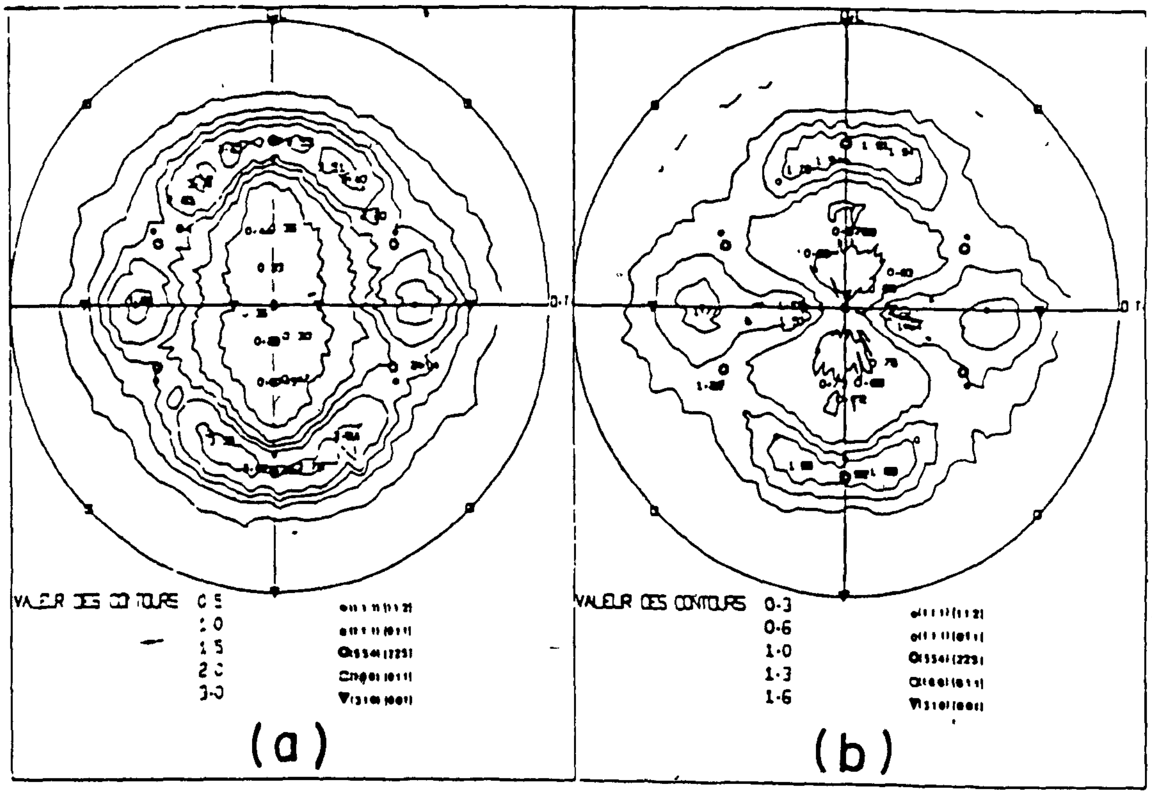

Fig.5.20 Experimental {100} pole figures for rolled and annealed steel sheets. After [135].(a) Al-killed steel ; and (b) rimming steel.

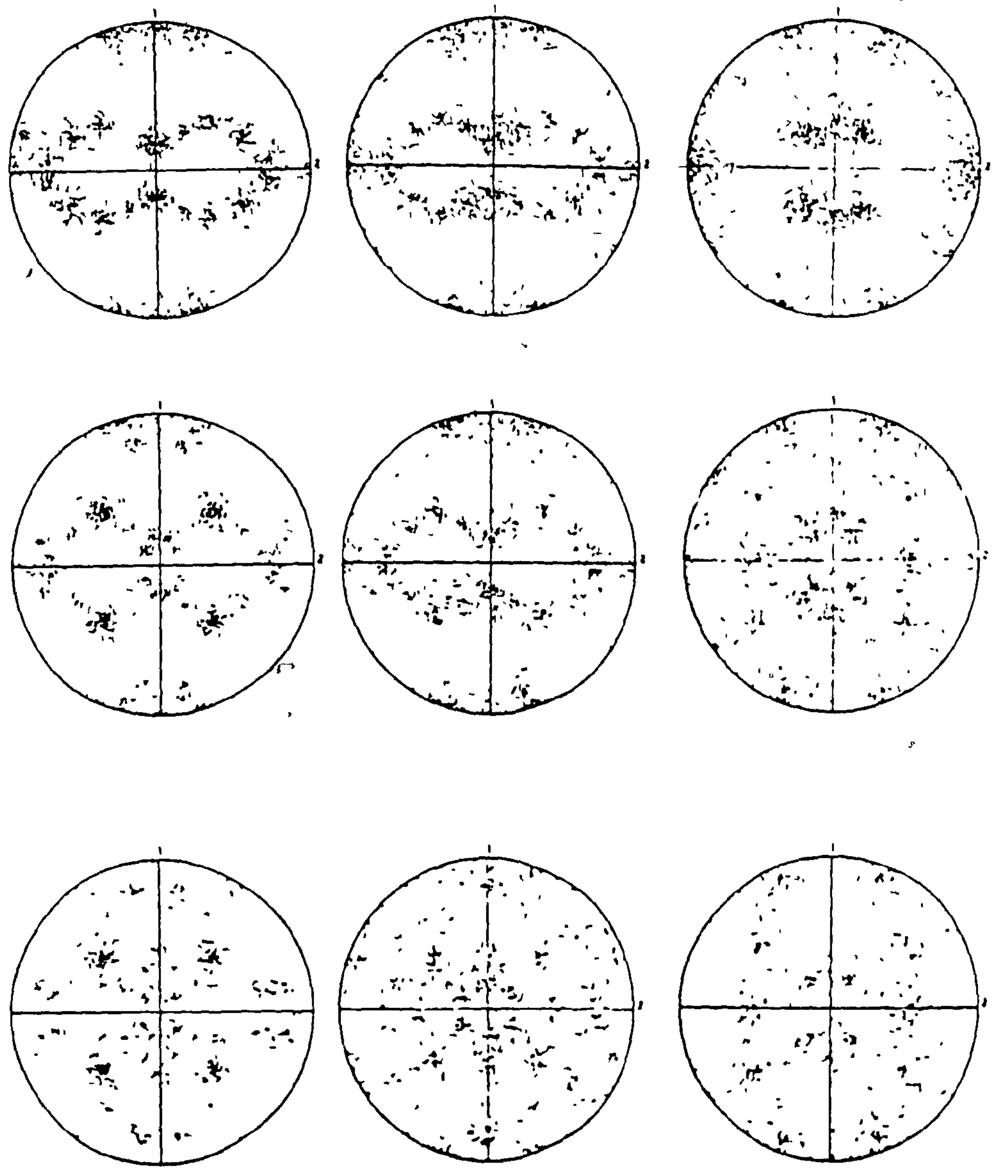

(a) (b) (c)

Fig.5.21 Simulated {111} pole figures (employing about 600 grains) for rolled and recrystallized sheets. Texture data (ideal orientations + volume fractions + spreads) from Hirsch et al. [12] (see also Table V.4). "R" - as rolled ; "P" - partially recrystallized; and "F"- fully recrystallized materials.(a) Cu; (b) Cu-5%Zn; and (c) Cu-20%Zn.

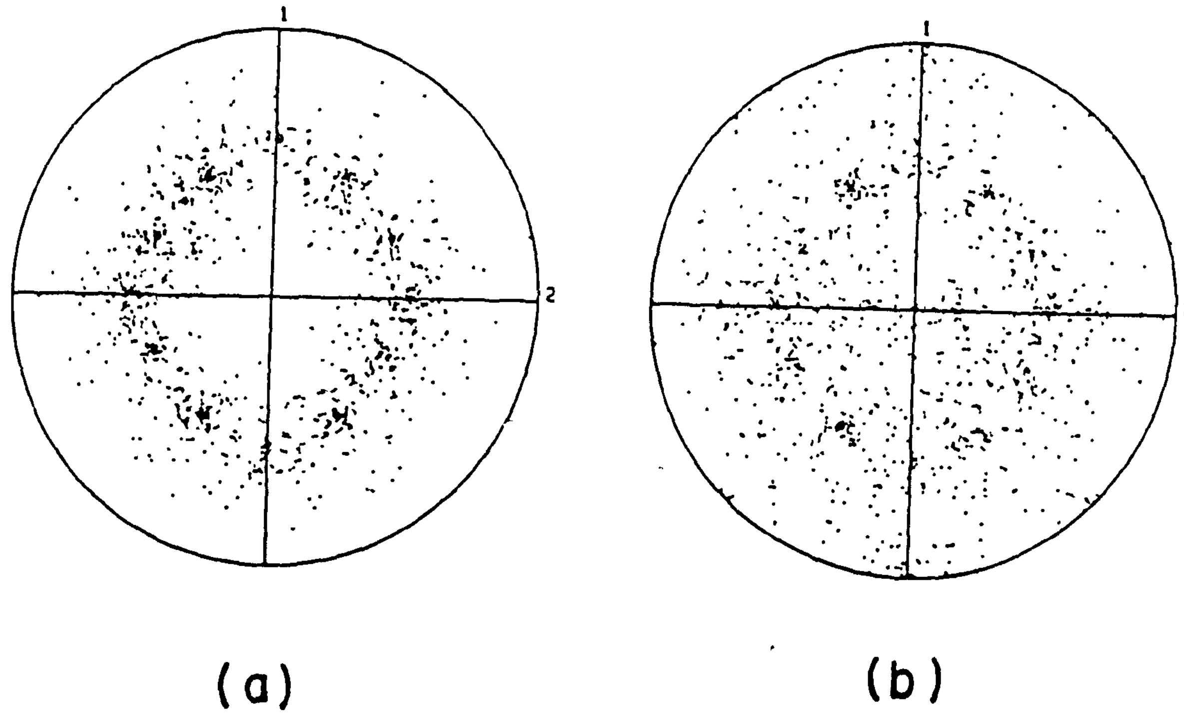

Fig.5.22 Simulated {100} pole figures (employing about 600 grains) for rolled and annealed steel sheets. Texture data (ideal orientations + volume fractions + spreads) estimated from Ref. [135].(a) Al-killed steel; and (b) rimming steel.

V.2.2.1. *Crystallographic calculations*

Taylor averaging - The crystallographic approach is easy to employ under these conditions. The envelope method described in section II was applied to restricted distributions made up of around 200 crystals (symmetry included) (in order to keep the computation time within reasonable limits). The results of some of these computations are shown as outer loci in Fig. 5.23 for the rolled and fully recrystallized copper and brass and in Fig. 5.24 for the two steels. Three θ directions were considered ($\theta = 0$, 22.5 and 45°) for the first series and only two ($\theta = 0$ and 45°) for the second one. These correspond to three and two different positions, respectively, of the S_{11} axis in the sheet plane. S_{22} is associated with the $(\theta + \pi/2)$ direction and S_{33} with the normal to the rolling plane.

The behaviours of the rolled copper and brass (Figs. 5.23a and 5.23b) are completely different because of their differences in texture : the former is characterized by a mix of the Bs, Cu and S components, whereas the Bs component is much stronger than the others in the latter. In the case of the fully recrystallized materials (Figs. 5.23c and 5.23d), the above-mentioned difference is more striking in directions other than the rolling direction ($\theta \neq 0$); in these cases, the copper locus is elongated along the $S_{11} = 0$ direction. Note that the symmetry in S_{11} and S_{22} observed when the axes are oriented 45° away from the rolling direction simply reflects the symmetry of the rolling process. It is of interest that no really sharp edges (corners in the yield surface projection) are obtained with the present method. This contrasts with the predictions of Canova et al.[11] for rolled sheet, which were obtained by means of the full and relaxed constraint methods of texture prediction, and which implied the presence of sharp corners after rolling. The introduction of disoriented grains in our calculations (in the simulated distributions) leads to a smoothing of the overall locus, which is considered to be more faithful to the nature of deformed materials.

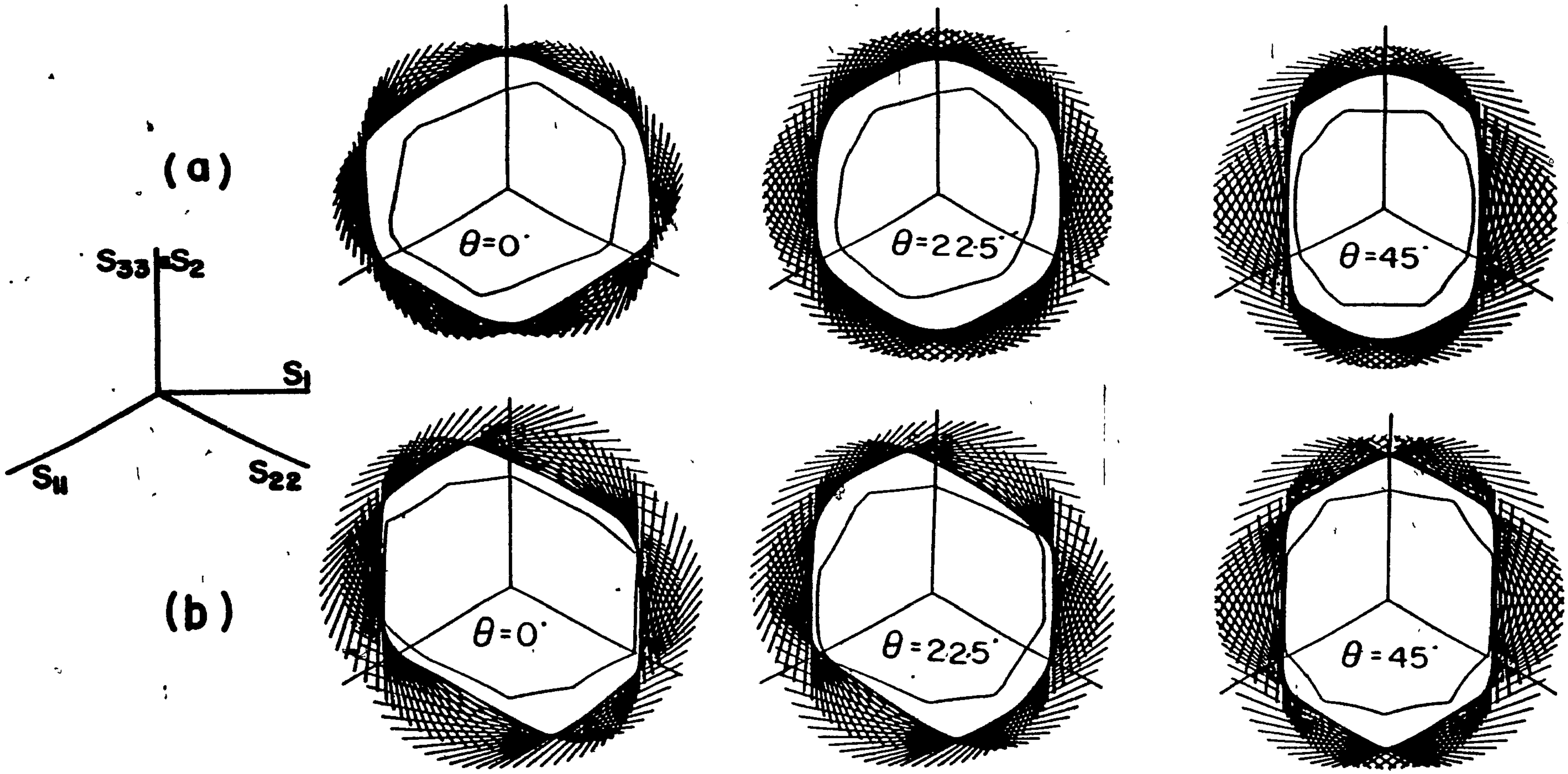

Fig.5.23 Crystallographic π-plane loci calculated for $\theta = 0, 22.5$ and $45°$ for the (a) Cu-R, (b) Cu-20%Zn-R, (c) Cu-F and (d) Cu-20%Zn-F sheets. The outer locus is computed using a classical Taylor (uniform strain) approach with restricted distributions made up of about 200 grains representing each of the pole figures of Fig. 5.19; it corresponds to the inner envelope of the hyperplanes specified by Eq. 3.6. The inner locus is obtained from the combination of loci by the Sachs method using Eqs. 3.25 in conjunction with the texture data of Table V.4.

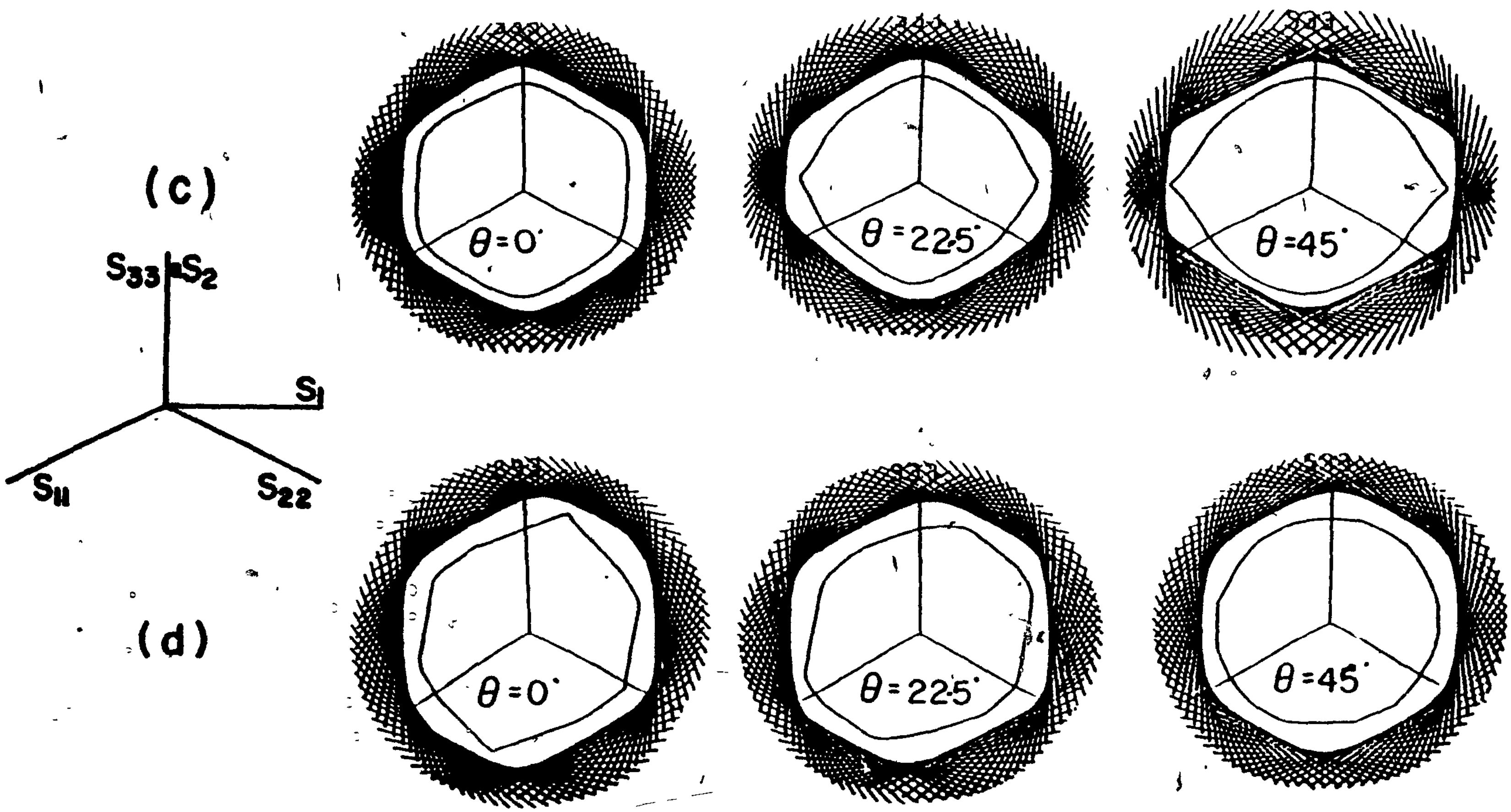

Fig.5.23 Crystallographic π-plane loci calculated for θ = 0, 22.5 and 45° for the (a) Cu-R, (b) Cu-20%Zn-R, (c) Cu-F and (d) Cu-20%Zn-F sheets. The outer locus is computed using a classical Taylor (uniform strain) approach with restricted distributions made up of about 200 grains representing each of the pole figures of Fig. 5.19; it corresponds to the inner envelope of the hyperplanes specified by Eq. 3.6. The inner locus is obtained from the combination of loci by the Sachs method using Eqs. 3.25 in conjunction with the texture data of Table V.4.

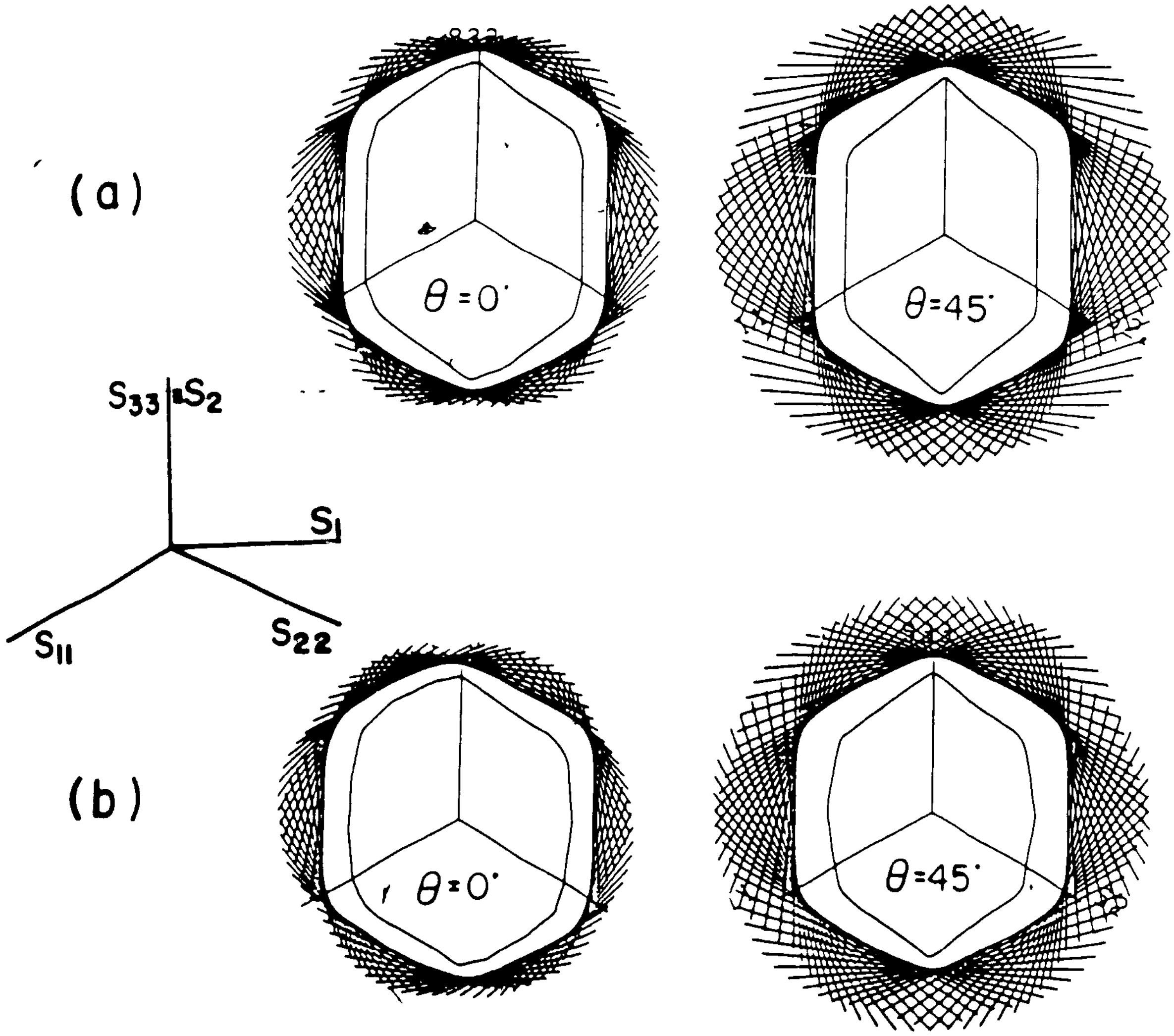

Fig.5.24 **Crystallographic** π-plane loci calculated for $\theta = 0$ and 45° for (a) an Al-killed steel and (b) a rimming steel. The outer locus is computed using the Taylor approach with restricted distributions made up of about 200 grains representing each of the pole figures of Fig. 5.20. The inner locus is obtained from the combination of loci by the Sachs method using Eqs. 3.25 in conjunction with the texture data of Table V.5.

In the case of the two steels (Fig. 5 24), very few differences are observed when changing the direction θ of the S_{11} axis, i e when considering different projections of the overall 5-dimensional yield surface. This is readily explained by the presence of a more or less strong fiber texture of the {111} type i e. a ⟨111⟩ direction which lies parallel to the normal to the sheet plane However, a more dispersed fiber in the case of the second steel leads to a yield surface which looks more random when compared to the one of Fig 3 6g

Averaging by the Sachs method - We turn now to the Sachs deformation model, for which a completely different approach must be used Here the disoriented single crystal yield loci of Eq. 3 25 (instead of the Bishop and Hill polyhedron) were reoriented in the specimen axes by means of the various texture components. They were then combined at constant stress ratios, as illustrated in Fig. 4.8b. The results obtained in this way are plotted as inner loci in Figs. 5 23 and 5.24 for the Cu/brass and steel series, respectively These surfaces are smaller than the Taylor loci, which is an expression of the geometric condition that a projection (say $\dot{\varepsilon}_{12}=\dot{\varepsilon}_{13}=\dot{\varepsilon}_{23}=0$) is always at least equal to if not larger than a section (say $\sigma_{12}=\sigma_{13}=\sigma_{23}=0$). As a result, the presence of large differences between the loci obtained with the two approaches generally suggests that higher shear stresses σ_{ij} are associated with the corresponding prescribed strain rate components $\dot{\varepsilon}_{ij}$.

Of particular interest is the non-convexity of the Sachs polycrystal loci in most of the cases, which is inconsistent with the thermodynamics of flow [136] By contrast, as shown in Appendix V.1, a Taylor model always leads to a convex overall yield surface, provided that the loci being combined are also convex, which is the case for ours. It can be anticipated that $R(\theta)$ curves predicted from these non-convex Sachs loci will be 'unreasonable', since they are related to their shape.

V.2.2.2. *CMTP model predictions*

The continuum surfaces were also evaluated by the two methods illustrated in Figs. 4.8a and b, i.e. the uniform strain rate and constant stress ratio methods of averaging. For simplicity, only the two CMTP predictions obtained with the n = 1 7 and PL4 criteria will be shown here. The other CMTP yield functions generally led to similar shapes of the plotted sections. The texture data of Tables V.4 and V.5 were employed to reorient the CMTP criteria in the specimen axes (using the Miller indices of the ideal orientations). The reoriented surfaces were then averaged on a volume fraction basis (using the experimental weights)

The results obtained with the n = 1 7 locus are shown in Figs 5.25 and 5 26 and those pertaining to the PL4 criterion in Figs. 5.27 and 5.28 for the Cu/brass and steel series, respectively. Once again, three angles ($\theta = 0$, 22 5 and 45°) were used for the FCC calculations and two ($\theta = 0$ and 45°) for the BCC ones. As can be seen from these figures, the differences between the Taylor and Sachs yield surfaces (outer and inner loci) are small, so that the dissimilarities in the derived R(θ) curves can be expected to be small. This contrasts with the observations reported above for the crystallographic method. It should also be noted that the departures from convexity mentioned for the Sachs averaging condition remain theoretically possible in the CMTP calculations, although no actual concavities were observed in the predicted yield surfaces.

The lack of sharp differences between the Sachs and Taylor predictions is primarily due to the smooth nature of the continuum yield surfaces. The combination of such rounded surfaces at constant stress ratios (Sachs) or constant strain rate ratios (Taylor) is thus seen to result in similar overall yielding characteristics.

When compared to the crystallographic loci of Figs. 5.23 and 5.24, the CMTP surfaces (Figs. 5.25 to 5.28) look different : i e. they are much smoother. Nevertheless, the PL4 predictions are somewhat less smooth in the case of the steel series, and some rounded vertices as well as flatter regions can be detected. It is also of interest that the general orientation of the CMTP surfaces is similar to that displayed in Figs. 5.23 and 5.24. This is particularly striking for the case of the Cu-20%Zn-R at $\theta = 0°$, where the polycrystalline locus is oriented along the $S_{11} = 0$ direction. It should be noted that the overall sizes are

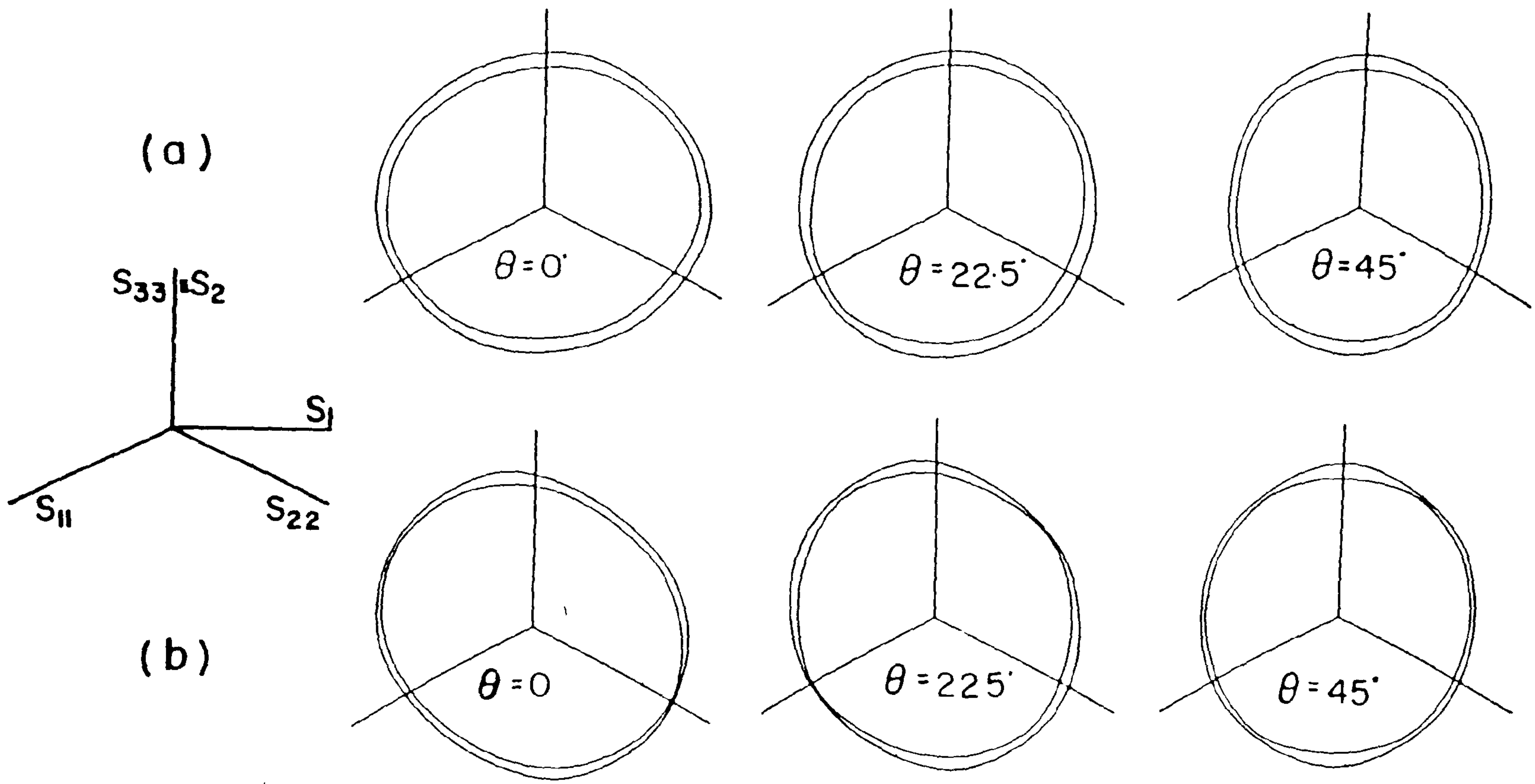

Fig 5 25 Theoretical CMTP π-plane yield surface cross-sections calculated for θ = 0, 22.5 and 45° for (a) Cu-R, (b) Cu-20%Zn-R, (c) Cu-F and (d) Cu-20%Zn-F sheets Texture data from Table V.4 [12]. Outer locus : Taylor model; inner locus : Sachs model. Predictions based on the CMTP n = 1 7 criterion.

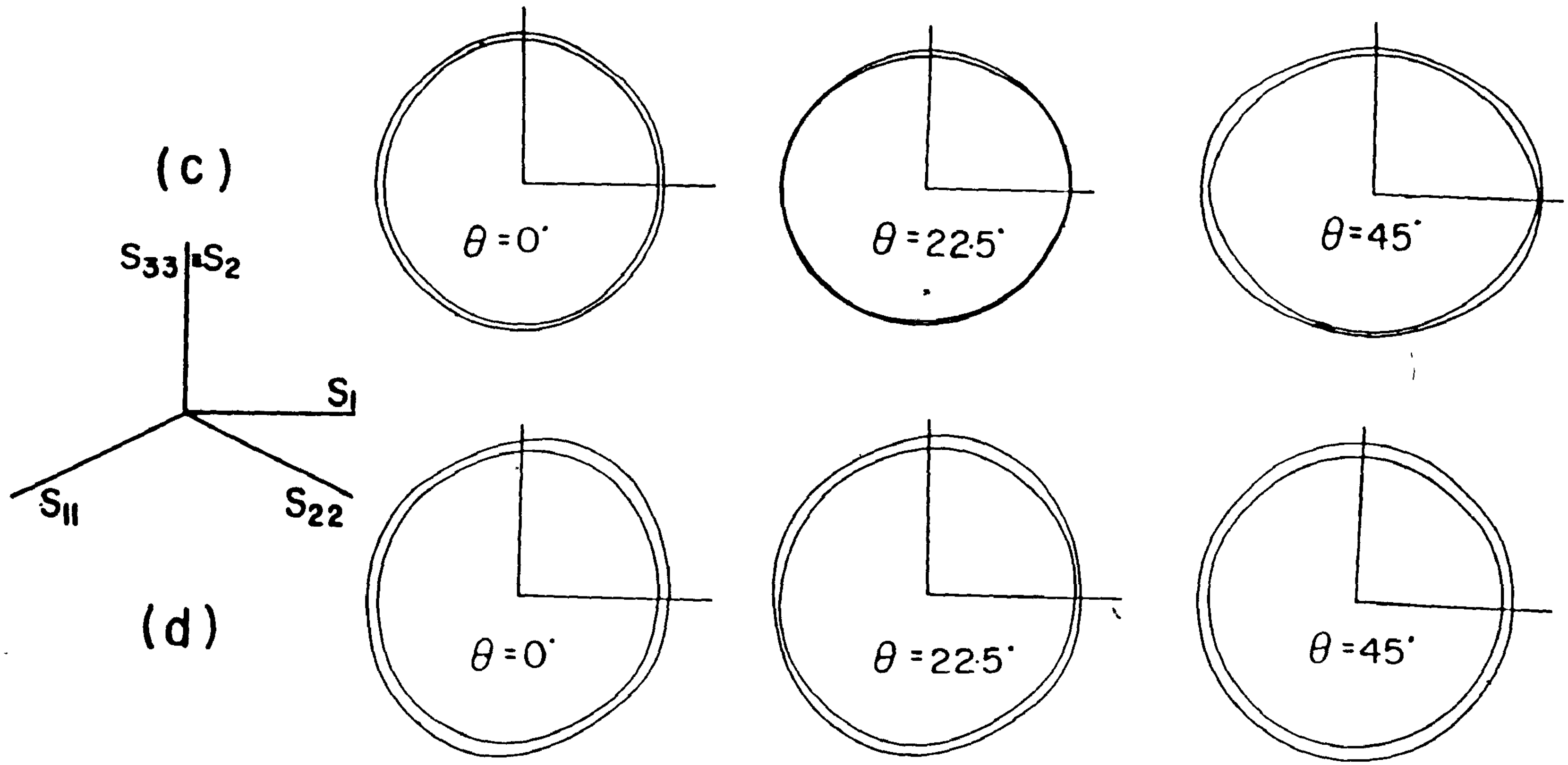

Fig.5.25 Theoretical CMTP π-plane yield surface cross-sections calculated for θ = 0, 22.5 and 45° for (a) Cu-R, (b) Cu-20%Zn-R, (c) Cu-F and (d) Cu-20%Zn-F sheets. Texture data from Table V.4 [12]. Outer locus : Taylor model; inner locus : Sachs model. Predictions based on the CMTP n = 1.7 criterion.

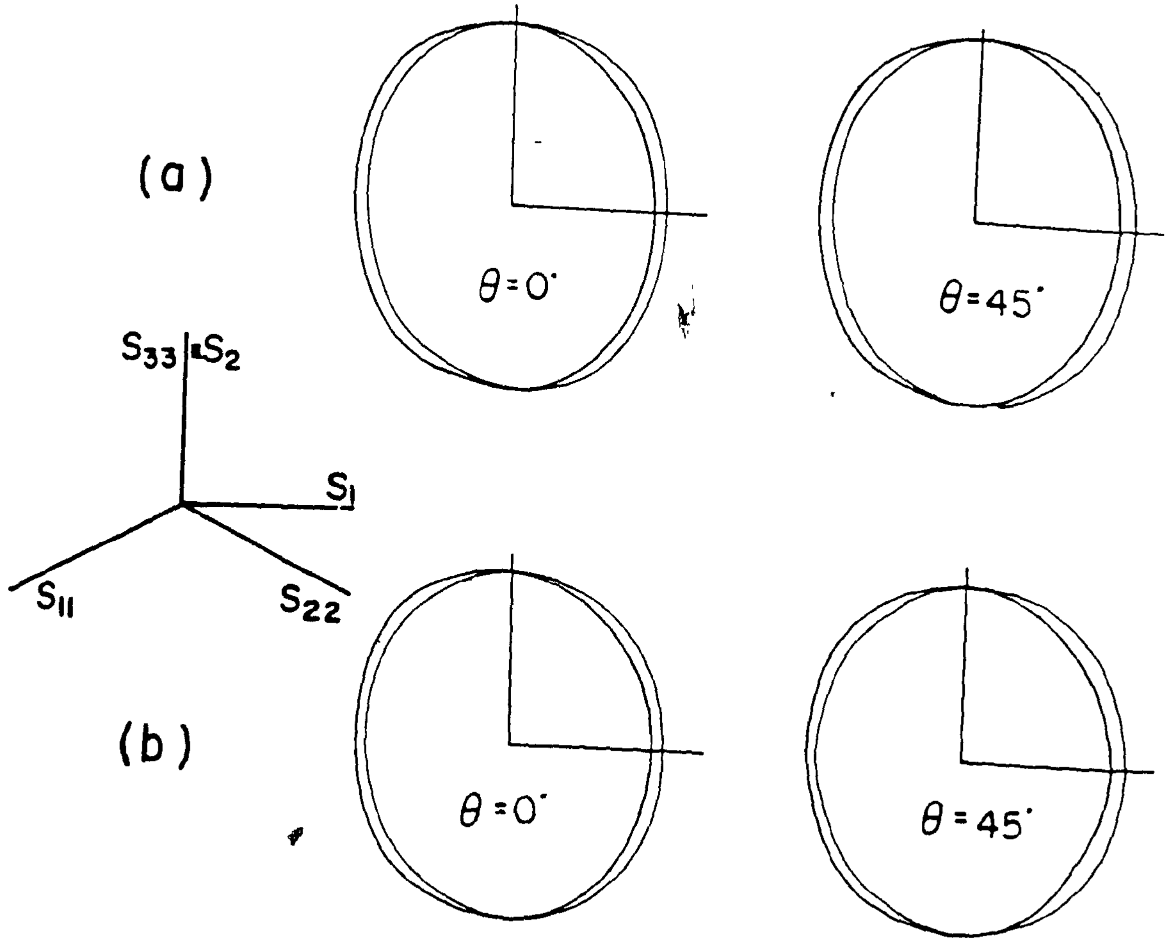

Fig.5.26 Theoretical CMTP π-plane yield surface cross-sections calculated for θ=0 and 45° for (a) an Al-killed steel and (b) a rimming steel, Texture data from Table V.5 [135]. Outer locus : Taylor model; inner locus : Sachs model. Predictions based on the CMTP n = 1.7 criterion.

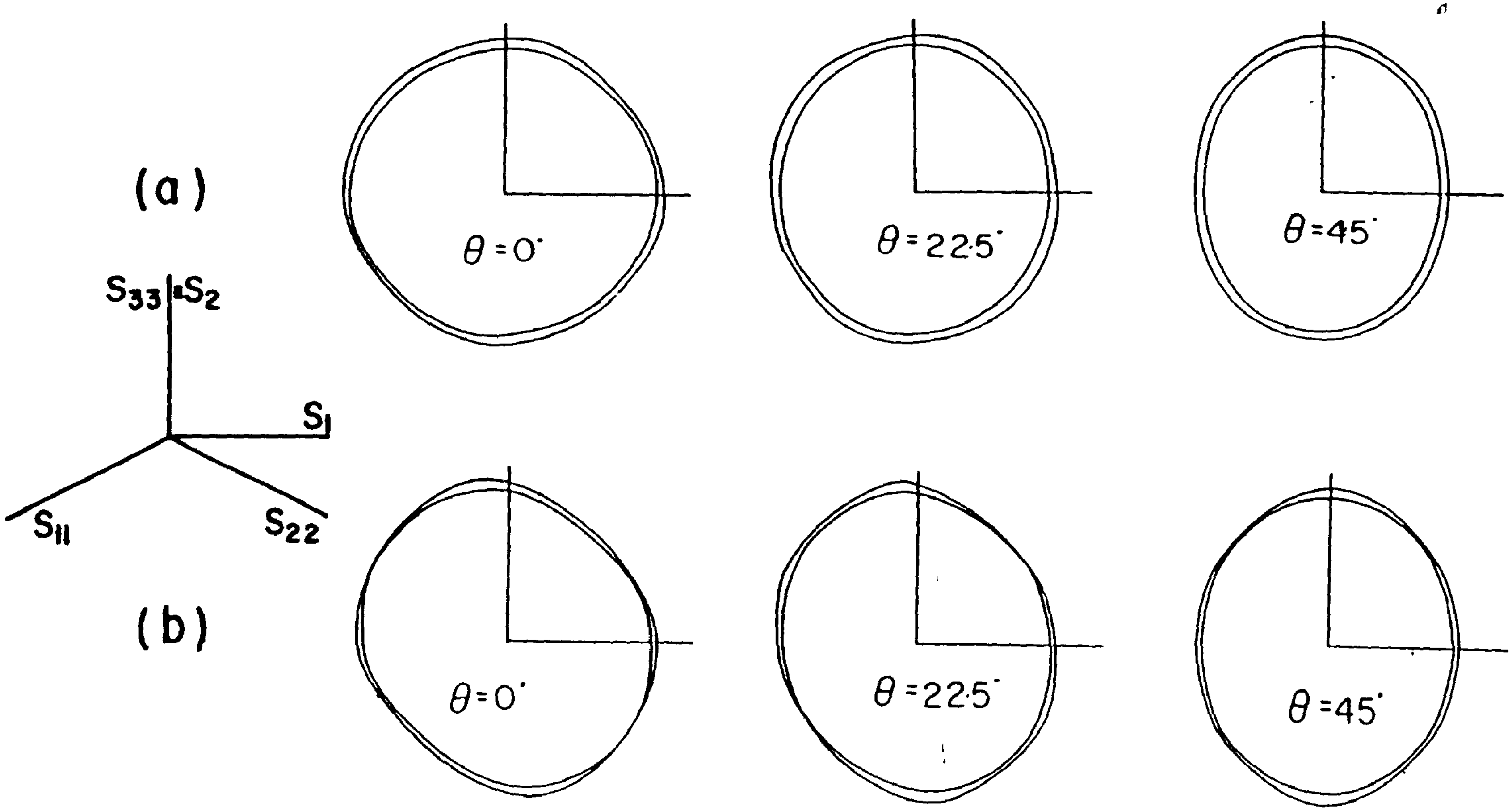

Fig.5.27 Theoretical CMTP π-plane yield surface cross-sections calculated for θ = 0, 22.5 and 45° for (a) Cu-R, (b) Cu-20%Zn-R, (c) Cu-F and (d) Cu-20%Zn-F sheets. Texture data from Table V.4 [12]. Outer locus : Taylor model; inner locus : Sachs model. Predictions based on the CMTP PL4 criterion.

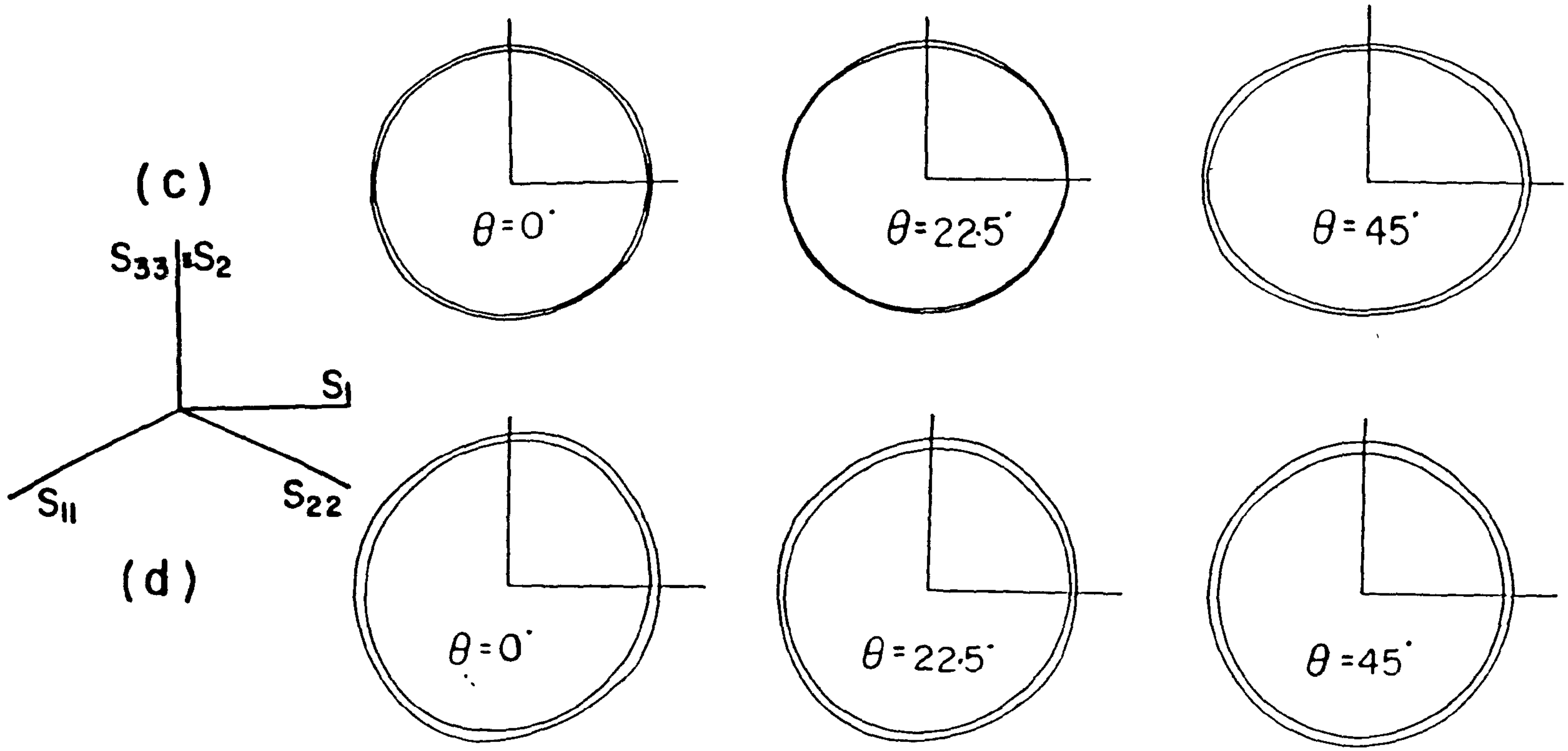

Fig.5.27 Theoretical CMTP π-plane yield surface cross-sections calculated for θ = 0, 22.5 and 45° for (a) Cu-R, (b) Cu-20%Zn-R, (c) Cu-F and (d) Cu-20%Zn-F sheets. Texture data from Table V.4 [12]. Outer locus : Taylor model; inner locus : Sachs model. Predictions based on the CMTP PL4 criterion.

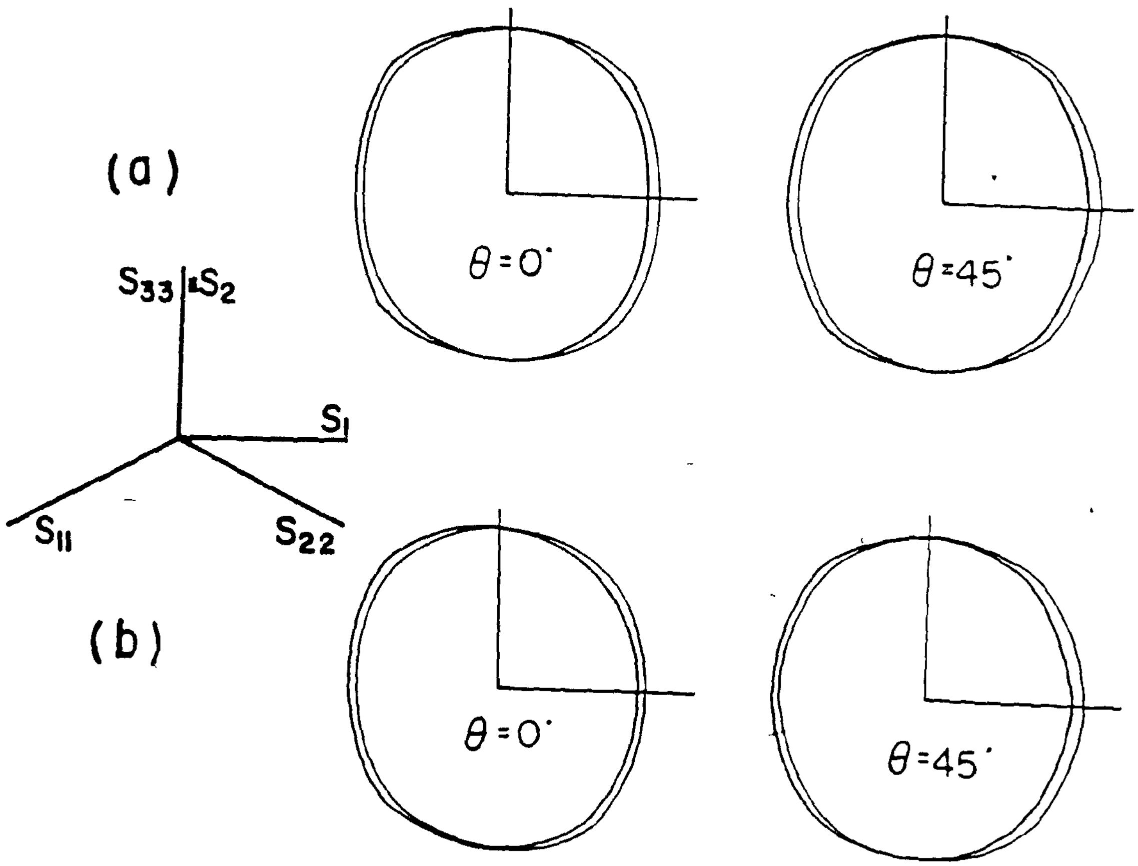

Fig.5.28 Theoretical $\overline{\text{C}}$MTP п-plane yield surface cross-sections calculated for θ=0 and 45° for (a) an Al-killed steel and (b) a rimming steel. Texture data from Table V.5 [135]. Outer locus : Taylor model; inner locus : Sachs model. Predictions based on the CMTP PL4 criterion.

similar for the crystallographic and continuum calculations (at least for the Taylor case). This is not surprising, since the yield criterion coefficients were fitted to the Bishop and Hill polyhedron (section 4.1.1).

V 2.2 3. *Comparison with experimental loci*

The previous section dealt with the parallel between the crystallographic and CMTP calculations. We turn now to a comparison between the CMTP predictions and experimentally determined yield surfaces. Here the experimental results of Viana et al. [38] (shown as tangent lines) are used together with their CODF data for two steels : (a) a 50% cold rolled and annealed rimming steel and (b) a 70% cold rolled and annealed Ti-bearing steel. The constituent texture components as well as their respective weights are reported, for ease of reference, in Table V.6.

The results of these computations are shown in Figs. 5.29 and 5.30 for the n = 1.7 and PL4 criteria, respectively. The surfaces obtained from the simplified 'disoriented' crystallographic approach described by Eqs. 3 25 are plotted in Fig. 5.31. For comparison purposes, the calculated loci have been normalized by the uniaxial tensile stress in the rolling direction. In the case of the two steels, the two CMTP predictions as well as the simplified crystallographic result give a good approximation of the tensile stress ratio $\sigma_{(TD)}/\sigma_{(RD)}$, which equals 1.02. However, different conclusions have to be drawn when the R-values are examined, as well as the plane strain stresses, which are given by the tangents to the yield surfaces in the TD and RD tensile directions.

For the rimming steel, the ratios of the plane strain to the uniaxial stresses are markedly underestimated by the three yield functions under consideration. The Sachs model appears to give somewhat better results when applied to the n = 1.7 or to the PL4 criteria. The two continuum functions also lead to good estimates of the strain rate ratios in the TD and RD directions, whereas the crystallographic model shows a much stronger divergence from the experimental tangents.

Texture component	Rimmed steel	Ti-bearing steel
{100}<011>	11	3
{211}<0$\bar{1}$1>	18	9
{111}<1$\bar{1}$0>	16	20
{111}<11$\bar{2}$>	12	19
{223}<1$\bar{1}$0>	18	15
{332}<1$\bar{1}$0>	12	14
{11 11 $\bar{8}$} <4 4 11>	13	20

Table V.6. Volume fractions (%) of the main texture components observed in rimmed and Ti-bearing steel sheet. From Ref. [38].

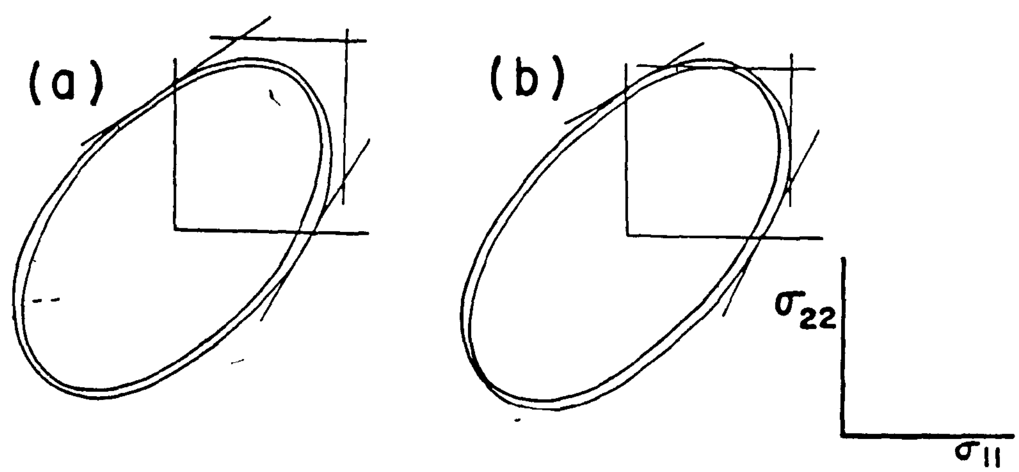

Fig.5.29 Comparison between the experimental (σ_{11},σ_{22}) yield surface cross-sections of Viana et al. [38] and the theoretical predictions obtained from the CMTP n = 1.7 criterion. The curves are normalized by the uniaxial yield stress σ_{11}. Texture data from Table V.6 [38]. Outer locus : Taylor model; inner locus : Sachs model. (a) 50% cold rolled and annealed rimming steel; and (b) 70% cold rolled and annealed Ti-bearing steel.

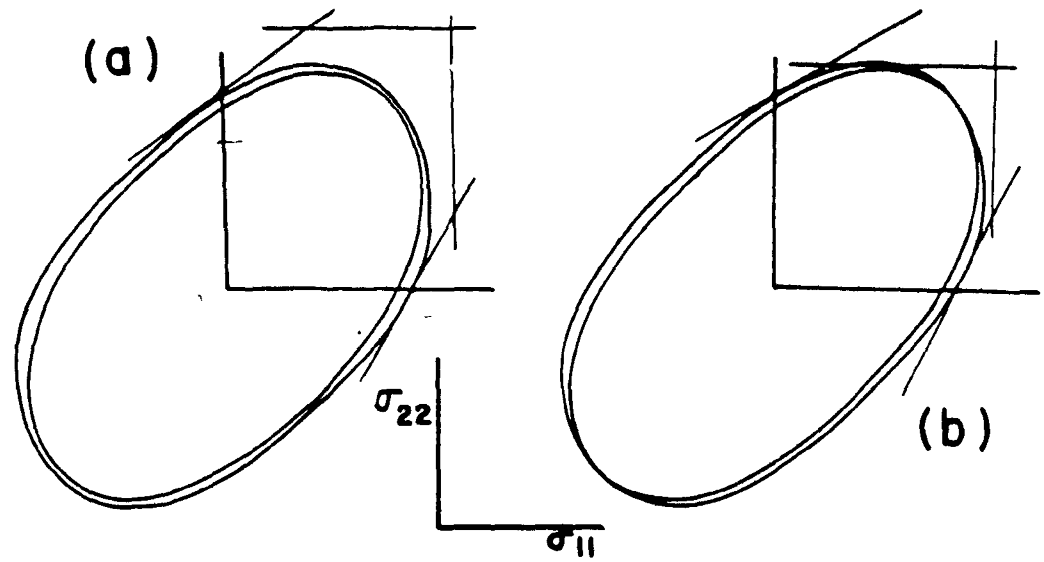

Fig.5.30 Comparison between the experimental (σ_{11},σ_{22}) yield surface cross-sections of Viana et al. [38] and the theoretical predictions obtained from the CMTP PL4 criterion. The curves are normalized by the uniaxial yield stress σ_{11}. Texture data from Table V.6 [38]. Outer locus : Taylor model; inner locus : Sachs model. (a) 50% cold rolled and annealed rimming steel; and (b) 70% cold rolled and annealed Ti-bearing steel.

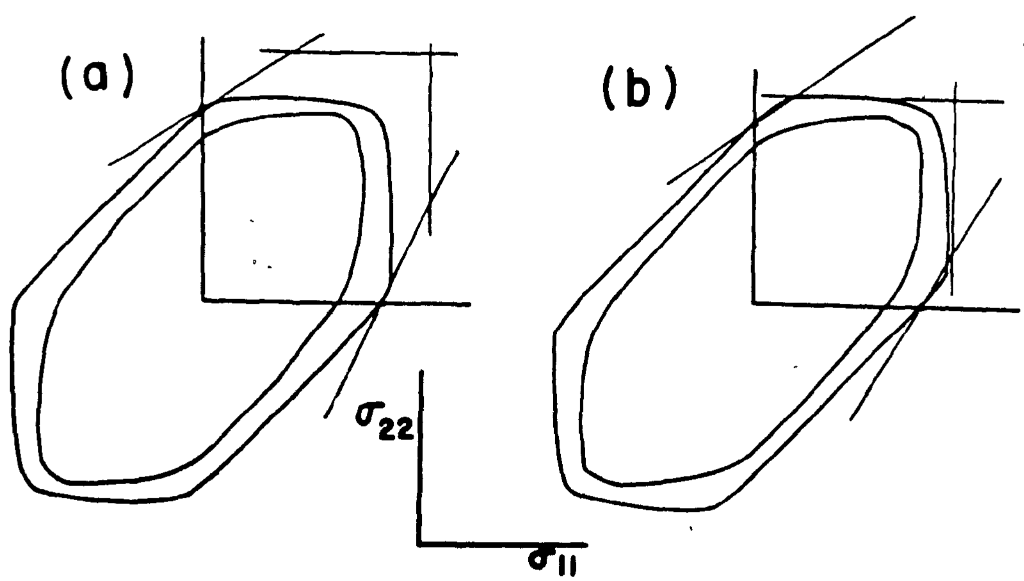

Fig.5.31 Comparison between the experimental (σ_{11},σ_{22}) yield surface cross-sections of Viana et al. [38] and the theoretical predictions obtained from the disoriented crystallographic locus of Eqs. 3.25. The curves are normalized by the uniaxial yield stress σ_{11}. Texture data from Table V.6 [38]. Outer locus : Taylor model; inner locus : Sachs model. (a) 50% cold rolled and annealed rimming steel; and (b) 70% cold rolled and annealed Ti-bearing steel.

By contrast, the predictions obtained for the Ti-bearing steel are in much better agreement with experiment. An almost perfect fit is seen when the Taylor averaging technique is applied to the $n = 1.7$ and PL4 continuum yield functions. The crystallographic approach also gives a good estimate of the plane strain vs uniaxial behaviour. However, the strain rate ratios in the latter case are in rather poor agreement with those reported by Viana et al. [38].

Similar sets of results are shown in Figs. 5.32a to 5.32c for the recrystallized aluminum tubes tested by Althoff and Wincierz [63]. Here the 1 and 2 axes refer to the tangential and axial stresses, respectively. As suggested by the authors [63], the texture was decomposed into 4 ideal orientations : $\{011\}\langle 1\bar{1}1\rangle$, $\langle 111\rangle$ fiber (approximated by equal parts of $\{112\}\langle 11\bar{1}\rangle$ + $\{123\}\langle 11\bar{1}\rangle$ + $\{134\}\langle 11\bar{1}\rangle$), $\{011\}\langle 6\bar{1}1\rangle$ and $\{001\}\langle 310\rangle$ (where $\{hkl\}$ and $\langle uvw\rangle$ are parallel to the radial and axial directions, respectively) in the volume fraction ratio 5:3:1:1. The CMTP continuum predictions normalized by the uniaxial tangential yield stress are in rather good agreement with the experimental loci. The experimental strain rate ratios (tangents to the locus) are in this case rather well approximated. However, the near plane strain stresses ($\dot{\varepsilon}_{tangential} = 0$) are somewhat overestimated. By contrast, while the simplified crystallographic approach based on Eqs. 3.25 leads to a reasonable fit for the stresses, it fails to reproduce the strain rate ratios, especially in the near biaxial region ($\sigma_{tangential} = \sigma_{axial}$).

V.2.2.4. *Comparison with other models*

Such comparisons are difficult to carry out since the inputs are generally non-uniform due to the different methods employed by the various authors. However, some interesting comments can be made at least from a qualitative point of view.

Viana et al. [38] carried out calculations of the upper bound (Taylor) and lower bound (Sachs) solutions of polycrystalline pencil glide yield loci. For this purpose, they employed the spherical harmonic (CODF) analysis of texture data. Both the rimming and Ti-bearing steels of section V.2.2.3 were treated. The results they obtained using the pencil glide model are shown in Fig.5.33 in

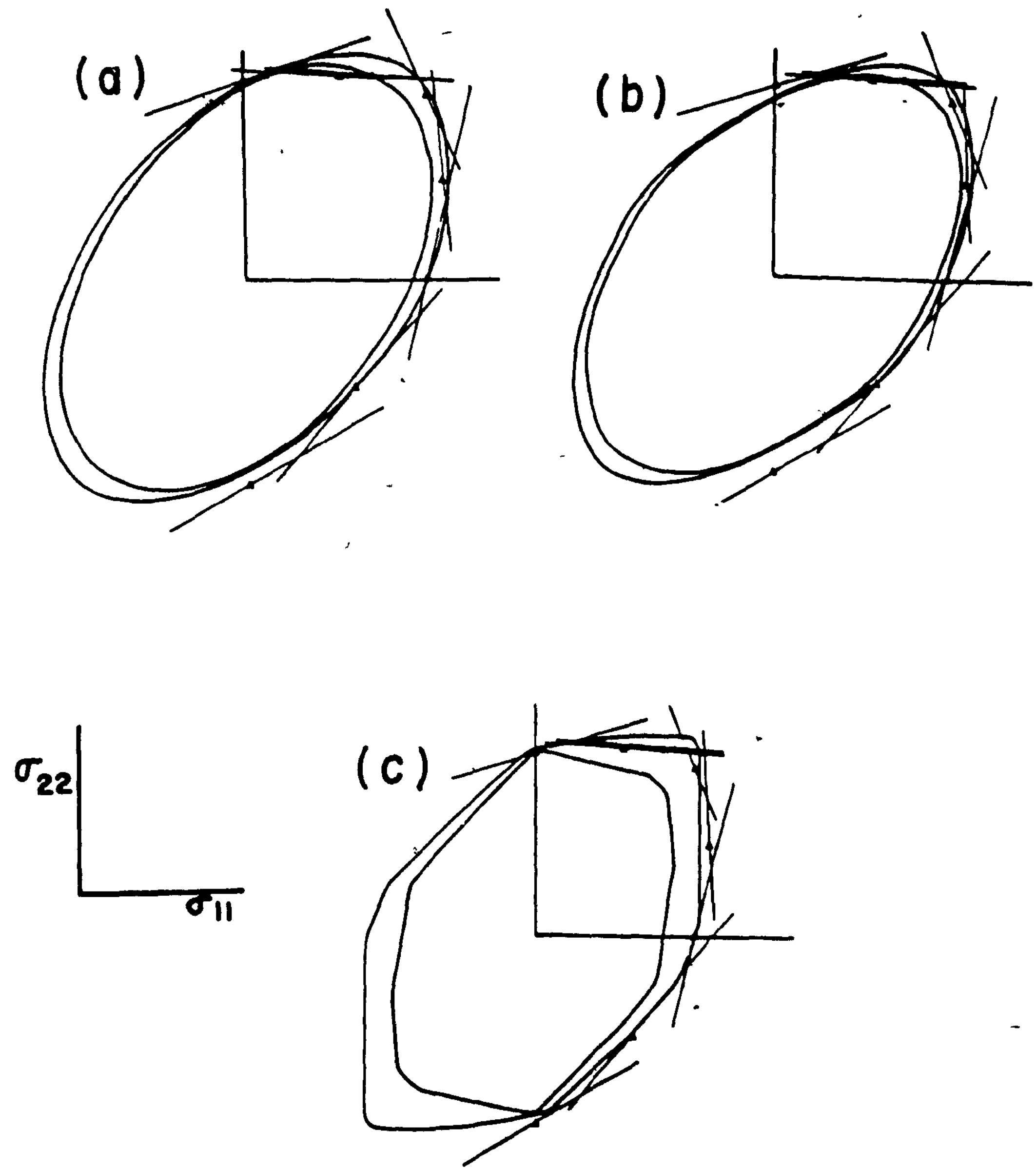

Fig.5.32 Comparison between the experimental (σ_{11},σ_{22}) yield surface cross-sections of Althoff and Wincierz [63] and the theoretical predictions obtained from the (a) n=1.7, (b) PL4 and (c) disoriented crystallographic (Eqs. 3.25) criteria for recrystallized Al tubes. Texture data from [63]. The yield stresses have been normalized by the uniaxial yield stress σ_{11}.

the form of broken lines. The yield loci predicted in this way display a rounded shape similar to the ones calculated by the CMTP method (see Figs. 5.29 and 5.30). Nevertheless the latter are somewhat more faithful to the experimental yield surfaces. These similarities can be explained in that the yield locus of a BCC single crystal in which pencil glide takes place is much more rounded than the Bishop and Hill polyhedron for a BCC metal undergoing $\{110\}<1\bar{1}1>$ slip Such a yield surface is thus probably better approximated by the rounded CMTP yield functions

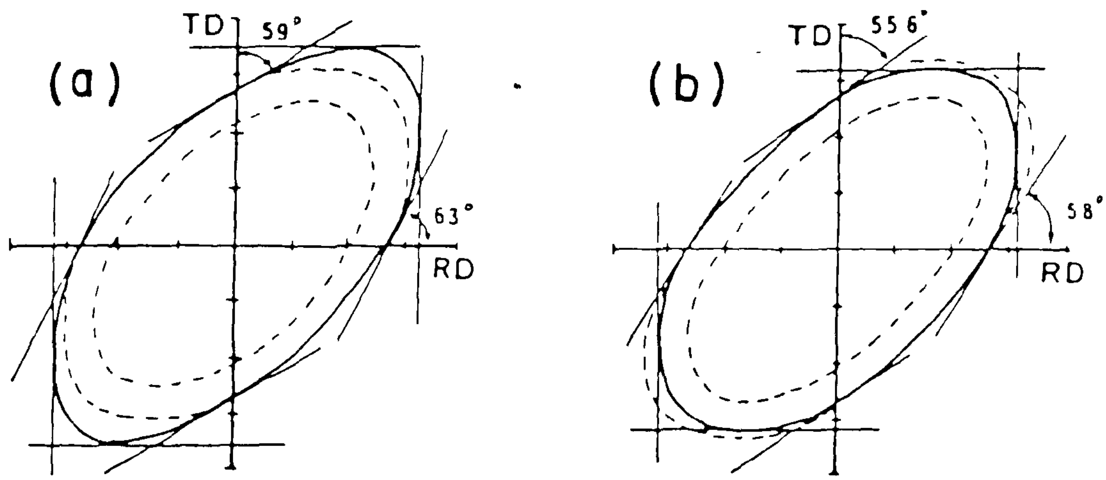

Fig.5.33 Comparison between experimental (σ_{11},σ_{22}) yield surface cross-sections (——) of Viana et al. [38] and their theoretical calculations based on a pencil glide model (– – – –) Outer locus Taylor model; inner locus : Sachs model. (a) Rimming Steel; (b) Ti-bearing Steel.Taken from [38].

CODF data, as expressed by spherical harmonic coefficients, have been widely used in the past fifteen years to reproduce accurately the distribution of grain orientations in deformed materials. The distribution function, which gives the probability that a crystal has a given orientation, is used as a weighting factor in the calculation of macroscopic values which must be averaged over the orientation distribution. By applying this technique to the Taylor factor, the polycrystalline yield surface can be readily calculated. The

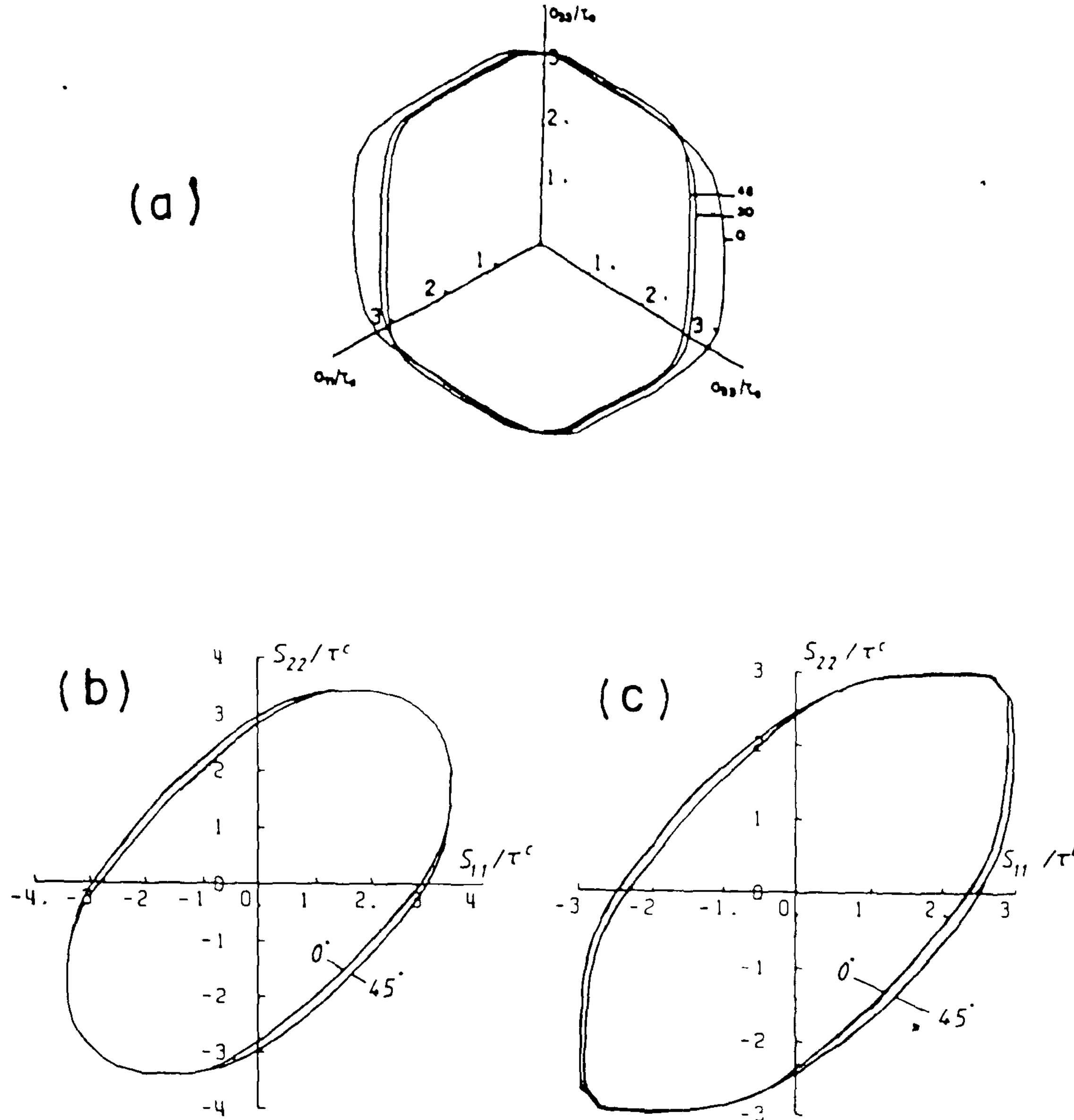

Fig 5 34 (a) π-plane yield locus for rolled copper calculated from the experimental CODF data [70]; (b-c) (σ_{11},σ_{22}) section of the yield locus using the CODF texture representation for a mild steel sheet, at $\theta = 0$ and 45°. (b) according to the FC model; and (c) according to the RC (pancake) model. Taken from [134].

results obtained in this way by Mols et al. [70] for a pure Taylor model (all $\dot{\varepsilon}_{ij}$ prescribed in the crystals as well as in the aggregate) applied to an FCC rolling texture are presented in Fig. 5.34a. These calculations based on {111}<1$\bar{1}$0> slip lead to a behaviour which is similar to the one calculated for the rolled copper (Fig. 5.23a) using the present crystallographic model.

The use of more complicated (and also more realistic) deformation models can lead to rather different shapes of the surfaces. In a more recent paper, van Houtte [111] employed a relaxed constraint (RC) theory, in which only a part of the strain rate tensor in the crystals was prescribed. This in turn is related to the change in shape of the grains as the deformation proceeds. Their flat pancake aspect at large strains renders the prescription of some of the shear components unrealistic. This difference between the RC and FC deformation models is illustrated in Fig. 5.34 b-c for a mild steel [111] in which the operation of both {1$\bar{1}$0} and {11$\bar{2}$} <111> slip systems was assumed. It appears that sharper vertices are obtained in the latter case.

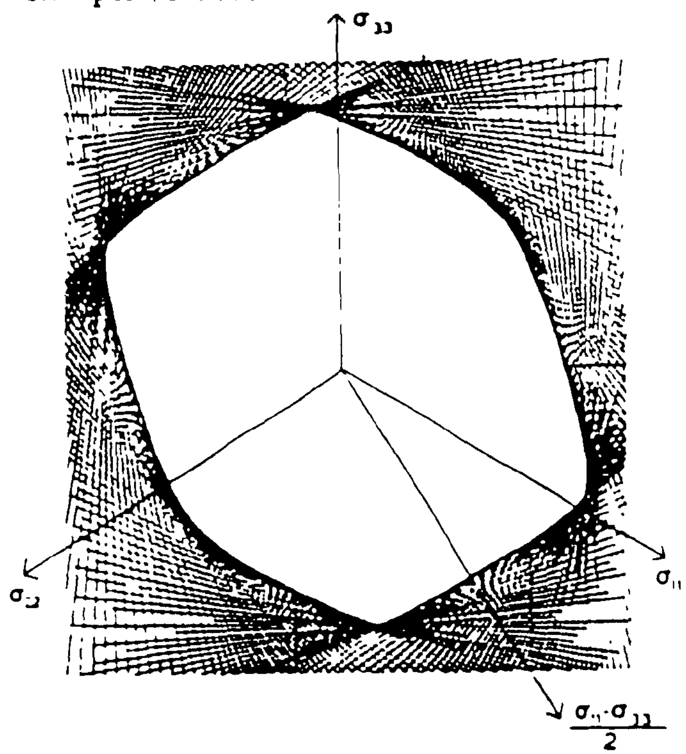

Fig.5.35 π - plane representation of a theoretical yield surface after a rolling reduction of $\varepsilon_{33} = -2$. The texture data have been calculated using an RC model. Note that the 11 and 22 axes must be inverted for comparison with the previous figures. Taken from [11].

In a similar vein, the calculations carried out by Canova et al. [11] for a texture predicted by the RC model also show this apparent accentuation of the flat regions and sharp corners (Fig. 5.35). By comparing it to the loci displayed in Fig. 5.23a, it is seen to resemble the surface obtained by the Sachs averaging technique (note, however, the permutation of the 1 and 2 axes). This suggests that the σ_{12} shear stress associated with the $\dot{\varepsilon}_{12}=0$ prescribed condition may not be too large. Associated with the further requirements $\sigma_{13}=\sigma_{23}=0$ of the RC theory, a small value of σ_{12} can be expected to lead to a yield surface projection ($\dot{\varepsilon}_{12}=\dot{\varepsilon}_{13}=\dot{\varepsilon}_{23}=0$) which would be more or less identical to its section ($\sigma_{12}=\sigma_{13}=\sigma_{23}=0$). The above statement is verified for the Cu component (for which the conditions $\sigma_{12}=0$ and $\dot{\varepsilon}_{12}=0$ are associated), which is the most intense orientation found in rolled FCC metals, and is also true to a lesser degree for the S component

V.2.3. Prediction of the plastic properties of textured polycrystals

The stress and strain rate characteristics of a metal workpiece can be readily deduced from knowledge of its yield surface. More specifically, the locus size gives the amplitude of the stresses, whereas its shape leads to the values of the strain rates, as obtained from the normality rule. In this way, once the polycrystalline yield surface has been determined (see section V.2.2), yield stresses as well as Lankford coefficients can be assessed geometrically, as illustrated in Fig. 5.36.

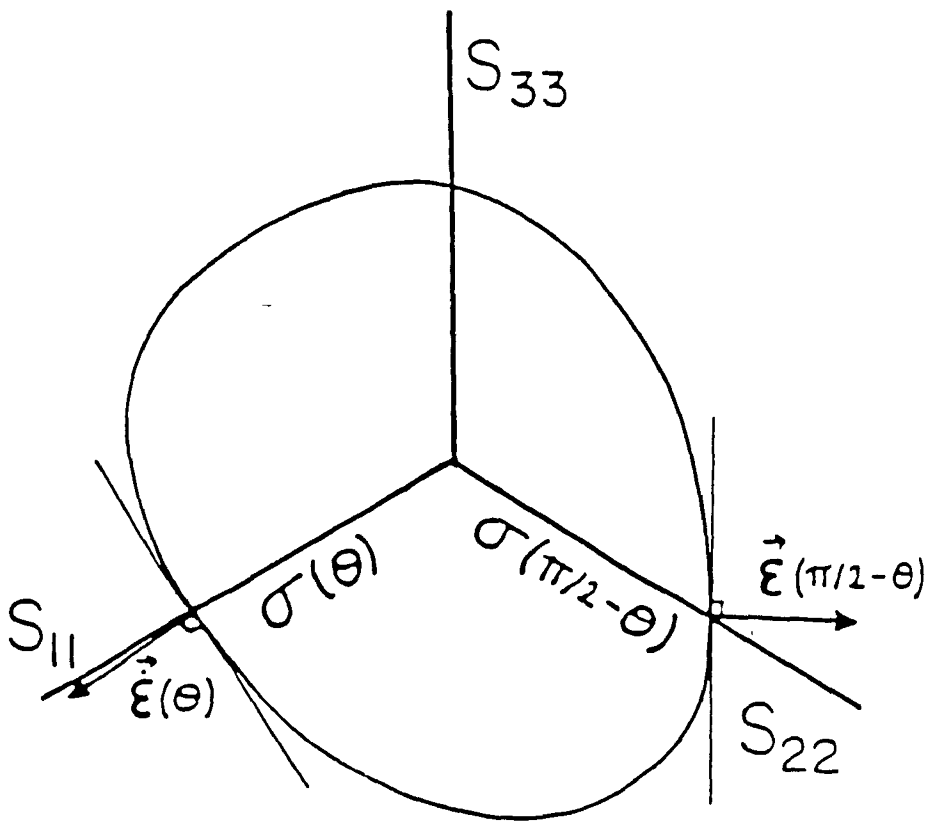

Fig. 5.36 Derivation of the yield stress $\sigma(\theta)$ and strain rate $R(\theta)$ ratio from a yield surface. $\sigma(\theta)$ is the distance from the origin to the locus in the loading direction S_{11} and $R(\theta)$ is deduced from the normal to the surface at the loading point. $\sigma(\pi/2-\theta)$ and $R(\pi/2-\theta)$ are derived from the characteristics of the yield surface in the S_{22} direction.

However, as long as only a part of the yield locus pertaining to the aggregate is needed or "useful" for many applications, somewhat more direct methods can be employed, as described in Chapter IV for the CMTP Taylor and Sachs predictions. For example, the yield stress vector $\sigma(\theta)$ induced during a tensile test, carried out in a direction inclined at an angle θ to the rolling direction and in the rolling plane, describes a single curve on the complete five-dimensional yield surface. Determination of the normal to this "loading" curve (which is related to the R-value) necessitates, however, some knowledge of its neighborhood on the locus. It can thus be readily understood that the computing time involved in R-value calculations can quickly attain unreasonable limits.

V.2.3.1 *R-value predictions in the literature*

The relation between texture and plastic properties has been investigated in the past by many authors. If exception is made of the predictions based on the traditional continuum analyses (see Chapter II), the strain rate $R(\theta)$ and yield stress $\sigma(\theta)/\sigma(0)$ ratios have usually been calculated by crystallographic methods. Tucker [35] first succeeded in predicting the important features of earing in cups pressed from aluminum single crystals. The criterion of the maximum resolved shear stress for slip on $\{111\}<1\bar{1}0>$ systems was used for this purpose. Fukuda [68] extended this analysis in a successful attempt to correlate crystallographic texture and R-value in steel sheet. In this case the 48 $\{1\bar{1}0\}$, $\{11\bar{2}\}$ and $\{12\bar{3}\}<111>$ slip systems were assumed to be activated in the same order as the sequence of magnitude of their resolved shear stresses. The $\{111\}$ and $\{100\}$ types of texture were found to lead to high and low R-values, respectively. Svensson [32] expanded the Taylor calculation (minimum of the sum of the glide shears) for polycrystalline yield strength predictions by introducing specific volume fractions for averaging over the orientation distribution. Reasonable agreement with yield stress ratios measured in an 1100 Al cold rolled sheet was obtained.

The CODF analysis which appeared in the 1960's received a considerable amount of attention because it attempted to quantify the texture/plastic properties relationship in an improved way. As the CODF gives a "true" representation of the probability that a grain has a specific orientation, it can be used as a weighting factor in the prediction of the various properties of interest. The method generally employed (see for example Refs.[8] and [10]) consists in calculating the Taylor factor M(q) by means of a classical Bishop and Hill approach. Here q (unknown) is the contraction ratio $q = R/(R+1)$. The mean value of $\overline{M}(q)$ for all the orientations present in the material is given by

$$\overline{M}(q) = \int M(q,g)\, f(g)\, dg \tag{5.7}$$

where f(g) is the orientation distribution function of the crystallites. The contraction ratio of the specimen is then assumed to be that value of q for which $\overline{M}(q)$ is a minimum. R is readily deduced from $R = q/(1\text{-}q)$. Such a technique generally leads to reasonable but not perfect agreement with experimental R-values and stress ratios. For example, Bunge [10] reported quite good results for a stabilized steel sheet, whereas Dabrowski et al. [114] observed that the discrepancies with respect to the measured R-values of an Al-killed steel can be fairly large, depending on the type of slip system selected. Sowerby et al. [69] stated that a good fit to experimental yield stress ratios can be calculated, but obtained some divergence with regard to the R(θ) curves pertaining to commercial purity copper sheet. Semiatin et al. [104], on the other hand, found reasonable agreement in their investigation of three cold-rolled and annealed low C steels. More sophisticated approaches including the solution of the stress equilibrium in the flange of drawn cups as well as the addition of a work hardening law [37,137] were conducive to adequate predictions of ear shape in cups of an aluminum alloy. Similarly, Kanetake et al. [138] satisfactorily reproduced the cup height in a drawn Al-Mg alloy and in Cu sheets by varying two parameters in the work hardening rule pertaining to a single crystal. Mols et al. [70] and van Houtte [111] have derived general methods of yield surface prediction from CODF's. They both used the hyperplane method in suitable five-dimensional stress spaces. However, the lengthy computations necessary for reasonable R(θ) predictions render this method unsuitable in its actual form for on line use.

Finally, the publications of Avery et al. [139], Elias et al. [106] and Wei [134] are worth noting in that they differ completely from the previous ones.

They developed methods which permit the rapid prediction of plastic anisotropy for any crystallographic texture, using (222) pole figures. Although reasonable predictions were reported for the HCP [139] and BCC [106] metals, fairly large divergences were observed in the case of aluminum sheets [134].

The sections that follow deal with a comparison between the experimental strain rate R(θ) and yield stress σ(θ)/σ(0) ratios found in the literature and the theoretical calculations obtained from both the present crystallographic and CMTP methods. The fundamental bases for these predictions have been reviewed in Chapter IV for the continuum model. Similar procedures are used for the disoriented Bishop and Hill (Eqs. 3.25) crystallographic method, the principles of which can be very simply visualized from Fig. 4.8.

V 2.3.2 *R-value predictions using the crystallographic and CMTP methods*

The aim of this section is to illustrate the validity as well as the limitations of the CMTP method for predicting R(θ) curves for polycrystalline sheets. Only the Taylor predictions are shown since the non-convexity of the Sachs type of crystallographic surface renders the use of the normality rule unsuitable. The results obtained from the crystallographic (and disoriented crystallographic) approach, as well as from the present n=2, n=1.7 and PL4 criteria are compared to experimental R-values.

<u>Results of Hirsch et al. [12]</u>

R(θ) curves were first determined geometrically (see Fig. 5.36) from the Bishop and Hill yield surfaces of Fig. 5.23 for the five angles θ = 0, 22.5, 45, 67.5 and 90°. The predictions obtained in this way are shown as crosses in Figs.5.37a-i. The texture data displayed in Table V.4 were then used in the conjunction with the disoriented crystallographic locus (Eqs. 3.25) to produce the light continuous lines in Figs. 5.37 a-i. Finally, the three CMTP criteria cited above were employed to obtain the predictions shown in Figs. 5.38 a-i. It can be seen that the crystallographic models strongly overestimate the experimental variations in R-value, especially in the diagonal direction θ = 45°.

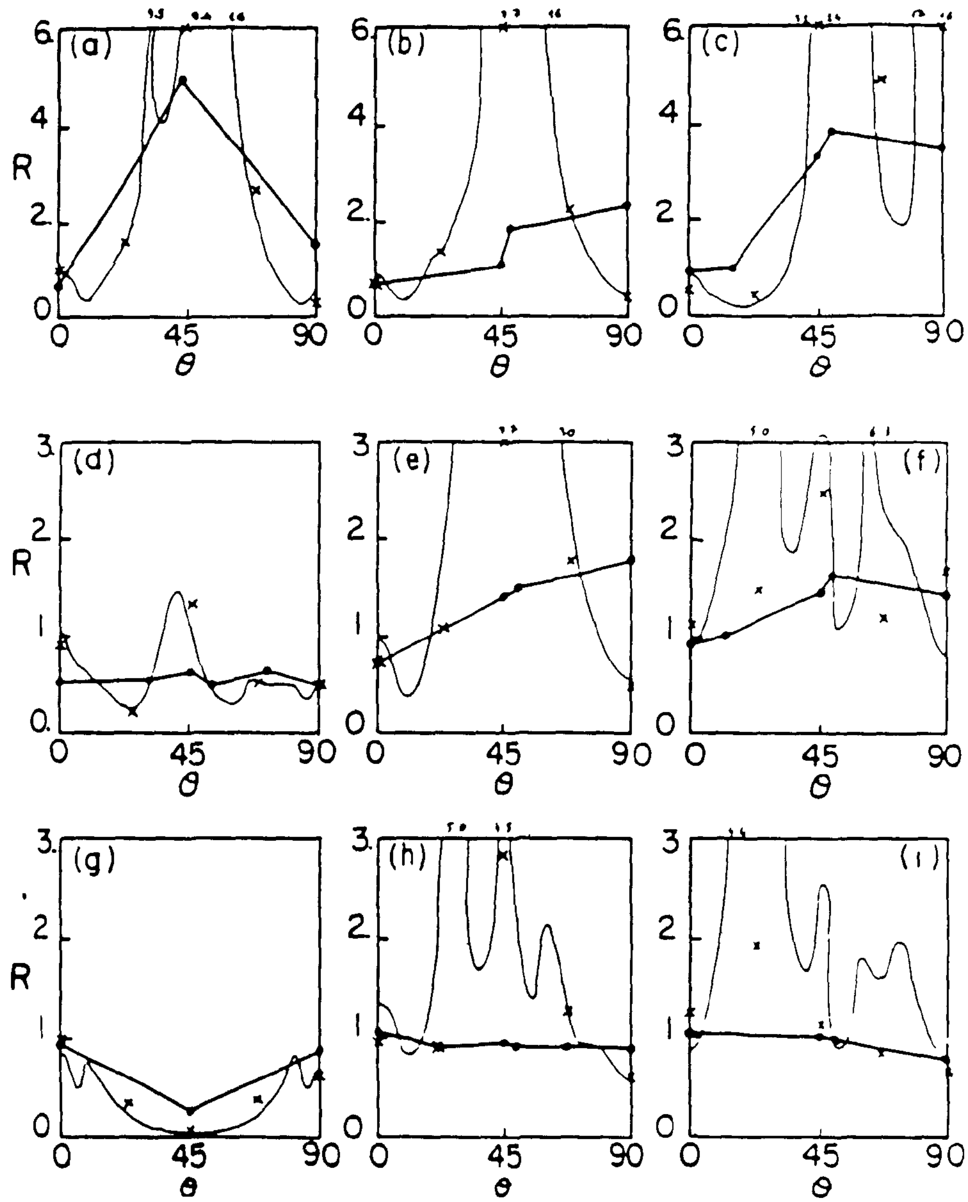

Fig. 5.37 R(θ) curves for the following rolled sheets : (a) Cu-R, (b) Cu-5%Zn-R, (c) Cu-20%Zn-R, (d) Cu-P, (e) Cu-5%Zn-P, (f) Cu-20%Zn-P, (g) Cu-F, (h) Cu-5%Zn-F and (i) Cu-20%Zn-F. (•) experimental R-values taken from Ref.[12]; (x) R-values derived geometrically from the Bishop and Hill loci of Fig. 5.23 and (———) R(θ) curves calculated from the disoriented crystallographic yield function of Eqs. 3.25.

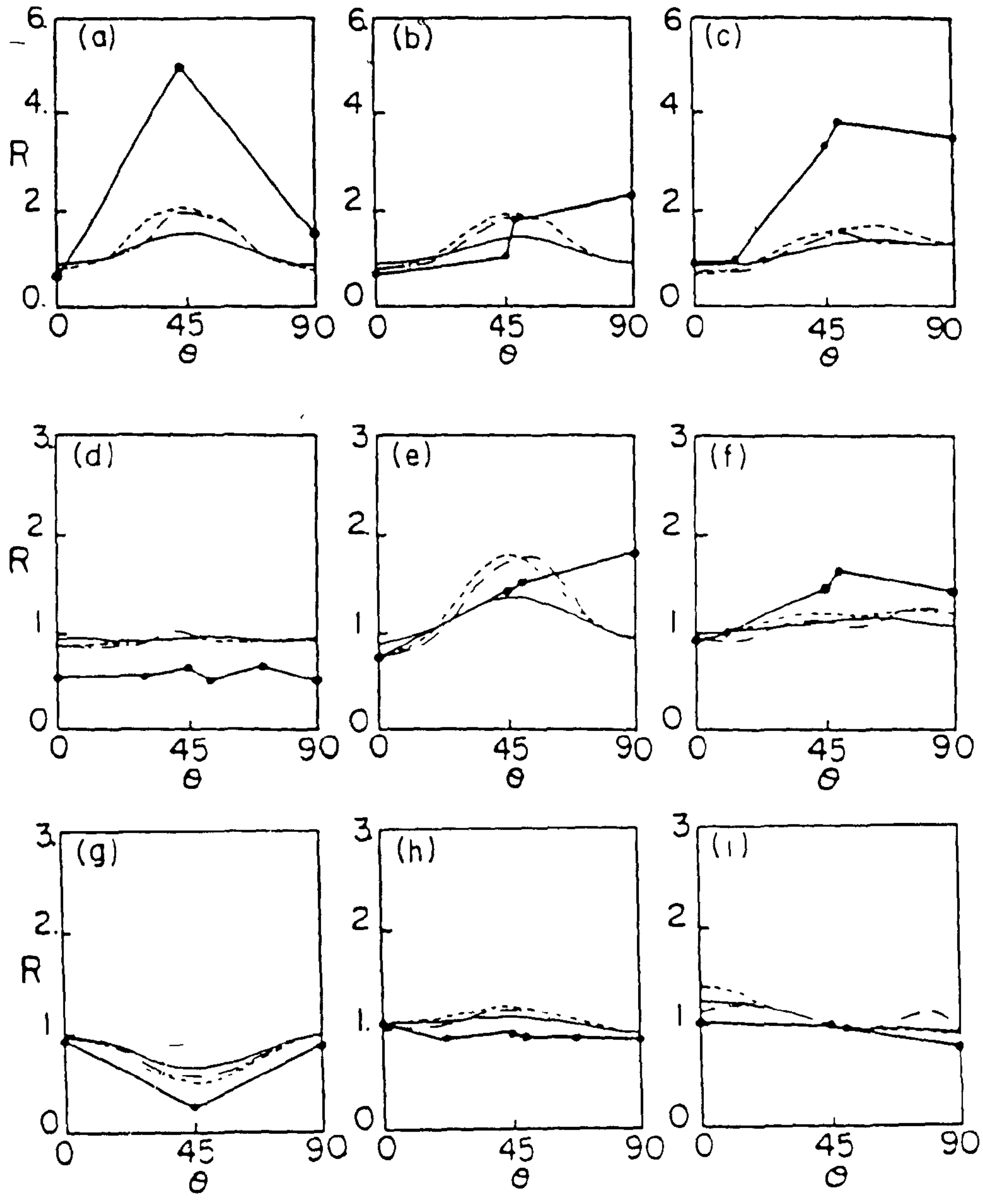

Fig. 5.38 R(θ) curves determined by the CMTP method for the sheets of Fig. 5.37 : (a) Cu-R, (b) Cu-5%Zn-R, (c) Cu-20%Zn-R, (d) Cu-P, (e) Cu-5%Zn-P, (f) Cu-20%Zn-P, (g) Cu-F, (h) Cu-5%Zn-F and (i) Cu-20%Zn-F. (•) experimental R-values taken from Ref. 12. (————) n = 2; (– – – – –) n = 1.7 and (— —) PL4 predictions. The texture data used are those reported in Table V.4.

The most likely explanation for this observation is the questionable nature of the Taylor assumption that all the grains undergo exactly the same strain as the polycrystal as a whole. If instead the pancake-shaped grains are permitted to shear, as in the relaxed model [11], a better representation of the properties in the $\theta = 45°$ direction is obtained, at least in the case of rolled copper, as reported by Canova et al. [11]. In the rolling and to a lesser degree transverse directions, on the other hand, the predictions obtained from our crystallographic calculations agree quite well with experiment.

In the case of the rolled copper and brasses tested by Hirsch et al.[12] (Figs. 5.38 a-c), the CMTP predictions deduced from the $n = 2$, $n = 1.7$ and PL4 functions underestimate the experimental values. It should be noted that the experimental $R(\theta)$ curve for the Cu-5%Zn brass is probably in error since it does not reproduce the earing behaviour shown in Fig. 5.39. In particular, the high R-value measured at $\theta = 90°$ does not coincide with the relatively small ear observed at $\theta = 0°$, as it should. Similar comments apply to the partially recrystallized Cu-5%Zn sheet. Note that the $n = 1.7$ and PL4 CMTP predictions give somewhat better results, in that the calculated variations are larger than the ones associated with the quadratic criterion. If exception is made for the experimental R-value mentioned above, then the predicted CMTP curves are in good qualitative agreement with experiment in terms of the positions of the maxima and minima, which are expected to correspond to the experimental peaks and troughs in the drawn cups. One has to keep in mind that very large uncertainties were involved in the experimental determination of R-value in the case of the rolled and of the partially recrystallized copper and brass, since inhomogeneous deformation and early fracture were reported [12].

Turning now to the recrystallized materials, it can be seen from Figs. 5.38d-i that the CMTP calculations lead to good quantitative agreement with the measured anisotropy. Except perhaps for the fully recrystallized copper sheet, the continuum calculations seem to be more accurate than those of the crystallographic methods, which call for $R(\theta)$ variations which are too large. Finally, it can be observed that the $n = 1.7$ and PL4 criteria lead to almost identical predictions, although the latter has the advantage that it permits much easier and faster computation. Its quadratic form facilitates the necessary inversion of the normality principle.

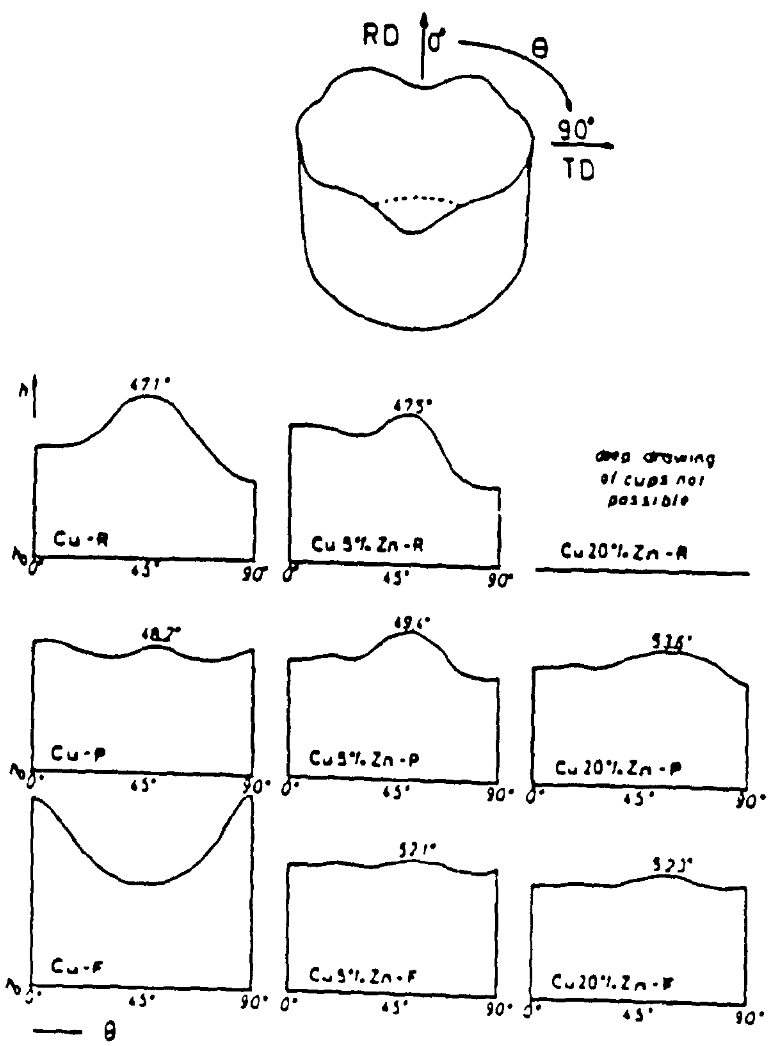

Fig. 5.39 Experimental earing behaviour of rolled (R), partially recrystallized (P) and fully recrystallized (F) Cu, Cu-5%Zn and Cu-20%Zn. After [12].

Results of Stephens [163]

Stephens studied texture and mechanical anisotropy in the copper-zinc system. Since no CODF facility was available to him, the volume fractions of the various texture components present in his materials were estimated directly from the pole figures, i.e. with a certain degree of uncertainty. Specimens were cut from the various cold rolled sheets at angles of 0, 10,..., 90° to the rolling direction in order to measure both the yield stresses and the strain rate ratios. Three major texture components were detected, i.e. the $\{311\}<\bar{1}12>$, $\{110\}<1\bar{1}2>$ (Bs) and $\{110\}<001>$ (Goss) orientations in different volume fraction ratios. The results obtained with the three CMTP criteria are presented in Fig. 5.40 a-d. The predictions of the disoriented crystallographic method are not reported here, as these were found to overestimate the $R(\theta)$ variations by a very large amount and to lead to unreasonably pronounced peaks and troughs. By contrast, the CMTP predictions agree well with the experimental values for all four materials investigated. As mentioned earlier, the $n = 1.7$ and PL4 functions lead to very similar results and show an acceptable ability to reproduce the experimental R variations, although a slight overestimation of the Lankford coefficients is observed.

Results of Arminjon [126]

The textures pertaining to the five grades of steels studied by Arminjon were decomposed into the four major components $\{111\}<1\bar{1}0>$, $\{111\}<11\bar{2}>$, $\{554\}<22\bar{5}>$ and $\{011\}<100>$. The experimental and theoretical $R(\theta)$ curves are shown in Figs. 5.41 a-e. It can be seen that the $n = 2$ predictions underestimate the variation in the Lankford coefficients to a considerable degree. This is not surprising when reference is made to Fig. 5.2a for the orientations considered here. By contrast, the PL4 criterion seems to overestimate the R variation amplitude. Furthermore, the peaks predicted at $\theta = 30$ and 60° (see also Fig. 5.2c) do not appear in the cups drawn from these steels. Finally, the calculations based on the $n = 1.7$ function are in reasonable agreement with the experimental R-values but are still unable to reproduce the full range of the deviations with θ.

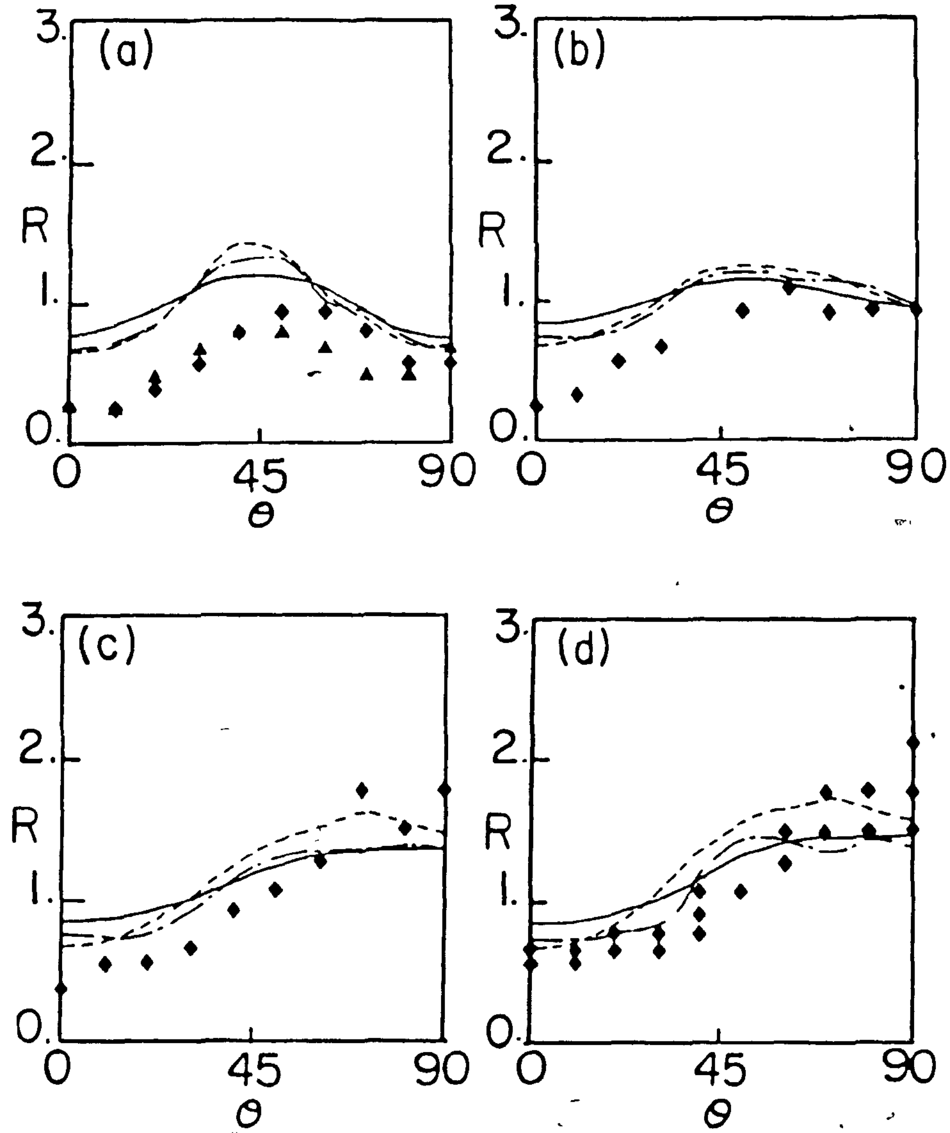

Fig. 5.40 R(θ) curves for copper and brass sheets; (◆)experimental R-values from Ref. [140]. (———) CMTP n = 2; (– – – – –) CMTP n = 1.7 and (—— ——) CMTP PL4 predictions. The texture components employed are {311}<$\bar{1}$12>, {110}<1$\bar{1}$2> and {110}<001> in the volume fraction ratios : (a) 4:2:0 for Cu (◆) and Cu-2.5%Zn (▲) ; (b) 3:2:1 for Cu-5%Zn; (c) 1:4:2 for Cu-10%Zn and (d) 0:5:2 for Cu-15%Zn, Cu-20%Zn, Cu-25%Zn, Cu-30%Zn and Cu-35%Zn.

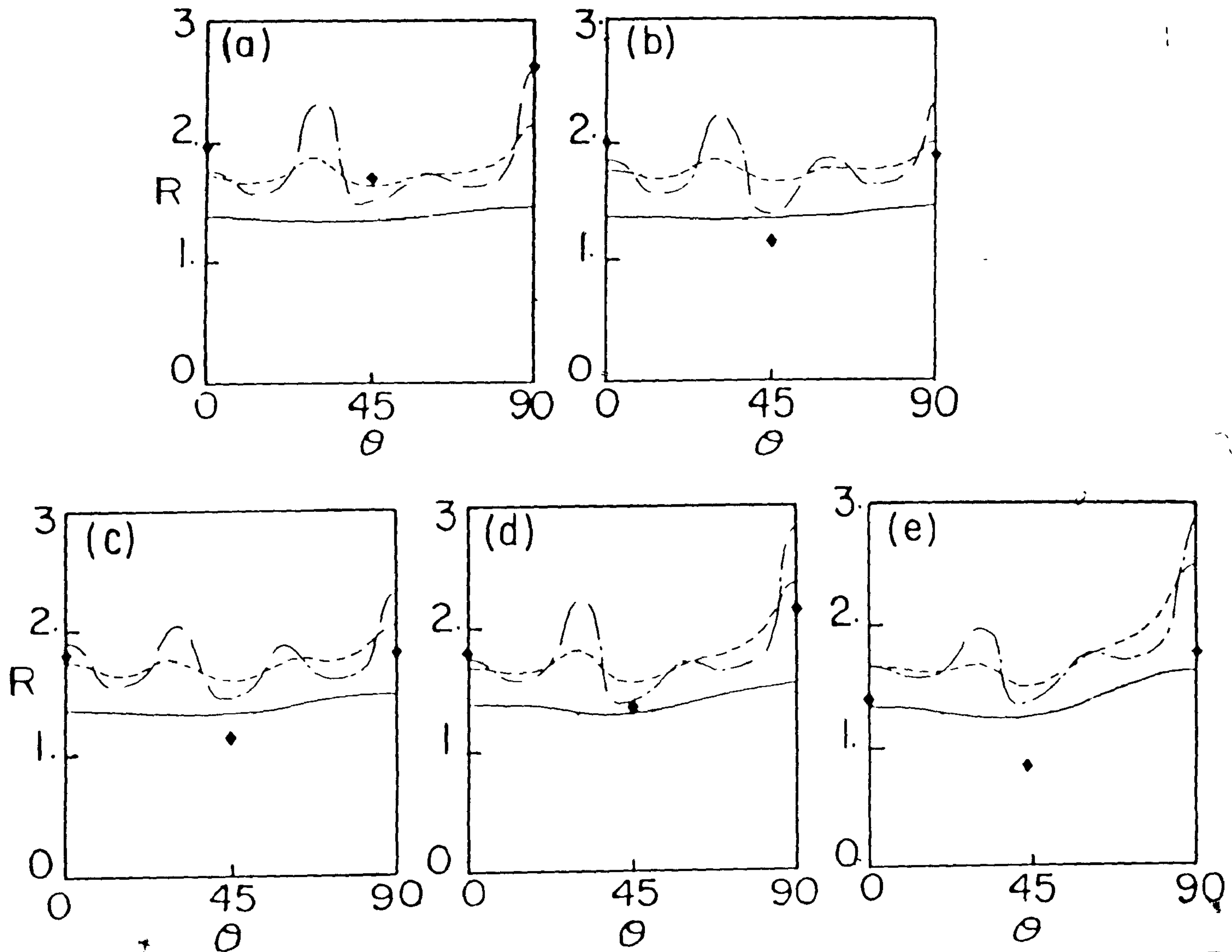

Fig 5 41 $R(\theta)$ curves for various grades of steel; (◆) experimental R-values taken from Ref [126]. (———) CMTP $n = 2$; (– – – – – –) CMTP $n = 1.7$ and (– — –) CMTP PL4 predictions. The texture components used are $\{554\}<22\bar{5}>$, $\{111\}<1\bar{1}0>$, $\{111\}<11\bar{2}>$ and $\{110\}<001>$ in the volume fraction ratios : (a) 25·25:50:0 for steel 1; (b) 15.35:50:0 for steel 2; (c) 30:40:30:0 for steel 3; (d) 50:20.30:0 for steel 4 and (e) 45:20:20:5 for steel 5

Results of Elias et al [106]

These are related to two grades of low C steel sheet · an Al-killed steel with a {111} type of texture and a rimmed steel heavily reduced and annealed displaying a combination of {100}<011> and {111}<11$\overline{2}$> components. The three CMTP criteria investigated lead to good agreement with experiment in the former case (Fig 5 42a); in the latter (Fig 5 42b), however, the limitations pertaining to the results of Arminjon [126] once again seem to apply

Results of Ito et al. [123]

The texture determinations of Ito and coworkers on cold rolled steel sheet were used in the same manner. Three different textures were produced and tensile tests were carried out to measure the R-values at a strain of 0 15 It is evident from Fig 5 43c that the sharp R-value variation is well predicted However, in the case of the first two steels, a somewhat less convincing prediction is obtained (Fig 5.43 a-b), in that the overall level of R is somewhat high

Results of Stickels and Mould [108] and Semiatin et al. [104]

R-value measurements for an Al-killed steel taken from these two papers are reported in Fig. 5.44. The CMTP predictions are consistent with the experimental strain rate ratios, but call for somewhat more variation than may be detectable experimentally, as already noted for the other types of steel discussed above.

Results of Parnière [135]

Similar comments hold for the R(θ) predictions obtained from the work of Parnière. The texture components used are those of Table V.5. The crystallographic predictions based on the Bishop and Hill yield surfaces of Figs. 5.24 at the five angles $\theta = 0$, 22.5, 45, 67.5 and 90° are illustrated in Fig. 5.45b. In the case of the first material (Al-killed steel), the results lie entirely outside the plotting frame; for the rimming steel, they also strongly overestimate the

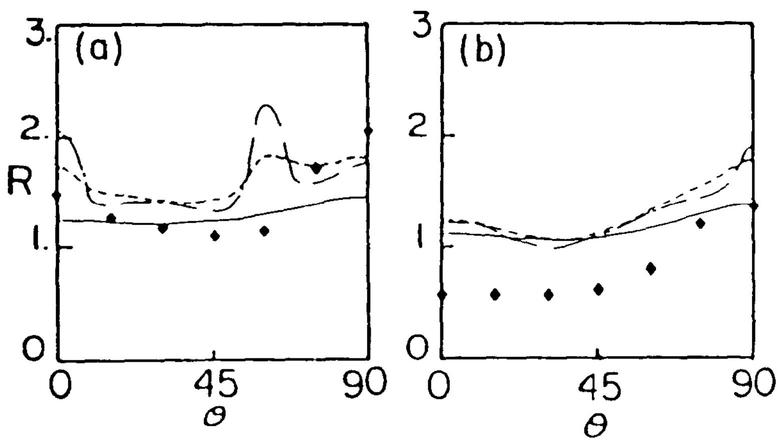

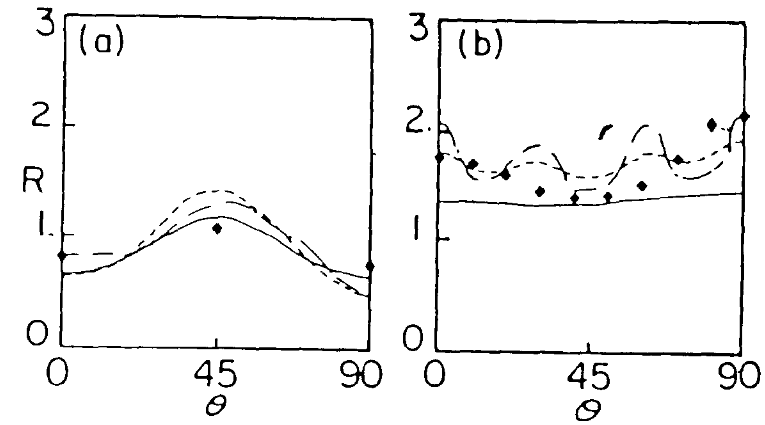

Fig. 5.42 R(θ) curves for two grades of low C steel sheet; (◆) experimental R-values from Ref. [106]. (————) CMTP n = 2; (– – – – – – –) CMTP n = 1.7 and (—— · —— —) CMTP PL4 predictions for (a) a rimmed steel with 40% {100}<011> + 40% {111}<11$\bar{2}$> + 20% random; and (b) an Al-killed steel with 50% {111}<1$\bar{1}$0> + 25% {111}<11$\bar{2}$> + 25% {554}<22$\bar{5}$> components.

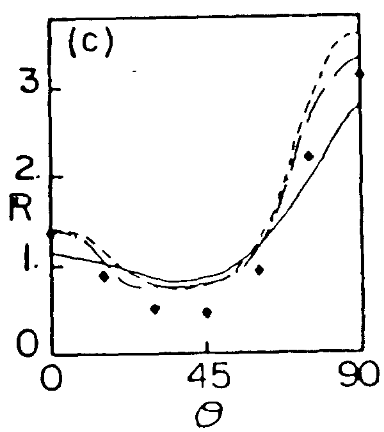

Fig 5.43 R(θ) curves for cold rolled steel sheet; (◆) experimental R-values taken from Ref. [123]. (————) CMTP n = 2; (– – – – – – –) CMTP n = 1.7 and (—— · —— · ——) CMTP PL4 predictions for steel sheets displaying (a) 60% {111}<01$\bar{1}$> + 10% {111}<11$\bar{2}$> + 10% {110}<001> + 20% random; (b) 10% {110}<001> + 20% {111}<11$\bar{2}$> + 70% random; and (c) 60% {110}<001> + 20% {112}<1$\bar{1}$0> + 20% random orientations.

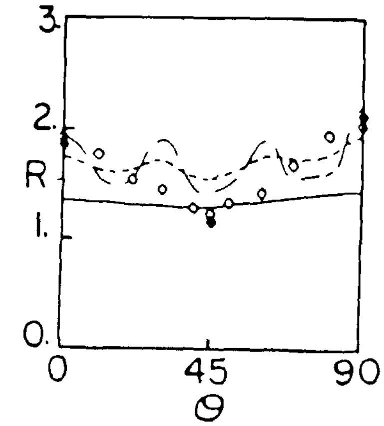

Fig 5.44 R(θ) curves for an Al-killed steel; experimental R-values taken from Refs 108 (◇) and 104 (◆). (————) CMTP n = 2, (– – – – – –) CMTP n = 1 7; and (—— ——) CMTP PL4 predictions The texture was decomposed into 40% $\{111\}\langle 1\bar{1}0\rangle$ + 25% $\{111\}\langle 11\bar{2}\rangle$ + 25% $\{554\}\langle 22\bar{5}\rangle$ + 10% random orientations

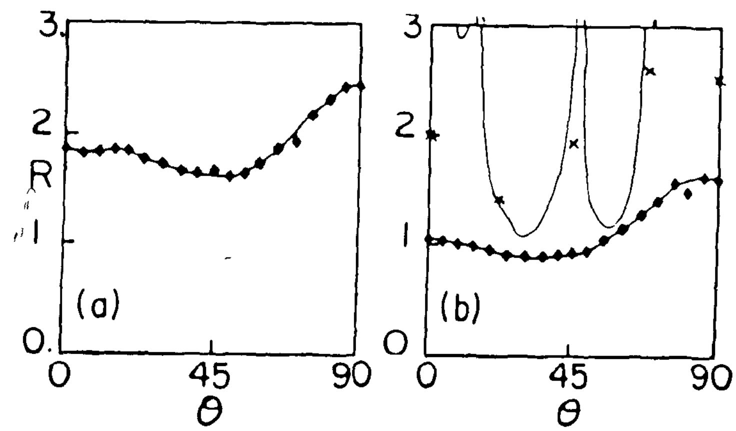

Fig. 5.45 R(θ) curves for (a) an Al-killed steel and (b) a rimming steel; (◆) experimental R-values taken from Ref. [135]. (x) R-values derived geometrically from the Bishop and Hill yield surfaces of Fig. 5.24; (————) R(θ) curves deduced from the disoriented crystallographic function of Eqs. 3.25 In case (a), the two crystallographic predictions lie entirely outside the frame of the drawing.

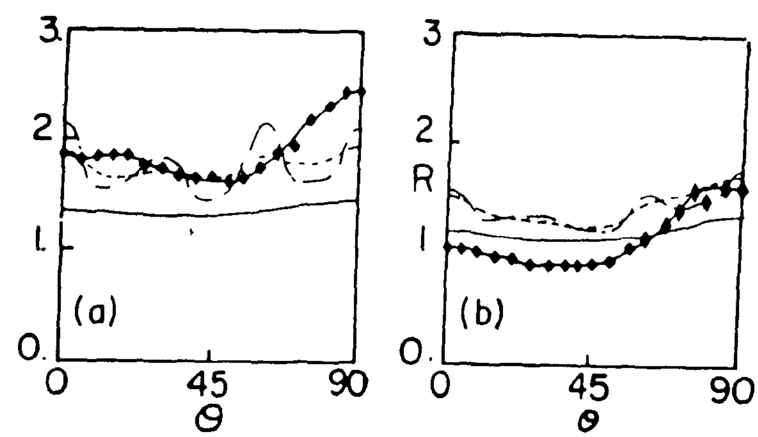

Fig. 5.46 R(θ) curves for (a) an Al-killed steel and (b) a rimming steel; (◆) experimental R-values taken from Ref. [135]. (————) CMTP n = 2; (– – – – – –) CMTP n = 1.7; and (—·——·—) CMTP PL4 predictions. The textures used for the two steels are displayed in Table V.5.

R(θ) curve. Similar divergences are obtained with the disoriented crystallographic method (Eqs. 3.25). By contrast, much better agreement is observed with respect to the CMTP predictions, Fig. 5.46, although the variation in R-value is not fully foreseen.

Results of Benferrah [65]

In a study of the development of anisotropy during the cold rolling of aluminum sheet, Benferrah carried out some tensile experiments at three angles $\theta = 0$, 45 and 90° on his rolled materials. Only the R-values pertaining to small rolling reductions ($\bar{\varepsilon} \leqslant 0.52$) could be measured directly, as inhomogeneous deformation occurred in the thinner sheets. His experimental results together with the CMTP predictions are illustrated in Fig 5.47, in which relatively good agreement is observed.

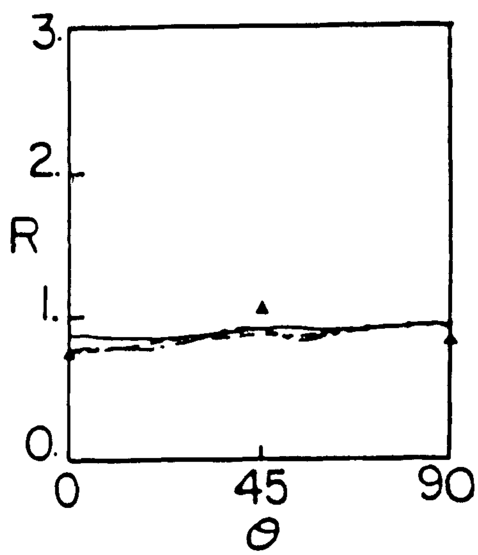

Fig. 5.47 R(θ) curves for a commercial purity aluminum sheet; (▲) experimental R-values taken from Ref. [65]. (————) CMTP n = 2; (– – – – – –) CMTP n = 1.7; and (—·—) CMTP PL4 predictions. The texture employed consisted of 25% {100}<001> + 25% {110}<1$\bar{1}$2> + 15% {123}<63$\bar{4}$> + 5% {112}<11$\bar{1}$> + 30% random components [65].

General considerations

From all these comparisons, carried out on both FCC and BCC metals, it can be concluded that the CMTP predictions agree better in most of the cases with the experimental R-values than the results of the crystallographic approach. It should be kept in mind, however, that these calculations are all based on a uniform strain approach. A more detailed discussion of the various deformation models will be carried out in Chapter VI. It should be noted here that large errors can be produced in the crystallographic calculations when fitting tangents to angular yield loci. Of interest also is the fact that CMTP calculations based on the Sachs assumption (and not reported here) do not lead to significant differences with respect to those carried out according to the Taylor model. As already discussed above for the yield surface predictions, this can be attributed to the much smoother nature of the CMTP functions.

An important feature of the present results involves the relative weakness of the CMTP functions in reproducing the full extent of the R-variations, especially for the steels displaying a {111} type of texture. In this case, a slip plane lies parallel to the rolling plane, so that very large shear stresses are expected to develop in the deformed materials The predictions obtained are consequently highly dependent on how well the CMTP functions fit the 'real' locus in this particular subspace. This is illustrated in Fig. 4.4 for the $n = 2$ and $n = 1.7$ loci, from which it can be noted that the C types of vertices are better approximated by the latter criterion. It is thus not surprising that the $n = 1.7$ yield function leads in this case to a better reproduction of the $R(\theta)$ curves. However, these improvements are obtained at the cost of increased computing time. To be more specific on this point, some data are reported in Table V.7. These are related to the time needed on an IBM PC AT microcomputer fitted with a DSI32 acceleration board in order to calculate the strain rate ratio $R(\theta)$, as well as the uniaxial $\sigma(\theta)$ and biaxial σ_b yield stresses for one ideal orientation (including the four rolling symmetries) at a specific angle θ. The large difference observed between the $n = 2$ or PL4 criterion on the one hand and the $n = 1.7$ function on the other is solely due to the necessary inversion of the normality rule, which has to be carried out numerically (as opposed to analytically) in the latter case.

V.2.3.3. *Yield stress predictions*

Yield stresses can be predicted by the classical crystallographic method, as has been done by Svensson [32] or Sowerby et al. [69], for example. In this

Yield criterion	Time to compute R(θ) at 19 values of θ (θ = 0, 5,..., 90°)		Computing time per orientation (+ symmetries) and per angle θ (no random component)
	for 3 orientations (+ their symmetries)	for 3 orientations (+ their symmetries) + random component	
CMTP n = 2	24 sec	40 sec	0.42 sec
CMTP n = 1.7	360 sec	403 sec	6.32 sec
CMTP PL4	35 sec	51 sec	0.61 sec
CMTP PL3	39 sec	55 sec	0.68 sec
disoriented crystallogra. function (Eqs.3.18)	90 sec	107 sec	1.58 sec

Table V.7. Comparison of the computing times necessary to calculate R(θ) values according to different CMTP criteria when using the uniform strain assumption. The computer employed was an IBM PC AT extended with a DSI 32 acceleration board.

section, the texture components displayed by the material before the tensile test is performed are used to estimate the yield stress ratio σ(θ)/σ(0) by means of the various CMTP criteria. The theoretical bases for these calculations have been given in Chapter IV.

Results of Stephens [140]

The experimental investigation carried out by Stephens and already presented in the previous section included yield stress measurements These are reported in Figs. 5.48 a-d for the various brasses studied. The CMTP predictions based on the n = 2 (full lines), n = 1 7 (dashed lines) and PL4 (mixed lines) criteria are seen to be in good agreement with experiment, especially when it is considered that the textures were decomposed into only two or three components (plus their symmetries).

Results of Kallend and Davies [14,15]

Kallend and Davies employed the CODF technique of texture characterization together with Taylor averaging and the Bishop and Hill maximum work procedure to calculate yield stresses in cold rolled and annealed copper and brasses. They found good agreement with the experimental measurements of the 0.2% proof stresses [14,15]. CMTP predictions were made by using the texture components they reported. The results obtained in this way are presented in Figs. 5.49 a-e. It is apparent that the predicted yield stress ratios are consistent with the observed values for both the rolled and annealed materials. Nevertheless, the theory leads to *larger* deviations in this case than those measured, especially in the brasses and in the near diagonal (θ = 45°) tensile directions.

Results of Svensson [28,32]

Svensson studied the anisotropy of yield strength (0.05% proof stress) in aluminum and steel sheets cold rolled to various reductions. The experimental and CMTP stress ratios are shown in Figs. 5.50 a-c, from which it can be seen that the agreement is not good in the case of the two aluminum sheets : i.e. the measured σ(θ)/σ(0) variations are considerably overestimated by the three

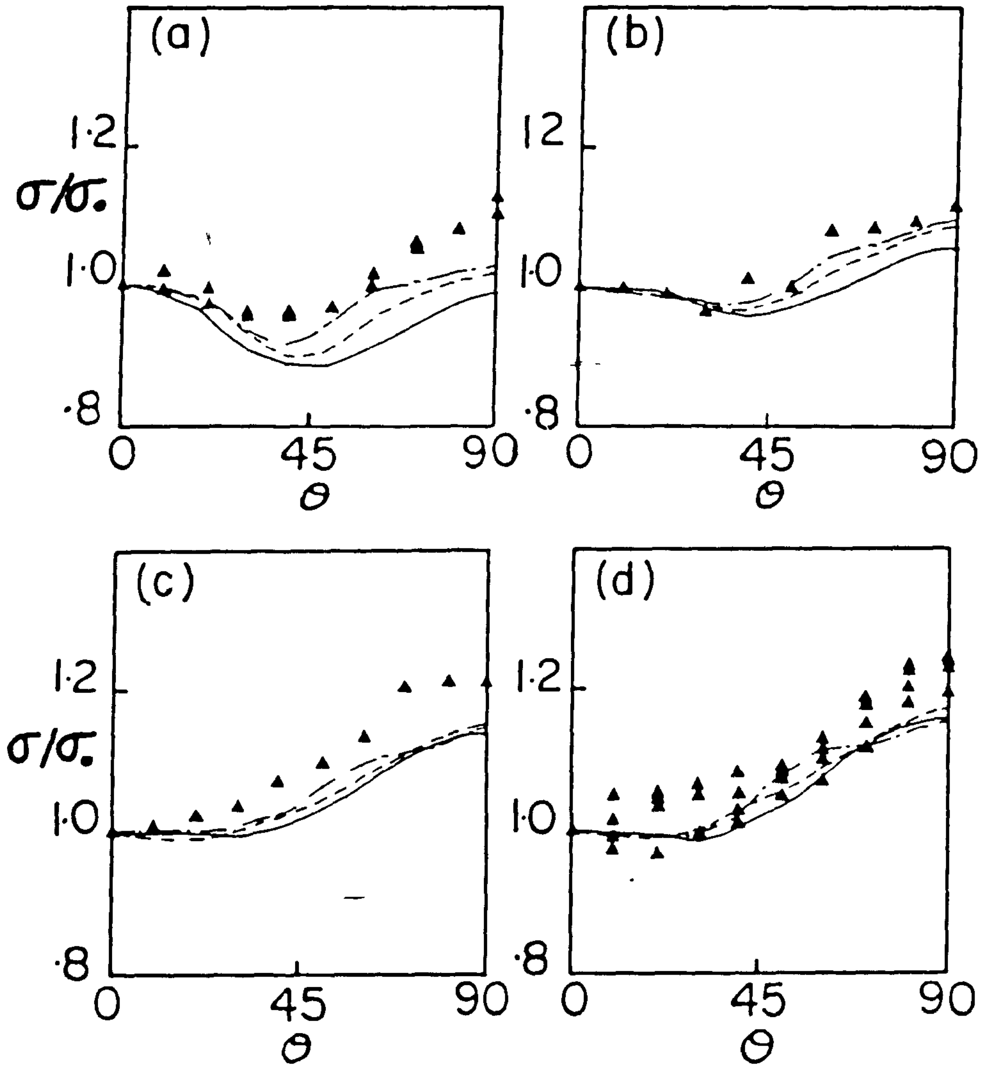

Fig. 5.48 Yield stress ratio σ(θ)/σ(0) curves for Cu and brass sheets; (▲) experimental stress ratios taken from Ref. [140]. (—————) CMTP n = 2; (– – – – – –) CMTP n = 1.7; and (—— · —— · —) CMTP PL4 predictions. The texture components used are the {311}<$\bar{1}$12>, {110}<1$\bar{1}$2> and {110}<001> orientations in the volume fraction ratios : (a) 4:2:0 for Cu and Cu-2.5%Zn; (b) 3:2:1 for Cu-5%Zn; (c) 1:4:2 for Cu-10%Zn and (d) 0:5.2 for Cu-15%Zn, Cu-20%Zn, Cu-25%Zn, Cu-30%Zn and Cu-35%Zn.

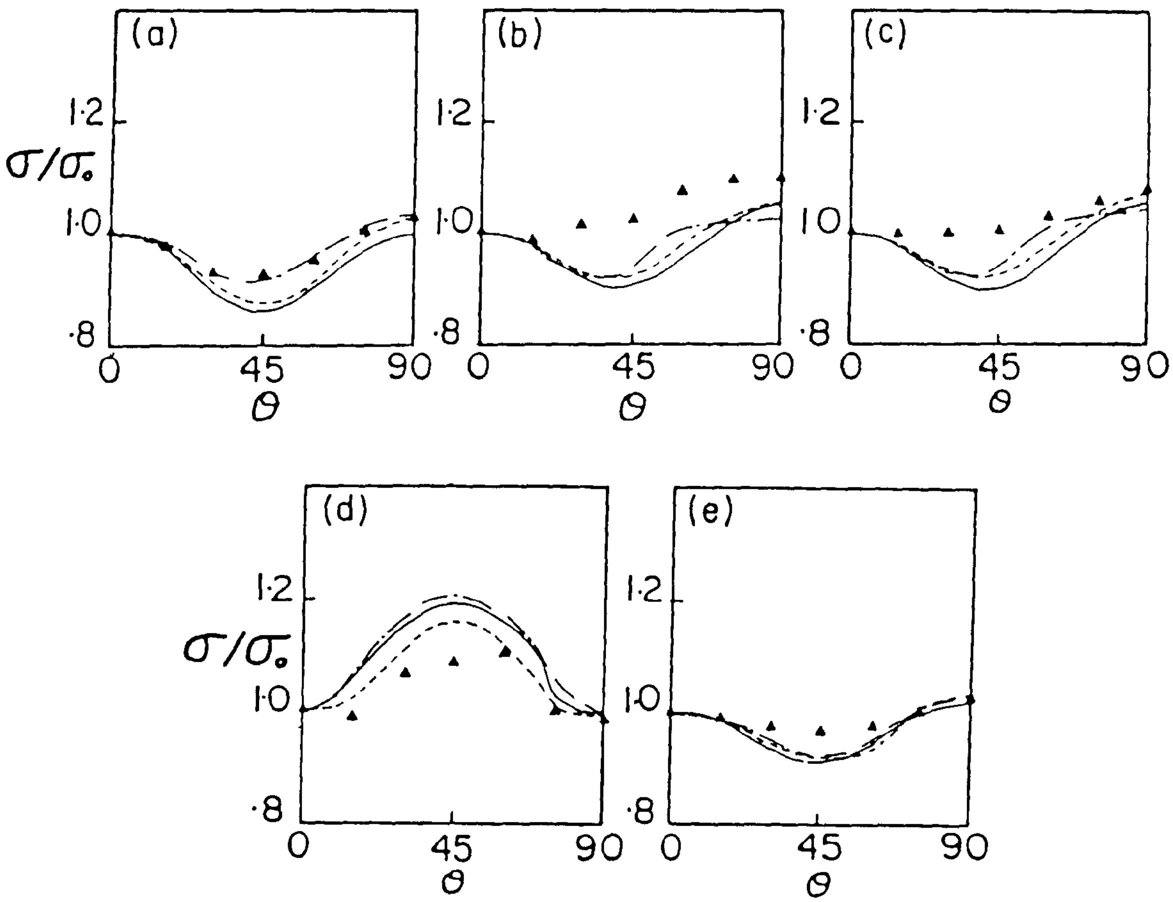

Fig. 5.49 Yield stress ratio σ(θ)/σ(0) curves for rolled and annealed Cu and brass; (▲) experimental stress ratios taken from Refs. [14,15]. (————) CMTP n = 2; (– – – – – – –) CMTP n = 1.7; and (—— · —— · ——) CMTP PL4 predictions for (a) Cu rolled to 90% reduction with 30% {110}<1$\bar{1}$2> + 30% {123}<63$\bar{4}$> + 30% {112}<11$\bar{1}$> + 10% random; (b) Cu-10%Zn cold rolled to 90% reduction with 60% {110}<1$\bar{1}$2> + 10% {123}<63$\bar{4}$> + 10% {111}<1$\bar{1}$0> + 20% random; (c) Cu-30%Zn cold rolled to 90% reduction with 65% {110}<1$\bar{1}$2> + 10% {123}<63$\bar{4}$> + 25% random; (d) annealed Cu with 70% {100}<001> + 10% {100}<011> + 20% random and (e) annealed Cu-30%Zn with 20% {111}<11$\bar{2}$> + 20% {100}<011> +20% {110}<1$\bar{1}$2> + 40 % random.

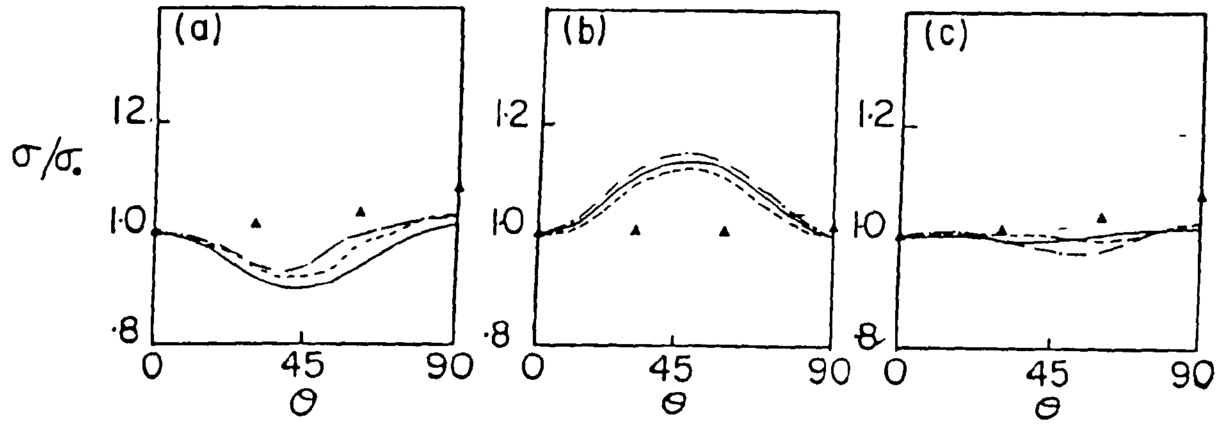

Fig. 5.50 Yield stress ratio $\sigma(\theta)/\sigma(0)$ curves for aluminum and steel sheets; (▲) experimental stress ratios taken from Refs.[28,32]. (————) CMTP n = 2; (– – – – – –) CMTP n = 1.7 and (—— · —— · —) CMTP PL4 predictions for (a) aluminum cold rolled to 80% reduction with 40% {311}<$\bar{1}$12> + 40% {110}<1$\bar{1}$2> + 20% random; (b) aluminum cold rolled to 10% reduction with 40% {100}<001> + 60% random; and (c) steel cold rolled to 80% reduction with 50% {113}<1$\bar{4}$1> + 30% {001}<110> + 20% random.

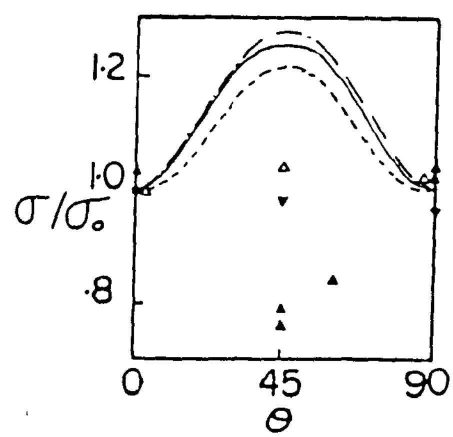

Fig. 5.51 Yield stress ratio $\sigma(\theta)/\sigma(0)$ curves for highly textured copper sheet; (▲) stress ratios [38] for a texture severity of 8.57; (▼) stress ratios [69] for a texture severity of 5.64 and (△) stress ratios [69] for a texture severity of 1.72. (————) CMTP n = 2; (– – – – – – –) CMTP n = 1.7; and (— —· —) CMTP PL4 predictions for a texture made up of 75% {100}<001> + 25% random components.

criteria used. This can be explained, at least in the first case of the specimen containing a high volume fraction of cube component, by the relative inability of the CMTP functions to reproduce the 'true' yield surface in shear stress space, as already noted in the previous section

Results of Viana et al. [38,69]

Experimental stress-strain data were reported by Viana et al. on highly textured copper sheets exhibiting the cube component. An excellent fit was obtained with the CMTP calculations, when the experimental and theoretical R(θ) curves, Fig. 5.3a, were compared. However, the CMTP yield stress predictions are in complete disagreement with the measured values, as seen in Fig. 5.51. The theory predicts an increase in stress ratio followed by a diminution when the test direction θ changes from 0 to 45° and from 45 to 90°; the experimental measurements indicate a reverse variation. However, an interesting feature in the data of Viana et al. is worth noting. The first set of values [38] (▲ in Fig. 5.51) is related to a very severe cube texture (severity parameter * = 8.57); the specimen in this case is nearly equivalent to a single crystal, as noted by the authors [38]. The second set of stresses [69] (▼ in Fig. 5.51) refers to a similar component, but with a texture severity of 5.64: i.e. the cube orientation is more dispersed, as confirmed by the experimental pole figures. The stress ratio in the diagonal direction is observed to be much higher (0.98) than in the first example (about 0.77). Finally, the Δ symbols characterize a cube textured sheet with a severity parameter of only 1.72. In this case, some secondary texture components are present in the material. Fig. 5.51 shows a still higher stress ratio (1.05) pertaining to a tensile test carried out at θ = 45°. The CMTP calculations are in somewhat better agreement, at least from a qualitative point of view, with the last data. This suggests (and also confirms) that the CMTP criteria are more suitable for dispersed orientations (spreads of around 15°) than for near 'single crystal' components.

---

* The severity parameter is defined as the standard deviation of the orientation distribution function from that for a random material [141].

V.2.3.4. *Prediction of other plastic properties*

Strain rate and yield stress ratio calculations are of practical importance as long as they characterize the anisotropic properties of the rolled and annealed sheets used in the production of beverage cans (for Al alloys) or motorcar parts (for steels). From a more theoretical point of view, however, it is of interest to study the plastic behaviour of twisted bars (or tubes), since torsion testing, as opposed to rolling, allows very large deformations to be attained without intermediate annealing.

<u>Torsional axial stresses</u>

No attempt was made in the present investigation to solve completely the texture/plastic anisotropy relationship in twisted samples. This is because Montheillet et al. [5] have already explained the main features of the link between the axial (tensile or compressive) stresses induced during the torsion testing of Al, Cu and α-Fe bars [133] and the textures developed. In this work, the CMTP n = 2 criterion was used and successful qualitative predictions were obtained by means of an analytical description of the axial stresses developed. The aim of the present short section is to review the geometrical derivation of this behaviour, as also discussed by Canova et al. [11].

For this purpose, the $(\sigma_{zz},\sigma_{\theta z})$ yield surface section has to be plotted. When dealing with fixed end torsion testing, the boundary condition $\dot{\varepsilon}_{zz} = 0$ can lead to a positive or a negative (i.e. tensile or compressive) induced axial stress σ_{zz}, as shown in Fig. 5.52a. Similarly, when the specimen is permitted to lengthen or to shorten (free end testing, $\sigma_{zz} = 0$), the $\dot{\varepsilon}_{zz}$ component can be derived from the normality principle and characterizes the rate of length change of the sample (Fig. 5.52b). This purely geometric approach can be applied to the various texture components observed in twisted bars in order to explore their influence on the axial stresses. These are the $\{1\bar{1}1\}<110>$, $\{\bar{1}1\bar{1}\}<\bar{1}\bar{1}0>$, $\{\bar{1}\bar{1}1\}<112>$, $\{11\bar{1}\}<112>$, $\{1\bar{1}2\}<110>$, $\{\bar{1}1\bar{2}\}<\bar{1}\bar{1}0>$ and $\{100\}<011>$ orientations in FCC metals, respectively referred to as A, $\bar{A}$, A_1^*, A_2^*, B, $\bar{B}$ and C in Ref. [133]; here {hkl} is the crystallographic plane near the transverse shear plane and <uvw> is the crystallographic direction near the macroscopic shear direction.

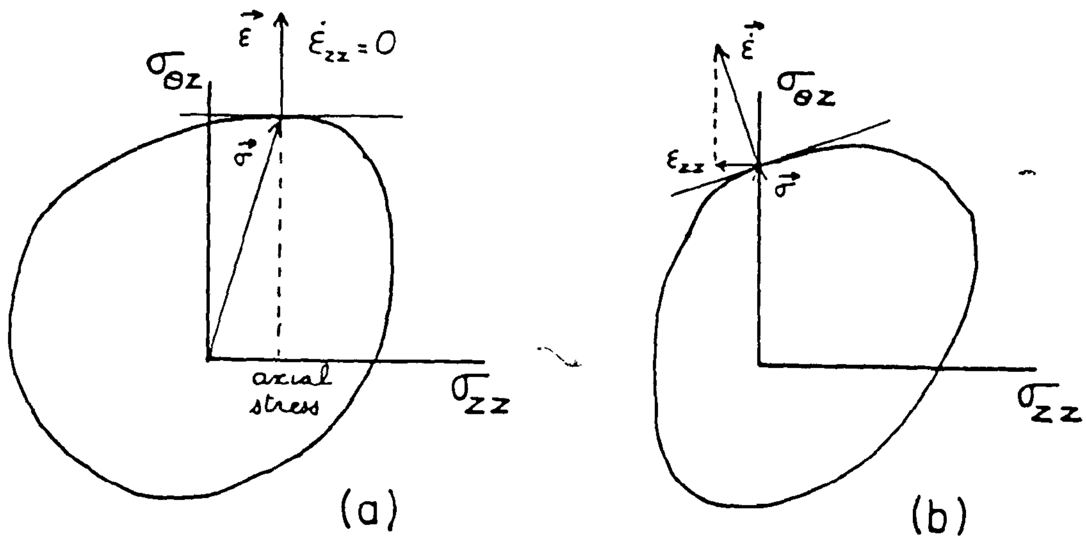

Fig. 5.52 Geometric derivation from the (σ_{zz}, $\sigma_{\theta z}$) yield surface cross-section of: (a) the axial stress developed during fixed end torsion testing; and (b) the rate of length change produced by a free end torsion test.

The crystallographic and CMTP (n = 2) (σ_{zz},$\sigma_{\theta z}$) yield surfaces for the A texture component are compared in Fig. 5.53 for three values of the tilt ϕ around the radial direction frequently observed in torsion pole figures [133]. It can be seen that the axial stresses induced during the fixed end torsion testing of a sample containing this unique orientation are highly dependent on the small tilt angle ϕ. It is also to be noted that the CMTP and crystallographic models predict similar signs for the σ_{zz} component. The results obtained for the other orientations mentioned above confirm the ones obtained analytically by Montheillet et al. [5].

An attempt to generalize the above predictions to polycrystalline materials containing several texture components is shown in Figs. 5.54 and 5.55. An experimental (111) pole figure pertaining to a copper bar twisted to a strain of 0.84 at room temperature (Fig. 5.54a) was simulated in a manner similar to that described in section V.2.1.2. The texture was in this case decomposed into 60% of A/$\bar{A}$ (tilt $\phi = -5°$), 10% of B/$\bar{B}$ (tilt $\phi = 0°$), 25% of C (tilt $\phi = -5°$) and 5%

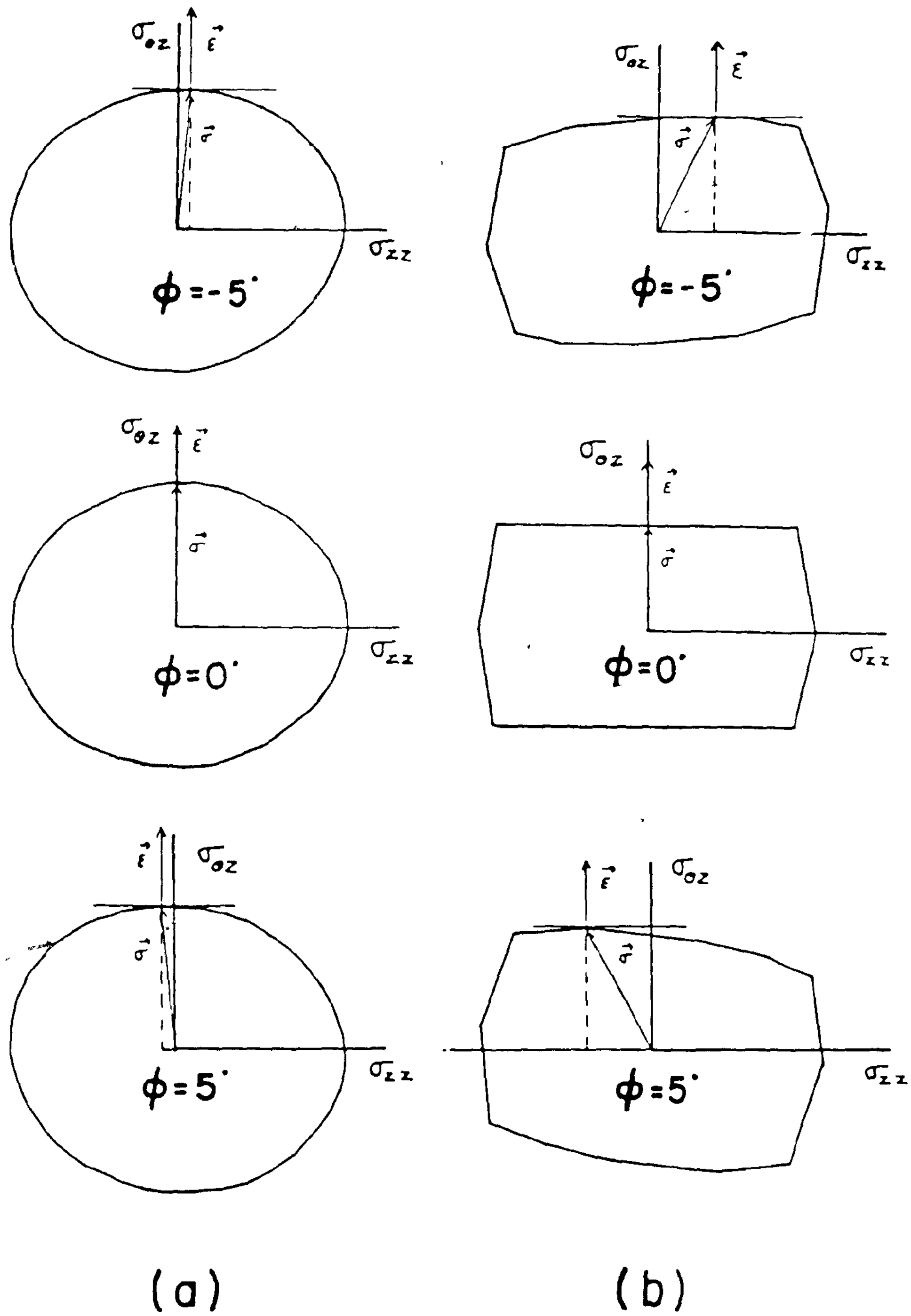

Fig. 5.53 (σ_{zz},$\sigma_{\theta z}$) yield surface cross-sections corresponding to the {1$\bar{1}$1}<110> orientation for three values of the tilt angle ϕ around the radial direction observed on experimental pole figures : $\phi = -5°$, $\phi = 0°$ and $\phi = +5°$. (a) CMTP n = 2 predictions and (b) crystallographic approach.

of A_1^* (tilt $\phi = 0°$), all with a spread $\omega_0 = 12.5°$. The result of this simulation is shown in Fig 5.54b, from which a reasonable similarity with the experimental pole figure is observed. The $(\sigma_{zz}, \sigma_{\theta z})$ yield surfaces (calculated from a representative set of 200 grain orientations in the case of the crystallographic approach and from the 6 components cited above with their respective weights in the case of the two CMTP calculations) are shown in Fig. 5 55. Slight inclinations of these loci are observed, which are nevertheless difficult to quantify, indicative of a positive (compressive) axial force. This is consistent with the experimental axial force/strain curves reported in Ref [133] However, as accurate quantitative forces are difficult to produce from this simple geometric approach, it is not known if the amplitudes of the predicted stresses are reasonable or not

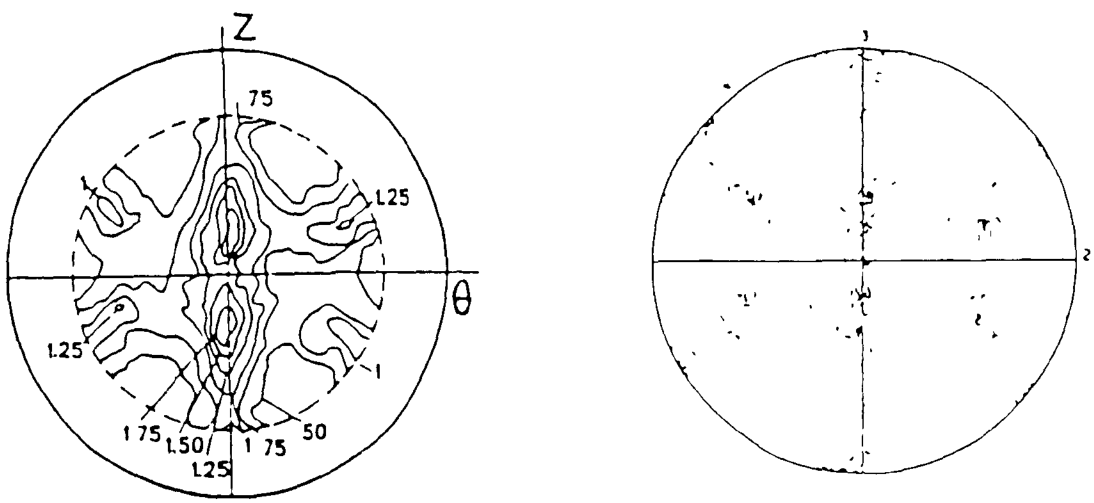

(a) (b)

Fig. 5.54 (a) Experimental [133] and (b) simulated {111} pole figures corresponding to a copper bar twisted to $\bar{\varepsilon} = 0.84$ at room temperature

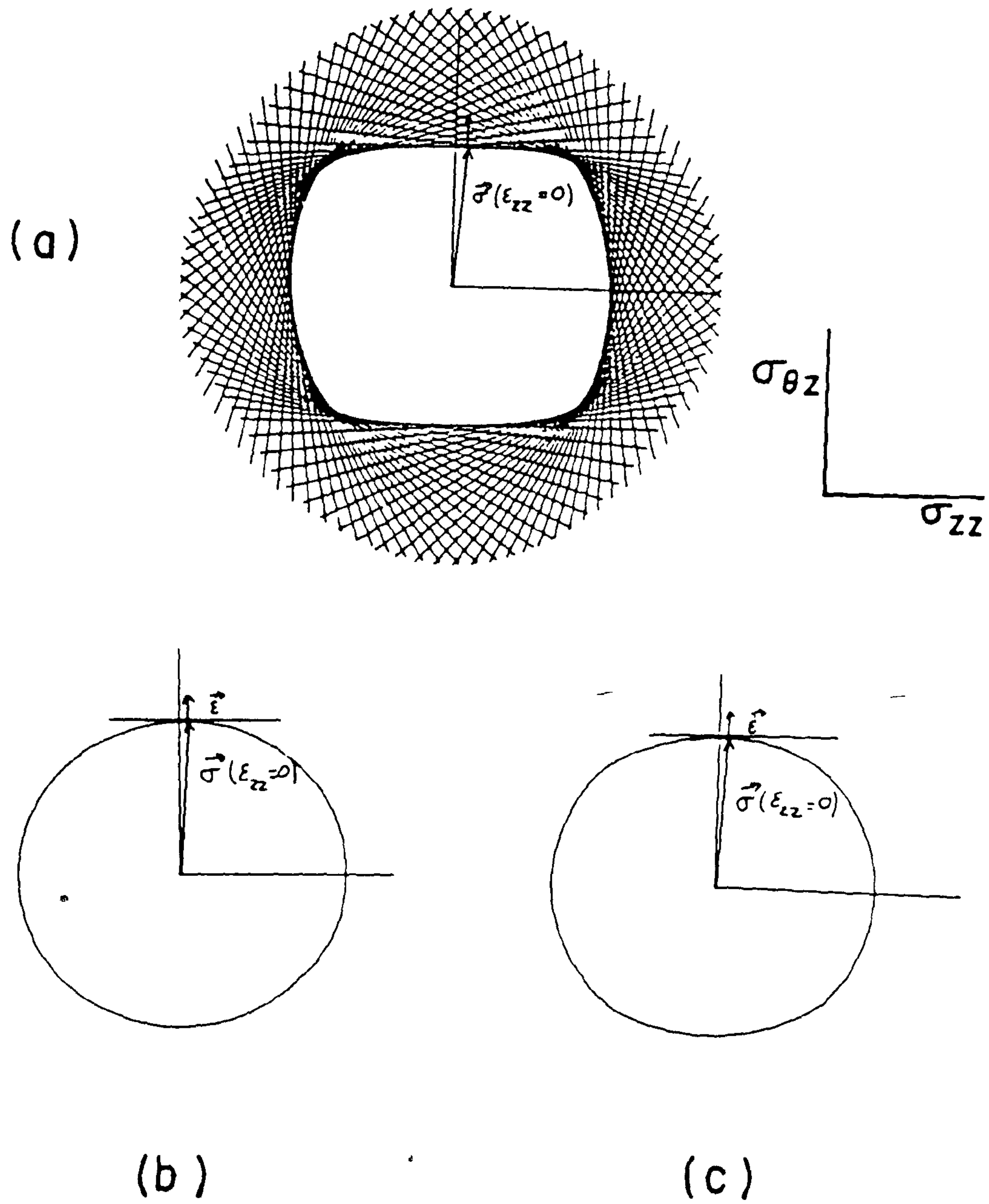

Fig. 5.55 (σ_{zz},$\sigma_{\theta z}$) yield surface cross-sections corresponding to a copper bar twisted to $\bar{\varepsilon}=0.84$ at room temperature. (a) crystallographic results obtained from a 200 grain orientation distribution; (b) CMTP n = 2 and (c) CMTP n = 1 7 calculations based on a texture made up of 60% A/$\bar{\text{A}}$ (tilt = −5°) + 10% B/$\bar{\text{B}}$ (tilt = 0°) + 25% C (tilt = −5°) + 5% A_1* (tilt = 0°) orientations.

Anomalous behaviour

The study of anomalous behaviour ($\sigma_b/\overline{\sigma_u} < 1$ together with $\overline{R} > 1$) carried out in section V.1.4 will now be generalized to polycrystalline materials containing more than one ideal orientation. In this case, the average strain rate ratio $\overline{R}$ and uniaxial yield stress $\overline{\sigma_u}$ (here averaging means over the angles θ) can be evaluated, for example, by the uniform strain assumption applied to the various CMTP criteria. The biaxial stress only needs to be calculated in one direction θ, as long as it does not depend on the testing direction. This is because a biaxial stress state ($\sigma_{11} = \sigma_{22}$) is equivalent to a through thickness (σ_{33}) compression state, as long as the superposition of a hydrostatic pressure is assumed not to influence plastic yielding. Thus the through thickness behaviour is not modified by the planar anisotropy which may be observed in the sheet plane.

Such calculations of the $\sigma_b/\overline{\sigma_u}$ and $\overline{R}$ ratios were carried out for all the examples investigated in sections V.2.3 1 and V 2.3.2. The n=2, n=1 7 and PL4 criteria were tested on the various materials using the experimental ideal orientations and their respective weights. From all these data, only one case of 'anomalous behaviour' was found, and that was for the copper sheet studied by Stephens [140]. The latter was rolled to 96% reduction and displayed two major $\{311\}<\bar{1}12>$ and $\{110\}<1\bar{1}2>$ components in a volume fraction ratio 2·1. For this material, the PL4 criterion predicts $\overline{R}$ = 0.973 and $\sigma_b/\overline{\sigma_u}$ = 1.012. It is not known, however, if the latter value is consistent with the experimental observations, as the biaxial stress was not measured by Stephens [140].

CHAPTER VI

DISCUSSION

Considerable attention has been focussed in the fabricating industry on the metallurgical aspects of plastic anisotropy, i.e. on how changes in the fabrication processes affect the texture on the one hand and the macroscopic anisotropy on the other. However, a link has been missing in this chain, i e. a simple quantitative relationship between the texture and the consequent plastic properties has not been available. Such quantifications have in fact been derived and are based on the crystallographic methods associated with the Bishop and Hill single crystal yield surface. This approach has even been extended to the case of slip by pencil glide. The predictions obtained by these means appear to be consistent with experimental results when the crystal orientation distribution is described by the full CODF. However, the crystallographic methods unfortunately lead to lengthy computations and are consequently unsuitable for the rapid assessment of plastic properties. Moreover, they are still undergoing rapid development and have not yet been stabilized into a standardized procedure. By contrast, the CMTP method provides an alternative, very simple way to quantify the texture/plastic anisotropy relationship, as discussed in the previous chapters.

In this chapter, the first section is concerned with some of the metallurgical parameters that can affect the texture of metal sheets. Some of the practical uses of the CMTP method are also given, before a critical examination of the various deformation models is carried out. Finally, the main advantages and limitations of the CMTP model are considered in turn.

VI.1. The relationship between texture and certain metallurgical parameters

The study of the plastic properties induced in deformed materials is a very difficult matter if one wants to take account of the full set of parameters which can play a role in the fabrication process. In this work, only the crystallographic anisotropy (or texture) has been considered as long as it is recognized to be the primary source of plastic anisotropy. However, one has to keep in mind that the final texture of a sheet results from all the successive modifications undergone by the initial texture during the various fabrication stages. For example, the hot rolled texture depends on the hot rolling characteristics, e.g. the temperature of the ingot as well as the rolling and cooling temperatures. The cold rolling texture, on the other hand, is influenced by the total reduction applied to the sheet, by the amount of reduction per pass, as well as by the hot rolling texture. Finally, the annealing texture is dependent on the heating rate, the annealing time and temperature, the atmosphere employed and the previous treatments of the sheet. It is thus possible to favor or to diminish the volume fraction of certain texture components 'at will' by varying these parameters.

Blickwede [31] published an excellent review paper on the influence of some of the rolling and material characteristics on the strain rate ratio R as well as on the strain hardening exponent n. For good stretchability, a high value of n is desired in order to avoid localized necking early in the stretching process. Similarly, high $\bar{R}$ and low planar ΔR strain rate ratios are recommended for good drawability. The problem is thus : how to obtain these two specific properties in combination?

It appears [31] that control of the strain hardening exponent of steel sheets can be reduced mainly to control of the grain size : a larger grain size is associated with a higher value of n. However, the former is concurrently detrimental to the surface appearance after forming. The average strain rate ratio $\bar{R}$ is raised by the presence of a {111} type of texture, which also reduces the planar anisotropy (ΔR). The latter texture is frequently observed after recrystallization at the expense of the {100} exponent; this is because the {111}-

oriented grains have the highest stored energy, so that they are the first to recrystallize. A larger $\bar{R}$-value seems to be obtained by increasing both the annealing temperature and the grain size. In this case, the recrystallized {111} grains continue to grow at the expense of the other orientations; such oriented grain growth thus favors the production of higher $\bar{R}$-values. Consequently, a low heating rate (leading to a larger grain size) as well as a long time at high temperature are both desirable. The interested reader is referred to Ref. [31] for a detailed discussion of these metallurgical factors.

VI.2 Some practical uses of the CMTP method

A question the reader may ask is the following : how can the CMTP method be applied to on-line measurements? The comparisons carried out in chapter V between theoretical (CMTP) and experimental $R(\theta)$ curves show that good agreement is observed when only a few texture components (say 3 or 4 plus their rolling symmetries) are considered. It is thus not unrealistic to think of an experimental device which could assess quickly the relative intensities of these 3 or 4 orientations. Such a device would be composed of 3 or 4 X-ray facilities oriented in 3 or 4 specific Bragg directions of interest. The assessment of the relative weights of the texture components is in this case very fast, as is the CMTP estimation of the corresponding $R(\theta)$ and/or $\sigma(\theta)$ curves. The metallurgical parameters affecting the texture can consequently be adjusted on line until the desired anisotropy (or absence of anisotropy) is attained. For rolled FCC metals, the orientations that play a significant role are the Bs- $\{011\}<1\bar{1}2>$, S- $\{123\}<63\bar{4}>$, Cu- $\{112\}<11\bar{1}>$ and Cube- $\{100\}<001>$ components; by contrast,the {100} and {111} types of textures have to be investigated in steel sheets.

Another interesting practical application of the CMTP method is related to the possible series development of the calculated analytical expressions for $R(\theta)$ and $\sigma(\theta)$. This approach is currently under investigation at the ALCAN research laboratories in Kingston [142]. According to this method, the orientation distribution function $f(g)$ is used as a weighting factor in the calculation of the $R(\theta)$ (or $\sigma(\theta)$) coefficients pertaining to the polycrystalline aggregate ·

$$R(\theta)_{(polycrystal)} = \int f(g)\, R(\theta, g)\, dg \qquad (6.1)$$

Here $R(\theta,g)$ is the analytic CMTP expression for the strain rate ratio corresponding to a given orientation g. Normally the CODF f(g) is not known analytically (unfortunately!); thus $R(\theta,g)$ has to be expanded in the form of a Fourier series with certain R_{lmn} coefficients to give $R(\theta)$ for the polycrystal. The application of such a technique to aluminum alloys, Fig. 6.1, reveals the weakness of the $n=2$ criterion (which was the only one to be tested) in reproducing the full extent of actual $\sigma(\theta)$ variations, as already noted above. This problem is accentuated by the variability in the $R(\theta)$ measurements which are generally used for comparison purposes, as shown in Fig. 6.2. Here it can be seen that the strain rate ratio is highly dependent on the length strain in the tensile test and that accurate R-values cannot be ascribed to the specimens at low strains. Nevertheless, without entering into detailed comparisons, it appears that the $R(\theta)$ curves predicted by the CMTP $n=2$ function and averaged by the CODF technique (Eq. 6.1) are not able to reproduce the observed variations with accuracy. A possible improvement could come from the use of the $n=1.7$ or PL4 criteria. Also another averaging technique could be used such as the following :

$$R(\theta)_{(polycrystal)} = \frac{\int f(g)\, \dot{\varepsilon}_{22}(\theta, g)\, dg}{\int f(g)\, \dot{\varepsilon}_{33}(\theta, g)\, dg} \qquad (6.2)$$

This is based on the Kochendorfer [143] (law of mixtures) model of averaging, which is discussed in more detail in section VI.3 below. Furthermore, the necessity of using a CODF representation in conjunction with the CMTP model should also be questioned. It has been shown indeed (see chapters III and IV) that the CMTP function already takes into account a certain dispersion (10 to 15°) about a specific ideal orientation. As a result, the complete texture of a given material need only be decomposed into a limited number of disoriented components. In fact, using the full CODF apparently leads to an 'oversmoothing' of the CMTP polycrystal yield surface (in as much as the 'single

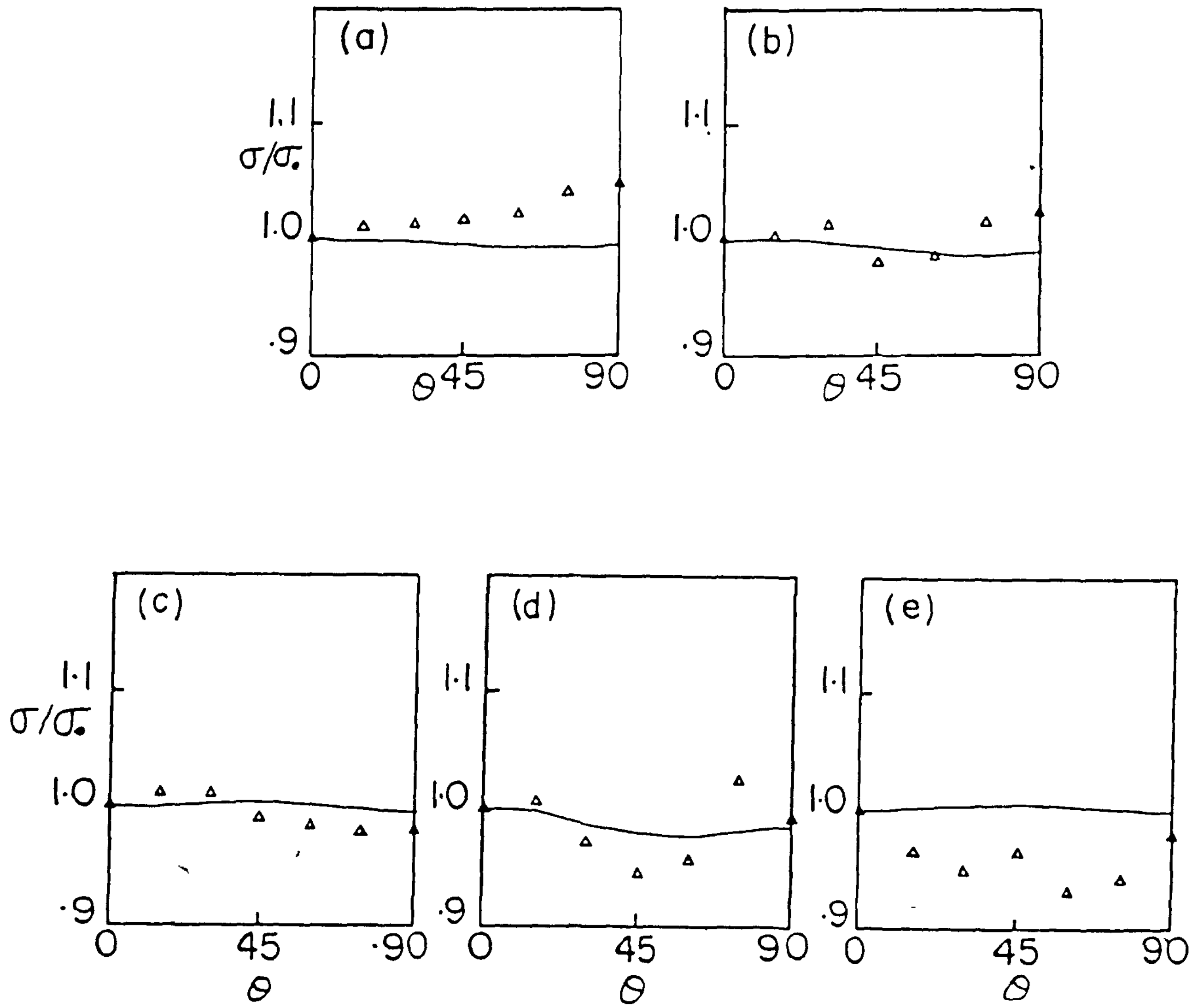

Fig. 6.1 Yield stress ratios $\sigma(\theta)/\sigma(0)$ predicted by the CMTP $n = 2$ method used in conjunction with the CODF technique of texture representation An averaging procedure similar to that specified by Eq. 6.1 was used. Calculations and experimental points from Ref. [142]. Commercial purity 1100 Al (a) cold rolled 30%; (b) cold rolled 60%; (c) cold rolled 60% and annealed; (d) cold rolled 90%; and (e) cold rolled 90% and annealed.

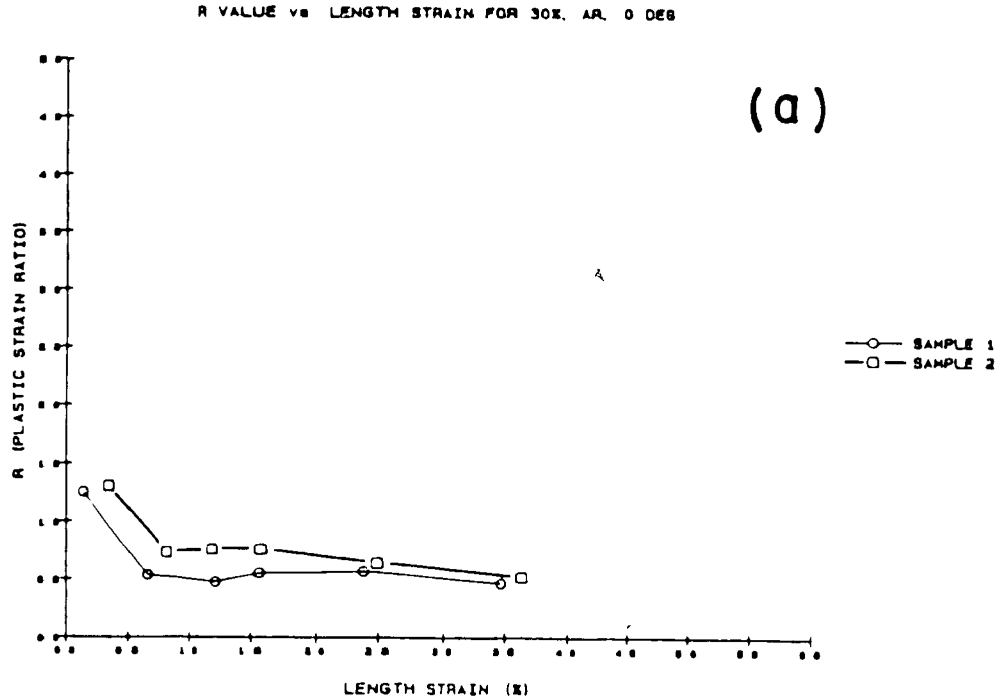

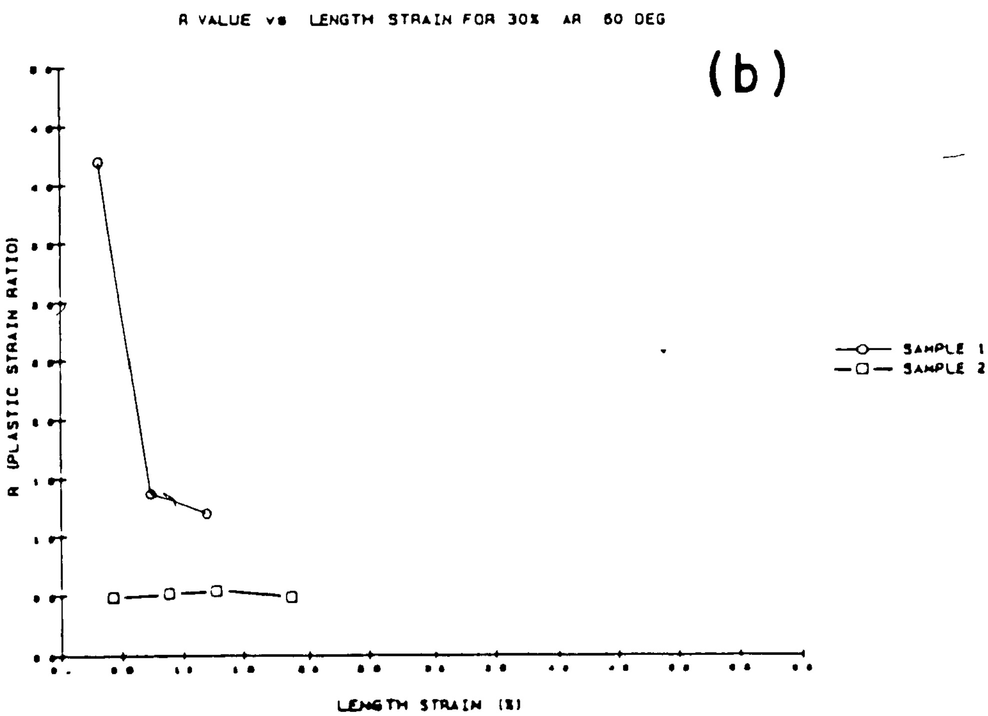

Fig. 6.2 R-value vs length strain for an 1100 Al sheet cold rolled 30%. (a) $\theta = 0$ and (b) $\theta = 60°$. From Ref. [142].

crystal' surface is relatively smooth). Such 'oversmoothing' is responsible for the reduced extent of the R(θ) and σ(θ) variations. In that spirit, it would be of interest to apply the CMTP method only to those orientations which correspond to the *peaks* of the orientation function f(g). The weights of the texture components derived in this way could simply be the required components of f(g).

One of the other practical applications of the CMTP model could be associated with FEM calculations. Most of the codes in service are based on the isotropic, von Mises flow behaviour. Obviously, after large deformations, the metal workpieces investigated (motorcar parts, for example) are textured; these induced anisotropic effects strongly influence the flow of the metal when a further deformation is applied. It is believed that the employment of anisotropic yield criteria (of the CMTP type, for example) could considerably improve the accuracy of FEM calculations without adding too much computing time to what may already be a long calculation.

VI.3. Grain interaction models

The predictions of plastic properties obtained by crystallographic means are very dependent on the grain interaction model employed, i.e. on how the various crystals of the aggregate are assumed to behave. In the previous chapters, only the two Taylor and Sachs deformation models were employed. In the former case, all the grains are assumed to undergo the same uniform strain as the polycrystal; in the latter, the same stress direction is prescribed to all the crystals (Fig. 4.8). In this way, two different overall yield surfaces are obtained from the unique yield locus pertaining to a single crystal.

The Sachs model does not allow for any accommodation between individual crystals, nor does it permit stress equilibrium to be attained internally; thus it is not conducive to a satisfactory description of real metals. This is confirmed by the occasional non-convexity of the polycrystalline surfaces calculated using this assumption. At the other extreme, the Taylor uniform strain model (FC or full constraints) is often considered to give a reasonable approximation of the behaviour of *equiaxed* grains, for which strain compatibility is an important requirement. However, after large deformations, the grains are no longer equiaxed and adopt elongated pancake shapes. In this case, some of the strain components can be 'relaxed', as long as the respective small boundary interfaces can allow for some strain incompatibilities without inducing large reaction stresses. This model has generally been referred to as the RC (relaxed constraints) model, see for example Refs. [67,98,101,102,111,144], and has been shown to lead to better agreement with experimental pole figures. Canova et al. [11] used such an approach successfully to calculate the yield surfaces of textured polycrystals, as well as the $R(\theta)$ curve for rolled copper. Of interest also is the self-consistent model, as developed by the team of Berveiller and coworkers [145,146], in which each grain is considered as an inclusion embedded in a homogeneous matrix.

In the previous chapters, the Taylor and Sachs models have been applied to the different CMTP functions and have been shown (see Figs. 5.25 to 5.28, for example) to lead to similar overall behaviours. This is again essentially due to the smooth nature of the CMTP surfaces. Consequently, an intermediate model, such as that of relaxed constraints, is not expected to lead to significant improvements in the predictive accuracy of the CMTP method. Nevertheless, there are other reasons for trying further grain interaction models. This is because the uniform strain assumption leads to rather long computations when the non-quadratic ($n \neq 2$) function is used (see Table V.7). It is therefore of interest to now examine other models for the calculation of $R(\theta)$ which take much less computing time than that of Taylor.

As already noted in Chapter IV, the use of the uniform strain model for predicting R-values necessitates the definition of the stress tensor as a non-uniaxial stress tensor, i.e. with a possible non-zero shear component σ_{12}. By contrast, it appears that the tensile test actually carried out to measure strain rate ratios is purely uniaxial, i.e. it is specified by the following stress and strain rate tensors :

$$\underset{\sim}{\sigma}_{(xyz)} = \begin{bmatrix} ? & 0 & 0 \\ 0 & 0 & 0 \\ 0 & 0 & 0 \end{bmatrix} \qquad \underset{\sim}{\dot{\varepsilon}}_{(xyz)} = \begin{bmatrix} \dot{\varepsilon}_{11} & ? & 0 \\ ? & ? & 0 \\ 0 & 0 & ? \end{bmatrix} \qquad (6.3)$$

in the (xyz) i.e. the tensile axes (see Fig. 2.2). The value of the strain rate component ε_{11} is prescribed and σ_{11} is unknown. The above conditions are ideally suited to the application of the Kochendörfer [143] hypothesis : i.e. that each crystal is submitted to the same stress direction ($\sigma_{ij}=0$ for $(i,j) \neq (1,1)$) as well as to the same arbitrary value of $\dot{\varepsilon}_{11}$ as the polycrystal. A calculation sequence similar to that developed in section IV.2.1 (Eqs 4.33 to 4.39) can then be employed for any analytic CMTP function, a procedure which can be summed up as follows :

(1) Transform $\underset{\sim}{\sigma}_{(xyz)}$ in the crystal (C) axes by means of the matrix P (Eq. IV.3.3 in Appendix IV.3)

$$\underset{\sim}{\sigma}_{(C)} = P\,\underset{\sim}{\sigma}_{(xyz)}\,\tilde{P} \tag{6.4}$$

(2) Apply the normality rule to obtain the strain rate components pertaining to the crystal axes

$$\dot{\varepsilon}_{ij\,(C)} = \dot{\lambda}\,\partial F(S_{ij}) / \partial S_{ij\,(C)} \tag{6.5}$$

Here $F(S_{ij})=0$ is the CMTP function selected.

(3) Calculate the scalar factor $\dot{\lambda}$. For a homogeneous function $F(S_{ij})=0$ of degree n, it is readily shown that

$$\dot{W} = S_{ij\,(C)}\,\dot{\varepsilon}_{ij\,(C)} = \dot{\lambda}\,S_{ij\,(C)}\,\partial F / \partial S_{ij\,(C)} = n\,\dot{\lambda} \tag{6.6}$$

so that
$$\dot{\lambda} = \dot{W} / n = \sigma_{11}\,\dot{\varepsilon}_{11} / n \tag{6.7}$$

when expressed in the (xyz) axes. As $\dot{\varepsilon}_{11}$ is prescribed ($\dot{\varepsilon}_{11} = 1s^{-1}$, for example), σ_{11} is readily calculated since the stress vector must lie on the CMTP yield surface.

(4) Transform $\underset{\sim}{\dot{\varepsilon}}_{(C)}$ into the (xyz) reference frame

$$\underset{\sim}{\dot{\varepsilon}}_{(xyz)} = \tilde{P}\,\underset{\sim}{\dot{\varepsilon}}_{(C)}\,P \tag{6.8}$$

By this means, the complete strain rate tensor $\dot{\underset{\sim}{\varepsilon}}_{(xyz)}$ can be very simply assessed for each texture component under consideration since the normality rule does not need to be inverted. When the polycrystalline texture is decomposed into N texture components, the resulting $\dot{\underset{\sim}{\varepsilon}}_{(xyz)}$ tensor can be obtained by applying the following Kochendorfer averaging procedure :

$$\dot{\underset{\sim}{\varepsilon}}_{(xyz)} = \frac{1}{4} \sum_{i=1}^{N} \sum_{j=1}^{4} \dot{\underset{\sim}{\varepsilon}}_{(xyz)} \{ (h_{ij} k_{ij} l_{ij}) [u_{ij} v_{ij} w_{ij}] \} \qquad (6.9)$$

where the summation over j includes the four necessary sets of Miller indices (hkl)[uvw], $(\bar{h}\bar{k}\bar{l})$[uvw], (hkl)$[\bar{u}\bar{v}\bar{w}]$ and $(\bar{h}\bar{k}\bar{l})[\bar{u}\bar{v}\bar{w}]$. This averaging procedure is not equivalent to Taylor averaging, in which a single set of strain rate components is calculated from the overall locus.

Fig. 6.3 illustrates the differences in the predictions obtained from the Taylor and Kochendörfer models when the CMTP n = 1.7 yield surface is employed. It can be seen that the general trends remain the same in the two cases, and that the amplitudes of the R variations are similar. Nevertheless, the Kochendorfer predictions are somewhat smoother than those founded on Taylor's model. However, an important practical difference must be pointed out which involves the times necessary to compute the R-value at a specific angle θ and for a single orientation (plus the required symmetries). The latter is about 3 sec for the Taylor averaging technique (see Table V.7) and only about 0.08 sec for the present model. This ratio of about 40 renders the Kochendorfer type of calculation very attractive.

The PL1, PL2, PL3 and PL4 functions were also employed in conjunction with the latter model. The results obtained are presented in Fig. 6.4 for some common orientations. It can be seen that the general features of the R(θ) curves remain the same for the four types of yield criterion : in particular, strong anisotropy can be observed for the cube (a), Goss (c), Bs (d), {112}<$1\bar{1}0$> (f), S (g) and {554}<$22\bar{5}$> (h) orientations. Concurrently, nearly planar isotropy is predicted for the {111} type of components, Fig. 6.4e. The PL2 and PL4 criteria seem to best reproduce the relatively high R values (near 2.5) frequently observed in steel sheets displaying both {111}<uvw> and {554}<$22\bar{5}$> components. The four functions cited above also lead to predictions that are

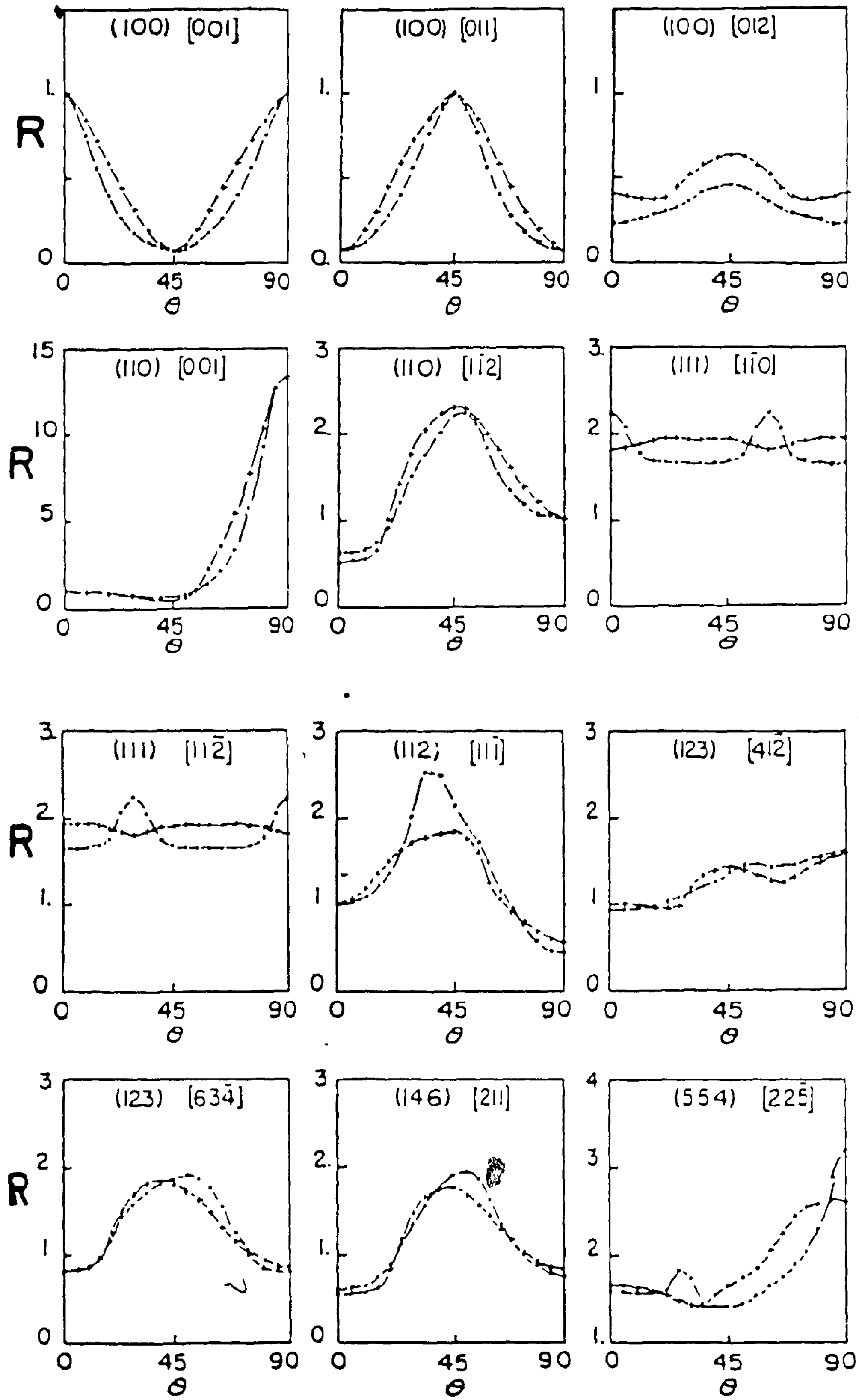

Fig. 6.3 Values of R(θ) predicted by the CMTP n = 1.7 criterion for common ideal orientations. The symmetry requirements of the rolling process are taken into account. (—• —) uniform strain model; (— + —) law of mixtures model.

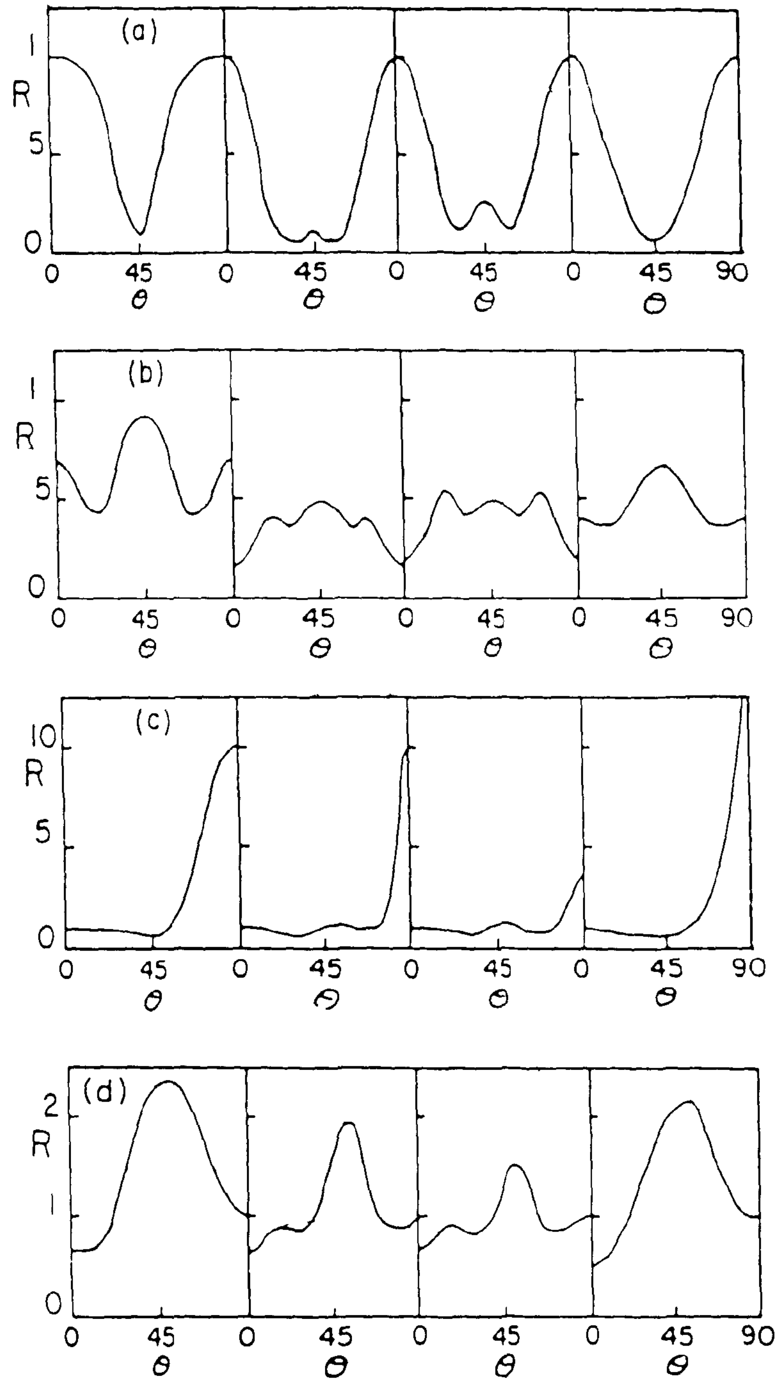

Fig. 6.4 Values of R(θ) predicted by the CMTP PL1, PL2, PL3 and PL4 (from left to right) criteria using the Kochendorfer (law of mixtures) model. The symmetry requirements of the rolling process are taken into account. (a) {100}<001>; (b) {100}<012>; (c) {110}<001>; (d) {110}<1$\bar{1}$2> orientations.

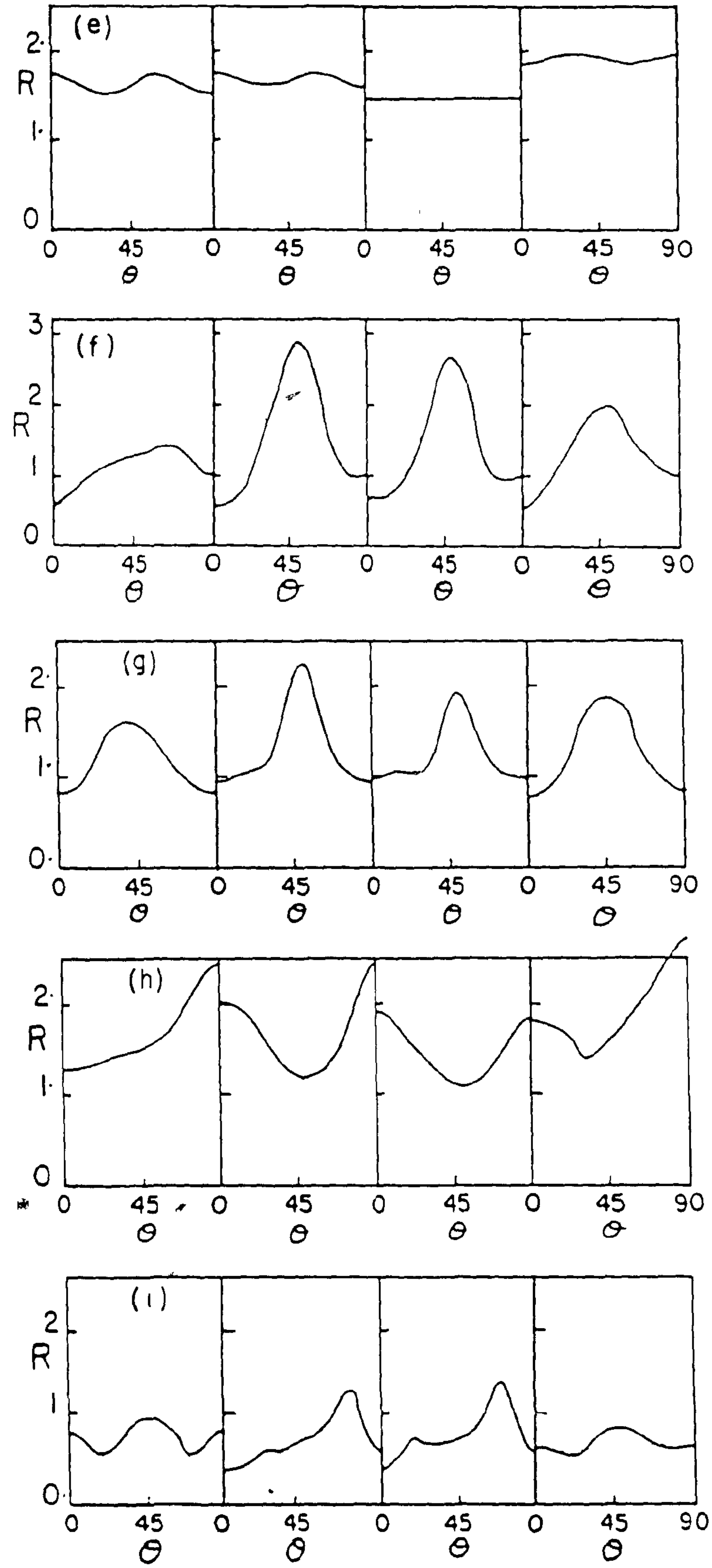

Fig. 6.4 Values of R(θ) predicted by the CMTP PL1, PL2, PL3 and PL4 (from left to right) criteria using the Kochendorfer (law of mixtures) model. The symmetry requirements of the rolling process are taken into account. (e) {111}<1$\bar{1}$0>; (f) {112}<1$\bar{1}$0>; (g) {123}<63$\bar{4}$>; (h) {554}<22$\bar{5}$>; and (i) {411}<14$\bar{8}$> orientations.

similar to the ones reported in section V.2 for multicomponent textures. However, the PL3 criterion (because of its quartic form) is unable to reproduce the large R values pertaining to steels.

The Kochendorfer analysis also permits the use of a Hill type of yield function with two different exponents. This criterion is very attractive since it takes account of the different behaviours observed in the normal and shear stress subspaces (see Chapters III and IV). The uniform strain assumption was difficult to apply in this case because the necessary inversion of the normality rule led to unreasonable computing times. By contrast, when the Kochendorfer model is used, rapid assessment of the R(θ) curves can be made (0.17 sec of computing time for each value of θ and for each orientation compared with 0.08 sec for the single exponent calculation). It is the inhomogeneity of the yield function which requires the use of a numerical method to determine the scalar factor $\dot{\lambda}$ of the flow rule (Eq. 6.5), and is responsible for the latter increase.

The R(θ) results obtained with the aid of the two exponent yield surface for some common ideal orientations are shown in Fig. 6.5. When dealing with multicomponent textures, the predictions obtained by the present analysis do not differ significantly from the ones displayed in Fig. 5.38 for the Cu-brass series of Hirsch [12], determined using the n = 1.7 and PL4 criteria. Only slight changes are observed, which still do not predict the full R variations measured in these rolled metals. For the various steels investigated in section V.2.3, by contrast, better predictions are obtained with the present two exponent locus than with the PL4 or n = 1.7 criteria. This is illustrated in Fig. 6.6. When compared with the corresponding predictions reported in Figs. 5.41 to 5.46, it can be seen that fewer undesirable peaks and troughs are observed than in the PL4 calculations. The curves are smoother and predict the $\bar{R}$-values quite well and the planar anisotropy ΔR to a lesser degree. The two exponent yield locus thus appears to lead to the best overall predictions when used with the Kochendorfer analysis.

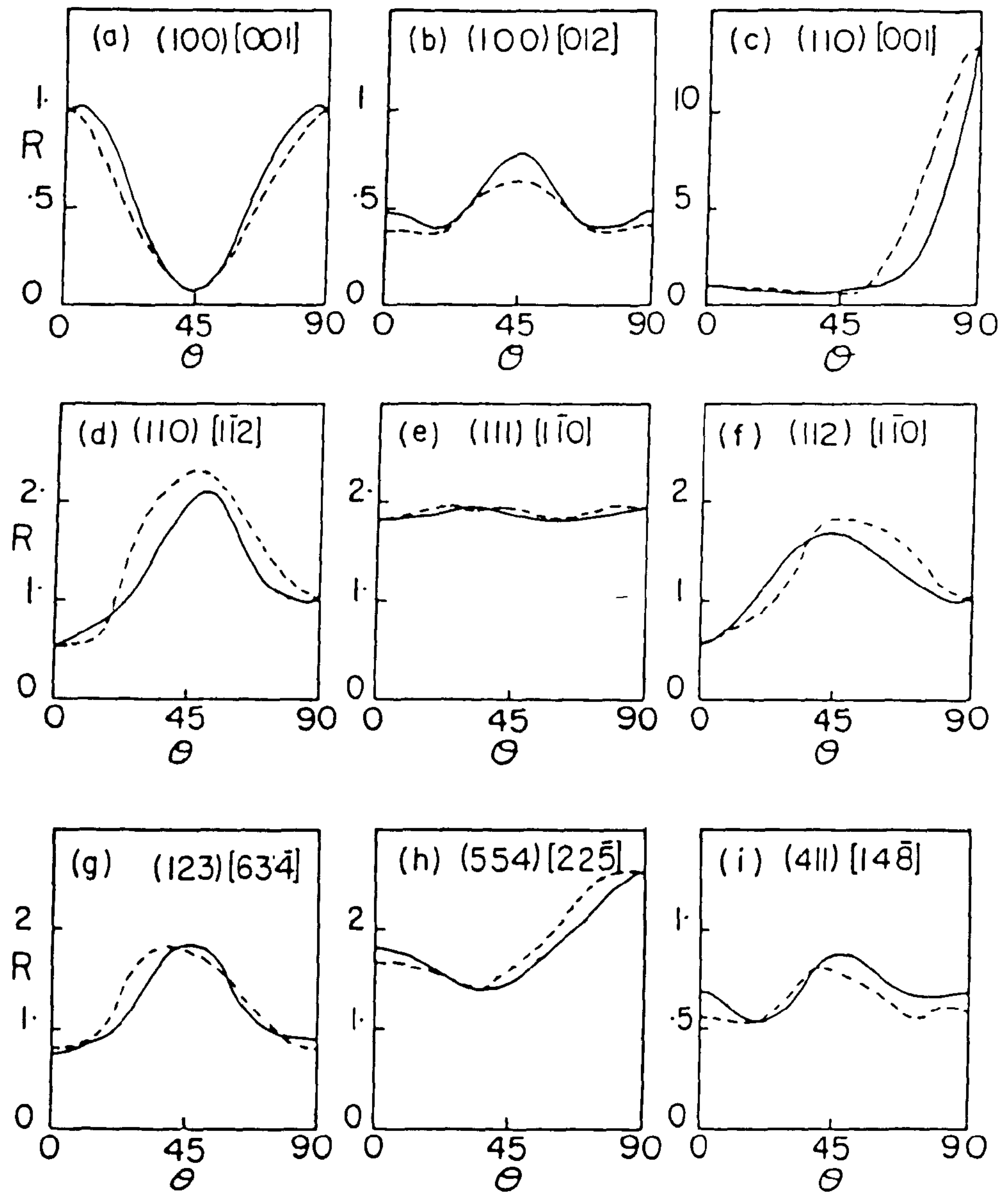

Fig. 6.5 Values of R(θ) predicted by the CMTP two exponent (————————) and the n = 1.7 (– – – – – – –) criteria using the Kochendorfer model for selected ideal orientations. The symmetry requirements of the rolling process are taken into account.

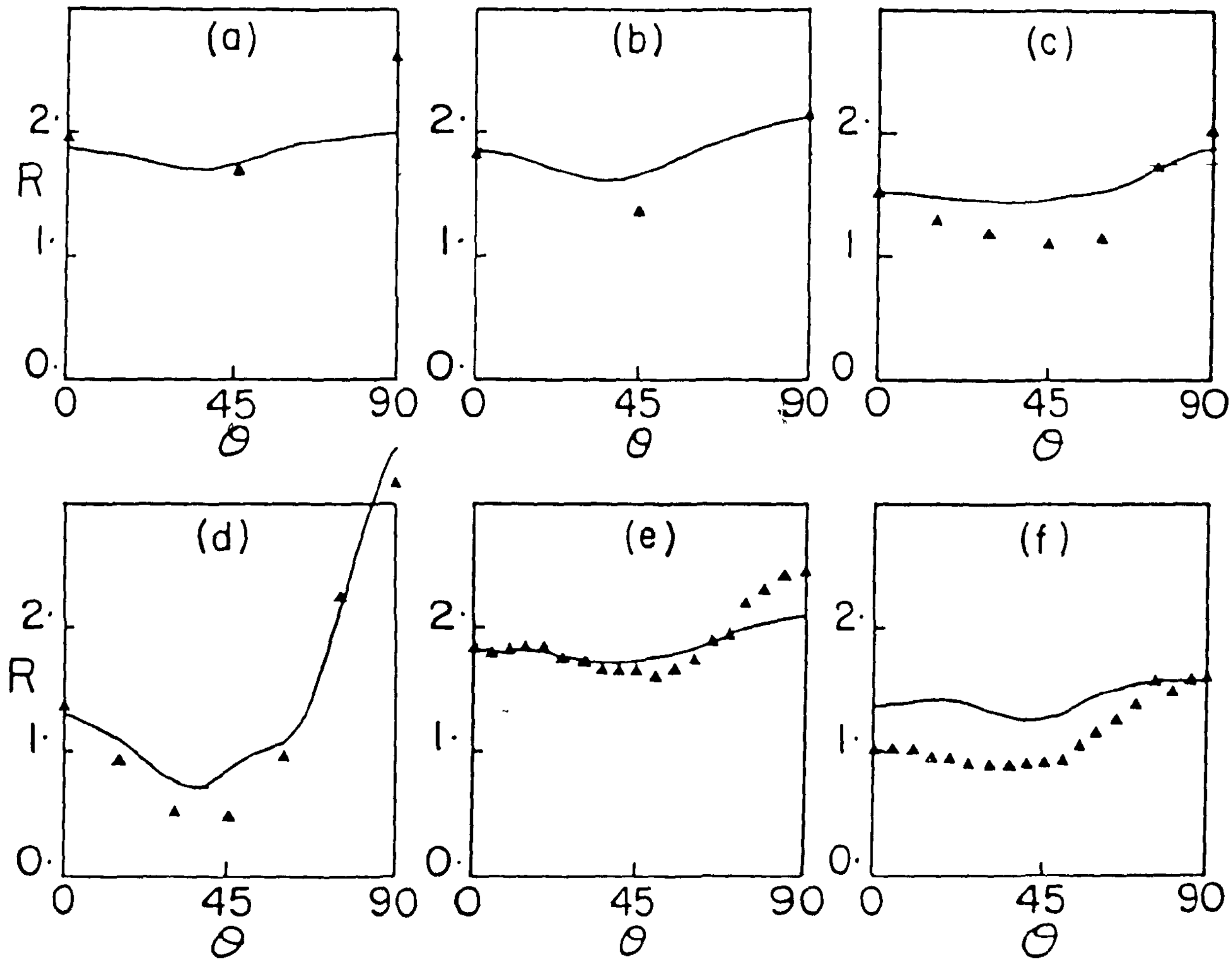

Fig. 6.6 Values of R(θ) predicted by the CMTP two exponent criterion for various grades of steel using the Kochendorfer model. (a) 25% {554}<22$\bar{5}$> + 25% {111}<1$\bar{1}$0> + 50% {111}<11$\bar{2}$>, after [126]; (b) 50% {554}<22$\bar{5}$> + 20% {111}<1$\bar{1}$0> + 30% {111}<11$\bar{2}$>, after [126]; (c) 60% {111}<1$\bar{1}$0> + 10% {111}<11$\bar{2}$> + 10% {110}<001> + 20% random, after [123]; (d) 60% {110}<001> + 20% {221}<1$\bar{1}$0> + 20% random, after [123]; (e) and (f) ideal orientations and volume fractions of Table V.5, after [135].

VI.4. The CMTP method : advantages and limitations

In this section, a critical examination of the CMTP model is carried out. As already noted in the course of this report, the CMTP technique has many advantages as well as some deficiencies which are underlined below.

(i) Simplicity of the procedure - Once the main texture components of a deformed material are known, the CMTP technique provides an easy way to assess the corresponding $R(\theta)$ or $\sigma(\theta)$ curves. This is because the analytic forms of the various functions are very supple and allow the plastic (strain rate) properties to be expressed analytically in most of the cases. This is especially true when the Kochendorfer hypothesis is used (section VI.3), which gives results comparable to those obtained from the somewhat less direct Taylor deformation model. In the former case, it should be noted that some of the calculations (involving the $n=2$ criterion for example) can be carried out on a hand held calculator.

(ii) Fast assessment of the plastic anisotropy - This property, which is essential for on line-measurement purposes, is directly related to the analytic character of the CMTP analysis. The law of mixtures (Kochendorfer) grain interaction model applied to the uniaxial tensile test leads to the fastest computation. At the other extreme, the uniform strain (Taylor) method is rather slow when used with the non-quadratic criteria.

(iii) Finite number of orientations - The crystallographic calculations carried out in Chapter III on disoriented single crystals led to yield surface cross-sections which are quite smooth in the π-plane. For typical experimental spreads (around 10 to 15°), these are almost circular and thus permit representation in near quadratic form. This conclusion only holds, however, in the subspace containing the normal stresses. The CMTP functions considered in this work can thus be considered to approximate rather well the yield locus pertaining to a disoriented grain with an orientation spread of around 10 to 15°. For more general polycrystalline predictions, the texture of a given aggregate can be represented by the superposition of a finite number of such disoriented grains, each with its own CMTP locus. By contrast, when the Bishop and Hill polyhedron is used instead of the present continuum approach, the full CODF must be known since the former surface only relates to a "pure" cubic single crystal. For accurate predictions of R(θ), it has been shown (Chapter III) that at least 600 grains are necessary for the crystallographic approach, whereas less than 10 (plus the rolling symmetries) are sufficient for the CMTP model. The computing time saved is thus appreciable.

(iv) Good R(θ) and σ(θ) predictions - From all the comparisons carried out with experimental data, it can be concluded that the CMTP technique leads to good approximations of observed stress and strain rate ratios. However, the average $\bar{R}$-value is generally better reproduced than the planar ΔR coefficient, e.g. the high R(θ) variations observed in rolled FCC metals are underestimated. This is essentially due to the smooth nature of the CMTP functions, which lead to yet smoother loci when they are combined. There was some hope that the PL1, PL2, PL3 and PL4 functions which were derived from the equations of the Bishop and Hill polyhedron would overcome this deficiency. Unfortunately, because of the difficulties encountered in the inversion of the normality rule when the Taylor assumption is used, only the quadratic types were kept. As a result, the interesting features of such functions are not readily available. The law of mixtures grain interaction model allows these 4 criteria to be used with n exponents less than 2. In these cases, they could lead to improvements in the calculated R-values. This possibility remains to be verified as only the quadratic form was investigated and this was not able to reproduce the full extent of the R(θ) variations.

(v) Yield surface predictions - No final comment can be made here regarding the accuracy of the CMTP predictions of macroscopic yield loci. This is because a yield surface has 5 dimensions in stress space, whereas the experimentally determined yield strengths almost always pertain to two dimensional sections and only provide a very limited representation of the overall yielding behaviour. It seems, nevertheless, that the CMTP functions are poor in reproducing the strain rate features of the loci pertaining to the highly textured materials which are similar to single crystals. In these cases, there is some experimental evidence suggesting the presence of rounded corners on the yield surfaces, a feature which is ignored by the CMTP predictions (Figs. 5.15 to

5.17). However, when dealing with polycrystalline materials displaying larger dispersions around their various texture components, much better agreement is found (Figs. 5.18 and 5.32).

There is considerable question in literature [11, 147] about the presence (or absence) of vertices on polycrystalline yield surfaces. Canova et al.[11] found very sharp corners in the loci they calculated (Fig. 5.35) using a rolling texture predicted by the RC method. By contrast, the yield surfaces corresponding to torsion were found to be much smoother, although flat edges were reported. Van Houtte [111] predicted FC and RC loci pertaining to fcc and bcc metals using the CODF technique of texture representation. In the latter case, both $\{1\bar{1}0\}$ and $\{11\bar{2}\}<111>$ types of slip system were considered, leading to an overall smoothing of the surfaces, so that no vertices were obtained. Nevertheless, his isotropic π-plane section of the fcc yield locus was characterized by a corner (for $S_{22} = S_{33} = 0$) when calculated by the relaxed constraint model [111]. The presence of a vertex is of practical importance since it can be related to the occurrence of flow localization. Indeed, a small stress variation around such a corner can be associated with a large variation in strain direction. Such small changes in the stresses are not unrealistic, when the material is not severely constrained.

The CMTP criteria (n = 1.7 and PL4) display a kind of vertex in the shear stress plane section (see for example Fig. 4.3); these are, however, not pronounced. When the functions are averaged over different orientations, the corners disappear and a smooth overall locus is obtained. Consequently, the CMTP formulation in its present form is not suitable for even a qualitative study of flow localization or shear band formation [148].

(vi) <u>What is the "best" yield surface?</u> - One of the major problems encountered in the use of the CMTP model is the selection of an appropriate yield function. By 'appropriate' is meant a criterion which is able to reproduce the main features of the five dimensional yield surface pertaining to a disoriented grain. It is indeed easy to find criteria which give almost perfect fits in various sections of the crystallographic locus. However, it is much more difficult to invent a function of the stresses which is able to reproduce the surface shape and size in the normal, shear, and mixed (normal + shear) stress subspaces. Such an attempt was carried out with the PL1 to PL4 criteria which are kinds of 'partial developments' of the Bishop and Hill polyhedron (see section IV.1.2). The necessity of using them in quadratic form (with the Taylor analysis) renders them less attractive and convincing. The two exponent type of criterion was also introduced for the purpose of providing a better fit to the crystallographic surfaces. The two exponents take into account the two different yielding behaviours observed in the normal and shear stress planes (see Chapter III). The improvement brought about by the introduction of these criteria is significant. Indeed, in the work carried out to date with the Kochendorfer (law of mixtures) assumption, the PL4 and two exponent yield functions seem to best reproduce the plastic properties (R-values) corresponding to a wide range of textures. However, it is possible that the law of mixtures analysis (section VI.3) applied to the PL1 to PL4 criteria with exponents less than 2 (or even with two different exponents) may lead to still better agreement with experimental observations.

(vii) <u>What kind of loading conditions?</u> - As already noted in the previous chapters, the R-value is calculated from a tensile test carried out along a certain direction θ of a sheet. Two types of testing condition can be considered :

(a) the uniaxial tensile test characterized by a possible non-zero $\dot{\varepsilon}_{12}$ shear component :

$$\underset{\sim}{\sigma} = \begin{bmatrix} ? & 0 & 0 \\ 0 & 0 & 0 \\ 0 & 0 & 0 \end{bmatrix} \qquad \underset{\sim}{\dot{\varepsilon}} = \begin{bmatrix} \dot{\varepsilon}_{11} & ? & 0 \\ ? & ? & 0 \\ 0 & 0 & ? \end{bmatrix} \qquad (6.10)$$

$\dot{\varepsilon}_{11}$ is imposed on the polycrystal. Such a test is rigorously valid only for long samples, in which the constraints due to the shoulders are small. The sheet type of specimen recommended in ASTM standard A370 is not fully consistent with these loading conditions (because the gage length is only 2 inches);

(b) the not-strictly uniaxial tensile test characterized by the following stress and strain rate tensors :

$$\underset{\sim}{\sigma} = \begin{bmatrix} ? & ? & 0 \\ ? & 0 & 0 \\ 0 & 0 & 0 \end{bmatrix} \qquad \underset{\sim}{\dot{\varepsilon}} = \begin{bmatrix} \dot{\varepsilon}_{11} & 0 & 0 \\ 0 & ? & 0 \\ 0 & 0 & ? \end{bmatrix} \tag{6.11}$$

Here $\dot{\varepsilon}_{11}$ is imposed, and $\dot{\varepsilon}_{22}$ and $\dot{\varepsilon}_{33}$ are unknown. Note that the condition $\sigma_{12} \neq 0$ cannot be fulfilled at the free surface of the specimen, so that Eq. 6.11 only applies to the interior of the sample, where the homogeneity of the deformation is questionable. These loading conditions are the ones usually adopted in R(θ) calculations [10, 11, 13, 16]. This is because the strain rate tensor only has one degree of freedom (since $\dot{\varepsilon}_{12}=0$ and $\dot{\varepsilon}_{33}=-\dot{\varepsilon}_{11}-\dot{\varepsilon}_{22}$) and thus allows easy computation when the Taylor assumption is used.

It should be noted that in both cases the conditions $\sigma_{13}=0$ and $\dot{\varepsilon}_{13}=0$ (or $\sigma_{23}=0$ and $\dot{\varepsilon}_{23}=0$) are equivalent. This is due to the fact that for rolled (or orthotropic) materials, the Z-axis or normal direction is an axis of mirror symmetry [11]. The differences attributable to the two tensile conditions are illustrated in terms of the stress and strain rate characteristics in Fig. 6.7 for a hypothetical (σ_{12},π-plane) anisotropic yield surface.

The lengths of the samples used for R(θ) measurements in the literature are generally small : Benferrah [65] and Truskowski and Jarominek [107] used 1 inch specimens, whereas 3.5 and 4 inch lengths are reported by Elias et al. [106] and Stickels and Mould [108], respectively. Thus the "not-strictly-uniaxial" tensile test may be more appropriate for the representation of at least the first two sets of experimental conditions.

(viii) Texture prediction - The theory of texture prediction is based on the possible activation of slip systems in order to accommodate the imposed macroscopic deformation. From knowledge of these activated systems, the orientation of a crystal can be calculated as the deformation proceeds. As long as the CMTP continuum functions are not strictly crystallographically based, crystal rotations cannot be calculated since no reference to any slip system is made. Nevertheless, since the CMTP criterion is fitted to the Bishop and Hill polyhedron, it has been suggested [153] that it may still be possible to extend the method so that texture predictions can be made.

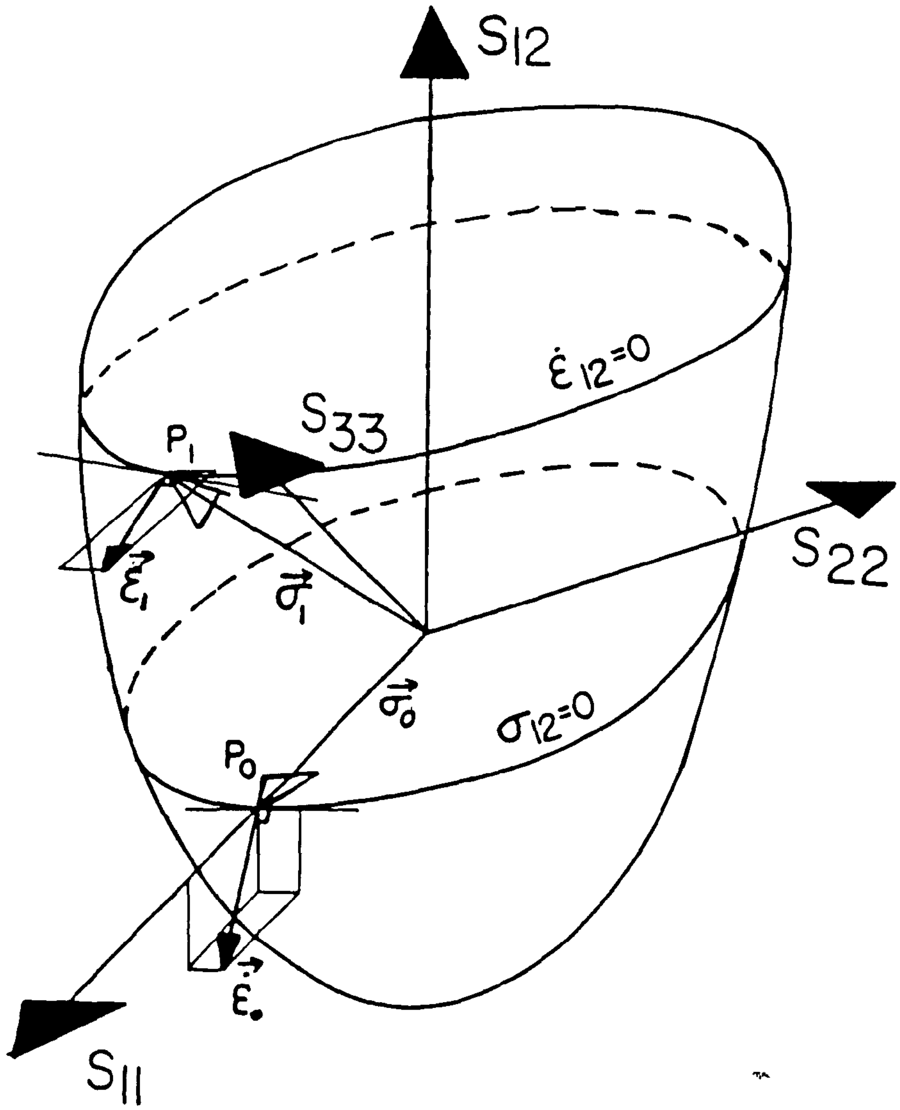

Fig. 6.7 Position of the loading point in the (σ_{12}, π-plane) subspace for (i) strictly uniaxial (point P_0) and (b) not-strictly-uniaxial (point P_1) tensile testing, as specified by Eqs. 6.10 and 6.11, respectively. $\vec{\sigma}_0$ and $\vec{\dot{\varepsilon}}_0$ are the stress and strain rate vectors corresponding to the completely uniaxial test (Eq. 6.10); $\vec{\sigma}_1$ and $\vec{\dot{\varepsilon}}_1$ correspond to the non-uniaxial test (Eq. 6.11).

VI.5. Sources of error

VI.5.1. Errors associated with the CMTP method

The intrinsically ellipsoidal shape of the CMTP criterion is its most attractive aspect as well as its major source of error. However, the latter may not be large. Indeed, the functions considered should not be compared to the Bishop and Hill polyhedron (which relates to a pure cubic single crystal) but to the yield surface of a disoriented grain, as calculated in chapter III. This is because, in its spirit, the CMTP model is applied to a finite number of scattered ideal orientations into which the overall texture has been decomposed. When such a comparison is carried out, it appears that:

(a) the general symmetries of the locus are retained;

(b) the normal stress plane section is very well approximated by all the criteria considered;

(c) the shear stress plane sections are generally oversmoothed (to various degrees) by the CMTP approximations;

(d) it is difficult to estimate the quality of the fit in the mixed stress spaces;

(e) the errors attibutable to the CMTP model are more important with regard to the strain rate characteristics (which are related to the *shape* of the locus) than with regard to the stress state (given by its *size*).

It is difficult to quantify the error due to oversmoothing of the yield surface, as it depends very much on the texture and loading conditions being considered. Furthermore, an error must be defined with respect to something known. Unfortunately, the loci calculated by purely crystallographic means do not give a fully accurate estimate of the plastic properties (in fact, the CMTP loci may be more realistic). When it comes to the experimental R-values, these are always determined with a fair degree of uncertainty, as discussed in more detail below.

A word must be added here regarding the slip systems considered in the crystallographic calculations (i.e. $\{111\}<1\bar{1}0>$ and $\{110\}<1\bar{1}1>$). Obviously more slip systems can be employed in the BCC metals in which pencil glide (or restricted $\{1\bar{1}0\}$, $\{11\bar{2}\}$ and $\{12\bar{3}\}$ $<111>$ glide) is often assumed. However, such additions lead to more rounded crystallographic yield surfaces [149], the sizes of which are not significantly different from the ones calculated above (Chapter III) for disoriented grains. Consequently, the CMTP fit to such surfaces is not expected to be changed to a significant degree.

VI.5.2.Errors associated with texture characterization

Texture characterization is also a possible source of error. This is not necessarily because of error in the determination of the main ideal orientations produced by rolling (these can be derived from simple pole figures, except in a few cases), but because of errors in the estimates of their respective volume fractions. The difference between 30 and 40% of the Goss component can lead to significant differences in the R(90) predictions (see for example Fig. 6.4c). Furthermore, the percentage of random component is difficult to estimate when a CODF analysis is not performed. It plays a non-negligible role as it can be quite intense, even in highly textured metals in which it has been estimated [69] to represent about 15% of the complete orientation distribution.

An important factor which has not been investigated too extensively in the literature is the change in the texture that occurs during tensile deformation. Interesting studies have been carried out by Ruano and Gonzalez [150] on aluminum alloys, as well as by Dabrowski et al. [114] on various grades of steel. In the former case, deformation tends to align a $<111>$ direction with the tensile axis, whether the tensile direction is parallel or normal to the rolling direction. Although these results hold for large tensile deformations (greater than 100%), it appears that such texture evolution can even affect the R-value significantly under more conventional experimental conditions (i.e. at deformations of around 10 to 15%).

In the case of a cold rolled and annealed Al-killed steel sheet, Dabrowski et al. [114] demonstrated that the $\{111\}<1\bar{1}0>$ texture component increases considerably at the expense of the {111}<11$\bar{2}$> orientation (or more precisely the {554}<22$\bar{5}$>) during tensile testing in the rolling direction. The reverse occurs after tension in the transverse direction. In these examples, the tensile elongations were about 20%. R(θ) predictions based on the CODF method of texture representation [10,16] showed a small increase in the strain rate ratio in the transverse direction. Similar calculations were carried out in this investigation with the CMTP model Their texture was decomposed into {111}<1$\bar{1}$0>, {554}<22$\bar{5}$> and random components in the density ratios 5:3:2 before tensile deformation, 9:2:2 after testing in the rolling direction and 3:7:2 after testing in the transverse direction. As can be seen from Fig. 6.8, only a small difference in the R(θ) predictions is produced by the second orientation distribution. Nevertheless, the larger volume fraction of the {554}<22$\bar{5}$> component obtained after tensile deformation parallel to the transverse direction, i.e. in the third distribution, induces a more pronounced anisotropy and leads to an R(90) value greater than in the undeformed state. These simplified simulations are consistent with the calculations reported by Dabrowski et al. [114].

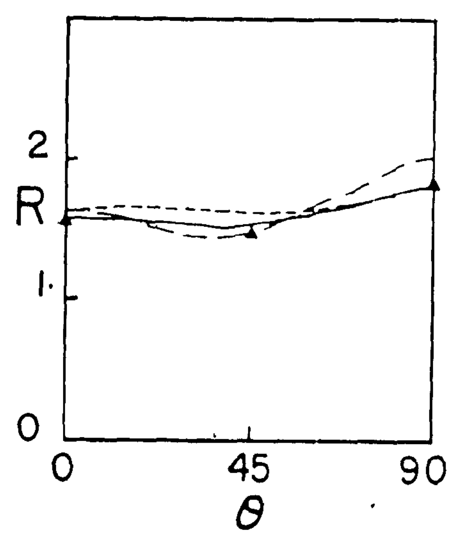

Fig. 6.8 R(θ) curves predicted by the CMTP two exponent criterion for an Al-killed steel using the Kochendorfer model. (▲) experimental values from Ref. [114]. CMTP predictions (———) before tensile deformation; (– – – –) after tensile deformation in the rolling direction; and (—·—·—) after tensile deformation in the transverse direction.

Finally, it should be kept in mind that a texture gradient is always present through the thickness of a rolled sheet, with a more intense shear type of texture at the surface because of friction against the rolls. Such a gradient can also influence the R-value measurements, and should, ideally, be taken into account when predictions are being made.

VI.5.3. Errors associated with R-value measurement

Measurements of strain rate ratio are always very critical, in that the R-value can vary with strain, as described above, and therefore take different values at different strains. In its original form [29], the R-value was defined as "the ratio of the width ε_w and thickness ε_t strains in the tensile test". It is thus related to the slope of the ε_w vs ε_t curve. However, as these strains frequently vary in a non-linear manner during tensile deformation, an instantaneous criterion relating the instantaneous rates of contraction in the width and thickness directions is preferred [151]. Welch et al. [152], among others, have discussed the differences associated with these two definitions, as well as with other integrated forms. Of the various possibilities, the incremental formula ($R = d\varepsilon_w/d\varepsilon_t$) has become the most popular for R-measurements. Furthermore, as the strain rate ratio should indicate the anisotropy of the sheet prior to tensile deformation, a back-extrapolation of the ε_w vs ε_t curve to zero tensile strain should be carried out, the slope of which at the origin gives the R-value. As illustrated in Fig. 6.2, such a definition can lead to difficulties at low strains when applied to rolled materials. Benferrah [65] avoided these problems in his extrapolations by using least square fittings on nearly linear ε_w vs ε_t curves and neglecting the points associated with very small strains. After high reductions ($\bar{\varepsilon} \geqslant 0.52$), inhomogeneous deformation takes place, as in the experiments of Hirsch et al. [12], so that still larger uncertainties are associated with the measured values after significant processing strain. An illustration of the difficulty of giving a "true" value to the Lankford coefficient is given in Fig. 6.9, taken from the work of Truskowski and Jarominek [107] on a rolled copper sheet; very different R ratios can be deduced from the experimental points, depending on the way these are treated.

In order to avoid the difficulties involved in such extrapolations, Welch et al. [152] proposed the use of an "integral" anisotropy parameter P defined over a particular strain range :

$$P = \frac{1}{\varepsilon_2 - \varepsilon_1} \int_{\varepsilon_1}^{\varepsilon_2} \frac{d\varepsilon_z}{d\varepsilon_t}(\varepsilon)\, d\varepsilon \tag{6.12}$$

However, this definition necessitates more computational work than the slope-based methods described above. In the literature, R-values have been generally determined at different strain levels, as already noted in this report. Because of the lack of a standard procedure, comparisons between different authors are difficult to carry out. Similarly, comparison with predicted R-values, which correspond to the ratios of incremental strains at zero tensile deformation, also involves ambiguities.

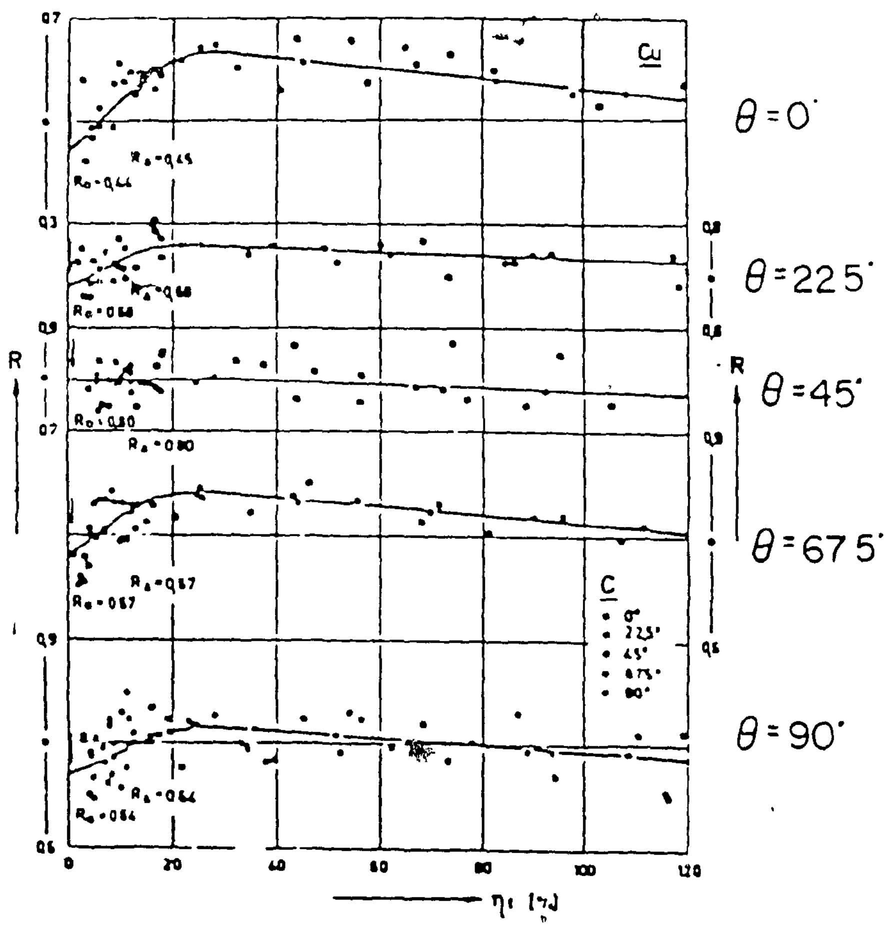

Fig. 6.9 R-value vs length strain (η_t) at various angles θ for a rolled copper sheet. After [107].

CONCLUSIONS

The CMTP (continuum mechanics of textured polycrystals) method, first introduced by Montheillet et al. [5] for the prediction of axial stresses in torsion testing, has been generalized to permit the calculation of plastic anisotropy in rolled sheet. New yield functions have been introduced, and three different averaging techniques employed over various grain orientation distributions pertaining to FCC and BCC metals. For comparison purposes, crystallographic calculations were also carried out according to the Bishop and Hill method. From this work, the following conclusions can be drawn :

1. Quadratic or near quadratic yield criteria are useful for approximating the yielding behaviour of grains displaying an experimental spread of around 10 to 15°. This conclusion is based on the shapes of the yield surfaces obtained from a classical Taylor/Bishop and Hill analysis applied to rotationally symmetric gaussian distributions of misorientations with scatter widths varying from 0° (single crystal) to 45°. For typical experimental spreads (10 to 15°), the crystallographic π-plane (or normal stress) sections are almost circular and can therefore be given a near quadratic ($n \approx 2$) representation. However, the shear stress plane sections remain quite angular, and so are better fitted with lower exponents ($n \approx 1.5$). An overall good fit is obtained with $n = 1.7$. The disoriented yield surfaces described above thus provide a good physical basis for the CMTP yield criteria.

2. Different continuum yield functions were derived according to the trends displayed by the crystallographic yield surfaces. Of these, the two exponent criterion gives the best fit to the shear and normal stress behaviours. Other functions based on the classical Hill criteria (quadratic and non-quadratic) as well as on a partial development of the equation of the Bishop and Hill polyhedron (PL1 to PL4), have also been investigated. In order to retain the relative simplicity of the analysis, only the homogeneous forms were considered. All these yield criteria give good fits to the π-plane cross-section of the yield surface pertaining to a disoriented grain. By contrast, they lead to

smoother loci in the shear stress planes than the crystallographic surfaces (with the exception of the PL4 and two exponent functions, which give reasonable overall fits).

3. Yield surfaces as well as R(θ) and σ(θ)/σ(0) curves pertaining to polycrystalline materials were evaluated by considering three different grain interaction models. On the one hand, the Taylor approach assumes that all the grains undergo the same strain as the polycrystal. The Sachs model, by contrast, prescribes the stress direction to be identical in all the grains of the aggregate. In these two cases, the overall loci can be readily calculated, from which the stress and strain rate characteristics can be derived. Finally, the Kochendorfer hypothesis, in which the uniaxial stress direction as well as the value of the $\dot{\varepsilon}_{11}$ strain rate component are prescribed for all the crystals, was employed for the calculation of R(θ). This method does not lead to the preparation of a yield surface. The predictions obtained from the three models are similar, because of the smooth nature of the CMTP functions. Consequently, it appears that a more sophisticated approach, such as that of relaxed constraints, will not lead to significant improvements in the CMTP predictions. Nevertheless, the Kochendorfer or law of mixtures analysis, which allows for much faster computation than the Taylor approach because of an almost completely analytical description of the yielding behaviour, appears to be the most promising for industrial purposes.

4. The CMTP yield surfaces calculated using either the Taylor (uniform strain) or Sachs (uniform stress direction) grain interaction models were compared to those obtained from crystallographic calculations. In the continuum cases, a limited number of disoriented texture components was sufficient to represent the behaviour, whereas, according to the classical approach, a simulated orientation distribution made up of a minimum of 200 grains is required. The CMTP functions, although they respect the symmetries of the crystallographic loci, are much smoother. Nevertheless, some flat regions are observed for the PL4 and $n < 1.5$ criteria in some cases. When the crystallographic approach is used, the Sachs assumption leads to concave yield surfaces, which violate the thermodynamics of flow and which thus differ distinctly from the fully convex ones obtained from the Taylor model. By contrast, the Sachs and Taylor

surfaces obtained from the CMTP predictions lead to similar overall shapes because of the smooth nature of the functions investigated.

5. Good agreement is observed between the predicted CMTP yield surface sections and experimental data for various metals when the orientations have dispersions of around 15°. However, for the highly textured polycrystals which can be considered as near single crystals, the CMTP method is unable to reproduce the rounded corners and flat edges of the experimental loci.

6. The strain rate $R(\theta)$ and yield stress $\sigma(\theta)/\sigma(0)$ ratios pertaining to rolled sheet were calculated for the common ideal orientations observed in both FCC and BCC metals. The general features of empirical $R(\theta)$ curves are given a ready analytical formulation in this way. In FCC metals, the cube $\{100\}\langle 001\rangle$ orientation leads to ears (maxima in the $R(\theta)$ curves) in the rolling and transverse directions, whereas the Cu- $\{112\}\langle 11\bar{1}\rangle$, Bs- $\{110\}\langle 1\bar{1}2\rangle$ and S-$\{123\}\langle 63\bar{4}\rangle$ components favor ear formation at $\theta = 45°$. In BCC materials, the $\{111\}$ type of texture is conducive to almost planar isotropic flow as well as to a high average $\bar{R}$-value (and thus to a better drawability), similarly the Goss-$\{110\}\langle 001\rangle$ orientation is characterized by a very high resistance to thinning (high $\bar{R}$-value) near the transverse direction. All these predictions are confirmed experimentally. When compared to experimental data pertaining to polycrystalline sheet, the CMTP calculations lead to a good estimate of the $R(\theta)$ and $\sigma(\theta)/\sigma(0)$ curves. However, the average value $\bar{R}$ of the Lankford coefficient is generally better reproduced than its variation (ΔR) with the angle θ, especially in the case of rolled FCC sheet. The positions of the extrema in the strain rate ratio curves (which give the locations of the ears in deep drawn cups) are also well approximated. There is a slight trend that the two exponent and PL4 criteria are better able to reproduce the full range of $R(\theta)$ curves observed in different cubic metals, especially when used in conjunction with the Kochendorfer analysis.

7. The CMTP method was also used to predict the rate of axial deformation in torsion testing as well as to reproduce the anomalous behaviour of sheet metals. In the former case, a good estimate of the ratio of longitudinal to torsional strain rate is produced when ~~{100}~~ $\langle 0vw\rangle$ textures are present in tubes submitted to free end torsion testing. In the latter, the PL4 criterion is able to

explain the anomalous behaviour when applied to a {012} type of texture or to some specific combinations of the texture components found in rolled copper sheet, although no experimental evidence has yet been found to support these predictions. Finally, a study of the orientations leading to optimum drawability ($\bar{R}$ maximum and ΔR minimum) was carried out, which indicates that the presence of the {111} type of texture is required, whatever the CMTP criterion considered. The two exponent function was not investigated in these examples.

8. Finally, it is suggested that the PL4 and two exponent criteria can be readily used for on line control purposes when a Kochendorfer (law of mixtures) analysis is employed. This is because the plastic anisotropy present in the material can be linked analytically and in a rapid way to the main texture components as well as to their respective weights. The ideal orientations displayed must of course be assessed on line for this purpose by using ultrasonic test methods or X-ray devices oriented in the Bragg directions of the specific orientations of interest.

SUGGESTED TOPICS FOR FURTHER INVESTIGATION

The CMTP analysis described above is a practical tool for correlating the plastic anisotropy of a metal workpiece to its texture in a simple and satisfactory way. For this reason, further investigations in which the validity of the CMTP method is tested should be carried out. These could include the following:

1. The derivation of new yield criteria in order to better reproduce the R-variations observed in FCC metals.

2. The theoretical and experimental study of the relation between limiting drawing ratio and texture.

3. The theoretical and experimental investigation of the effect of texture on the characteristics of biaxial and plane strain work hardening compared to that of uniaxial deformation.

4. The theoretical and experimental evaluation of the influence of various orientations on limit strain in sheet metals, i.e. on the forming limit diagram.

The last three projects should lead to particularly useful data as the predictions depend sensitively on the shape of the locus being considered. Finally, further investigations should be carried out regarding the possibility of predicting deformation textures with CMTP yield functions.

STATEMENT OF ORIGINALITY AND CONTRIBUTION TO KNOWLEDGE

The present work includes the following original contributions :

1. A new five-dimensional orthonormal reference frame was introduced in which the five base vectors defining the stress and strain rate spaces have the same length. In this way, stress and strain rate vectors can be decomposed onto a single set of axes along which the five unit vectors lead to equilibrated work conjugated components. Compared to older representations, this notation facilitates the plotting of yield surface cross-sections. Furthermore, it permits an orthogonal 5x5 transformation matrix to be defined which enables changes of reference frame to be carried out more rapidly.

2. Classical Taylor/Bishop and Hill crystallographic calculations were performed on a series of idealized cube textures which were specified in terms of a rotationally symmetric gaussian distribution of misorientations with scatter widths increasing from 0° (single crystal) to 45°. The normal stress (π-plane) cross-sections were shown to evolve from a hexagonal form (single crystal) to a nearly circular one (when the scatter widths are in the range 10 to 15°), to a rounded hexagonal form once again (when the orientations are fully random). This evolution has not been previously described in the literature. By contrast, in the shear stress planes, the shape of the yield surface cross-sections was demonstrated to evolve gradually from a square form (single crystal) to a circular one (random aggregate). This analysis of the effect of scatter width on the shape of crystallographic yield surfaces provides a good foundation for the fitting of continuum yield functions.

3. New continuum yield functions were derived, which were formulated so as to represent the yield surface of a disoriented grain. These were generalizations of the quadratic CMTP criterion first proposed by Montheillet et al. [5]. Some of these new functions were deduced from a development of the equation of the

Bishop and Hill polyhedron and adapted so as to preserve the relative simplicity of the present type of calculation.

4. The random contribution to plastic properties was simulated using a simple analytic representation. In the π-plane, the random Taylor/Bishop and Hill yield surface was fitted by an analytic function of the 9th order. By contrast, a quadratic criterion was used to reproduce the spherical shape calculated in the shear stress subspace. The parameters of these functions were computed from knowledge of the uniaxial and plane strain tension Taylor factors calculated by the Bishop and Hill technique. This new representation of the random yield surface allows the contribution to the plastic anisotropy made by the random "background" observed in experimental pole figures to be calculated in a simple manner.

5. Algorithms were developed which permit the calculation of (a) strain rate ratio $R(\theta)$ curves; (b) yield stress ratio $\sigma(\theta)/\sigma(0)$ curves; (c) the biaxial stress σ_b, and (d) any two dimensional cross-section of the macroscopic yield surface. The method applies to any combination of texture components (with their respective weights) and employs the Sachs (uniform stress direction), Taylor (uniform strain) or Kochendorfer (law of mixtures) grain interaction models for averaging purposes. The particular advantages for engineering calculations of the lattermost method of averaging have been illustrated. The $R(\theta)$ and $\sigma(\theta)$ vs. ideal orientation relationships which have been implicit in the past with the use of crystallographic methods, have received for the first time an explicit and simple formulation. Similarly, the "anomalous behaviour" of metals is linked readily to the presence of certain texture components. The only investigation carried out earlier, to our knowledge, on this particular subject was based on a crystallographic Bishop and Hill analysis [77]. Finally, the axial effects observed in free end torsion tests have been correlated analytically to the orientations present. Only a rough description of this relationship has been proposed in the past [91].

REFERENCES

1. J.F.W. Bishop and R. Hill, Phil. Mag., 1951, 42, p.414.

2. G.I. Taylor, J. Inst. Met., 1938, 62, 307.

3. G. Sachs, Z. d. Ver. deut. Ing., 1928, 72, p.734.

4. R. Hill, Proc. Roy. Soc. London, Ser.A, 1948, 193, p.281.

5. F. Montheillet, P. Gilormini and J.J. Jonas, Acta Metall., 1985, 33, p.705.

6. J.F.W. Bishop and R. Hill, Phil. Mag., 1951, 42, p.1298.

7. G.Y. Chin and W.L. Mammel, Trans. AIME, 1969, 245, p.1211.

8. W.F. Hosford and W.A. Backofen, "Fundamentals of Deformation Processing", Edited by W.F. Hosford et al., Syracuse University Press, p.259, 1964.

9. H.R. Piehler and W.A. Backofen, in "Textures in Research and Practice", Eds.J. Grewen and G. Wassermann , Springer-Verlag, 1969, p.436.

10. H.J. Bunge, Krist. u. Technik, 1970, 5, p.145.

11. G.R. Canova, U.F. Kocks, C.N. Tomé and J.J. Jonas, J. Mech. Phys. Solids, 1985, 33, p.371.

12. J. Hirsch, R. Musick and K. Lucke, Proc. ICOTOM 5, March 28-31, 1978, Aachen (Germany), Vol. II, p.437.

13. H.J. Bunge, in "Quantitative Texture Analysis", Ed. H.J. Bunge and C. Esling, 1982, p.383.

14. J.S. Kallend and G.J. Davies, J. Inst. Metals, 1970, 98, p.242.

15. J.S. Kallend and G.J. Davies, J. Inst. Metals, 1971, 5, p.257.

16. H.J. Bunge, "Texture Analysis in Materials Science", Akademie-Verlag, Berlin, 1969.

17. R. Hill, "Mathematical Theory of Plasticity", Oxford University Press, London, 1950.

18. H. Tresca, Comptes Rendus Acad. Sci. Paris., 1864, 59, p.754.

19. R. von Mises, Gottinger Nachrichten, Math.-Phys. Klasse, 1913, p.582.

20. A.N. Bramley and P.B. Mellor, Int. J. Mech. Sci., 1968, 10, p.211.

21. A.N. Bramley and P.B. Mellor, Int. J. Mech. Sci., 1966, 8, p.101.

22. C. Vial, PhD Thesis, University of Michigan, 1980.

23. C. Vial, W.F. Hosford and R.M. Caddell, Int. J. Mech. Sci., 1983, 25, p.899.

24. W.F. Hosford, Int. J. Mech. Sci., 1985, 27, p.423.

25. M. Gotoh, Int. J. Mech. Sci., 1977, 19, p.513.

26. M. Gotoh, Int. J. Mech. Sci., 1977, 19, p.505.

27. I.L. Dillamore, R.J. Hazel, T.W. Watson and P. Hadden, Int. J. Mech. Sci., 1971, 13, p.1049.

28. N.L. Svensson, J. Inst. Met., 1966, 94, p.284.

29. W.T. Lankford, S.C. Snyder and J.A. Bauscher, Trans. Am. Soc. Metals, 1950, 42, p.1197.

30. R.L. Whiteley, Trans. ASM, 1960, 52, p.154.

31. D.J. Blickwede, Trans. ASM, 1968, 61, p.651.

32. N.L. Svensson, Trans. AIME, 1966, 236, p.1004.

33. K.T. Aust and F.R. Morral, J. Metals, March 1953, p.431.

34. L. Bourne and R. Hill, Phil. Mag., 1950, 41, p.671.

35. G.E.G. Tucker, Acta Metall., 1961, 9, p.275.

36. D.V. Wilson and R.D. Butler, J. Inst. Metals, 1963, 90, p.473.

37. P.M.B. Rodrigues and P.S. Bate, Proc. of the AIME Symp. on "Textures in Non-Ferrous Metals and Alloys", Sept. 1984, Detroit, Eds. H.D. Merchant and J.G. Morris, 1985, p.173.

38. C.S. da C.Viana, J.S. Kallend and G.J. Davies, Int. J. Mech. Sci., 1979, 21, p.355.

39. R.W. Logan, PhD Thesis, The University of Michigan, 1985.

40. D.J. Meulemann, PhD Thesis, University of Michigan, 1980.

41. W.F. Hosford and C. Kim, Met. Trans. A, 1976, 7A, p.468.

42. B.A. Riggs, Sheet Met. Ind., 1973, 50, p.620.

43. W.F. Hosford, in "Formability : Analysis, Modeling, and Experimentation", Eds. S. Hecker, A. Ghosh and H.L. Gegel, The Metallurgical Society of AIME, New York, 1978.

44. M. Atkinson, Sheet Met. Ind., 1967, 44, p.167.

45. D.V. Wilson, J. Inst. Metals, 1966, 94, p.84.

46. D.J. Lloyd, Sheet Met. Ind., 1962, 39, p.83.

47. J.L. Duncan, Letter to the Editor, Int. J. Mech. Sci., 1967, 9, p.157.

48. P.B. Mellor and A.N. Bramley, Letter to the Editor, Int. J. Mech. Sci., 1967, 9, p.158.

49. J. Woodthorpe and R. Pearce, Int. J. Mech. Sci., 1970, 12, p.341.

50. R. Pearce, Int. J. Mech. Sci., 1968, 10, p.995.

51. A.J. Ranta-Eskola, Metals Technology, 1980, 7, p.45.

52. R.M.S.B. Horta, W.T. Roberts, and D.V. Wilson, Int. J. Mech. Sci., 1970, 12, p.231.

53. G.S. Kullar and M.J. Hillier, Int. J. Mech. Sci., 1972, 12, p.631.

54. I.L. Dillamore, J. Phys. D. Appl. Phys., 1974, 7, p.979.

55. R.W. Logan and W.F. Hosford, Int. J. Mech. Sci., 1980, 22, p.419.

56. Z. Marciniak and K. Kuczynski, Int. J. Mech. Sci., 1967, 9, p.609.

57. R. Sowerby and J.L. Duncan, Int. J. Mech. Sci., 1971, 13, p.217.

58. R. Venter, W. Johnson and M.D. Malherbe, Int. J. Mech. Sci., 1971, 13, p.299.

59. Z. Marciniak, K. Kuczynski and T. Pokora, Int. J. Mech. Sci., 1973, 15, p.789.

60. A. Parmar and P.B. Mellor, Int. J. Mech. Sci., 1978, 20, p.385.

61. J. Woodthorpe and R. Pearce, Sheet Met. Ind., 1969, 46, p.1061.

62. M. Azrin and W.A. Backofen, Trans. Met. Soc. AIME, 1965, 233, p.71.

63. J. Althoff and P. Wincierz, Z. Metallkde, 1972, 63, p.623.

64. D. Grzesik, Z. Metallkde, 1972, 63, p.618.

65. M. Benferrah, M.Eng. Thesis, McGill University, Montreal, Canada, 1986.

66. M.G. Stout, P.L. Martin, D.E. Helling and G.R. Canova, Int. J. Plast., 1985, 2, p.163.

67. U.F. Kocks and G.R. Canova,2nd Riso Int. Symp. on Metallurgy and Mat. Sci., Risö, Denmark, Sept. 1981, p.35.

68. H. Bunge, in "Quantitative Texture Analysis", Eds H. Bunge and C. Esling, Deutsche Ges. fur Metallkde, 1982, p.383.

69. R. Sowerby, C.S. da C. Viana and G.J. Davies, Mats. Sci. Engng., 1980, 46, p.23.

70. K. Mols, K. van Praet and P. van Houtte, Proc. ICOTOM 7, Noordwijkerhout, Holland, Sept. 1984, Eds. C.M. Brakman et al., 1985, p.651.

71. R. Hill, Math. Proc. Cambridge Philos. Soc., 1979, 85, p.179.

72. S. Kobayashi, R.M. Caddell and W.F. Hosford, Int. J. Mech. Sci., 1985, 27, p.509.

73. B. Dodd and R.M. Caddell, Int. J. Mech. J., 1984, 26, p.113.

74. A.Parmar and P.B. Mellor, Int. J. Mech. Sci., 1978, 20, p.707.

75. W.F. Hosford, Jr., Seventh N. American Metalworking Res. Conf. Proc., 1979, p.191.

76. J.L. Bassani, PhD Thesis, Harvard University, 1978.

77. J.L. Bassani, Int. J. Mech. Sci., 1977, 19, p.651.

78. P.B. Mellor and A. Parmar, in "Mechanics of Sheet Metal Forming", Proc. Conf. Warren, MI, Eds. D.P. Koistinen and N.M. Wang, Plenum, 1978, p.53.

79. M. Taghvaipour and P.B. Mellor,Proc. Inst. Mech. Engrs., 1970, 185, p.593.

80. W.F. Hosford and R.M. Caddell, "Metal Forming, Mechanics and Metallurgy", Prentice-Hall, 1983.

81. W.F. Hosford, Proc. ICSMA 3, Cambridge, England, August 1973, p.137.

82. A. Backofen, "Deformation Processing", Addison Wesley, Reading, Massachusetts, 1972.

83. C.F. Shih and D. Lee, J. Eng. Mat. Tech., 1978, 100, p.294.

84. R. Sowerby and W. Johnson, Mater. Sci. Eng., 1975, 20, p.101.

85. R. Sowerby, Proc. AIME Symp. on "Textures in Non-Ferrous Metals and Alloys", Sept. 1984, Detroit, Eds. H.D. Merchant and J.G. Morris, 1985, p.99.

86. P.B. Mellor, Int. Metals Reviews, 1981, 27, p.1.

87. P.B. Mellor, in "Mechanics of Solids : The Rodney Hill 60th Anniversary Volume", Ed. H.G. Hopkins et al., Manchester, Pergamon Press, April 1980, p.383.

88. Ph. Lequeu, P. Gilormini, F. Montheillet, B. Bacroix and J.J. Jonas, Acta Metall., 35, in press.

89. B. Orlans, B. Bacroix, J. Driver, F. Montheillet and J.J. Jonas, to be published.

90. K. Lucke, J. Pospiech, K.H. Virnich and J. Jura, Acta Metall., 1981, 29, p.167.

91. W. Rose and H.P. Stuwe, Z. Metallkde, 1968, 59, p.396.

92. A. Skalli, R. Fortunier, R. Fillit and J.H. Driver, Acta Metall., 1985, 33, p.997.

93. A. Skalli, Thèse de Doctorat d'Etat, Grenoble, 1984.

94. P. Van Houtte, Text. and Microstruct., 1984, 6, p.137.

95. J. Pospiech, Krist. u. Technik, 1972, 7, p.1057.

96. U.F. Kocks, G.R. Canova and J.J. Jonas, Acta Metall., 1983, 31, p.1243.

97. P. van Houtte, private communication.

98. B. Bacroix, Ph.D. Thesis, McGill University, Montreal, Canada, 1986.

99. U.F. Kocks, Acta Metall., 1960, 8, p.345.

100. G.R. Canova, U.F. Kocks and J.J. Jonas, Acta Metall., 1984, 32, p.211.

101. P. van Houtte, Proc. ICSMA 7 Conf., Montreal, Canada, August 1985, Eds. H. McQueen et al., Pergamon Press, vol.3, 1986, p.1701.

102. P. van Houtte, Proc. ICOTOM 6, Tokyo, Japan, Ed. S. Nagashima, Iron and Steel Inst. Japan, 1981, p.428.

103. Ph. Lequeu, F. Montheillet and J.J. Jonas, Proc. ICSMA7 Conf., Montreal, 1985, Vol.1, p.269.

104. S.L. Semiatin, P.R. Morris and H.R. Piehler, Texture of Cryst. Solids, 1979, 3, p.191.

105. S.R. Goodman and H. Hu, Met. Trans., 1970, 1, p.1629.

106. J.A. Elias, R.H. Heyer and J.G. Smith, Trans. AIME, 1962, 224, p.678.

107. W. Truskowski and J. Jarominek, Mem. Sci. Rev. Metal., 1973, 6, p.433.

108. C.A. Stickels and P.R. Mould, Metall. Trans., 1970, 1, p.1303

109. M. Hatherley and W.B. Hutchinson, in "An Introduction to Textures in Metals", The Institution of Metallurgists, Chameleon Press Ltd, London, 1979, p.12.

110. R. Fortunier and J.H. Driver, Acta Metall., 1986, 34, in press.

111. P. van Houtte, submitted to Texture and Microstruct., 1986.

112. J.L. Bassani, private communication.

113. W.I. Zangwill, in "Non-linear Programming - A Unified Approach", Prentice Hall, Englewood Cliffs, N.J., 1969.

114. W. Dabrowski, J. Karp and H.J. Bunge, Arch. Eisenhüttenwes., 1982, 53, p.361.

115. C.S. Barrett and T.B. Massalski, "Structure of Metals", McGraw-Hill, New York, 3rd ed., 1966.

116. I.L. Dillamore and W.T. Roberts, Metall. Reviews, 1965, 10, p.271.

117. D.N. Hawkins, Metals Tech., 1976, 3, p.417.

118. G.F. Melloy and J.D. Dennison, in "The Microstructure and Design of Alloys", vol.1, London, the Institute of Metals, 1973, p.60.

119. B.L.Bramfitt and A.R. Marder, Symp. on "Processing Conditions and Properties of Low Carbon Steels", AIME, 1971, p.191.

120. D.L. Bourell, Metall. Trans. A, 1983, 14, p.2487.

121. H. Eichelkraut, J. Hirsch and K. Lücke, Z. Metallkde, 1984, 75, p.113.

122. P. Parnière and L. Roesch, Mem. Sci. Rev. Met., 1975, 72, p.221.

123. Y. Ito, K. Hashiguchi and N. Ohashi, Proc. Int. Conf. on "The Science and Tech. of Iron and Steel", Part II, Trans. Iron and Steel Inst. Japan, 1971, p.958.

124. R.S. Burns and R.H. Heyer, Proc. Intern. Symp. on "The Annealing of Low-Carbon Steel", Cleveland, 1957, p.9.

125. P.M.B. Rodrigues, H. Bichsel and P. Furrer, Proc. of the AIME Symp on "Textures in Non-Ferrous Metals and Alloys", Sept. 1984, Detroit, Eds. H.D. Merchant and J.G. Morris, 1985, p.45.

126. M. Arminjon, private communication.

127. R.W. Vieth and R.L. Whiteley, Third Intern. Colloquium on "Forming and Testing of Sheet Metal", IDDRG, London, 1964.

128. R.L. Whiteley, Metal Progress, 1968, 94, p.81.

128b. M. Fukuda, Trans. Iron Steel Inst. Japan, 1968, 8, p.68.

129. W.G. Fricke Jr., Proc. of the AIME Symp. on "Textures in Non-Ferrous Metals and Alloys", Sept. 1984, Detroit, Eds. H.D. Merchant and J.G. Morris, 1985, p.213.

130. D. Hardwick and W.J. Mc G. Tegart, Mem. Sci. Rev. Met., 1961, 58, p.869.

131. H.W. Swift, Engineering, April 1947, p.253.

132. F. Morozumi, Nippon Kokan Techn. Report, Feb. 1965, no 4, p.67.

133. F. Montheillet, M. Cohen and J.J. Jonas, Acta Metall., 1984, 32, p.2077.

134. C-H. Wei, M.Eng., The University of Tennessee, 1973.

135. P. Parnière, Thèse Docteur Es-Sciences Phys., Centre d'Orsay, Université de Paris Sud, 1978.

136. D.C. Drucker, Proc. 1st U.S. Nat. Congress, Appl. Mech., 1951.

137. A. Pochettino, Thèse de Docteur Ingénieur, Centre d'Orsay, Université de Paris Sud, 1981.

138. N. Kanetake, Y. Tozawa and T. Otani, Int. J. Mech. Sci., 1983, 25, p.237.

139. D.H. Avery, W.F. Hosford and W.A. Backofen, Trans. AIME, 1965, 233, p.71.

140. A.W. Stephens, Ph.D. Thesis, University of Arizona, 1968.

141. J.S. Kallend and G.J. Davies, Texture, 1972, 1, p.51.

142. M. Bull and D.J. Lloyd, ALCAN Lab., Kingston, Ontario, private communication.

143. A. Kochendörfer, Reine und Angewandte Metallkde, Springer, Berlin, 1941.

144. H. Honeff and H. Mecking, Proc. ICOTOM5, Eds. G. Gottstein and K. Lucke, Springer, Berlin, 1978, Vol.1, p.265.

145. M. Berveiller, A. Hihi and A. Zaoui, Proc ICOTOM6, Ed. S. Nagashima, The Iron and Steel Inst. of Japan, 1981, Vol.1, p.452.

146. M. Berveiller, A. Hihi and A. Zaoui, in "Deformation of Polycrystals", Eds. N. Hansen et al., Risö Nat. Lab., Denmark, 1983, p.145.

147. U.F. Kocks, in "Unified Constitutive Equations for Plastic Deformation and Creep of Engineering Alloys", Chapter 2, Ed. A.K. Miller, in press.

148. G.R. Canova, U.F. Kocks and M.G. Stout, Scripta Metall., 1984.

149. P. Parnière and C. Sauzay, Mat. Sci. and Eng., 1976, 22, p.271.

150. O.A. Ruano and G. Gonzalez, Scripta Metall., 1985, 19, p.27.

151. G. Jegaden, J. Voinchet and P. Roquet, Mem. Sci. Rev. Met., 1962, 59, p.273.

152. P.I. Welch, L.Ratke and H.J. Bunge, Proc. 13th IDDRG Congress, Melbourne, Australia, Feb. 1984, p.436.

153. F. Montheillet, private communication.

154. J. Grewen and G. Wasserman, Acta Metall., 1955, 3, p.354.

155. I.L. Dillamore and W.T. Roberts, Acta Metall. 1964, 12, p.281.

156. Y.C. Liu and W.R. Hibbard, Trans. AIME, 1955, 203, p.1249.

157. H.Hu, P.R. Sperry and P.A Beck, Trans. AIME, 1952, 194, p.76.

158. Y.C. Liu and W.R. Hibbard, Trans. AIME, 1953, 197, p.672.

159. E.R.W. Jones and E.A. Fell, Acta Metall., 1957, 5, p.689.

160. M.N. Parthasarathi and P.A. Beck, Trans. AIME, 1961, 221, p.61.

APPENDIX III.1

RELATIONS BETWEEN THE ROTATION AXIS d AND ANGLE ω AND THE EULER ANGLES

Three independent parameters are required for the description of the orientation of a crystallite in a polycrystalline material. For ease of reference, the relations derived by Pospiech [95] between the Euler angles of Bunge (ϕ_1, Φ, ϕ_2) and the rotation axis d(δ, ψ) and angle ω employed here (see Fig. 3.2) are given below.

$$\begin{cases} \sin(\omega/2)\sin\delta = \sin(\Phi/2) \\ \cos(\omega/2) = \cos(\Phi/2)\cos((\phi_1+\phi_2)/2) \\ \psi = \frac{1}{2}(\phi_1-\phi_2) \end{cases} \qquad \text{(III.1.1)}$$

The transformation matrix for passage from the C_0 reference system to the C system is [16, 95]:

$$P = \begin{bmatrix} \cos\phi_1\cos\phi_2-\sin\phi_1\sin\phi_2\cos\Phi & \sin\phi_1\cos\phi_2+\cos\phi_1\sin\phi_2\cos\Phi & \sin\phi_2\sin\Phi \\ -\cos\phi_1\sin\phi_2-\sin\phi_1\cos\phi_2\cos\Phi & -\sin\phi_1\sin\phi_2\mp\cos\phi_1\cos\phi_2\cos\Phi & \cos\phi_2\sin\Phi \\ \sin\phi_1\sin\Phi & -\cos\phi_1\sin\Phi & \cos\Phi \end{bmatrix} \qquad \text{(III.1.2)}$$

$$= \begin{bmatrix} (1-d_1^2)\cos\omega+d_1^2 & d_1d_2(1-\cos\omega)+d_3\sin\omega & d_1d_3(1-\cos\omega)-d_2\sin\omega \\ d_1d_2(1-\cos\omega)-d_3\sin\omega & (1-d_2^2)\cos\omega+d_2^2 & d_2d_3(1-\cos\omega)+d_1\sin\omega \\ d_1d_3(1-\cos\omega)+d_2\sin\omega & d_2d_3(1-\cos\omega)-d_1\sin\omega & (1-d_3^2)\cos\omega+d_3^2 \end{bmatrix}$$

where $d_1 = \sin\delta\cos\psi$, $d_2 = \sin\delta\sin\psi$ and $d_3 = \cos\delta$

An element of volume in each of the two orientation spaces is specified as follows:

$$\begin{cases} dg = d(\cos\Phi)\,d\phi_1\,d\phi_2\,/\,8\pi^2 \\ dg = \sin^2(\omega/2)\,d\omega\,d(\cos\delta)\,d\psi\,/\,\pi^2 2 \end{cases} \qquad \text{(III.1.3)}$$

APPENDIX III.2

FIVE-DIMENSIONAL REPRESENTATION OF STRESS AND STRAIN RATE VECTORS

It is the aim of this appendix to express the stress and strain rate vectors of interest to crystal plasticity in a five-dimensional orthonormal reference frame. This preoccupation is related to the fact that the six component tensors under consideration only have 5 independent components.

Let us consider a vector $\vec{V} = (V_{ij})$ that can be decomposed on a 9-dimensional orthonormal basis $(\vec{i}_k)$:

$$\vec{V} = V_{11}\vec{i}_1 + V_{22}\vec{i}_2 + V_{33}\vec{i}_3 + V_{23}\vec{i}_4 + V_{31}\vec{i}_5 + V_{12}\vec{i}_6 + V_{32}\vec{i}_7 + V_{13}\vec{i}_8 + V_{21}\vec{i}_9 \tag{III.2.1}$$

From symmetry considerations, let us also define five vectors $(\vec{u}_k)$ as follows :

$$\begin{bmatrix} \vec{u}_1 \\ \vec{u}_2 \\ \vec{u}_3 \\ \vec{u}_4 \\ \vec{u}_5 \end{bmatrix} = \begin{bmatrix} a_{11} & a_{12} & a_{13} & 0 & 0 & 0 & 0 & 0 & 0 \\ a_{21} & a_{22} & a_{23} & 0 & 0 & 0 & 0 & 0 & 0 \\ 0 & 0 & 0 & a_{34} & 0 & 0 & a_{37} & 0 & 0 \\ 0 & 0 & 0 & 0 & a_{45} & 0 & 0 & a_{48} & 0 \\ 0 & 0 & 0 & 0 & 0 & a_{56} & 0 & 0 & a_{59} \end{bmatrix} \begin{bmatrix} \vec{i}_1 \\ \vec{i}_2 \\ . \\ . \\ \vec{i}_9 \end{bmatrix} \tag{III.2.2}$$

Here, the a_{ij}'s must be calculated so that the $(\vec{u}_k)$ vectors form an orthonormal set. The $\vec{u}_1$ and $\vec{u}_2$ vectors are chosen arbitrarily in a plane perpendicular to the direction (1,1,1,0,0,0,0,0,0) : this plane corresponds to the so-called π-plane in deviator stress space ($S_{11} + S_{22} + S_{33} = 0$) (see Fig. III.2.1). In this way

$$\begin{cases} \vec{u}_1 = a_{12}(\vec{i}_2 - \vec{i}_1) \\ \vec{u}_2 = a_{23}(\vec{i}_3 - (\vec{i}_1 + \vec{i}_2)/2) \\ \vec{u}_3 = a_{34}\,\vec{i}_4 + a_{37}\,\vec{i}_7 \\ \vec{u}_4 = a_{45}\,\vec{i}_5 + a_{48}\,\vec{i}_8 \\ \vec{u}_5 = a_{56}\,\vec{i}_6 + a_{59}\,\vec{i}_9 \end{cases} \tag{III.2.3}$$

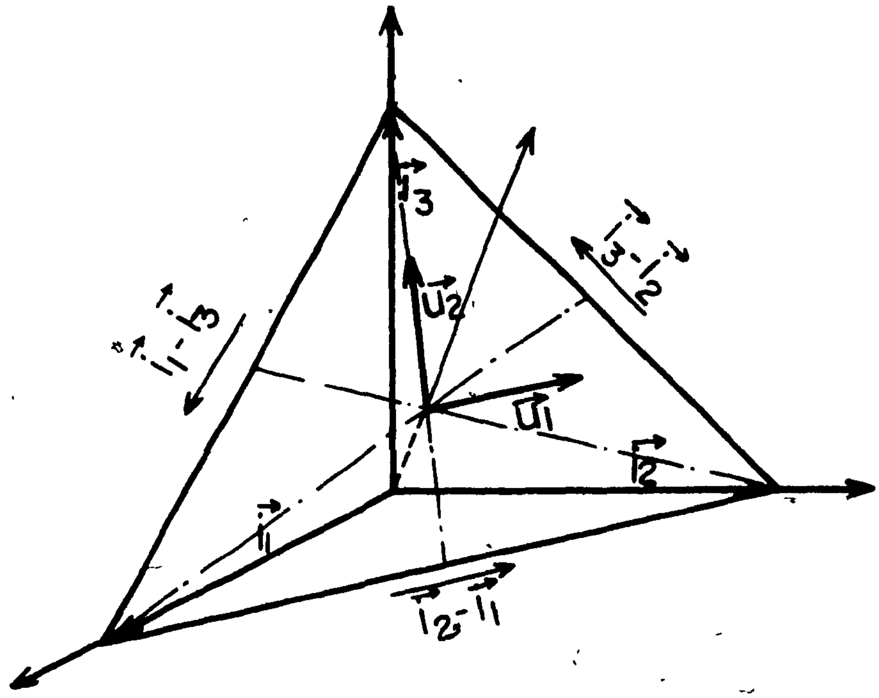

Fig. III.2.1 Definition of the ($\vec{u}_1,\vec{u}_2$) vectors.

Since the ($\vec{i}_k$) set is orthogonal by definition, the ($\vec{u}_k$) one is also orthogonal in as much as :

$$\vec{u}_k \cdot \vec{u}_j = 0 \qquad \text{for } j \neq k \tag{III.2.4}$$

The ($\vec{u}_k$) reference frame will therefore be orthonormal if

$$\|\vec{u}_k\| = 1 \qquad \text{for } k = 1 \text{ to } 5 \tag{III.2.5}$$

that is, if

$$\begin{cases} a_{12} = 1/\sqrt{2} \\ a_{23} = \sqrt{2/3} \\ a_{34}^2 + a_{37}^2 = 1 \\ a_{45}^2 + a_{48}^2 = 1 \\ a_{56}^2 + a_{59}^2 = 1 \end{cases} \tag{III.2.6}$$

$\vec{V}$ can now be expressed in the two bases (Eq. III.2.1 and $\vec{V} = V_k \vec{u_k}$), from which it can be shown that :

$$\begin{cases} V_{11} = -V_1/\sqrt{2} - V_2/\sqrt{6} \\ V_{22} = +V_1/\sqrt{2} - V_2/\sqrt{6} \\ V_{33} = +V_2\sqrt{2/3} \\ V_{23} = a_{34}\, V_3 \\ V_{32} = a_{37}\, V_3 \\ V_{31} = a_{45}\, V_4 \\ V_{13} = a_{48}\, V_4 \\ V_{12} = a_{56}\, V_5 \\ V_{21} = a_{59}\, V_5 \end{cases} \qquad \text{(III.2.7)}$$

If the 'shear' components of $\vec{V}$ are assumed to be symmetrical ($V_{ij} = V_{ji}$), which is the case for the current stress and strain rate vectors, Eq. III.2.6 can be employed to deduce that

$$\begin{cases} a_{34} = a_{37} = \pm 1/\sqrt{2} \\ a_{45} = a_{48} = \pm 1/\sqrt{2} \\ a_{56} = a_{59} = \pm 1/\sqrt{2} \end{cases} \qquad \text{(III.2.8)}$$

although only the positive values are retained here.

A vector $\vec{V}$ verifying the conditions $V_{ij} = V_{ji}$ and $V_{11} + V_{22} + V_{33} = 0$ can thus be decomposed onto two different reference frames :

$$\begin{aligned} \vec{V} &= V_{11}\vec{i_1} + V_{22}\vec{i_2} + V_{33}\vec{i_3} + V_{23}(\vec{i_4} + \vec{i_7}) + V_{31}(\vec{i_5} + \vec{i_8}) + V_{12}(\vec{i_6} + \vec{i_9}) \\ &= V_1\vec{u_1} + V_1\vec{u_2} + V_3\vec{u_3} + V_4\vec{u_4} + V_5\vec{u_5} \end{aligned} \qquad \text{(III.2.9)}$$

with

$$\begin{cases} \vec{u_1} = (\vec{i_2} - \vec{i_1})/\sqrt{2} \\ \vec{u_2} = \sqrt{2/3}\,(\vec{i_3} - (\vec{i_1} + \vec{i_2})/2) \\ \vec{u_3} = (\vec{i_4} + \vec{i_7})/\sqrt{2} \\ \vec{u_4} = (\vec{i_5} + \vec{i_8})/\sqrt{2} \\ \vec{u_5} = (\vec{i_6} + \vec{i_9})/\sqrt{2} \end{cases} \qquad \text{(III.2.10)}$$

and
$$\begin{cases} V_1 = (V_{22} - V_{11}) / \sqrt{2} \\ V_2 = \sqrt{3/2}\, V_{33} \\ V_3 = \sqrt{2}\, V_{23} \\ V_4 = \sqrt{2}\, V_{31} \\ V_5 = \sqrt{2}\, V_{12} \end{cases} \tag{III.2.11}$$

An interesting consequence of Eq. III.2.11 is that the two sets of stress $\vec{S}$ and strain rate $\vec{\dot{\varepsilon}}$ vectors are work conjugate, i.e.

$$S_k \, \dot{\varepsilon}_k = S_{ij} \, \dot{\varepsilon}_{ij} \tag{III.2.12}$$

A verification of the normality rule can also be performed. The problem consists of determining if the $\vec{\dot{\varepsilon}} = (\dot{\varepsilon}_k)$ vector expressed by Eq. III.2.11 is perpendicular to the 5-dimensional yield surface $F'(S_k) = 0$, provided that $\vec{\dot{\varepsilon}} = (\dot{\varepsilon}_{ij})$ is normal to the 9-dimensional locus $F(S_{ij}) = 0$.

The latter condition is represented by

$$\dot{\varepsilon}_{ij} = \dot{\lambda} \, \partial F / \partial S_{ij} \tag{III.2.13}$$

The differential dF can be expressed in the following two ways :

$$dF = (\partial F / \partial S_{ij}) \, dS_{ij} = (\partial F' / \partial S_k) \, dS_k \tag{III.2.14}$$

since $F(S_{ij}) = F(S_{ij}(S_k)) = F'(S_k)$. Furthermore, using Eq. III.2.11 and the condition that $dS_{11} + dS_{22} + dS_{33} = 0$, it can be shown that

$$\begin{cases} dS_1 = -dS_{11} / \sqrt{2} + dS_{22} / \sqrt{2} \\ dS_2 = -\sqrt{3/2}\,(dS_{11} + dS_{22}) \\ dS_3 = \sqrt{2}\, dS_{23} \\ dS_4 = \sqrt{2}\, dS_{31} \\ dS_5 = \sqrt{2}\, dS_{12} \end{cases} \tag{III.2.15}$$

so that, by identity :

$$\left\{\begin{array}{l} \partial F' / \partial S_1 = (\partial F / \partial S_{22} - \partial F / \partial S_{11}) / \sqrt{2} = (\dot{\varepsilon}_{22} - \dot{\varepsilon}_{11}) / \sqrt{2} / \dot{\lambda} = \dot{\varepsilon}_1 / \dot{\lambda} \\ \partial F' / \partial S_2 = \sqrt{3/2}\, \partial F / \partial S_{33} = \sqrt{3/2}\, \dot{\varepsilon}_{33} / \dot{\lambda} = \dot{\varepsilon}_2 / \dot{\lambda} \\ \partial F' / \partial S_3 = \sqrt{2}\, \partial F / \partial S_{23} = \sqrt{2}\, \dot{\varepsilon}_{23} / \dot{\lambda} = \dot{\varepsilon}_3 / \dot{\lambda} \\ \partial F' / \partial S4 = \sqrt{2}\, \partial F / \partial S_{31} = \sqrt{2}\, \dot{\varepsilon}_{31} / \dot{\lambda} = \dot{\varepsilon}_4 / \dot{\lambda} \\ \partial F' / \partial S5 = \sqrt{2}\, \partial F / \partial S_{12} = \sqrt{2}\, \dot{\varepsilon}_{12} / \dot{\lambda} = \dot{\varepsilon}_5 / \dot{\lambda} \end{array}\right. \qquad (\text{III}.2.16)$$

The normality principle is thus obeyed in the 5-dimensional space specified by Eq. III.2.10, as long as it is valid in the complete 9-dimensional space.

It should be noted that the same kind of demonstration could have been carried out starting directly with the conventional 6-dimensional stress or strain rate space (in which the 'shear' components are already symmetrical).

APPENDIX IV.1

CONVEXITY REQUIREMENTS OF THE YIELD SURFACES ASSOCIATED WITH MATERIALS OF CUBIC SYMMETRY

The convexity of a general yield function defined by

$$F(S_{ij}) = \alpha [|S_{11} - S_{22}|^n + |S_{22} - S_{33}|^n + |S_{33} - S_{11}|^n] + 2\beta [|S_{12}|^m + |S_{23}|^m + |S_{31}|^m] - 1 = 0 \qquad \text{(IV.1.1)}$$

can be tested using the so-called Hessian matrix [112,113]. The $\ell \times \ell$ elements of this matrix are defined as

$$h_{ij} = \partial^2 F(S_k) / \partial S_i \partial S_j \qquad \text{(IV.1.2)}$$

The function $F(S_i) = 0$ is concave with respect to the origin if H is a positive semi-definite matrix, i.e. if all its ℓ eigenvalues are positive or zero :

$$\lambda_i \geqslant 0 \qquad i = 1, 2, \ldots, \ell \qquad \text{(IV.1.3)}$$

In this appendix, it is shown that the continuum yield functions defined by Eq. IV.1.1 are convex in the present five-dimensional space (S_1, S_2, S_3, S_4, S_5), whatever the two exponents n and m $\geqslant 1$. Using the definitions of Eq. 3.9 :

$$S_1 = (S_{22} - S_{11})/\sqrt{2}, S_2 = \sqrt{3/2}\, S_{33}, S_3 = \sqrt{2}\, S_{23}, S_4 = \sqrt{2}\, S_{31}, S_5 = \sqrt{2}\, S_{12} \qquad \text{(IV.1.4)}$$

the yield function can be written as :

$$F(S_i) = \alpha\, 2^{-n/2} [|2S_1|^n + |S_1 - \sqrt{3}S_2|^n + |S_1 + \sqrt{3}S_2|^n] + 2\beta 2^{-m/2} [|S_3|^m + |S_4|^m + |S_5|^m] - 1 = 0 \qquad \text{(IV.1.5)}$$

where the coefficients α and β are positive. When the cubic symmetry of the present materials is taken into account, the convexity requirements can be restricted to the ranges :

$$S_1 \geq 0;\ S_2 \geq S_1/\sqrt{3};\ S_3 \geq 0;\ S_4 \geq 0;\ S_5 \geq 0 \qquad \text{(IV.1.6)}$$

The two first conditions follow from the symmetry properties of the п-plane yield locus for cubic materials.

In this reduced range, the yield function can be expressed more simply as :

$$\begin{aligned} F(S_\iota) = {} & \alpha\, 2^{-n/2} \left[(2S_1)^n + (-S_1 + \sqrt{3}S_2)^n + (S_1 + \sqrt{3}S_2)^n \right] \\ & + 2\beta 2^{-m/2} \left[S_3{}^m + S_4{}^m + S_5{}^m \right] - 1 = 0 \end{aligned} \qquad \text{(IV.1.7)}$$

The non-zero second derivatives of $F(S_\iota)$ are the following .

$$\left\{ \begin{aligned} h_{11} &= \partial^2 F / \partial S_1{}^2 = \alpha n(n-1) 2^{-n/2} \left[2^n S_1{}^{n-2} + (\sqrt{3}S_2 - S_1)^{n-2} + (S_1 + \sqrt{3}S_2)^{n-2} \right] \\ h_{22} &= \partial^2 F / \partial S_2{}^2 = \alpha n(n-1) 2^{-n/2}\, 3 \left[(\sqrt{3}S_2 - S_1)^{n-2} + (S_1 + \sqrt{3}S_2)^{n-2} \right] \\ h_{12} &= h_{21} = \partial^2 F / \partial S_1 \partial S_2 = \partial^2 F / \partial S_2 \partial S_1 \\ &= \alpha n(n-1) 2^{-n/2} \sqrt{3} \left[-(\sqrt{3}S_2 - S_1)^{n-2} + (S_1 + \sqrt{3}S_2)^{n-2} \right] \\ h_{\iota\iota} &= \partial^2 F / \partial S_\iota{}^2 = 2\beta m(m-1)\, 2^{-m/2}\, S_\iota{}^{m-2} \qquad \iota = 3, 4, 5 \end{aligned} \right. \qquad \text{(IV.1.8)}$$

The eigenvalues of the Hessian matrix are the roots of the equation :

$$det(H - \lambda I) = \begin{vmatrix} h11-\lambda & h12 & 0 & 0 & 0 \\ h12 & h22-\lambda & 0 & 0 & 0 \\ 0 & 0 & h33-\lambda & 0 & 0 \\ 0 & 0 & 0 & h44-\lambda & 0 \\ 0 & 0 & 0 & 0 & h55-\lambda \end{vmatrix} = 0 \qquad \text{(IV.1.9)}$$

which leads to :

$$\left| \begin{aligned} & \lambda^2 - (h_{11} + h_{22})\lambda + h_{11}h_{22} - h_{12}{}^2 = 0 \\ & \lambda = h_{33} \\ & \lambda = h_{44} \\ & \lambda = h_{55} \end{aligned} \right. \qquad \text{(IV.1.10)}$$

or to :

$$\begin{cases} \lambda_1 \lambda_2 = h_{11}\, h_{22} - h_{12}{}^2 \\ \lambda_1 + \lambda_2 = h_{11} + h_{22} \\ \lambda_3 = h_{33} \\ \lambda_4 = h_{44} \\ \lambda_5 = h_{55} \end{cases} \qquad \text{(IV.1.11)}$$

It can be seen from Eqs. IV.1.8 that

$$\lambda_1 + \lambda_2 = h_{11} + h_{22} \geqslant 0 \qquad \textit{for } n \geqslant 1 \qquad \text{(IV.1.12)}$$

and that $\lambda_\iota = h_{\iota\iota} \geqslant 0 \qquad (\iota = 3, 4, 5) \qquad \textit{for } m \geqslant 1$ (IV.1.13)

Furthermore, it is easily shown that $h_{11}h_{22} - h_{12}{}^2 \geqslant 0$, so that, whatever the exponent n,

$$\lambda_1 \lambda_2 \geqslant 0 \qquad \text{(IV.1.14)}$$

It therefore follows that the five eigenvalues of H are positive or zero, so that the five-dimensional yield locus defined by Eq. IV.1.7 is convex for all n and $m \geqslant 1$.

APPENDIX IV.2

INVERSION OF THE NORMALITY RULE IN THE CASE OF A HILL TWO EXPONENT YIELD FUNCTION

The prediction of certain plastic properties as well as the calculation of polycrystalline yield surfaces on the basis of Taylor (uniform strain) averaging necessitates the inversion of the normality principle. In such cases, the stress components have to be calculated from the knowledge of the characteristics of the strain rate.

This can be done by first expressing the Hill two exponent yield function in the present five-dimensional stress space (Eq. 3.9)

$$\begin{aligned} F(S_i) = {} & \alpha\, 2^{-n/2} \left[\, |2S_1|^n + |S_1 - \sqrt{3}S_2|^n + |S_1 + \sqrt{3}S_2|^n \,\right] \\ & + 2\beta 2^{-m/2} \left[\, |S_3|^m + |S_4|^m + |S_5|^m \,\right] - 1 = 0 \end{aligned} \qquad \text{(IV.2.1)}$$

Applying the normality (or flow) rule

$$\dot{\varepsilon}_i = \dot{\lambda}\, \partial F / \partial S_i \qquad \text{(IV.2.2)}$$

it is readily shown that :

$$\left\{ \begin{aligned} \dot{\varepsilon}_1 &= \dot{\lambda}\, \alpha\, n\, 2^{-n/2} \left[2^n \frac{|S_1|^n}{S_1} + \frac{|S_1 + \sqrt{3}S_2|^n}{S_1 + \sqrt{3}S_2} + \frac{|S_1 - \sqrt{3}S_2|^n}{S_1 - \sqrt{3}S_2} \right] \\ \dot{\varepsilon}_2 &= \dot{\lambda}\, \alpha\, n\, 2^{-n/2} \sqrt{3} \left[\frac{|S_1 + \sqrt{3}S_2|^n}{S_1 + \sqrt{3}S_2} - \frac{|S_1 - \sqrt{3}S_2|^n}{S_1 - \sqrt{3}S_2} \right] \\ \dot{\varepsilon}_i &= \dot{\lambda}\, \beta\, m\, 2^{1-m/2} \frac{|S_i|^m}{S_i} \qquad i = 3, 4, 5 \end{aligned} \right. \qquad \text{(IV.2.3)}$$

Here the $\dot{\varepsilon}_i$ components are prescribed, and the S_i's are unknown.

No attempt will be made to describe the complete method used in this work; only the key points will be outlined.

It is first of interest to note that

$$\text{(i) } \dot{\varepsilon}_i = 0 \Leftrightarrow S_i = 0 \qquad \textit{for } i = 1 \textit{ to } 5 \tag{IV.2.4}$$

$$\text{(ii) } S_i \text{ and } \dot{\varepsilon}_i \text{ have the same sign} \tag{IV.2.5}$$

This is an expression of the symmetry of the yield function being considered. The discussion that follows is restricted to the case $\dot{\varepsilon}_1 \neq 0$. When $\dot{\varepsilon}_1 = 0$, similar techniques can be used for the estimation of the S_i's.

Bearing in mind that

$$\begin{cases} S_1 = S \cos \phi \\ S_2 = S \sin \phi \end{cases} \tag{IV.2.6}$$

we calculate the ratio $\dot{\varepsilon}_2/\dot{\varepsilon}_1$ from Eq. IV.2.3 in order to eliminate the factors $\dot{\lambda}$ and S :

$$(\sqrt{3}\dot{\varepsilon}_1 - \dot{\varepsilon}_2)\frac{|2\cos(\phi - \pi/3)|^n}{2\cos(\phi - \pi/3)} - (\sqrt{3}\dot{\varepsilon}_1 + \dot{\varepsilon}_2)\frac{|2\cos(\phi + \pi/3)|^n}{2\cos(\phi + \pi/3)} - \dot{\varepsilon}_2\frac{|2\cos\phi|^n}{2\cos\phi} = 0 \tag{IV.2.7}$$

A secant method can be used at this point in order to calculate ϕ, leading to the ratio $X_2 = S_2/S_1 = \tan \phi$.

We compute now the ratio $\dot{\varepsilon}_i/\dot{\varepsilon}_1$ (i = 3, 4, 5) from Eq. IV.2.3 :

$$\frac{|S_i|^{m-1}}{|S_1|^{n-1}} = \left|\frac{\dot{\varepsilon}_i}{\dot{\varepsilon}_1}\right| \frac{a\,n}{2\beta m}\, 2^{(m-n)/2} \left[2^n + \frac{|1+\sqrt{3}X_2|^n}{1+\sqrt{3}X_2} + \frac{|1-\sqrt{3}X_2|^n}{1-\sqrt{3}X_2} \right] = X_i \tag{IV.2.8}$$

Since the vector (S_i) must terminate on the yield locus, the value of S_1 can be evaluated from the following equation :

$$|S_1|^n \{ \alpha 2^{-n/2} [2^n + |1+\sqrt{3}X_2|^n + |1-\sqrt{3}X_2|^n] \} + |S_1|^{m(n-1)/(m-1)} \{ \beta 2^{1-m/2} [|X_3|^{m/(m-1)} + |X_4|^{m/(m-1)} + |X_5|^{m/(m-1)}] \} - 1 = 0 \tag{IV.2.9}$$

The other stress components S_2, S_3, S_4 and S_5 are then derived using the respective calculated ratios X_i.

When the Hill one exponent yield function (n = m) is employed, the computations are somewhat shorter since the value of S_1 is given directly by Eq. IV.2.9. In the case of the quadratic criterion (n = m = 2), however, analytical expressions for the S_i components can be derived, i.e.

$$\begin{cases} S_i = \dot{\varepsilon}_i / 6\alpha \dot{\lambda} & i = 1, 2 \\ S_j = \dot{\varepsilon}_j / 2\beta \dot{\lambda} & j = 3, 4, 5 \end{cases} \tag{IV.2.10}$$

The scalar $\dot{\lambda}$ is then calculated :

$$\dot{\lambda} = \dot{W}/2 = S_i \dot{\varepsilon}_i / 2 = \{(\dot{\varepsilon}_1{}^2 + \dot{\varepsilon}_2{}^2)/12\alpha + (\dot{\varepsilon}_3{}^2 + \dot{\varepsilon}_4{}^2 + \dot{\varepsilon}_5{}^2)/4\beta\} / \dot{\lambda} \tag{IV.2.11}$$

so that $$\dot{\lambda} = \{(\dot{\varepsilon}_1{}^2 + \dot{\varepsilon}_2{}^2)/12\alpha + (\dot{\varepsilon}_3{}^2 + \dot{\varepsilon}_4{}^2 + \dot{\varepsilon}_5{}^2)/4\beta\}^{1/2} \tag{IV.2.12}$$

APPENDIX IV.3

PREDICTION OF R(θ) AND σ(θ) BY THE CMTP QUADRATIC METHOD

Let {hkl}<uvw> represent the ideal orientation of interest, where {hkl} is a crystallographic plane close to the rolling plane, and <uvw> is a crystallographic direction close to the rolling direction. For the present purpose, the subscripts (S), (C) and (xyz) represent the specimen (RD,TD,ND), crystal <100>, and reference axes for the measurement of R(θ), respectively (see Fig.2.2). Let P_1 and P_2 be the matrices for transformation from the crystal to the specimen and from the specimen to the (xyz) axes, respectively.

$$P_1 = \begin{bmatrix} r_1 & u_1 & n_1 \\ r_2 & u_2 & n_2 \\ r_3 & u_3 & n_3 \end{bmatrix} \tag{IV.3.1}$$

where $r_1 = u/\sqrt{u^2+v^2+w^2}$, $r_2 = v/\sqrt{u^2+v^2+w^2}$, $r_3 = w/\sqrt{u^2+v^2+w^2}$
$n_1 = h/\sqrt{h^2+k^2+l^2}$, $n_2 = k/\sqrt{h^2+k^2+l^2}$, $n_3 = l/\sqrt{h^2+k^2+l^2}$
and $u = n \times r$

$$P_2 = \begin{bmatrix} \cos\theta & -\sin\theta & 0 \\ \sin\theta & \cos\theta & 0 \\ 0 & 0 & 1 \end{bmatrix} \tag{IV.3.2}$$

The matrix for transformation from the crystal to the (xyz) axes is therefore P :

$$P = P_1 P_2 = \begin{bmatrix} a_1 & b_1 & c_1 \\ a_2 & b_2 & c_2 \\ a_3 & b_3 & c_3 \end{bmatrix} \tag{IV.3.3}$$

where
$$\begin{cases} a_i = r_i \cos\theta + u_i \sin\theta \\ b_i = -r_i \sin\theta + u_i \cos\theta \end{cases} \qquad \text{for } i=1,2,3 \tag{IV.3.4}$$

The stress tensor in the crystal axes can now be expressed as

$$\underset{\sim}{\sigma}_{(C)} = P\,\underset{\sim}{\sigma}_{(xyz)}\,\tilde{P} \qquad where \qquad \underset{\sim}{\sigma}_{(xyz)} = \begin{bmatrix} \sigma & 0 & 0 \\ 0 & 0 & 0 \\ 0 & 0 & 0 \end{bmatrix} \tag{IV.3.5}$$

which leads to

$$\underset{\sim}{\sigma}_{(C)} = \sigma \begin{bmatrix} a_1{}^2 & a_1 a_2 & a_1 a_3 \\ a_1 a_2 & a_2{}^2 & a_2 a_3 \\ a_1 a_3 & a_2 a_3 & a_3{}^2 \end{bmatrix} \tag{IV.3.6}$$

The deviator stress tensor is then given by

$$\underset{\sim}{S}_{(C)} = \sigma \begin{bmatrix} a_1{}^2 - 1/3 & a_1 a_2 & a_1 a_3 \\ a_1 a_2 & a_2{}^2 - 1/3 & a_2 a_3 \\ a_1 a_3 & a_2 a_3 & a_3{}^2 - 1/3 \end{bmatrix} \tag{IV.3.7}$$

Applying the normality principle to the CMTP yield criterion, we obtain

$$\underset{\sim}{\dot{\varepsilon}}_{(C)} = 2\,\dot{\lambda}\,\sigma \begin{bmatrix} (3a_1{}^2 - 1)/2 & 2a_1 a_2/3 & 2a_1 a_3/3 \\ 2a_1 a_2/3 & (3a_2{}^2 - 1)/2 & 2a_2 a_3/3 \\ 2a_1 a_3/3 & 2a_2 a_3/3 & (3a_3{}^2 - 1)/2 \end{bmatrix} \tag{IV.3.8}$$

and finally, $\underset{\sim}{\dot{\varepsilon}}_{(xyz)} = \tilde{P}\,\underset{\sim}{\dot{\varepsilon}}_{(C)}\,P$, or

$$\underset{\sim}{\dot{\varepsilon}}_{(xyz)} = \dot{\lambda}\,\sigma \begin{bmatrix} (5(a_i{}^4) + 1)/3 & 5(a_i{}^3 b_i)/3 & 5(a_i{}^3 n_i)/3 \\ 5(a_i{}^3 b_i)/3 & 5(a_i{}^2 b_i{}^2)/3 - 1 & 5(a_i{}^2 b_i n_i)/3 \\ 5(a_i{}^3 n_i)/3 & 5(a_i{}^2 b_i n_i)/3 & 5(a_i{}^2 n_i{}^2)/3 - 1 \end{bmatrix} \tag{IV.3.9}$$

where the summations over the index i are extended from 1 to 3.

The strain rate ratio can be deduced from this tensor to be :

$$R(\theta) = \frac{\dot{\varepsilon}_{yy}}{\dot{\varepsilon}_{zz}} = \frac{\frac{5}{3}\,\Sigma\,(a_i^2 b_i^2) - 1}{\frac{5}{3}\,\Sigma\,(a_i^2 n_i^2) - 1} \tag{IV.3.10}$$

With the aid of Eq. IV.3.4, this leads to

$$R(\theta) = \frac{\dot{\varepsilon}_{yy}}{\dot{\varepsilon}_{zz}} = \frac{\frac{1}{4}\Sigma\,(u_i^4 + r_i^4 - 2u_i^2 r_i^2)\sin^2 2\theta + \Sigma\,(u_i^2 r_i^2)\cos^2 2\theta + \frac{1}{2}\Sigma\,(r_i u_i^3 - u_i r_i^3)\sin 4\theta - \frac{3}{5}}{\Sigma\,(r_i^2 n_i^2)\cos^2\theta + \Sigma\,(u_i^2 n_i^2)\sin^2\theta + \Sigma\,(r_i u_i n_i^2)\sin 2\theta - \frac{3}{5}} \tag{IV.3.11}$$

Furthermore, since $\dot{W} = 2\,\dot{\lambda} = \underset{\sim}{\sigma}_{(xyz)}\,\underset{\sim}{\dot{\varepsilon}}_{(xyz)} = \dot{\lambda}\,\sigma^2\,(5\,\Sigma\,a_i^{\,4} + 1)\,/\,3$, it can be shown that

$$\sigma(\theta) = \{(5\,\Sigma\,a_i^{\,4} + 1)\,/\,6\,\}^{-1/2}$$

or

$$\sigma(\theta) = \{\,[\,5\,\Sigma\,(\,r_i\cos\theta + u_i\sin\theta\,)^4 + 1]\,/\,6\}^{-1/2} \tag{IV.3.12}$$

APPENDIX V.1

CONVEXITY OF A YIELD SURFACE DERIVED FROM A COMBINATION OF CONVEX YIELD LOCI

In this appendix, it is shown that the combination of convex yield loci at constant strain rate ratios (Taylor) leads to a convex overall surface, whereas the Sachs averaging technique (carried out at a constant stress ratio, Fig. 4.8) may lead to locally concave results.

Definitions of the convexity

(i) geometric definition

A function $F(S_i) = 0$ (and thus its representation in S_i space) is convex if

$$(\vec{S}' - \vec{S}).\vec{\dot{\varepsilon}} < 0 \tag{V.1.1}$$

whatever the vectors $\vec{S}$ and $\vec{S}'$ located on the locus $F(S_i) = 0$. Here, $\vec{\dot{\varepsilon}}$ is the normal to the surface at the point S (Fig. V.1.1). This expresses the geometric fact that the point S' can never be exterior to the tangent to the locus at the point S.

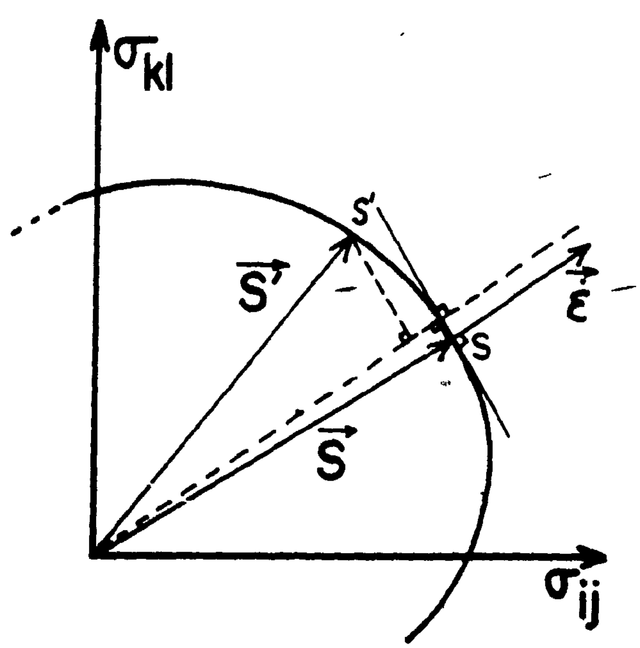

Fig. V.1.1 Geometric derivation of the convexity condition for a general yield surface. $\vec{\dot{\varepsilon}}$ is the normal to the locus at the point S.

(ii) mathematical definition

A function $F(S_i)=0$ (and thus its representation in S_i space) is convex if the Hessian matrix $H=\partial^2F / \partial S_i \partial S_j$ is positive semi-definite, i.e. all its eigenvalues are positive (or zero). This definition provides a very practical test for the convexity of a continuum yield function whose equation is known. It was used successfully in appendix IV.1.

Yield surface combination at constant strain rate ratio

In this case, the first definition is the easiest to use. Let us define N yield surfaces, $F_i(S_k)=0$ (for $i=1$ to N and $k=1$ to P),which are assumed to be convex. The 'average' locus is defined as the locus of the points

$$S_j = \sum_{i=1}^{N} a_i S_{ij} \qquad j=1 \text{ to } P \qquad \text{(V.1.2)}$$

where a_i are the weighting factors ($\Sigma\, a_i=1$). The N components S_{ij} are calculated from the imposed strain rate components by means of the normality rule

$$\dot{\varepsilon}_j = \dot{\lambda}_i \frac{\partial F_i(S_k)}{\partial S_{ij}} \qquad \text{(V.1.3)}$$

applied to the ith yield locus $F_i(S_k)=0$ and inverted to give the S_{ij} components.

Each of the N functions F_i is convex, so that

$$(\vec{S}'_i - \vec{S}_i)\vec{\dot{\varepsilon}} \le 0 \qquad \forall S'_i \in F_i \qquad \text{(V.1.4)}$$

where S_i is the point on the ith locus whose normal is $\vec{\dot{\varepsilon}}$. It is equivalent to write Eq. V.1.4. in terms of the S_i and $\dot{\varepsilon}$ components

$$\sum_{j=1}^{P} (S'_{ij} - S_{ij})\dot{\varepsilon}_j \le 0 \qquad \forall S'_i \in F_i \qquad \text{(V.1.5)}$$

Since the a_i parameters are positive ($a_i \in [0,1]$), it follows that

$$\sum_{j=1}^{P} (a_i S'_{ij} - a_i S_{ij})\dot{\varepsilon}_j \le 0 \qquad \forall S'_i \in F_i \quad \forall i \in [1,N] \qquad \text{(V.1.6)}$$

so that

$$\sum_{i=1}^{N} [\sum_{j=1}^{P} (a_i S'_{ij} - a_i S_{ij})\dot{\varepsilon}_j] \leq 0 \qquad \forall S'_i \in F_i \qquad \text{(V.1.7)}$$

Using the permissible permutation of the sums, the following is obtained

$$\sum_{j=1}^{P} [\sum_{i=1}^{N} a_i S'_{ij} - \sum_{i=1}^{N} a_i S_{ij}]\, \dot{\varepsilon}_j \leq 0 \qquad \forall S'_i \in F_i \qquad \text{(V.1.8)}$$

As long as the S'_i vectors can be chosen arbitrarily on each surface F_i, it is possible to select them to correspond to the same strain rate state. In this way, the vector S' defined as $S'_j = \Sigma\, a_i\, S'_{ij}$ belongs to the overall locus since its components satisfy Eq. V.1.2. Eq. V,1.8 thus leads to :

$$\sum_{j=1}^{P} (S'_j - S_j)\dot{\varepsilon}_j \leq 0 \qquad \text{(V.1.9)}$$

and then to :

$$(\vec{S}' - \vec{S}).\vec{\dot{\varepsilon}} < 0 \qquad \text{(V.1.10)}$$

whatever the vector $\vec{S'}$. As long as this demonstration can be carried out for any vector $\vec{\dot{\varepsilon}}$ and therefore for any vector $\vec{S}$ of the overall locus, the latter is convex.

Yield surface combination at constant stress ratios

The simple example shown in Fig. V.1.2 illustrates the local non-convexity of such a combination. The two functions F_1 and F_2 are obviously convex, whereas their combination is not.

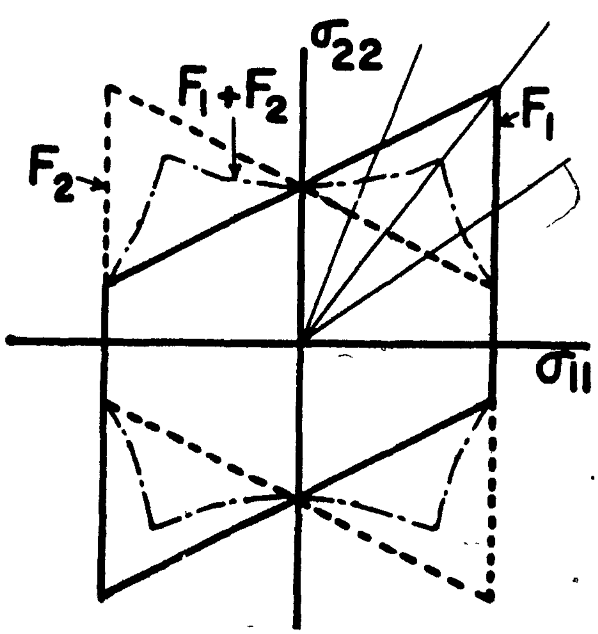

Fig. V.1.2 Yield surface combination at constant stress ratios. F_1 and F_2 are convex, whereas "F_1+F_2" is not.